Tether Dynamics Analysis and Guidance & Control Design for Active Space Debris Removal

H. T. K. Linskens

Technische Universiteit Delft

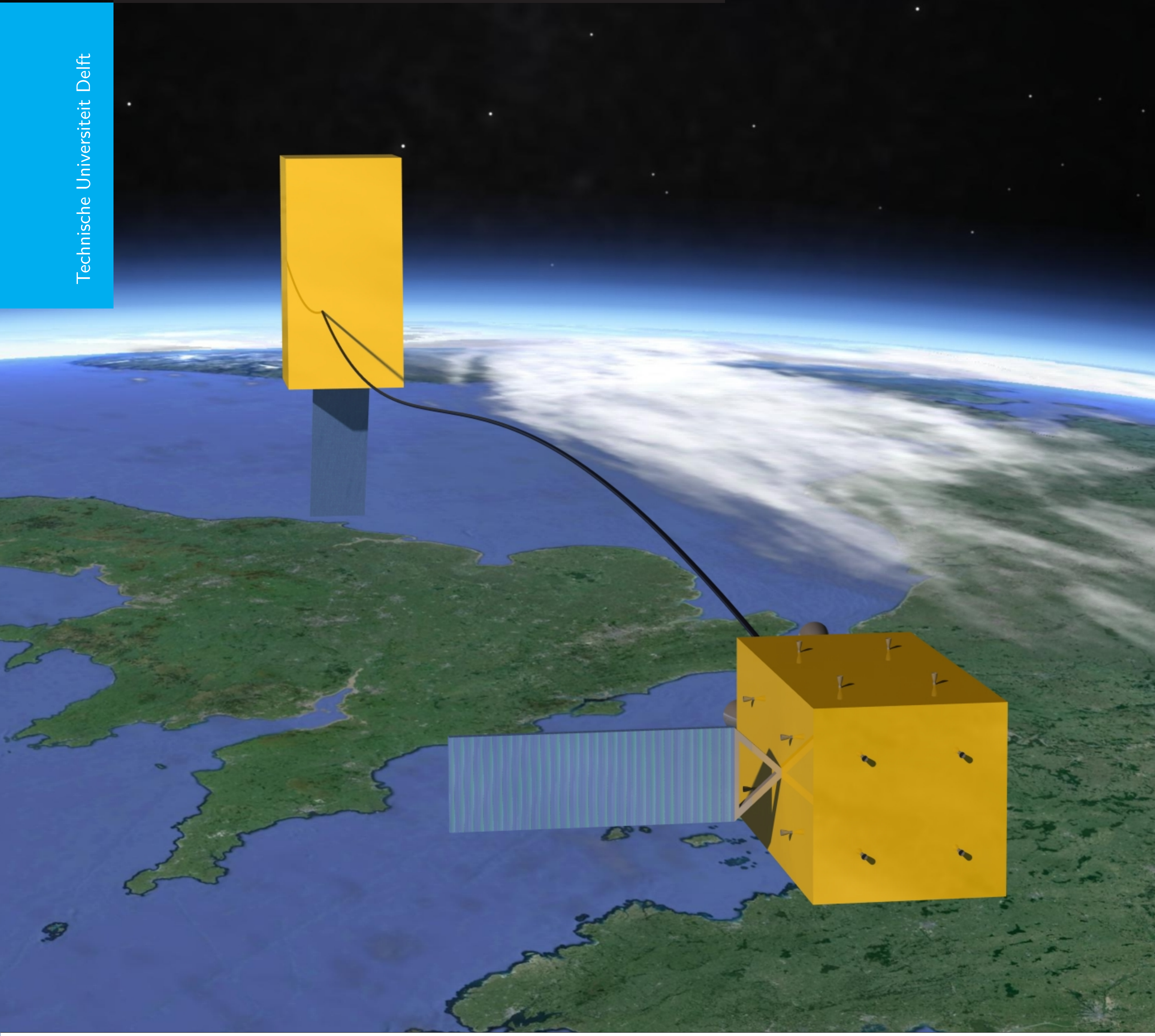

Delft University of Technology

Challenge the future

Cover image background courtesy of Google Earth™, satellite models made using Dassault Systèmes Catia®

TETHER DYNAMICS ANALYSIS AND GUIDANCE & CONTROL DESIGN FOR ACTIVE SPACE DEBRIS REMOVAL

by

H. T. K. Linskens

in partial fulfillment of the requirements for the degree of

Master of Science
in Aerospace Engineering

at the Delft University of Technology,
to be defended publicly on Friday April 24 2015 at 10:00 AM.

Supervisor:	Dr. ir. E. Mooij	TU Delft
Thesis committee:	Prof. dr. ir. P. N. A. M. Visser,	TU Delft
	Ir. K. Cowan,	TU Delft
	Dr. M. Oort,	Airbus Defence & Space Netherlands

“Remember kids, the only difference between screwing around and science is writing it down”

- Adam Savage

PREFACE

Since before I can remember, I have had a near-obsession with everything related to outer space. Whether it was in the form of astronomy, science fiction, or actual space flight, something about the vast universe beyond the frail atmosphere of our home planet has always been able to capture my imagination. Therefore, I like to see this thesis not only as the final result of my six years of study at the Delft University of Technology, but also as the culmination of a life-long fascination with the topic.

Sentimental reminiscing aside, I would like to spend a few words on the background of this thesis. When ESA released a call for proposals for the design of a GNC system for deorbiting the derelict Envisat in early 2013, it was originally envisioned that the Delft University of Technology would join forces with Dutch Space, now Airbus Defence & Space Netherlands, to submit such a proposal. Furthermore, such a proposal would permit room for an MSc thesis topic, and the MSc coordinator of our department, Ron Noomen, suggested me as a candidate. While the actual proposal itself unfortunately fell through, the thesis topic remained, along with the cooperation with Dutch Space, who graciously allowed me to use the GGNCSIM simulator libraries. With the actual mission to deorbit Envisat well underway, now is an exciting time to be working in the field of active debris removal!

Of course, I could not have tackled this challenging thesis topic on my own, and owe a debt of gratitude to a great many people. First, and foremost, I would like to thank my direct supervisor at the Delft University of Technology for this thesis research, Erwin Mooij, for being an outstanding tutor as well as a great sounding board for my ideas. The discussions we had, both on and off topic, proved invaluable for the successful completion of the research and for the preservation of my peace of mind. I would also like to thank Ron Noomen, also of the Delft University of Technology, for proposing me as a candidate for this research in the first place. Furthermore, I would like to thank Marc Oort, Marcel Ellenbroek, and Lex Meijer, all of Dutch Space (forgive my use of the old name), for allowing me to use GGNCSIM, as well as attentively discussing my findings. Remaining in the space industry, I would like to thank Alexander Cropp, of ESA ESTEC, for patiently answering all my questions on the topic. To all my fellow graduate students in the MSc rooms at the faculty, thank you all for making the time I spent there unforgettable. Finally, I would like to thank my family, friends, and girlfried for supporting (and putting up with) me over the course of the past year: I wouldn't have been able to do it without you.

H. T. K. Linskens
Delft, April 2015

ABSTRACT

Recent years have seen a steep increase in research being performed towards active space debris removal: space debris has proven to be a very real threat to operational spacecraft, and studies indicate that the frequency of collisions will only increase if nothing is done to remove large pieces of debris. In particular, ESA has done studies towards removing Envisat from orbit, after communications were lost and were unable to be reestablished. To this end, a scenario was proposed in which a robotic chaser satellite would use a tether to interface with Envisat, either using a net or a harpoon, and proceed to deorbit the resulting tethered system.

This research tackles two main challenges relating to this scenario. First, a suitable model for the tether was developed by discretizing the tether into a number of point masses and massless Kelvin-Voigt elements. The influence of the number of nodes was investigated, showing that increasing the number of nodes used does not significantly increase the fidelity of the solution. Therefore, it was chosen to model the tether with two nodes and three elements. Additionally, multiple combinations of tether length, stiffness, and damping were investigated.

Second, a preliminary design for a guidance and control system was developed. This system uses multiple fixed-duration burns as the main deorbit strategy. The guidance system controls the relative state of the chaser with respect to the target during and after these main engine burns: during burns, a hold point is established at the equilibrium length of the tether, and during coasting phases the tether is kept slightly in tension to reduce target and tether motion. At the transition between thrusting and coasting phases, the thrust is gradually throttled down to further decrease these motions. The control system is designed to keep the chaser level with the local horizon at all times. During the design process, the performance of guidance and control systems based on linear quadratic regulators was used as a baseline for the same systems based on sliding-mode control. Furthermore, three different thrust levels for the deorbit burn were examined.

It was found that the system based on sliding-mode control offered considerable performance improvements over the LQR-based system: total propellant consumption was reduced by an average of 48%, while adhering to the same tolerances. Furthermore, it was determined that high thrust levels are desirable for both reducing propellant consumption as well as reducing target rotation. In terms of safety, collision can best be avoided by using lower thrust levels or longer tethers. While this seems to conflict with minimizing required propellant, minimal target rotation and minimal propellant consumption can still be achieved by using long tethers with high stiffness. Finally, it was found that while sensitive to small changes in the initial conditions, the precision of the terminal point is still high enough to allow the target to be deorbited in the Soutỉ Pacific Ocean. This result was independent of tether model, although higher thrust levels do increase the precision further.

CONTENTS

LIST OF SYMBOLS

Symbol	Description	Unit
A	Cross-sectional area	[m^2]
a	Semi-major axis	[m]
$\mathbf{C}$	Direction cosine matrix	[-]
C_D	Drag coefficient	[-]
c	Damping coefficient	[Ns/m]
$\mathscr{E}_{tot}$	Orbital energy	[J]
E_{mat}	Young's modulus	[Pa]
E	Eccentric anomaly	[rad]
$\hat{\mathbf{e}}$	Unit Euler-axis vector	[-]
$\mathbf{e}$	Eccentricity vector	[-]
e	Eccentricity	[-]
$\mathbf{F}$	Generic force vector	[N]
F	Generic force magnitude	[N]
g_0	Earth surface gravity	[m/s^2]
$\mathbf{H}$	Generic angular momentum vector	[kgm^2/s]
$\mathbf{h}$	Orbital angular momentum vector	[m^2/s]
h	Altitude	[m]
$\mathbf{I}$	Inertia tensor	[kgm^2]
I_{sp}	Specific impulse	[s]
i	Inclination	[rad]
J_2	Earth oblateness gravitational coefficient	[-]
k	Spring constant	[N/m]
L_0	Natural length	[m]
L	Length	[m]
M	Mean anomaly	[-]
m	Mass	[kg]
N	Number of tether nodes	[-]
n	Mean motion	[rad/s]
$\mathbf{Q}_w$	LQR state weighting matrix	[-]
$\mathbf{q}$	Quaternion vector	[-]
q_i	Quaternion element	[-]
$\mathbf{R}$	Position vector	[m]
$\mathbf{R}_w$	LQR control weighting matrix	[-]
R_E	Earth radius	[m]
r	Instantaneous satellite radius	[m]
$\mathbf{S}$	Linear switching surface matrix	[-]
$\mathbf{s}$	Sliding mode	[-]
$\mathbf{T}_r$	Regular form transformation matrix	[-]
t	Generic time	[s]
$\mathbf{V}$	Velocity vector	[m/s]
$\mathbf{x}$	State vector	[-]

α	Generic rotation angle	[rad]
δ_{BL}	Control boundary layer width	[-]
δ_{CM}	Control margin	[-]
δ_{DB}	Deadband width	[-]
δ_L	Offset constant	[m]

$\boldsymbol{\epsilon}$	Rate of extension vector	[m/s]
ζ	Damping ratio	[-]
θ	Euler pitch angle	[rad]
μ	Gravitational parameter	[m^3/s^2]
ϕ	Euler roll angle	[rad]
ψ	Euler yaw angle	[rad]
ν	True anomaly	[rad]
ρ	Density	[kg/m^3]
$\boldsymbol{\sigma}$	Switching surface matrix	[-]
τ	Time of previous periapsis passage	[s]
Ω	Right ascension of the ascending node	[rad]
$\boldsymbol{\omega}$	Angular velocity vector	[rad/s]
ω	Argument of periapsis	[rad]
ω_d	Damped natural frequency	[rad/s]
ω_n	Natural frequency	[rad/s]

Subscript	**Description**	**Unit**
0	Initial	[-]
arm	Moment arm	[-]
b	Burn	[-]
C	Chaser	[-]
c	Control	[-]
D	Drag	[-]
d	Damping	[-]
E	Earth	[-]
eq	Equilibrium	[-]
eqv	Equivalent	[-]
err	Error	[-]
ext	External	[-]
f	Final	[-]
G	Spacecraft geometric reference frame	[-]
g	Guidance	[-]
H	Hill (Clohessy-Wiltshire) reference frame	[-]
$hold$	Hold point	[-]
I	Earth-centered inertial reference frame	[-]
i,j,k	Generic counters	[-]
lim	Limit	[-]
nom	Nominal	[-]
off	Offset	[-]
orb	Orbit	[-]
$proj$	Projected	[-]
$prop$	Propellant	[-]
R	Earth-centered, Earth-fixed reference frame	[-]
reg	Regular	[-]
rel	Relative	[-]
s	Satellite	[-]
sec	Secular	[-]
T	Target	[-]
$teth$	Tether	[-]
thr	Thrust	[-]
tr	Transfer	[-]

LIST OF ACRONYMS

AOCS	attitude and orbit control system
ADR	active debris removal
CW	Clohessy-Wiltshire
DCM	direction cosine matrix
EAM	European Apogee Motor
ECI	Earth-centered inertial
ECEF	Earth-centered, Earth-fixed
EDT	electrodynamic tether
EOL	end-of-life
ESA	European Space Agency
GEO	geostationary orbit
GGNCSIM	Generic Guidance, Navigation, and Control Simulator
GC	guidance and control
GNC	guidance, navigation, and control
IADC	Inter-Agency Space Debris Coordination Committee
ISS	International Space Station
LEO	low-Earth orbit
LQR	linear-quadratic regulator
MXT	momentum exchange tether
RAAN	right ascension of the ascending node
SMC	sliding mode controller
SPOUA	South Pacific Ocean Unpopulated Area
SSO	Sun-synchronous orbit
TLE	two-line element set
TSDS	tethered satellite-debris system
TCP	tether connection point
USM	Unified State Model
V&V	verification and validation

1

INTRODUCTION

Since the launch of the first satellite Sputnik in 1957, mankind has placed countless spacecraft in orbit around the Earth. Today, less than 10 percent of the trackable objects orbiting the Earth are operational satellites. The remainder, along with the myriad of objects in orbit too small to observe, is simply junk, and has been gathered under the common denominator of space debris. Space debris is becoming an increasingly serious problem, which has been underlined by recent events, such as the collision of the operational Iridium 33 and the inactive Kosmos 2251 satellites on the February 10, 2009 [1]. Such events, along with the longstanding studies towards the evolution of debris belts by Kessler [2], have given a sense of urgency to find a solution to the space debris problem. In the worst-case scenario, some orbits might already have a sufficiently dense debris population to render them useless in the future, unless something is done to lower the collision risks. Furthermore, it has become increasingly clear that to achieve this, the only solution is that space debris must be actively removed from orbit. In the current economical, social, and political environment, this must additionally happen in a reliable, safe, and cost-effective manner.

To provide such a means for active space debris removal, the application of orbital tethers is a promising field of study. In the most common theoretical applications, orbital tethers offer the possibility of orbital transfer without expending traditional propellants, and can therefore be very mass-effective. Additionally, they offer a method of interfacing with the debris to be removed. However, issues still exist regarding the safety and practicality of orbital tethers: these tethers tend to be quite large and are therefore susceptible to debris strikes themselves. Much research is being done towards increasing safety and practicality of orbital tethers, but very few missions have actually flown with them as of yet. Despite this, the use of tethers to actively remove space debris from orbit seems one of the most viable options available. With this in mind, it is possible to formulate the following main research question:

"How can a tethered system of an active satellite and a large piece of space debris in Low-Earth Orbit be safely, reliably, and cost-effectively removed from orbit?"

From this research question, more specific research objectives could be distilled: the first objective was to develop an appropriate model for the dynamics of a tethered system of an active satellite and a large piece of space debris; the second was to develop a preliminary design for a guidance and control system, and to asses the influence of the tether parameters on mission performance.

Thus, two main fields of study were identified from the research objectives [3]. First, it was clear that the dynamics of the tethered system would have to be adequately modeled to be able to draw any meaningful conclusions from the research. Therefore, suitable models for the tether dynamics were created and verified. Second, using these dynamics models, a preliminary design of a guidance and control system for the active debris removal satellite was developed. This satellite, known in shorthand as the chaser, would use the tether to interface with the selected large space debris, or target, and to transfer the momentum required for orbital removal to the target. Within these fields, the effect of different modeling and physical parameters of the tether itself will be investigated, along with different possibilities for stabilizing the resulting system while achieving a successful debris removal mission. Ultimately, this is done to identify relationships between the tether properties and mission-performance parameters. This allows recommendations to be formed as to which models are most suited for particular requirements, again relating these back to reliability, safety, and cost-effectiveness.

To achieve this, Chapter 2 will kick off by more precisely defining the problem space, as a good definition of this permits the research to be conducted in a more focused manner. This includes stipulated requirements as well as the scope of the research performed. Chapter 3 then proceeds to summarize the mission heritage of space debris removal and orbital tethers. This is done to provide a conceptual base of what techniques are currently being considered for active debris removal, and what the state of the art is concerning orbital tethers. Then, Chapter 4 will provide an overview of the reference systems used to express the mathematical models of the system dynamics, which will be treated in Chapter 5. This will cover the orbital and angular dynamics of the chaser and the target, as well as the dynamical model of the tether itself. Chapter 6 will then proceed to detail the theoretical background of the chosen control algorithms in a general sense. Using the developed mathematical models and control algorithms, the exact implementation of these will be discussed in Chapter 7. Finally, the results of the analysis will be presented in Chapter 8, allowing conclusions to be drawn and recommendations to be formulated in Chapter 9.

2

PROBLEM FORMULATION

ADR represents a field of research involving missions and system designs which are highly complex in nature. Thus, it was important to clearly demarcate the limits of the problem to be tackled during the course of the performed research. This chapter will therefore aim to provide the reader with a complete understanding of the problem space, as well as provide an overview of the assumptions that were made to make the problem manageable. First, the problem background will be summarized in Section 2.1, after which the boundaries of the problem space will be defined in Section 2.2.

2.1. PROBLEM BACKGROUND

The main driver behind the performed research is the unexpected loss of contact with the European Space Agency (ESA) Earth-observation satellite Envisat on April 8, 2012 [4]. Envisat is the largest Earth-observation satellite ever launched, clocking in at more than 8000 kg in mass and a spacecraft bus length of nearly 10 m. Furthermore, Envisat is located in a densely-populated and highly-popular Sun-synchronous orbit (SSO), which is home to many other operational Earth-observation satellites. The lack of a communications link coupled with its massive size thus makes it a serious collision hazard to operational satellites. Besides posing a threat due to the risk of a direct collision, large pieces of orbital debris, such as Envisat, also represent a long-term hazard to the orbits they populate. This will be discussed in more depth in Section 3.1.

Because of this, ESA initiated several studies towards the possibilities of reducing the threat posed by Evnisat [5]. From these studies, it was concluded that deorbiting Envisat was the most viable option for eliminating the risk it poses to the current satellite population. Not only would this be the first mission to actively remove space debris from orbit, it would also provide a technological basis for doing so more in the future. Again, the necessity of this will be further detailed in Section 3.1.

Subsequent investigations by ESA towards deorbiting Envisat have resulted in a number of mission concepts [5]. All of these concepts involve sending a robotic satellite to rendezvous with Envisat, capture it, and subsequently deorbit it using a propulsion system on-board the chaser. Different capture mechanisms were examined in these mission concepts, among which is the idea to catch Envisat with a net or harpoon. This method would thus require the use of a tether to transfer required momentum to Envisat to remove it from orbit.

The concept of using orbital tethers has been a topic of much research and debate in the past several decades, a topic which will be discussed in more detail in Section 3.4. Although orbital tethers are a very promising field of study, they also represent immense challenges for mission and system design, among others with respect to the GNC of the tethered satellites. Thus, ESA released a call for proposals for the GNC system of a robotic “chaser” satellite with the objective to deorbit Envisat, ambiguously dubbed the “target” [3].

Based on the proposed Envisat deorbit scenario, an assignment for the performed thesis research was created. This research was focused on two main points: the first was to investigate the dynamics of the system in orbit formed by the target and the chaser connected by a tether. The second was to design a GNC system capable of successfully completing the proposed mission.

2.2. DEFINITION OF PROBLEM SPACE

The design of a complete GNC system, along with the required modeling of the system dynamics, is a complex task. Therefore, it was of importance to clearly define the problem space for the performed research. This would not only prevent the research from taking much longer than the allocated time, but would also aid in performing focused literature reviews and thus efficient gathering of knowledge. Furthermore, two main topics were the focus of this research: the analysis of the tethered system dynamics and the design of a suitable GNC system. These two areas are strongly coupled, and it is therefore important to know exactly what aspects of each need to be investigated.

First, an overview of the considered ADR scenario as proposed by ESA will be given, such that the elements relating to this can be more clearly defined. Then, the most critical areas within this context were identified, allowing the topics for research to be determined. This was first done for the topic of orbital tethered system dynamics, and then done for the field of GNC system design.

2.2.1. ADR SCENARIO OVERVIEW

The overarching ESA study towards the removal of Envisat has been termed e.deorbit, as part of their Clean Space program [5]. This study comprises both the investigations towards tethered options for deorbiting Envisat, as well as more conventional clamping mechanisms or robotic arms. Particularly for the tethered option, the deorbit GNC system was identified as a major challenge, inciting a call for proposals for such a system [6].

ESA has proposed a scenario in the context of which the GNC system should operate [3]. The scenario begins with the chaser and target already tethered together, with both being in a circular SSO at 800 km altitude. This is important to note, as recent studies have indicated that Envisat has begun to tumble in its orbit, making the capture and subsequent tranquilization phases distinctly nontrivial [7]. Nonetheless, it was assumed that the rendezvous, capture, and stabilization of the target has already been performed successfully for the performed research.

Then, the center of mass of the target defines the local reference frame in which the relative state of the chaser can be expressed (discussed further in Chapter 4). In this frame, the chaser starts a certain distance behind the target with the tether slack, as well as being slightly below and out-of-plane with the target. This initial condition for the simulation is schematically shown in Figure 2.1.

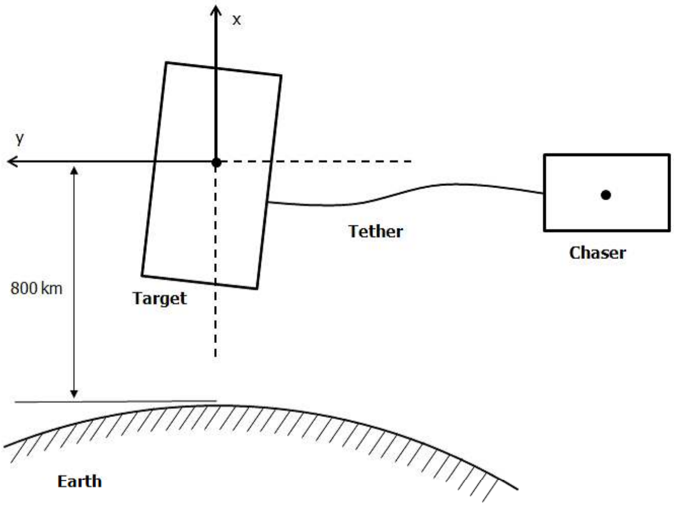

Figure 2.1: Initial condition for the TSDS simulation scenario.

From the initial condition detailed above, the chaser must deliver the required momentum for deorbit to the target, and re-enter the atmosphere along with it [3]. It is important to note that the tether is not connected to the center of mass of either the chaser or the target, so during the mission both forces and moments will be induced by the tether. Furthermore, the target was assumed to be completely uncooperative, so no internal "safe mode" would help stabilize its attitude and no information would be actively supplied to the chaser. These factors are important when considering the design of the GNC system of the chaser.

2.2.2. TETHERED SYSTEM ANALYSIS

One of the groundbreaking features of the proposed ADR mission is to use a tether to connect the chaser to the target. As the dynamics of such systems are still the subject of much research (see Section 3.4, a number of different baseline models for the tether were presented by ESA [3]. These models are shown in Table 2.1, with E_{mat} being the Young's modulus of the material, A the cross-sectional area of the tether, L_0 the natural tether length, m the tether mass, N the number of tether nodes, and c the tether damping constant.

Table 2.1: Physical tether models proposed by ESA [3].

ESA ID	E_{mat} [Pa]	A [m^2]	L_0 [m]	m [kg]	N	c [Ns/m]
1	$1 \cdot 10^8$	$2 \cdot 10^{-5}$	200	5	2	0.3
2	$1 \cdot 10^8$	$2 \cdot 10^{-5}$	200	-	0	0.3
3	$1 \cdot 10^8$	$2 \cdot 10^{-5}$	800	20	2	0.3
4	$4 \cdot 10^8$	$2 \cdot 10^{-5}$	80	2	2	0.3
5	$1 \cdot 10^8$	$2 \cdot 10^{-5}$	200	5	2	0.001
6	$1 \cdot 10^8$	$2 \cdot 10^{-5}$	200	5	4	0.3

The proposed tether models encompass a range of different parameters to test, both in terms of modeling the tether as well as its physical properties. Model 1 represents the nominal tether model. Models 2 and 6 then change the number of nodes used to represent the tether, and thus are designed to compare different simulation models of the tether. Model 3 represents a long tether with nominal stiffness and damping, while model 4 represents a short tether with high stiffness and nominal damping. Finally, model 5 reduces the damping coefficient dramatically, while maintaining the nominal stiffness value.

The models presented in Table 2.1 provide a baseline set for investigations towards the influence of the listed tether parameters on the deorbiting performance of the chaser. This forms the main challenge for modeling the system dynamics, as the translational and rotational motion of arbitrary bodies in Earth orbit is very well understood. Thus, a good representation for the tether dynamics had to be created, verified, and integrated in the complete model. This model was based on discretizing the continuous tether into a discrete number of nodes N to simplify the analysis [3], which will be discussed further in Section 5.4.

To allow for more time for the development of the mathematical model of the tether dynamics, it was decided to use the Generic Guidance, Navigation, and Control Simulator (GGNCSIM) made by Dutch Space (now Airbus Defense & Space Netherlands) to develop the orbital environment and dynamics model. GGNCSIM consists of a set of Simulink libraries, which are designed to facilitate the building of a simulator for a spacecraft in the space environment [8, Ch. 15]. To this end, these libraries include environmental models, equations of motion, frame transformations, and various mathematical vector and matrix operations not indigenous to Simulink. Furthermore, extensive verification and validation (V&V) has been performed on these models, ensuring that if properly implemented, the results will be reliable.

GGNCSIM has a very modular nature, but does not actually provide the simulator itself. Instead, it provides the building blocks necessary for the rapid construction of simulators specifically tailored to suit the needs of the user. Thus, it is not hampered by the limitations of currently existing simulators, and allows the user a lot of freedom when evaluating a specific scenario. Furthermore, this modular nature makes it very intuitive to integrate the designed tether models.

With these points in mind, it was possible to determine a list of tasks which must be performed with respect to modeling the system dynamics:

1. Construct models for chaser and target dynamics using GGNCSIM libraries.
2. Develop the mathematical model for the tether dynamics.
3. Integrate the tether dynamics model into the simulation.
4. Evaluate the proposed tether models with respect to mission performance.
5. If necessary, define additional tether models to better identify relations between tether parameters and mission performance.
6. Evaluate the new tether models and compare them to the baseline models.
7. Evaluate the relations between mission performance and tether parameters.

2.2.3. GNC SYSTEM DESIGN

The design of a GNC system consists, as the name suggests, of three main components: guidance, navigation, and control [9]. Generally speaking, guidance relates to the translational motion of the satellite system, navigation covers the determination of the state of the system, and control relates to the rotational motion of the satellite system. More specifically, the navigation system first uses sensors and other measurement devices to measure the state of the system [10]. This includes both its position and velocity as well as its orientation and rotational rate. Both the guidance and control systems then use this measured state to generate commands for actuators, which then apply forces and/or moments to the system according to these commands.

The general relations between the system dynamics, guidance, navigation, and control of a satellite in orbit can be schematically represented as in Figure 2.2 (adapted from [9]). Note that in some cases, such as for reentry vehicles or vehicles with a fixed engine, the attitude of the vehicle might influence its translational motion, as well.

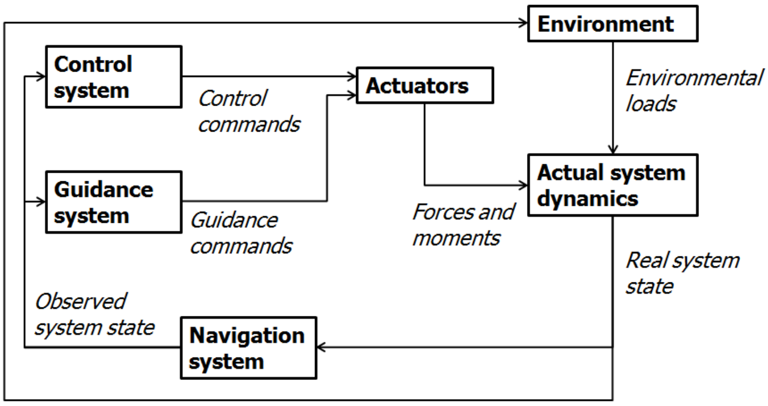

Figure 2.2: Schematic representation of a typical GNC system for a satellite.

Generally, a GNC system implemented on an actual satellite will have to cope with the rigors of reality. This implies that it is not trivial to precisely determine the states of the system at any given time, and that the behavior of the system may not be exactly as expected. For this reason, the system dynamics poses a problem for the development of a simulator: as all test will be performed computationally, it is necessary to have some kind of model of the actual system behavior. This model must provide reasonable approximations of the behavior of the satellites, as well as the tether, in the orbital environment.

It was chosen to focus on the system dynamics, guidance, and control, in descending order of importance, while leaving navigation out of the equation altogether. However, this does not mean that navigation is less important, as obtaining sufficiently accurate information on the system state can be immensely challenging as well. Nonetheless, it was decided that navigation was the least relevant when considering the influence of tether dynamics on the system performance. This was also done to keep the research within the allocated time. The system dynamics have already been discussed in the previous section; thus, a short discussion on the guidance and control (GC) system will be shown next.

GUIDANCE

The development of a suitable guidance system is of great importance for a tethered ADR mission. Since the tether is elastic, there is a large risk of collision between the chaser and the target during operation. Additionally, it is required to somehow deorbit the TSDS to achieve mission success. Therefore, the goal of the guidance system is twofold: first, it must deorbit the TSDS, and second, it must do so without the chaser and target colliding with each other.

The simplest form of using a tether for ADR is to use it as a medium for transferring thrust produced by the chaser to the target. ESA proposed a baseline strategy for the guidance system based on this principle, using multiple fixed-duration, constant-magnitude burns from the chaser to lower the periapsis of the TSDS to induce a controlled reentry [3]. This strategy was used as a starting point for the guidance system development, and based on the results of the analysis it would be judged if this strategy was sufficient or if alternatives had to be devised. For collision avoidance, no baseline strategy was presented, thus the design of guidance logic to achieve this was also necessary.

It was decided to implement two types of control algorithms in the guidance system, which will be discussed further in Chapter 6. First, a baseline for performance would be established using a traditional state-feedback controller in the form of a LQR. This type of control system has been widely used, and provides an optimal solution to the control problem. Then, it was chosen to implement a SMC-based system as well: SMCs have proven to be very capable at dealing with uncertainties in the model [11], and thus are promising for application in a tethered system. The performance of the SMC could then be compared to that of the LQR baseline. Thus, it was possible to define the tasks necessary for the design of the guidance system:

1. Define constraints with respect to the safety of the operation.
2. Define a collision-avoidance strategy in compliance with the baseline strategy.
3. Set up the LQR and SMC guidance algorithms.
4. Set up the baseline system using fixed-duration, constant-magnitude burns.
5. Evaluate this baseline system with respect to safety and performance.
6. Evaluate the performance of the SMC compared to the LQR baseline.

CONTROL

Finally, the control system was expected to be the least complex part of the GC system development, but this does not make it any less essential. As the main thruster is fixed along one of the chaser body axes [3], the control system is responsible for keeping the chaser in the correct orientation during deorbit burns in the baseline strategy. This correct orientation is defined as simply along the y-axis of the target local reference frame. Furthermore, this orientation was to be maintained at all times, effectively forming a very simple control law.

As with the guidance system, an LQR and an SMC were implemented in the control system, resulting in a similar list of tasks to be performed. These can then be compared to each other in terms of performance. A complete list of tasks relating to the control system is shown below:

1. Set up the LQR and SMC control algorithms.
2. Set up the baseline system for keeping the chaser oriented correctly at all times.
3. Evaluate the baseline system with respect to mission performance.
4. Evaluate the performance of the SMC compared to the LQR baseline.

2.2.4. CONCLUDING REMARKS

In this section, the main challenges of this research were identified. For the tethered system analysis, it was determined that the design of an appropriate model and the selection of suitable physical parameters is of primary importance. This is due to the fact that the proposed concept is beyond the state-of-the-art for orbital tethers, as discussed later in Section 3.4.

For the GC system, it was decided to implement two different control algorithms, with the more common LQR providing benchmark performance characteristics with which to compare the results from the more advanced SMC. These would be implemented both in the guidance and the control system, and the effect of each on mission performance will be investigated. It was also determined that collision avoidance is a main goal of the guidance system, requiring the development of a suitable guidance law. The control system has as primary function to keep the chaser level with the local horizon at all times.

3

MISSION HERITAGE

The idea to remove space debris from orbit using tethers poses many challenges to the design and testing of a GC system. Therefore, an important first step was investigating the mission heritage of both space debris removal activities and orbital tethers. Thus, this chapter aims to provide a good overview of the heritage and legacy of both fields: Sections 3.1 and 3.2 will examine the history and future of space debris removal in practice, respectively. Then, the heritage of orbital rendezvous and proximity operations will be discussed in Section 3.3, as this proves a vital field for ADR. Finally, the history of realized space-tether missions and the current research in this field are summarized in Section 3.4.

3.1. HISTORY OF SPACE DEBRIS REMOVAL

In this section, a brief history of space debris removal activities up to the present will be discussed. Currently, space debris mitigation is a more accurate description than space debris removal for the activities being performed, as these have so far been confined to the realms of detecting and tracking objects in orbit, and the limitation of the growth of the population of these objects. A few exceptions exist to this, however. First, the tracking of space debris will be clarified, and second, a summary of the methods used to limit the growth of space debris will be given.

3.1.1. DETECTION AND TRACKING OF SPACE DEBRIS

Before anything can be done about mitigating space debris, these objects must be detected and tracked. The United States Space Command catalogues and tracks around 15,000 objects in Earth orbit, with sizes upwards of 10 cm in LEO and upwards of 1 m at geosynchronous altitude [12, Ch. 7.5]. The orbits of these objects, of which only around 1000 are operational satellites, are analyzed and the predictions made can be used by satellite operators to perform avoidance maneuvers [12, Ch. 19.2]. A computer generated image of the objects in Earth orbit currently being tracked is shown in Figure 3.1.

However, a significant population of objects smaller than the 10 cm detection limit exists in low-Earth orbit (LEO) due to previous collisions or simply by operational practices. This consists of objects such as lost lens caps or explosive bolt fragments [12, Ch. 7.5]. These objects cannot be effectively detected or tracked, meaning the only mitigation method currently in existence is to add shielding to a spacecraft [12, Ch. 7.5]. However, adding shielding means that mass must be added to the system, and to provide enough shielding against the larger untrackable objects would require excessively heavy shielding.

3.1.2. DEBRIS GROWTH LIMITATION METHODS

The current policy of most space agencies is to implement methods to limit the growth of space debris. These practices are intended to prevent runaway growth in what is known as the Kessler syndrome: a case in which collisions between orbiting objects create a cascade of debris particles and further collisions, effectively rendering an orbital belt unusable [2].

The Inter-Agency Space Debris Coordination Committee (IADC) is an international committee of national space agencies and ESA for coordinating activities relating to space debris, which has set a number of guidelines relating to the limitation of the growth of space debris [12, Ch. 30.1]. In doing so, the IADC has defined two “protected” regions of space around the Earth: the LEO region is defined as the sphere around the Earth

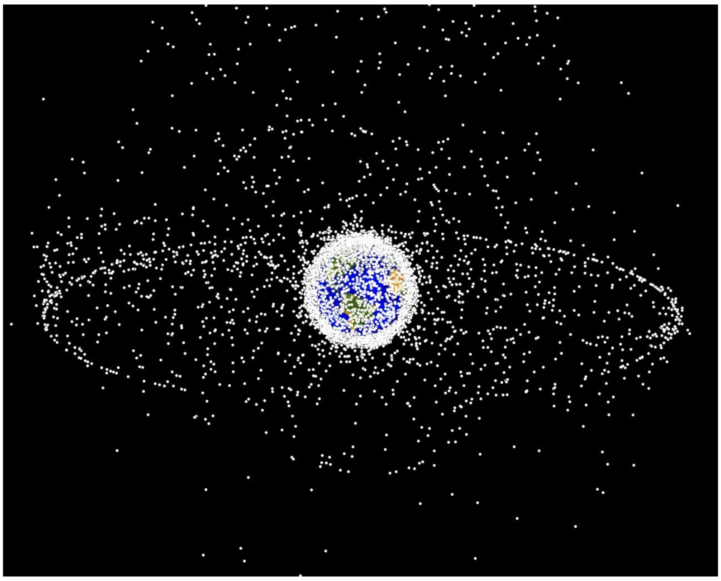

Figure 3.1: Computer generated image of tracked orbital objects [13].

up to an altitude of 2000 km, and the geostationary orbit (GEO) region is defined as geosynchronous altitude (35786 km) plus and minus 200 km, with inclinations of zero plus and minus 15 degrees [14]. It is stipulated that satellites at the end of their mission should be removed from these protected regions, a practice known as end-of-life (EOL) disposal. These protected regions are visualized in Figure 3.2.

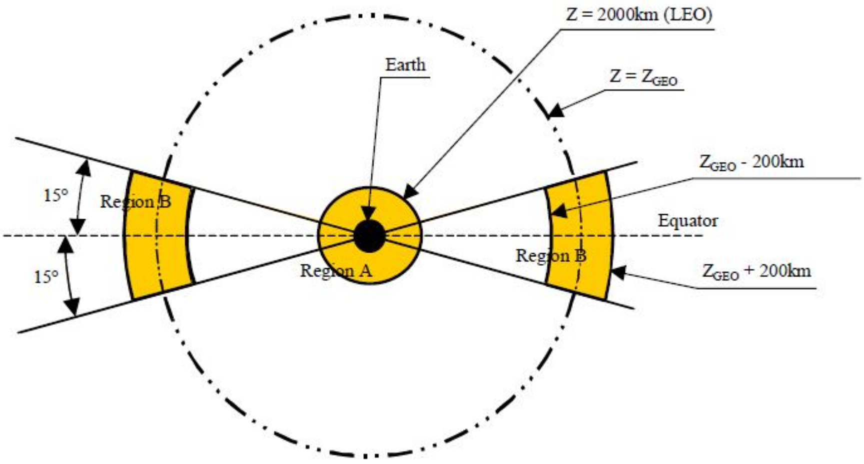

Figure 3.2: Schematic representation of IADC protected regions [14].

For the LEO region, several options are presented [14]: the preferred method for space debris mitigation is to perform a direct, controlled re-entry of the satellite. This causes the satellite to burn up in the atmosphere or to fall into the ocean, if the satellite is too large to burn up completely. However, this requires sufficient capability of the attitude and orbit control system (AOCS), as well as sufficient propellant reserves to perform the maneuver. This leads to an increase in the necessary propellant mass and therefore increasing the costs [12, Ch. 30.2].

It is also possible to boost the satellite into a so-called graveyard orbit at EOL [12, Ch. 30.2]. As with the option of direct re-entry, a significant amount of propellant allocated to this maneuver is required. For LEO, graveyard orbits are defined as stable orbits with a perigee above 2000 km and an apogee below 35586 km, thereby encompassing the region between the two protected regions defined previously. Analysis shows that it is only more beneficial from a propellant point of view to use this option if the initial mission orbit is above 1400 km altitude [12, Ch. 30.2]. Furthermore, this method does not have the benefit of actually having removed the satellite from orbit, and care must be taken to avoid common orbits, such as the 12-hour orbit altitude popular with navigation satellites.

Finally, it is possible to place the the satellite in an orbit with a sufficiently low perigee that it will naturally decay within 25 years [12, Ch. 30.2]. It must be noted that while this option (usually) requires the lowest amount of propellant, the re-entry will in fact be over a relatively random location on Earth. It therefore must be proven that the satellite will fully burn up in the atmosphere, and will not pose a hazard to the public or cause excessive environmental damage [14].

For GEO disposal, the common practice is to raise the orbit to a very near-circular orbit with a stipulated minimum perigee altitude of 36021 km, along with an extra margin depending on the satellite parameters [14].

In all disposal cases, the satellite is stipulated to be put into a passive state, minimizing the on-board energy and reducing the risk of on-orbit break-up. This includes venting propellant or burning leftover propellant to change the orbit, discharging batteries, relieving pressure vessels, and deactivating gyros and momentum wheels [14].

A problem with the IADC guidelines summarized above is that they are not yet legally binding, and it is therefore the responsibility of the operators and agencies to ensure they are enforced [12]. In most cases, scientific and military operations follow these guidelines, while commercial operators might elect not to, due to the increased costs associated with EOL disposal.

3.1.3. ACTIVE DEBRIS REMOVAL ACTIVITIES

The practices summarized in the previous subsection are all methods to limit the growth of the space debris population, and thus do not provide a solution for space debris already present in orbit. ADR is the practice of actively removing space debris from orbit, to reduce the number of objects in orbit, and thus lowering the risk of collisions and the onset of the Kessler syndrome. Research has suggested that ADR practices are already necessary to prevent the Kessler syndrome from occurring [2].

However, up to the present the concept of ADR has been the field of theoretical study only (and will be discussed further in Section 3.2), with a few exceptions: on four Space Shuttle missions, hardware in orbit was recovered by the Shuttle and returned to Earth [15]. The recovery of the Westar VI satellite during STS-51A is shown in Figure 3.3.

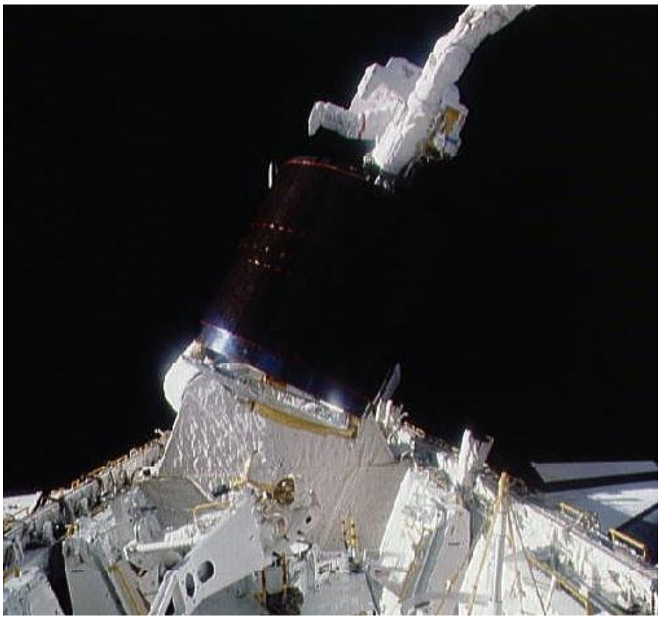

Figure 3.3: Westar VI being berthed in the cargo bay of Discovery using the Orbiter's robotic arm [16].

The hardware retrieved during these Space Shuttle missions consisted both of derelict commercial satellites as well as scientific experiments, and can therefore not solely be considered ADR activities. The basic concept of removing objects from orbit is the same, however, proving, in part, the feasibility of the concept.

3.2. FUTURE OF SPACE DEBRIS REMOVAL

This section will focus on research being done in the field of ADR, which comprises a wide range of research topics. This section will attempt to concisely summarize the most popular topics being investigated in ADR. However, this list is by no means all-inclusive with respect to each individual piece of research.

Research towards the need of ADR was performed by Liou [17], in which the evolution of the existing debris environment is re-evaluated (comparing the results to Kessler's work) and the effectiveness of certain ADR activities is examined. The conclusion of this work is that the current debris environment indeed poses a threat to the long-term use of the LEO regime, and that ADR activities would indeed be effective at mitigating this threat. Several methods of actively removing debris under recent investigation are detailed in the remainder of this section. Particular focus will be on the use of tethers for ADR.

3.2.1. LASERS FOR ADR

Some of the earlier investigations towards ADR involve the use of high-power lasers, proposed both by Schall [18] and Monroe [19] in the early 1990s. A crucial difference between these two investigations is that Schall proposes to place the laser in orbit, while Monroe suggests a ground-based installation. The concept of a ground-based installation is again examined by Phipps et al. [20] in 2012, taking recent developments into account. This technique is most applicable to small pieces of debris, up to 10 cm in diameter [19] and 1 kg in mass [18, 20], which, incidentally, are the most difficult pieces of debris to track [12, Ch. 7.5]. However, both Phipps et al. and Monroe state that larger pieces can also be de-orbited, but simply would require multiple firings to accomplish this.

Once the debris would have been located and tracked, the laser would be fired at the piece of debris as it comes "towards" the laser station. This is crucial, as the principle behind using lasers to remove debris is not to completely vaporize the debris, but to impart a de-orbiting impulse on the debris: simply put, one side of the debris will be irradiated, and will expel vaporized material due to this radiation. Thus, similar to a conventional rocket engine, the debris will experience a thrust-like force opposite to the direction the laser beam was fired from. This causes the debris to lose velocity, which lowers the semi-major axis and increases the eccentricity of its orbit, causing it to burn up in the atmosphere. Therefore, the effectiveness of such a system is greater at low altitudes.

It must be noted that the social and political implications of high-powered lasers in orbit around the Earth was not included in the scope of these investigations.

3.2.2. EXISTING PROPULSION TECHNOLOGY FOR ADR

Another trend is to use existing spacecraft propulsion technologies for ADR. As already discussed in Chapter 2, ESA's e.deorbit study focuses on using a robotic chaser to rendezvous with the debris, interface with it, an subsequently deorbit it using conventional chemical propulsion [6]. This technique is irrespective of the interfacing mechanism considered. Furthermore, the emphasis of this research is the safety and cost of the entire mission, as it is targeted for very near-future application.

Bonnal et al. [21] and Martin et al. [22] suggest using robotic probes to install propulsion kits on pieces of space debris, which would then be fired an would subsequently cause the space debris to de-orbit. This is, however, only a practical option for large pieces of space debris, such as rocket stages or derelict satellites. Also, if the debris is tumbling, proper orientation of the thruster pack may prove challenging.

Pergola et al. [23] suggest using a low-thrust, high-efficiency electric propulsion system to power a robotic probe, which will approach a piece of debris and apply an expanding foam to the debris, greatly enlarging the area-to-mass ratio thereof and causing it to decay more quickly due to aerodynamic drag. An advantage of this technique is that no docking system between the probe and debris is required, and that the probe can be re-used after applying the foam to the debris. However, due to this technique's reliance on aerodynamic drag, it can only be feasibly performed at low altitudes.

More exotic is the concept of ion beam shepherding proposed by Bombardelli and Peláez [24]. The concept is to use an ion propulsion system on board the "shepherding" satellite to project an ion beam at the piece of debris, imparting momentum on the debris. At the same time, a similar ion propulsion system on the shepherd is fired in the opposite direction, maintaining close proximity of the shepherd to the debris. The momentum being transferred to the debris would alter its orbit and cause it to re-enter. An advantage of this system over many other types of debris removal is that, again, no physical attachment between the shepherd and the debris is required. However, this technique is also only more applicable to larger debris.

3.2.3. TETHERS FOR ADR

By far the greatest current trend in ADR research is the investigation of tether-based systems. The application of this technology towards ADR was first published by Forward et al. in 2000 [25]. This proposal, coined the "Terminator Tether™," was first proposed as a cost-effective means of EOL disposal in 1998 [26], but was later expanded to apply to ADR. The concept uses a so-called electrodynamic tether (EDT), which in principle is a long (multi-km), conducting wire extended from the spacecraft. Since this conducting wire would be moving through the Earth's magnetic field, a drag-like Lorentz force would be induced, slowing the satellite down and causing it to de-orbit. A great advantage of EDT systems is that they are passive when used in the drag-inducing configuration considered for ADR, meaning that no traditional propellants are required to de-orbit the debris.

The Terminator Tether™ would be a self-contained system, which could be attached to a satellite with minimal interaction required between the Terminator Tether™ and the satellite, apart from a physical attachment point [25]. However, how the Terminator Tether™ would be attached to a piece of debris already in orbit is not examined further.

Following the proposal of the concept, a number of studies were performed concerning the risks of operating such long tethers in orbit. Van der Heide and Kruijff [27] investigated the risks of the EDT concept, as well as so-called the momentum exchange tether (MXT) concept, the latter of which use tethers to mechanically transfer momentum between objects. They conclude that while both types of technology show great promise, care must be taken to not create more debris if the tether is severed. Therefore, the use of DU-tethers is suggested, which simply are tethers made out of a material which is degradable by ultraviolet radiation. This research is unique in that it also considers MXTs, while the rest of the field is focused on EDT systems.

Pardini et al. [28] investigated the survivability of EDT systems in the case of an impact with space debris. The probability of such an occurrence is relatively high, due to the fact that proposed tether designs are generally a number of kilometers in length. They conclude that using multi-strand tethers with multiple knots and loops spaced equally across the tether length increases the probability of survival for a tether during a de-orbit mission. Further work was performed by Pardini et al. [29] towards the safety of operating EDTs and their survivability with the risk of debris strikes in cooperation with the IADC.

Bombardelli et al. [30] have conducted a first-order design of an EDT system, and evaluated its performance at de-orbiting several classes of upper rocket stages of which there are large populations in LEO. Only the tether itself is considered in this investigation, with the method of connecting this system to the debris not being discussed. It is concluded that with the proposed tether system, the aforementioned upper rocket stages can be de-orbited in a number of weeks during worst-case conditions.

The design of a microsatellite system for ADR using EDT technology was proposed by Nishida et al. [31]. This research focuses on the design of the actual ADR system itself, rather than wholly on the functioning of the EDT. Therefore, it includes the design of a robotic arm for grappling the piece of debris which is to be de-orbited.

The design of an EDT-based mission plan for removing large amounts of space debris was presented by Levin et al. [32], using an EDT system designed previously by Pearson et al. [33]. Using this plan, it is suggested that the costs per unit mass to remove space debris would only be a small fraction of typical launch costs per unit mass, and that it is possible to affordably remove 2500 pieces of debris over 2 kg in mass from LEO in 7 years. Doing so would virtually eliminate the risk of collisions with debris in LEO.

3.2.4. CONCLUDING REMARKS

In summary, the field of research towards active debris removal is quite diverse, with a surprising amount of research being done towards EDTs to de-orbit space debris. This technology makes it possible to de-orbit large pieces of debris in relatively short time spans, while being a completely passive system. A potential disadvantage is the great length of these systems, making them vulnerable to debris strikes themselves, although this problem can be solved through smart tether design.

In general, it can be concluded that the concept of using space tethers to deorbit debris, either EDTs or MXTs, is promising. However, no mention is made of using the tether simply as an interface between the ADR satellite and the debris, and using traditional propulsion techniques to deorbit the debris. Therefore, additional examination of the research towards the applications of orbital tethers will be done in Section 3.4.

3.3. RENDEZVOUS MISSIONS

This section will explore the history of orbital rendezvous missions. As seen in Section 3.2, most ADR methods require close-proximity operations between the removal satellite and the debris. Due to this close interaction, it is important to know what proximity operations have been done so far to understand the limits of current technology. First, the early attempts at orbital rendezvous during the height of the space race will be summarized; second, this will be done for the more modern practices.

3.3.1. EARLY INVESTIGATIONS TOWARDS ORBITAL RENDEZVOUS

The early space programs performed very preliminary investigations into the concept of orbital rendezvous. The Russian Vostok program performed several “dual launches”, in which two spacecraft were launched into identical orbits within the span of one day [34]. These spacecraft then closed to within a few kilometers, but due to the limited maneuvering capability of the Vostok spacecraft, these formations could not be maintained. The American Mercury program primarily focused on the physical ability of astronauts to actively pilot spacecraft, as the philosophy of the American space program was to perform manual maneuvers due to the greater initial flexibility [34].

GEMINI AND APOLLO PROGRAMS

The findings of the Mercury program allowed the USA to truly perform tests with manned orbital rendezvous in the Gemini program. During the course of this program, rendezvous was first performed between two Gemini spacecraft, which approached to a distance of 30 centimeters [34]. Docking was also performed several times between a Gemini chaser and an Agena target vehicle. The final approach procedures in the Gemini program were performed manually by the pilot of the capsule. A view from the cockpit of Gemini 8, which performed the first on-orbit docking flight, is shown in Figure 3.4.

The rendezvous and docking procedures necessary for the Apollo program were based on those of the Gemini missions [35]. For Apollo, these were necessary for the Lunar Ascent Module to dock with the Command and Service Module in orbit, after lifting off from the surface of the Moon. Again, as with Gemini, the Apollo rendezvous procedures were controlled by the pilots [34].

It is interesting to note that the American rendezvous philosophy of manual control, while allowing greater initial flexibility as mentioned before, made no attempt to standardize orbital rendezvous procedures [35]. This made it necessary for unique trajectories to be computed for each mission, and as mentioned previously, the final approaches were performed manually, fully relying on the skills of the pilot. For the Gemini and Apollo missions, a lot of time was spent on training the crews to perform the specific mission, resulting in high costs [35].

SOYUZ/PROGRESS PROGRAM

The Russian Soyuz program was the successor to the Vostok program, and was intended to demonstrate advanced manned operations in orbit [34]. As opposed to the Vostok, the Soyuz was designed to be a far more capable spacecraft, which could perform fully autonomous rendezvous and docking. This was demonstrated with the Kosmos 186 and 188 spacecraft, which performed the first ever fully autonomous docking between two unmanned spacecraft [34]. Also, a few years later, two manned Soyuz spacecraft performed a docking maneuver and exchanged crew members between two spacecraft (even before this was managed by the Apollo program) [34].

The Soyuz proved to be a versatile spacecraft with good longevity. It is currently still in operation, and both it and its unmanned cargo derivative Progress perform routine flights to the International Space Station (ISS) [34]. The spacecraft has been refitted with more advanced systems compared to those used in the early days of the space race, but is essentially unchanged.

3.3.2. RECENT ORBITAL RENDEZVOUS PRACTICES

Orbital rendezvous is an important part of modern-day space operations. While spacecraft such as the Soyuz/Progress have proven their worth, newer systems specifically tailored towards performing orbital rendezvous have become increasingly prevalent. Such systems include the Space Shuttle and all activities related to the construction and resupply of large space stations such as the ISS.

SPACE SHUTTLE PROGRAM

The Space Shuttle was designed to perform a wide variety of rendezvous missions, such as crew and cargo transfer to space stations, satellite servicing and retrieval missions, and on-orbit assembly missions [34]. The

Figure 3.4: View of the Agena target vehicle from Gemini 8 [36].

situation is made even more complex due to the fact that many targets would not possess navigation aids, and would not have been designed to interface with the Orbiter [15]. However, although these missions are a good deal more complex than the missions performed for the Gemini and Apollo programs, the basic rendezvous procedures used are very similar to those missions [35]. Due to thruster-plume-impingement constraints, however, the final approach trajectory was altered from the tried-and-tested methods used on Gemini and Apollo [15].

Another large difference between the Space Shuttle the Gemini and Apollo programs is the use of a robotic arm to retrieve and berth satellites slated for retrieval or servicing, as opposed to directly docking with these satellites [15]. To resupply the ISS, however, the Orbiter did perform a direct docking maneuver.

CURRENT ISS RESUPPLY ACTIVITIES

Apart from the aforementioned Progress vehicles, several other unmanned vehicles are currently used to resupply the ISS [37]. Of these vehicles, the ATV [38] also performs a fully automated docking maneuver, while the Dragon [39], HTV [39], and Cygnus [40] are berthed using the robotic arms installed on the station.

3.3.3. CONCLUDING REMARKS

Based on the material presented in this section, it is clear that close proximity operations are well-understood aspects of space flight. In addition, it is apparent that it is possible to perform these operations autonomously, as done by the Progress and ATV. Thus, it is concluded that close proximity operations between orbiting bodies is definitely possible, and does not form a significant obstacle for ADR.

3.4. SPACE TETHER MISSIONS

This section will discuss the use of tethers in space flight, together with a discussion on the applicability of space tethers to the active-space-debris-removal problem. As has already been seen, orbital tethers are both a promising and a controversial research topic, offering both immense gains as well as massive risks. First, the history of tether usage in space will be reviewed, including which missions have incorporated tethers in their design. Then, current trends in space tether research will be highlighted.

3.4.1. HISTORY OF SPACE-TETHER APPLICATIONS

The earliest usage of space tethers is found in the concept of space elevators and skyhooks [41]. While these concepts are of a much larger scale than the studies conducted more recently in this field, as will be seen later on, they did spark interest in the use of tethers in various ways to transport payloads.

A number of missions has performed experiments with space tethers over the course of the space age, even as far back as two Gemini missions in 1967 [41]. The most well-known space tether missions were the TSS-1 and TSS-1R missions performed during the Space Shuttle Program [41]. Both missions were intended to deploy a 20 km EDT, although neither was fully successful in doing so: the tether on TSS-1 severed after only 260 m of deployment, while the TSS-1R managed to deploy 19.6 km of tether before the tether snapped [41]. However, the tether on TSS-1R was deployed to such a length that some of the scientific objectives could still be met [42]. An artist's impression of the TSS-1 system and the deployment of TSS-1R can be seen in Figures 3.5 and 3.6, respectively.

Figure 3.5: Artist's impression of the TSS-1 system [43].

Figure 3.6: Deployment of the TSS-1R system [44].

Several other orbital experiments with long tethers were conducted with more success. The TiPS mission in 1996 utilized a nonconducting, 4 km long tether, and conducted experiments in tether physics [41]. More impressively, the YES2 mission was slated to deploy a 30 km tether, which would be used to de-orbit a re-entry capsule using swinging momentum exchange [41]. However, due to an error in the deployment system, the tether was overdeployed to an estimated 31.7 km, after which it was severed [45]. This was later estimated to have given the required impulse to the de-orbit the re-entry capsule, although the capsule itself could not be tracked or recovered [45]. This is of particular interest for the topic of ADR, as it proves the validity of the concept of using momentum exchange to provide a de-orbiting impulse to a piece of space debris.

3.4.2. CURRENT TRENDS IN SPACE TETHER RESEARCH

Space tethers are a "hot topic" in the field of space flight, and current research into this field is very diverse [46]. One of the most tantalizing aspects of space tethers is the possibility of providing transportation in space without the use of "traditional" propellants (such as chemical or ion propulsion). The use of both MXTs and EDTs are proposed to this end, with mission applications ranging from simply attitude control [47] to the grander scope of interplanetary transfer [48].

Much research is also being done towards the dynamics of tethers in space [46]. Often, tethers have been modeled as a dumb-bell system, in which two massive bodies are connected by a rigid tether of low to negligible mass. However, this is not always the case, as tethers are most definitely not rigid and therefore subjected to flexural effects [46]. Recent studies have therefore also focused on including the non-rigid properties of tethers in the models used to analyze such systems.

GUIDANCE & CONTROL OF SPACE TETHERS

While the dynamics of space tethers are under much scrutiny, the application of these dynamics models to guidance and control laws is actually limited [46]. Most research being done into the control of space tethers is in the deployment and retrieval strategies of tethers, with additional emphasis on tether stability during these operations.

Also, the attitude stability of tethered spacecraft is identified as an issue [46]. Some research has been done towards this problem: the implementation of a kite-like tether for attitude control is proposed in [49], focusing on a two-tether design which is passive in nature. A later study focuses on stabilizing the attitude of the base spacecraft while keeping tether perturbations small [50].

SPACE TETHERS AND SPACE DEBRIS

The use of tethers for ADR has already been discussed in Section 3.2. However, within the total scope of research being done in tethered space systems, research towards using tethers for ADR actually only represents a small fraction of this [46]. Also, most proposed tether designs are of the order of kilometers in length, and are therefore susceptible to space debris themselves, although the survivability of tethers is subject to some investigation [46].

Therefore, there seems to be a paradox when investigating the use of tethers as described in the majority of the research for ADR: due to the fact that tethers of sufficient length to provide the impulse to de-orbit space debris are more susceptible to being struck by debris, they might not be the safest or most sustainable method to do so. Therefore, MXTs and EDTs as described in the literature still face major hurdles before these can be implemented.

3.4.3. CONCLUDING REMARKS

While the use of tethers for ADR is a promising field of research, a number of obstacles still need to be overcome before actual implementation is possible. Most important of these is the lack of research towards the guidance and, to a lesser degree, control of space tether systems, especially when an ADR system of an active and a passive satellite is considered. If tethered ADR is to be realized, research must be performed towards this topic.

In addition, no research could be identified in which tethers are considered solely as a mechanical means of transferring momentum from an engine on an active chaser to a passive target: most research towards MXTs focuses on methods involving libration, spin, and impractically long tether designs. Furthermore, EDT designs are also generally require very long tethers, and interactions with the Earth's magnetic field can also be complex to model. Therefore, using tethers for simple mechanical momentum transfer seems a more practical solution in the short term.

4

COORDINATE SYSTEMS

It is clear that modeling the dynamics of orbital tether systems poses a significant problem. However, before the mathematical models used to analyze the motions of the TSDS can be properly detailed, it is important to categorize the different coordinate systems in which these models are described. Also, it is important to know how one system can be transformed into another.

Therefore, this chapter will provide a threefold summary of the used coordinate systems. First, the reference frames themselves will be described in Section 4.1. Second, the state variables used to express the state of the TSDS will be listed in Section 4.2. Third, a number of general and specific reference system transformations will be presented in Section 4.3.

To avoid confusion, it must first be stated that a reference frame will refer specifically to the set of axes used in three-dimensional space in which the state variables are expressed. A coordinate system thus encompasses the combination of the used reference frame and state variables.

4.1. REFERENCE FRAMES

This section will provide an overview of the different reference frames which were used during the performed research. These frames can be divided into two categories: Earth-centered reference frames and vehicle-centered reference frames. Both types of reference frame have their specific uses when considering an ADR mission, and both the frames themselves and their usage will be described. Note that all described reference frames are orthogonal right-handed frames.

4.1.1. EARTH-CENTERED REFERENCE FRAMES

As the name suggests, Earth-centered reference systems are reference systems which have the origin located at the center of mass of the Earth [51]. This makes Earth-centered frames useful for determining satellite orbits about the Earth, as the dominant force in Earth orbit is provided by the Earth's gravity. Two frames will be discussed here, the Earth-centered inertial (ECI) frame and the Earth-centered, Earth-fixed (ECEF) frame.

GEOCENTRIC EQUATORIAL (ECI) REFERENCE FRAME

The Geocentric Equatorial reference frame [52, Ch. 1.4] has the xy-plane located in the equatorial plane of the Earth, with the x-axis pointing towards the vernal equinox and the z-axis pointing towards the geographic North pole, with the y-axis completing the right-handed coordinate system. This is visualized in Figure 4.1.

The Geocentric Equatorial frame is often considered a so-called ECI reference frame, and will be referred to simply as the inertial (I) frame throughout the remainder of the text. However, strictly speaking it is at best a pseudoinertial frame. This is due to the fact that both the equatorial and ecliptic planes, which define the Geocentric Equatorial frame, vary in time [52, Ch. 1.7]. Common practice is therefore to define a certain ECI frame as the Geocentric Equatorial frame at a certain epoch. These resulting ECI frames are very useful for the computation of satellite orbits around the Earth, as long as the considered time spans are not too long. In this case, specifically, the J2000 frame will be used, which was defined on January 10, 2000, at 12:00.

Since it can be considered an inertial frame, however, the ECI frame is ideal for formulating the equations of motion of Earth-orbiting satellites. In this case, no apparent forces have to be introduced in the model, making it very intuitive to implement. Further adding to its intuitive implementation is the alignment of the *z*-axis with the North pole, and thus the coincidence of the equatorial plane with the ECI *xy*-plane. The axis orientations of the Geocentric Equatorial frame are summarized below.

- Origin in the geometric center of the Earth
- *x*-axis in the direction of the vernal equinox in Earth's equatorial plane
- *y*-axis perpendicular to the *x*-axis in Earth's equatorial plane, completing the right-handed system
- *z*-axis in the direction of the North pole, perpendicular to the *xy*-plane

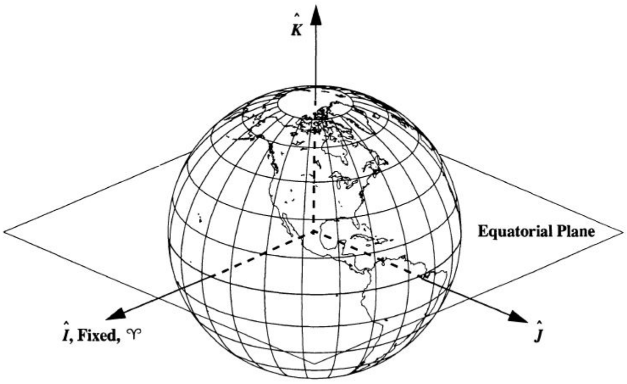

Figure 4.1: Schematic representation of the Geocentric Equatorial frame [52, Ch. 1.4].

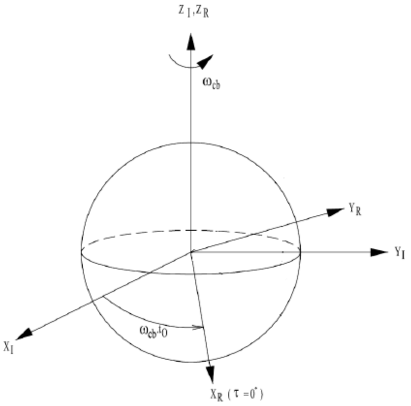

Figure 4.2: Relation between ECI and ECEF frames [9, Ch. 3.2].

ECEF (*R*) REFERENCE FRAME

The ECEF reference frame [52, Ch. 1.4] is a geocentric coordinate system which rotates along with the Earth: the origin of this system is still located at the geometric center of the Earth, but now the axes are defined by topographical features instead of celestial features. As with the ECI frame, the *xy*-plane of the ECEF frame is still located in the equatorial plane, with the *z*-axis again passing through the North pole and is thus aligned with the rotation axis of the Earth. However, the *x*-axis is now defined by the Greenwich meridian, and the *y*-axis completes the right-handed reference frame by passing through the line of longitude at 90°E. The relation between the ECI and ECEF frames can be seen in Figure 4.2.

Since the ECEF frame rotates in Earth-centered inertial space, it is a non-inertial frame. Therefore, care must be taken to take inertial forces into account when modeling dynamics in this frame. However, since it is fixed to the topography of the Earth, it is very important for defining target areas for the final deorbit of the TSDS, as settled areas should be avoided as a target zone. It is common to use an area in the Pacific Ocean known as the South Pacific Ocean Unpopulated Area (SPOUA) for deorbiting satellites, shown in Figure 4.3 [53]. The axis orientations of the ECEF frame is summarized below.

- Origin in the geometric center of the Earth
- *x*-axis in the direction of the Greenwich Meridian in Earth's equatorial plane
- *y*-axis perpendicular to the *x*-axis in Earth's equatorial plane, completing the right-handed system
- *z*-axis in the direction of the North pole, perpendicular to the *xy*-plane

4.1.2. VEHICLE-CENTERED REFERENCE FRAMES

Apart from the Earth-centered reference frames discussed previously, vehicle-centered reference frames prove to be useful for expressing the relative orbit dynamics of satellites. Additionally, they are indispensable for describing the orientation of the satellite to which they are fixed. These frames are usually centered in the center of mass of the satellite, although this need not be the case. No single convention exists for the axis orientations, either: it is possible for these to be fixed to the satellite body, or to be defined for instance by the position or velocity of the satellite. Two such frames will be defined: the *RSW*-frame and the satellite geometric frame.

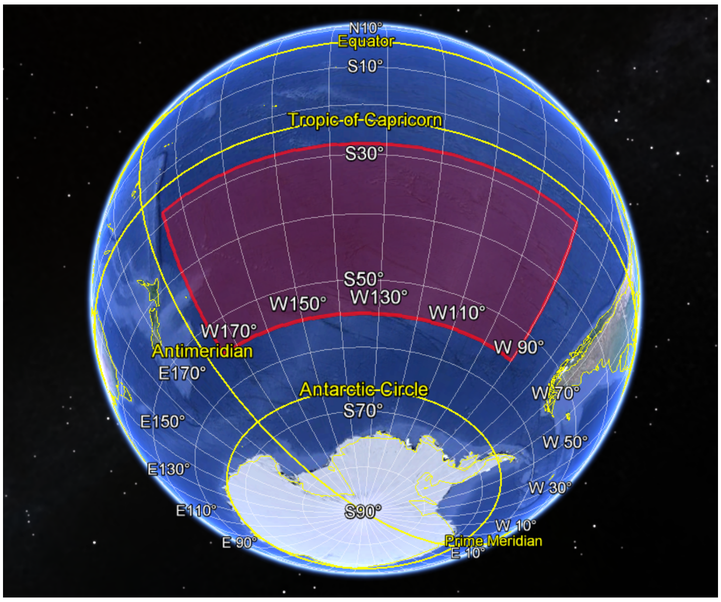

Figure 4.3: Location of the SPOUA, taken from Google Earth. Visible are New Zealand to the left, Antarctica at the bottom, and South America to the right. The SPOUA is the red square [53].

RSW (*H*) FRAME

The *RSW*-frame is a vehicle-centered frame which is principally defined by the radius vector from the geometric center of the Earth to the invariant center of mass of a satellite [52, Ch. 1.4]. The *R*-axis points outwards along the radius vector, the *S*-axis is perpendicular to the radius vector in the orbital plane (and points in the same direction as the velocity vector at perigee and apogee), and the *W*-axis is normal to the orbital plane, completing the right-handed frame (which places it in the same direction as the angular momentum vector of the orbit). This is visualized in Figure 4.4.

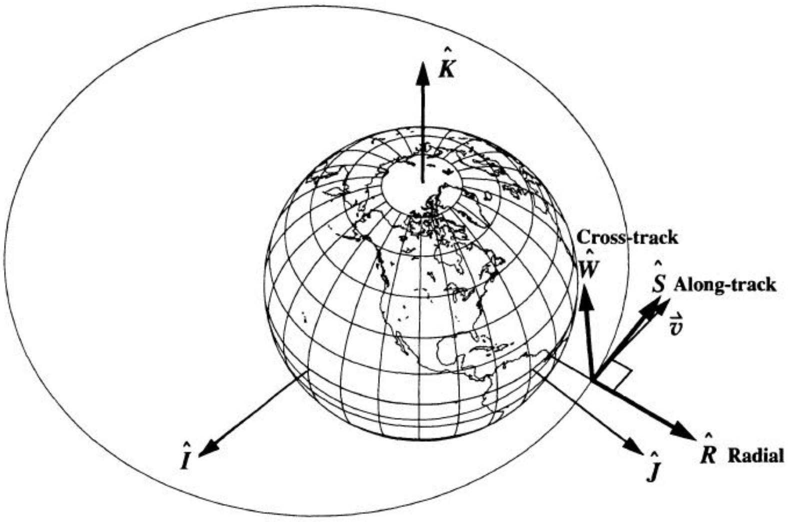

Figure 4.4: Schematic representation of the *RSW* frame [52, Ch. 1.4].

The *RSW*-frame is also known as the Hill frame, as this frame is used to express the linearized Hill equations (also known as the Clohessy-Wiltshire equations), which govern the relative motion between two satellites in close proximity [51, Ch. 9.1]. Thus, it will be referred to as such throughout the remainder of the text. Since it is defined by the instantaneous radius of the satellite, it is also a non-inertial frame. The axes are also known by the designations R-bar, V-bar, and H-bar, as (in a circular orbit) they point along the radius, velocity, and orbital angular momentum vectors. The axis orientations are further summarized below.

- Origin in the (invariant) center of mass of satellite
- *x*-axis in the direction of the outwards radial
- *y*-axis perpendicular to the *x*-axis in the orbital plane of the satellite
- *z*-axis in the direction of the orbital angular momentum vector, perpendicular to the *xy*-plane

SPACECRAFT GEOMETRIC (*G*) FRAME

The spacecraft geometric frame is the final frame discussed in this section. This frame has the right-handed *x*, *y*, and *z*-axes fixed with respect to the spacecraft body. While the orientation can be relatively arbitrary, it is common to align these axes along the three principal axes of inertia of the satellite body. Furthermore, the origin is, in this case, located in the center of mass of the satellite, although this does not have to be the case. Note that this center of mass may vary, due to the assumed model of each satellite: in this case, the initial center of mass is used to express these frames.

Due to the fact that the spacecraft geometric frame is fixed to the satellite body, it is very convenient for expressing the orientation of the satellite with respect to the other reference frames used. Also, due to this body-fixed nature, it is natural to express the torques acting on the satellite in this frame. Two such frames will be considered for this research: one for the chaser, and one for the target. Both frames are attached to the invariant center of mass of the respective satellite, and are visualized in Figures 4.5 and 4.6, respectively [3].

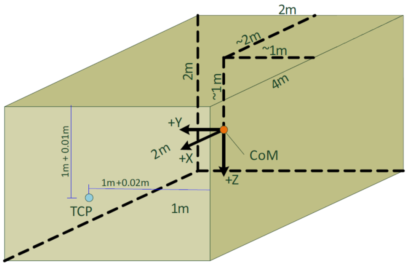

Figure 4.5: Schematic representation of the chaser model, including the chaser *G* frame [3].

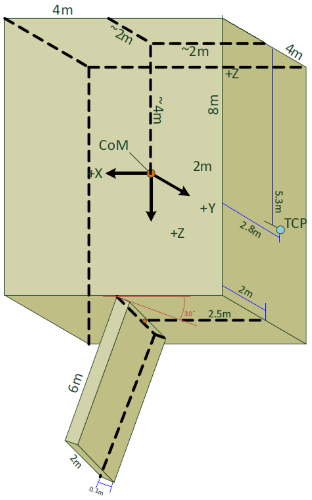

Figure 4.6: Schematic representation of the target model, including the target *G* frame [3].

4.2. STATE VARIABLES

Within the reference frames presented in the previous section, different element sets can be used to represent the actual state of a system in these frames. Therefore, this section will summarize the state variables used to describe the TSDS in orbit. Two subsets of these state variables can be identified: first, the position and motion of a satellite in orbit must be defined, and second, the attitude and rotations of the spacecraft itself must be represented. This will be done in Sections 4.2.1 and 4.2.2, respectively.

4.2.1. ORBITAL STATE REPRESENTATION

To define the position and motion of a satellite in its orbit, two different state representations are used: the Cartesian elements and the Keplerian elements. These sets were selected for implementation and intuitiveness: the GGNCSIM libraries use the Cartesian elements to formulate the equations of motion, and the Keplerian elements offer insight towards the size, shape, and orientation of a satellite orbit. In each set, six variables are necessary to fully define the state of the satellite, as both the position and motion in three-dimensional space must be accounted for. The specific use of each element set will also be discussed.

CARTESIAN ELEMENTS

The six Cartesian elements to represent the state of an orbiting satellite are in essence very simple: These consist of the *xyz*-components of the satellite position in the chosen frame and the time rates of change of these components (denoted as $\dot{x}$, $\dot{y}$, and $\dot{z}$, respectively) [54]. This makes the Cartesian set very easy to work with. However, it is not readily apparent from the instantaneous Cartesian elements what orbit the satellite under consideration is in, and thus no *a priori* knowledge of the motion can be used to ease the computational load of a simulation using this set. The Cartesian elements of a body with position **R** and velocity **V** are shown in Figure 4.7.

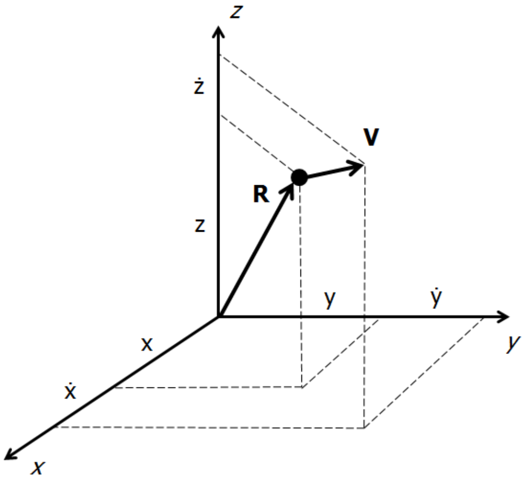

Figure 4.7: Cartesian elements of a body with position **R** and velocity **V**.

As mentioned, the routines in the GGNCSIM libraries use the Cartesian elements as the integration variables of the simulation. Therefore, it was decided to use these to formulate the equations of motion of the TSDS in orbit as well. This was done, because utilizing a different set to formulate the equations would require additional transformations, thus increasing the risk of introducing errors. Since the routines in the GGNCSIM libraries have been extensively tested already, it was not considered worth the risk of introducing a different element set. In addition to this, many orbital perturbations, as well as the guidance forces and control moments, can be conveniently expressed using the Cartesian elements.

KEPLERIAN ELEMENTS

While the Cartesian elements were used as the integration variables, it is useful to have an understanding of the Keplerian elements as well. The Keplerian elements [55, Ch. 2.4] can be used to define the orbital state of a satellite in terms of parameters that relate to the size, shape, and orientation of the orbit, which are invariant in a classical two-body type problem. For the first-order analysis of satellites in LEO, such a problem type is often a valid assumption. Thus, the Keplerian elements have the advantage over the Cartesian elements in that these provide insight into the physical properties of the orbit being described. The six elements making up the Keplerian set are the semi-major axis a, the eccentricity e, the inclination i, the right ascension of the ascending node (RAAN) Ω, the argument of periapsis ω, and the true anomaly ν.

As the Keplerian elements relate to the physical path followed by the satellite in its orbit, it is useful to have a visual understanding of what each individual element describes. This is provided in Figure 4.8: the semi-major axis a, eccentricity e, and true anomaly ν are measured in the orbital plane, while the inclination i, RAAN Ω, and argument of periapsis ω define the orientation of the orbital plane in the chosen reference frame. It is noted that the chosen frame must be a (pseudo)inertial frame for the Keplerian elements to have a meaningful physical representation.

The first two Keplerian state variables relate to the geometry of the orbit itself, and are measured in the orbital plane. The semi-major axis defines the distance between periapsis and apoapsis (or closest and farthest point in the orbit to the body being orbited), and therefore gives an indication of the size of the orbit. The eccentricity gives an indication of the elongation of the orbit: an eccentricity of zero indicates a circular orbit, while an eccentricity of close to one indicates a very elongated, but still closed, orbit, the shape of which is elliptical. An eccentricity of one or higher indicate open orbits, forming parabolas or hyperbolas, respectively.

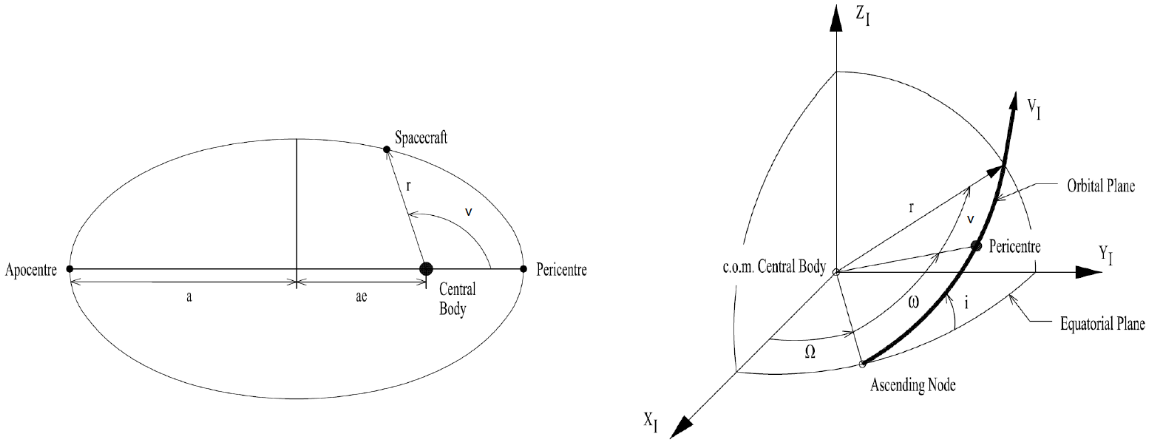

Figure 4.8: Graphical representation of the in-plane (left) and out-of plane (right) Keplerian elements (adapted from [9, Ch. 3.2]).

The inclination is the angle between the orbital plane and the xy-plane of the chosen reference frame, measured at the ascending node. The ascending node is defined as the point where the satellite crosses the xy-plane, traveling in the positive z-direction. This angle is therefore defined between 0° to 180°, meaning an inclination 0° corresponds to a prograde equatorial obit around Earth, while an inclination of 180° implies a retrograde equatorial orbit. An inclination of 90° defines a polar orbit.

The RAAN is defined as the angle between the x-axis of the chosen frame and the ascending node. Therefore, this angle is defined from 0° to 360°. Care must be taken to use the correct quadrant when using this angle in equations. The RAAN is undefined for orbits which lie perfectly in the xy-plane of the chosen reference frame, as there is no definable ascending node in this case. Around Earth, this corresponds to perfectly equatorial orbits. In this case, an artificial ascending node is often defined as a reference, for instance the x-axis of the chosen reference frame.

The argument of periapsis is defined as the angle in the orbital plane between the ascending node and the periapsis. This angle is again defined between 0° and 360°. However, for both perfectly equatorial or perfectly circular orbits, it is undefined: perfectly equatorial orbits have no definable ascending node, and perfectly circular orbits have no definable periapsis. With equatorial orbits, an artificial ascending node is often defined, as described previously. For circular orbits, an artificial periapsis is often defined as a reference, for instance at the RAAN.

The final Keplerian element, the true anomaly, is related to the position of the satellite itself within the orbital plane. The true anomaly is defined as the angle between the periapsis and the position of the satellite, measured from the center of mass of the attracting body. Thus, it is defined between 0° to 360°. However, as opposed to the other Keplerian elements (in an unperturbed orbit), the true anomaly varies in time. The direct relation between true anomaly and time is quite complicated [51], and therefore it can be chosen to replace the true anomaly with the mean anomaly M, which is defined in Equation (4.1), also known as Kepler's equation:

$$M = n(t-\tau) = E - e\sin(E) \tag{4.1}$$

In Equation (4.1), the eccentric anomaly E in this equation is a geometric parameter, which can be related to the true anomaly using Equation (4.2) [52, Ch. 4.2]:

$$\tan\left(\frac{E}{2}\right) = \sqrt{\frac{1-e}{1+e}}\tan\left(\frac{\nu}{2}\right) \tag{4.2}$$

Similarly, the mean motion n is a function of semi-major axis and the gravitational parameter of the main body, which is shown in Equation 4.3 (see also Section 5.2.1):

$$n = \sqrt{\frac{\mu}{a^3}} \tag{4.3}$$

Finally, the $(t-\tau)$ term in Equation (4.1) reflects the time since the last periapsis passage. This equation clearly presents a simple relation between position and time of the satellite in orbit.

In particular, the Keplerian elements are very useful for expressing ideal orbits, and thus knowing what the Keplerian elements of the body under consideration are will give information on the (approximate) size, shape, and orientation of its orbit. Additionally, the simulation can then be compared to the theoretical ideal case. To this end, the conversion from Cartesian to Keplerian elements and vice versa will be described in Section 4.3.

OTHER ORBITAL STATE SETS

The Keplerian elements do suffer from a number of singularities, particularly when some of the elements are zero, and the Cartesian elements do not offer any information on the physical properties of the orbit. Of course, many other orbital state representations exist, each with their own unique strengths and weaknesses. Thus, a brief overview of some common additional sets will be given. Specifically, the equinoctial and modified equinoctial elements, and the Unified State Model (USM) will be described.

The equinoctial set of orbital elements [55, Ch. 2.4] attempts to resolve some of the issues of orbital elements being undefined that arise in special cases with the Keplerian elements, as described previously. This set does so by choosing combinations of Keplerian elements such that these occurrences are negated. However, in this process, much of the physical meaning of the Keplerian elements is lost. In the equinoctial set, the semi-major axis a is the only unchanged Keplerian element, with five additional elements defining the shape and orientation of the orbit. Instead of the semi-major axis, the semiparameter p, defined for closed orbits as $a(1-e^2)$, can be used, forming the modified equinoctial elements [54, 56].

The USM differs from the previous element sets in the fact that it uses seven state variables: three to define the shape of the orbit, and four quaternion components (see Section 4.2.2) to define the orientation of the orbit with respect to the chosen inertial frame [57]. This quaternion actually defines the orientation of an *RSW* reference frame fixed to the orbiting body, and therefore is continuously changing in time. Furthermore, it can be defined using the angular Keplerian elements. Finally, the three shape parameters are defined in the velocity space, rather than the position space used by the Keplerian and (modified) equinoctial elements. Note that it is also possible to form a USM state vector with six elements by replacing the quaternion parameters with (modified) Rodrigues parameters or an exponential map, see Section 4.2.2.

While each of these element sets offers significant advantages in, for instance, computational load [54], it was decided to not use these in the simulator for the reasons described previously: Cartesian elements form the backbone of the GGNCSIM routines, and the Keplerian elements offer insight towards the behavior of the orbit.

4.2.2. ATTITUDE STATE REPRESENTATION

As mentioned in Section 4.1, the attitude of a spacecraft is expressed by the differences between the axes of a body-fixed reference frame and a different frame. In essence, all attitude representations can be written most clearly as the so-called direction cosine matrix (DCM) **C**. Such a DCM describing the transformation from a generic orthogonal A frame to a generic orthogonal U frame expresses the x-, y-, and z-axes of this U frame *uvw* in terms of the x-, y-, and z-axes of the orthogonal A frame *abc* [58, A.2]. The definition of the direction cosine matrix, which shows the components of each body-fixed axis along each vehicle-fixed axis, is given in Equation (4.4), with this situation visualized in Figure 4.10.

$$\mathbf{C}_{A2U} = \begin{bmatrix} u_a & u_b & u_c \\ v_a & v_b & v_c \\ w_a & w_b & w_c \end{bmatrix} \tag{4.4}$$

While the DCM is a very useful representation of spacecraft attitude, the fact that it requires nine parameters to do so makes it less attractive from a computational efficiency point of view. Therefore, it is common to use parameter sets that require less parameters. Two such sets will be discussed: Euler angles and quaternions.

EULER ANGLES

Euler angles provide a more intuitive manner of expressing satellite attitude than the DCM [58, A.3]. The Euler angles express rotations over single axes of an orthogonal reference frame U, a series of which is then used to express the complete orientation of U with respect to a different orthogonal frame A. Each subsequent rotation in the sequence is then performed over the respective axis of the resulting intermediate frame:

thus, the order of these rotations becomes important. However, only a maximum of three of these angles is necessary to define any orientation, rather than the nine elements required for the DCM.
Commonly, the roll angle ϕ is defined as a rotation about the body x-axis, the pitch angle θ as a rotation about the body y-axis, and the yaw angle ψ as a rotation about the body z-axis. A rotation sequence consisting of first the yaw, then the pitch, then the roll is visualized in Figure 4.9.

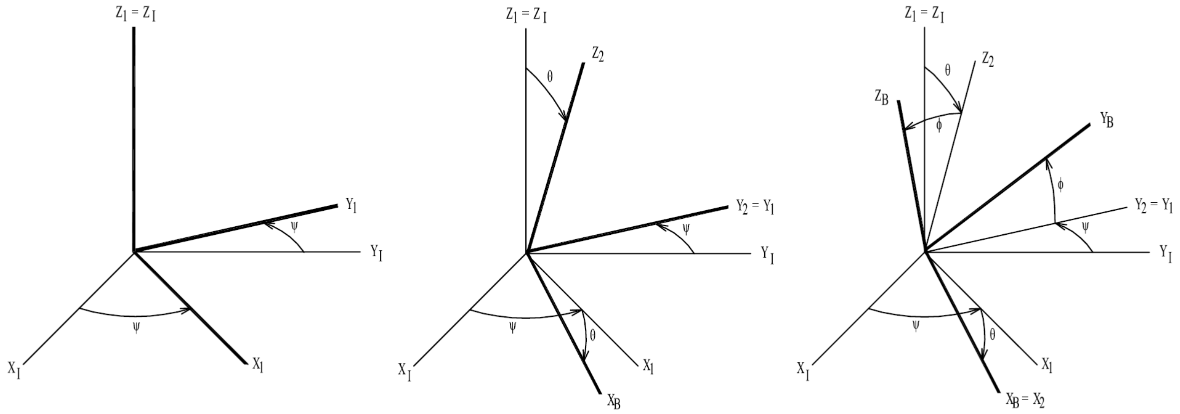

Figure 4.9: Yaw-pitch-roll rotation sequence: first the frame is rotated by the yaw ψ about the z_I axis, then by the pitch θ over the y_1 axis, and finally by the roll ϕ about the x_2 axis (adapted from [9, Ch. 3.2]).

As mentioned, the order in which these rotations occur becomes important when using Euler angles [58, A.3]. Commonly, the aforementioned yaw-pitch-roll sequence is used to transform between the body-fixed frame and the frame of reference, particularly when considering aircraft dynamics. In this case, it is possible to define the DCM based on the corresponding Euler angles as shown in Equation (4.5), with cos being denoted as c and sin as s [58, A.3].

$$\mathbf{C}(\psi,\theta,\phi) = \begin{bmatrix} c\theta c\psi & c\theta s\psi & -s\theta \\ -c\phi s\psi + s\phi s\theta c\psi & c\phi c\psi + s\phi s\theta s\psi & s\phi c\theta \\ s\phi s\psi + c\phi s\theta c\psi & -s\phi c\psi + c\phi s\theta s\psi & c\phi c\theta \end{bmatrix} \tag{4.5}$$

A major issue with using the Euler angle representation is that certain rotation sequences introduce singularities into the equations. For instance, when using the mentioned yaw-pitch-roll rotation sequence a singularity occurs for a pitch angle of 90°. This can lead to a phenomenon called gimbal lock in certain gyroscopic inertial systems [58, Ch. 4.7]. While this condition is not often found when considering commercial aircraft, it can easily occur in space vehicles. For this reason, it is not practical to use Euler angles to formulate the equations of motion of satellites in orbit. Therefore, a singularity-free solution is often used, in the form of quaternions.

QUATERNIONS

To remove the possibility of singularities, quaternions can be used to represent the attitude dynamics of spacecraft. Quaternions are based on a property of the DCM, which is a real, orthogonal matrix: any such matrix must have at least one eigenvector $\hat{\mathbf{e}}$ which has an eigenvalue of one [58, A.4]. This eigenvector, also called the unit Euler-axis vector, has the same components along the body axes as along the chosen reference frame axes, which allows any attitude transformation to be defined by a single rotation over an angle α about the vector $\mathbf{e}$. This is also known as Euler's rotation theorem, and is visualized in Figure 4.11. The quaternion vector $\mathbf{q}$ itself can be expressed in terms of the unit Euler-axis vector $\hat{\mathbf{e}}$ and the rotation α, as shown in in Equation (4.6) [58, A.4]:

$$\mathbf{q} = \begin{bmatrix} q_1 \\ q_2 \\ q_3 \\ q_4 \end{bmatrix} = \begin{bmatrix} \hat{e}_1 \sin(\alpha/2) \\ \hat{e}_2 \sin(\alpha/2) \\ \hat{e}_3 \sin(\alpha/2) \\ \cos(\alpha/2) \end{bmatrix} \tag{4.6}$$

As the norm of the unit Euler-axis vector is one, the norm of the quaternion vector will also be one. This allows q_4 to be expressed in terms of the other three quaternion elements, as shown in Equation (4.7):

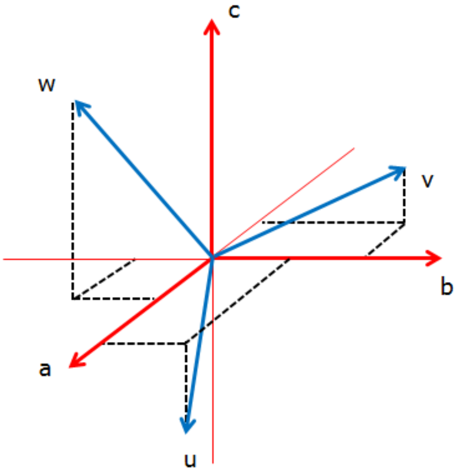

Figure 4.10: Schematic representation of the definition of the DCM defining the U frame from the A frame.

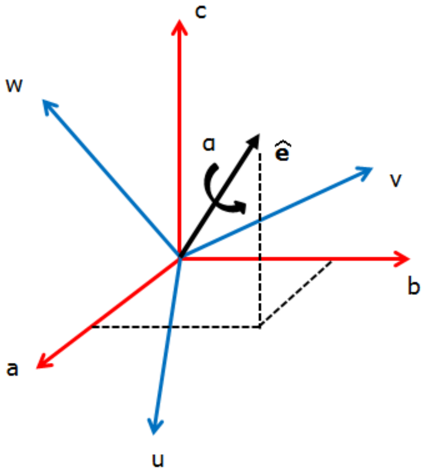

Figure 4.11: Schematic representation of the definition of a quaternion defining the U frame from the A frame.

$$q_4 = \sqrt{1 - q_1^2 - q_2^2 - q_3^2} \tag{4.7}$$

From Equation (4.6), it is clear that quaternions are essentially similar to Euler angles, with one important difference: rather than rotating about one of the axes of the used frame, the rotation axis is defined separately. Thus, only the single rotation is necessary, and the influence of the exact rotation sequence is eliminated. The DCM can also be represented in terms of quaternions, using Equation (4.8) [58, A.4]:

$$\mathbf{C}(q) = (q_4^2 - \bar{\mathbf{q}}^2)\mathbf{1} + 2\bar{\mathbf{q}}\bar{\mathbf{q}}^T - 2q_4\mathbf{Q}' \tag{4.8}$$

The definition of $\mathbf{Q}'$ in Equation (4.8) is given in Equation (4.9):

$$\mathbf{Q}' = \begin{bmatrix} 0 & -q_3 & q_2 \\ q_3 & 0 & -q_1 \\ -q_2 & q_1 & 0 \end{bmatrix} \tag{4.9}$$

Finally, the expression for the DCM in terms of quaternions given in Equation (4.10) [58, A.4]:

$$\mathbf{C}(q) = \begin{bmatrix} q_1^2 - q_2^2 - q_3^2 + q_4^2 & 2(q_1q_2 + q_3q_4) & 2(q_1q_3 - q_2q_4) \\ 2(q_1q_2 - q_3q_4) & -q_1^2 + q_2^2 - q_3^2 + q_4^2 & 2(q_2q_3 + q_1q_4) \\ 2(q_1q_3 + q_2q_4) & 2(q_2q_3 - q_1q_4) & -q_1^2 + q_2^2 + q_3^2 + q_4^2 \end{bmatrix} \tag{4.10}$$

Conversely, it is possible to express the quaternion elements in terms of the DCM [58, A.4]. There are four different methods of doing so, with each method first determining one of the quaternion elements based on the norm equations expressed in Equation (4.7), and the other three being determined both by the DCM elements as well as the determined quaternion element. The four sets produce identical results, which makes them seem initially redundant. However, in the case that one of the quaternion parameters turns out to be very small, it is not desirable use that parameter to determine the other three due to numerical inaccuracies. Thus, a different set is selected. The sets are described in Equations (4.11) through (4.14).

$$\begin{aligned} q_4 &= \pm\frac{\sqrt{1+C_{11}+C_{22}+C_{33}}}{2} \\ q_1 &= \frac{C_{23}-C_{32}}{4q_4} \\ q_2 &= \frac{C_{31}-C_{13}}{4q_4} \\ q_3 &= \frac{C_{12}-C_{21}}{4q_4} \end{aligned} \tag{4.11}$$

$$\begin{aligned} q_1 &= \pm\frac{\sqrt{1+C_{11}-C_{22}-C_{33}}}{2} \\ q_2 &= \frac{C_{12}+C_{21}}{4q_1} \\ q_3 &= \frac{C_{13}+C_{31}}{4q_1} \\ q_4 &= \frac{C_{23}+C_{32}}{4q_1} \end{aligned} \tag{4.12}$$

$$\begin{aligned} q_3 &= \pm\frac{\sqrt{1-C_{11}-C_{22}+C_{33}}}{2} \\ q_1 &= \frac{C_{13}+C_{31}}{4q_3} \\ q_2 &= \frac{C_{23}+C_{32}}{4q_3} \\ q_4 &= \frac{C_{12}-C_{21}}{4q_3} \end{aligned} \tag{4.13}$$

$$\begin{aligned} q_2 &= \pm\frac{\sqrt{1-C_{11}+C_{22}-C_{33}}}{2} \\ q_1 &= \frac{C_{12}+C_{21}}{4q_2} \\ q_3 &= \frac{C_{23}+C_{32}}{4q_2} \\ q_4 &= \frac{C_{31}-C_{13}}{4q_2} \end{aligned} \tag{4.14}$$

Special cases for quaternions exist when one of the quaternion elements is equal to one, and the others are zero. In the case that q_4 is one, the resulting quaternion expresses a null rotation: the unit Euler-axis vector is $[0,0,0]$ and the rotation angle is also zero. In the case that either q_1, q_2, or q_3 are equal to one, the quaternion represents a rotation of 180° about the x-, y-, or z-axis, respectively.

A final important definition in quaternion algebra is the definition of an error quaternion. Due to the nature of the quaternion vector, it is not possible to express the error between two quaternion orientations by simply subtracting each quaterion element of the target orientation from each element of the satellite's orientation. Instead, the error quaternion is defined as in Equation (4.15), with $\mathbf{q}_T$ being the desired quaternion and $\mathbf{q}_s$ the satellite quaternion [58, Ch. 7.2.4].

$$\mathbf{q}_{err} = \mathbf{q}_s \otimes \mathbf{q}_T = \begin{bmatrix} q_{T4} & q_{T3} & -q_{T2} & -q_{T1} \\ -q_{T3} & q_{T4} & -q_{T1} & -q_{T2} \\ q_{T2} & -q_{T1} & -q_{T4} & -q_{T3} \\ -q_{T1} & -q_{T2} & -q_{T3} & q_{T4} \end{bmatrix} \begin{bmatrix} -q_{s1} \\ -q_{s2} \\ -q_{s3} \\ q_{s4} \end{bmatrix} \tag{4.15}$$

It is clear from Equation (4.6) that quaternions require one more parameter to express orientation than when using Euler angles, and are thus non-minimal parametrizations of spacecraft attitude. However, since the equations of motion in terms of quaterions only require multiplications instead of the trigonometric functions used for Euler angle representations, they are computationally more efficient. Furthermore, due to the fact that singularities do not occur when expressing attitude with quaternions, they are preferred over Euler angles when formulating the equations of motion. Thus, this is also the variable used to represent attitude in the GGNCSIM libraries. Euler angles still retain a useful purpose in intuitively expressing the attitude of a satellite, so the transformation from a quaternion to Euler angles will be discussed in Section 4.3.

OTHER ANGULAR STATE SETS

While quaternions offer a solution which is successful at removing singularities, this comes at the cost of an additional state variable. Other sets have therefore been defined, in an attempt to represent the attitude of spacecraft using only three variables while avoiding singularities. A brief overview of several of these methods will be given here, in the form of Rodrigues and modified Rodrigues parameters and exponential mapping.

The Rodrigues parameters are based on quaternions, only reducing the number of parameters from four to three by dividing q_1, q_2, and q_3 by q_4 [59, Ch. 5.4]. However, a potential problem with doing this is that a singularity has been introduced for rotations of 180° [60]. At this point, q_4 becomes zero, and thus the Rodrigues vector becomes undefined. This can be remedied by dividing the first three quaternion parameters by $(1+q_4)$, which forms the modified Rodrigues parameters. However, this only delays the onset of a singularity to rotations of 360° [57, 60]. Nonetheless, the modified Rodrigues parameters can be used without singularities by switching to a so-called shadow set, which flips the sign of the quaternion vector without changing the physical representation of the rotation. Thus, for large rotations, the shadow set can be implemented to avoid singularities.

Exponential mapping is an alternative minimal parametrization using the quaternion elements [57]. Specifically, the exponential map formed by scaling the unit Euler-axis vector by the rotation angle. While this solution also contains a singularity for rotations of 360°, a shadow set can again be implemented to avoid this by switching between sets when the rotations become large.

While minimal parametrizations of spacecraft attitude are capable of producing solution sets without singularities, it was chosen to use quaternions as these, again, provide the backbone of attitude representation in GGNCSIM. Thus, the potential reduction in computational load by reducing the number of state variables by one was not considered worth the risk of introducing additional errors.

4.3. TRANSFORMATIONS

In this sections, transformations between reference systems will be discussed. As has been mentioned in the preceding sections, different reference systems have different strengths and weaknesses. Thus, being able to transform between different systems allows the most suitable reference system to be used. These transformations can be divided into two categories: first, transformations between reference frames will be described, and second, conversions between different sets of state variables will be summarized.

4.3.1. REFERENCE FRAME TRANSFORMATIONS

Transforming vectors from one reference frame to another is essential when considering an ADR mission. For instance, the body-fixed thrust forces produced by the chaser must be converted to the ECI frame to add these to the equations of motion. In essence, a frame transformation between two static frames will involve a translational component, describing the offset between the origins of the two frames, and a rotational component, describing the difference in orientation between the axes of the two frames. Again taking the generic frames A and U, the general equation for transforming from frame A to frame U is shown in Equation (4.16) [9, Ch. 3.2]:

$$\mathbf{x}_U = \mathbf{O}_{AU} + \mathbf{C}_{A2U}\mathbf{x}_A \tag{4.16}$$

In Equation (4.16), the translation vector $\mathbf{O}_{AU}$ describes the position of the origin of A in frame U. However, it should be noted that this equation only depends on instantaneous parameters. It is of course possible that frame A is moving and rotating with respect to U, instead of being static. In this case, the time derivative of the vector $\mathbf{x}$ in frame U can be expressed as shown in Equation (4.17) [9, Ch. 3.2]:

$$\dot{\mathbf{x}}_U = \dot{\mathbf{O}}_{AU} + \mathbf{C}_{A2U}\dot{\mathbf{x}}_A + \boldsymbol{\omega}_{AU} \times (\mathbf{C}_{A2U}\mathbf{x}_A) \tag{4.17}$$

In Equation (4.16), the vector $\boldsymbol{\omega}_{AU}$ describes the rotational rate of A with respect to U. Furthermore, the two preceding equations have been formulated using the DCM, which, as mentioned in Section 4.2, require a large number of parameters to describe the rotation. It is possible to formulate this rotation using either Euler angles or quaternions. Transformations using these parameters will be described in the subsequent subsections.

TRANSFORMATIONS USING EULER ANGLES

The basic principle of performing transformations using Euler angles is centered on the so-called unit-axis transformations [9, Ch. 3.2]. If the generic orthogonal frame A and the equally generic orthogonal frame U are separated by an angle α about a single axis, these unit axis transformations can be used to express the components of a vector in frame U in the components of the same vector in frame A. Three different unit-axis transformations exist, one for each of the x-, y-, and z-axes, shown in Equations (4.18) through (4.20), respectively:

$$\begin{bmatrix} u \\ v \\ w \end{bmatrix} = \begin{bmatrix} 1 & 0 & 0 \\ 0 & \cos\alpha & \sin\alpha \\ 0 & -\sin\alpha & \cos\alpha \end{bmatrix} \begin{bmatrix} a \\ b \\ c \end{bmatrix} = \mathbf{C}_x(\alpha) \begin{bmatrix} a \\ b \\ c \end{bmatrix} \tag{4.18}$$

$$\begin{bmatrix} u \\ v \\ w \end{bmatrix} = \begin{bmatrix} \cos\alpha & 0 & -\sin\alpha \\ 0 & 1 & 0 \\ \sin\alpha & 0 & \cos\alpha \end{bmatrix} \begin{bmatrix} a \\ b \\ c \end{bmatrix} = \mathbf{C}_y(\alpha) \begin{bmatrix} a \\ b \\ c \end{bmatrix} \tag{4.19}$$

$$\begin{bmatrix} u \\ v \\ w \end{bmatrix} = \begin{bmatrix} \cos\alpha & \sin\alpha & 0 \\ -\sin\alpha & \cos\alpha & 0 \\ 0 & 0 & 1 \end{bmatrix} \begin{bmatrix} a \\ b \\ c \end{bmatrix} = \mathbf{C}_z(\alpha) \begin{bmatrix} a \\ b \\ c \end{bmatrix} \tag{4.20}$$

As mentioned previously, a maximum of three of these unit-axis transformations must be performed to transform between different reference frames in three-dimensional space. In this case, the $n+1^{th}$ rotation in the sequence is performed over the transformed reference frame which is a result of the n^{th} rotation [58, A.3]. The unit-axis rotation matrices are then multiplied in a particular order, with the first rotation appearing at the right of the multiplication, the second in the middle, and the third at the left. The result of such a multiplication is then the DCM of one frame with respect to another, also shown for the common yaw-pitch-roll sequence in Equation (4.21):

$$\begin{bmatrix} u \\ v \\ w \end{bmatrix} = \mathbf{C}_x(\phi)\mathbf{C}_y(\theta)\mathbf{C}_z(\psi) \begin{bmatrix} a \\ b \\ c \end{bmatrix} \tag{4.21}$$

Again, it is noted depends on the specific transformation what this order is, and if the full three rotations are even necessary.

TRANSFORMATIONS USING QUATERNIONS

To perform frame transformations using quaternions, a similar procedure can be followed as described for the Euler angles [58, A.4]: this is due to the fact that the DCM can also be expressed in terms of the quaternion elements. Thus, if defining the first rotation as $\mathbf{C}(q)$ and the second as $\mathbf{C}(q')$, the complete rotation $\mathbf{C}(q'')$ can be described as shown in Equation (4.22):

$$\mathbf{C}(q'') = \mathbf{C}(q')\mathbf{C}(q) \tag{4.22}$$

However, due to the unique properties of the unit Euler-axis vector defining the quaternion, this problem can also be solved as a direct quaternion multiplication This allows the total rotation to be defined as shown in Equation (4.23) [58, A.4]:

$$\begin{bmatrix} q_1'' \\ q_2'' \\ q_3'' \\ q_4'' \end{bmatrix} = \begin{bmatrix} q_4' & q_3' & -q_2' & q_1' \\ -q_3' & q_4' & q_1' & q_2' \\ q_2' & -q_1' & q_4' & q_3' \\ -q_1' & -q_2' & -q_3' & q_4' \end{bmatrix} \begin{bmatrix} q_1 \\ q_2 \\ q_3 \\ q_4 \end{bmatrix} \tag{4.23}$$

4.3.2. STATE VARIABLE TRANSFORMATIONS

Transformations between sets of state variables are vital for expressing the state of a system in an informative manner, as often the most convenient variables for setting up the equations of motion are not the most intuitive. A good example is the transformation from a relatively unintuitive quaternion to the intuitive Euler angles. Additionally, the conversion from Cartesian to Keplerian elements and vice versa will be discussed, as this will be essential for model verification later on, as well as understanding what happens to the orbit of the TSDS during the ADR mission.

QUATERNION TO EULER ANGLE TRANSFORMATION

Since quaternions will be used to formulate the equations of motion, it is important to be able to represent a quaternion orientation in a more intuitive form. Thus, to transform an attitude representation in terms of the four quaternion parameters into the roll, pitch, and yaw angles in the yaw-pitch-roll sequence, the transformation shown in Equation (4.24) can be used [61]. This gives the magnitudes of the three angles ϕ, θ, and ψ in terms of q_1, q_2, q_3, and q_4.

$$\begin{bmatrix} \phi \\ \theta \\ \psi \end{bmatrix} = \begin{bmatrix} \text{atan2}\left(-2q_1q_2 + 2q_4q_3, q_1^2 + q_4^2 - q_3^2 - q_2^2\right) \\ \text{asin}\left(2q_1q_3 + 2q_4q_2\right) \\ \text{atan2}\left(-2q_2q_3 + 2q_4q_1, q_3^2 - q_2^2 - q_1^2 - q_4^2\right) \end{bmatrix} \tag{4.24}$$

CARTESIAN TO KEPLERIAN TRANSFORMATION

To convert from Cartesian to Keplerian coordinates [62, Ch. 2.7], first the position and velocity vectors **R** and **V** are created with the given Cartesian states. Following this, it is directly possible to find expressions for the semi-major axis a and eccentricity e, using Equations (4.25) through (4.27).

$$a = \frac{1}{\frac{2}{r} - \frac{|\mathbf{V}|^2}{\mu}} \tag{4.25}$$

$$\mathbf{e} = \frac{\mathbf{V} \times \mathbf{h}}{\mu} - \frac{\mathbf{R}}{r} \tag{4.26}$$

$$e = |\mathbf{e}| \tag{4.27}$$

Furthermore, using the position **R** and velocity **V**, the orbital angular momentum vector **h** can be defined as shown in Equations (4.28):

$$\mathbf{h} = \mathbf{R} \times \mathbf{V} \tag{4.28}$$

Using the result from Equation (4.28), the inclination i can be found using Equation (4.29):

$$i = \mathrm{acos}\left(\frac{h_z}{|\mathbf{h}|}\right) \tag{4.29}$$

The true anomaly can be found using the eccentricity vector **e** from Equation (4.26), as shown in Equation (4.30):

$$\nu = \nu_{sign} \cdot \mathrm{acos}\left(\frac{\mathbf{R}}{|\mathbf{R}|} \cdot \frac{\mathbf{e}}{|\mathbf{e}|}\right) \tag{4.30}$$

The argument ν_{sign} determines the correct sign of ν, and is defined in Equation (4.31):

$$\nu_{sign} = 1 \text{ if } (\mathbf{e} \times \mathbf{R}) \cdot \mathbf{h} > 0; \;\; -1 \text{ otherwise} \tag{4.31}$$

To determine the RAAN and argument of periapsis, a conversion vector **N** can first be defined. This conversion vector is found using Equation (4.32):

$$\mathbf{N} = \begin{bmatrix} 0 \\ 0 \\ 1 \end{bmatrix} \times \mathbf{h} \tag{4.32}$$

Then, it is possible to determine the argument of periapsis ω using Equation (4.33):

$$\omega = \omega_{sign} \cdot \mathrm{acos}\left(\frac{\mathbf{e}}{|\mathbf{e}|} \cdot \frac{\mathbf{N}}{|\mathbf{N}|}\right) \tag{4.33}$$

The argument ω_{sign} is defined in Equations (4.34):

$$\omega_{sign} = 1 \;\text{ if } (\frac{\mathbf{N}}{|\mathbf{N}|} \times \mathbf{e}) \cdot \mathbf{h} > 0; \;\; -1 \text{ otherwise} \tag{4.34}$$

Using Equation (4.32), it is also possible to define the parameter N_{xy} in Equation (4.35):

$$N_{xy} = \sqrt{N_x^2 + N_y^2} \tag{4.35}$$

The result of Equation (4.35) finally allows the RAAN Ω to be determined, as shown in Equation (4.36):

$$\Omega = \mathrm{atan2}\left(\frac{N_y}{N_{xy}}, \frac{N_x}{N_{xy}}\right) \tag{4.36}$$

It must be mentioned that since some of the Keplerian elements can be undefined in special cases, the conversion method shown in Equations (4.25) through (4.36) can suffer the same problems. If the orbit is circular, the eccentricity vector **e** in Equation (4.26) will be zero, and thus both ν in Equation (4.30) and ω in Equation (4.33) will be undefined. Furthermore, if the orbit is equatorial, the conversion vector **N** in Equation (4.32) will be zero, and thus Ω in Equation (4.36) and again ω in Equation (4.33) will be undefined.

KEPLERIAN TO CARTESIAN TRANSFORMATION

To transform back from an instantaneous set of Keplerian coordinates to a Cartesian position and velocity, first a perifocal reference frame is defined, with the x-axis pointing towards periapsis and the y-axis perpendicular to this in the orbital plane [62, Ch. 2.7], with the origin in the center of the main body of the system. The Cartesian position can then be expressed as shown in Equation (4.37):

$$\begin{bmatrix} x \\ y \\ z \end{bmatrix} = \begin{bmatrix} l1 & l2 \\ m1 & m2 \\ n1 & n2 \end{bmatrix} \begin{bmatrix} x_{pf} \\ y_{pf} \end{bmatrix} \tag{4.37}$$

The definition of the arguments in Equation (4.37) can be found in Equations (4.38)-(4.39):

$$\begin{aligned} l_1 &= \cos\Omega\cos\omega - \sin\Omega\sin\omega\cos i \\ l_2 &= -\cos\Omega\sin\omega - \sin\Omega\cos\omega\cos i \\ m_1 &= \sin\Omega\cos\omega + \cos\Omega\sin\omega\cos i \\ m_2 &= -\sin\Omega\sin\omega + \cos\Omega\cos\omega\cos i \\ n_1 &= \sin\omega\sin i \\ n_2 &= \cos\omega\sin i \end{aligned} \tag{4.38}$$

$$\begin{aligned} x_{pf} &= r\cos\nu \\ y_{pf} &= r\sin\nu \end{aligned} \tag{4.39}$$

In Equation (4.39), r defines the instantaneous radius from the center of the main body to the satellite. This can be defined as shown in Equation 4.40.

$$r = \frac{a(1-e^2)}{1+e\cos\nu} = a(1-e\cos E) \tag{4.40}$$

If the true anomaly ν is not known, as is the case with, for instance, a two-line element set (TLE) set, the radius must be solved for from the mean anomaly M, which is used to calculate the eccentric anomaly E as shown in Equation (4.41):

$$E_{i+1} = E_i + \frac{M - E_i + e\sin(E_i)}{1 - e\cos(E_i)} \tag{4.41}$$

Note that Equation (4.41) is simply a rewritten form of Equation (4.1), and must be solved iteratively. Then, the true anomaly can be found using Equation 4.42:

$$\nu = 2\text{atan}\left(\sqrt{\frac{1+e}{1-e}}\tan\left(\frac{E}{2}\right)\right) \tag{4.42}$$

The Cartesian velocity can then also be obtained using the same arguments presented in Equation (4.38) and the orbital angular momentum magnitude $|\mathbf{h}|$, seen in Equation (4.43):

$$|\mathbf{h}| = \sqrt{\mu a(1-e^2)} \tag{4.43}$$

Finally, the Cartesian velocity components themselves can be expressed as seen in Equation (4.44):

$$\begin{aligned} \dot{x} &= \frac{\mu}{|\mathbf{h}|}(-l_1\sin\nu + l_2(e+\cos\nu)) \\ \dot{y} &= \frac{\mu}{|\mathbf{h}|}(-m_1\sin\nu + m_2(e+\cos\nu)) \\ \dot{z} &= \frac{\mu}{|\mathbf{h}|}(-n_1\sin\nu + n_2(e+\cos\nu)) \end{aligned} \tag{4.44}$$

5

MATHEMATICAL MODELS

With all the necessary reference systems defined in the previous chapter, it is possible to formulate the appropriate equations of motion using these. Four different areas can be discerned when doing so: first, it is necessary to form a representative model of the environment the satellites in the TSDS are present in, shown in Section 5.1. Second, the equations of motion governing the orbital dynamics of these bodies are developed in Section 5.2. Third, in a similar fashion, the attitude dynamics are described in Section 5.3. Fourth, an appropriate model for the tether itself is constructed, as shown in Section 5.4.

5.1. ENVIRONMENTAL MODEL

The choice of environmental model has a large impact on the accuracy and speed of the simulation. If the model is too basic, the simulation will no longer be a good representation of reality, and if too much is taken into account, this negatively affects the performance of the simulator. Therefore, striking the right balance between these two parameters is imperative for producing an efficient simulator.

An overview of the different accelerations commonly encountered in Earth orbit and their magnitudes is presented in Figure 5.1. The values in this figure were determined using a satellite with an area-to-mass ratio of 0.01 m^2/kg for all non-gravitational perturbations, which is the ratio possessed by a cubical satellite with 1 m sides and a mass of 100 kg.

The ADR mission occurs in LEO, and the maximum altitude during this mission is 800 km [3]. Thus, the line representing Iridium in Figure 5.1 can be conveniently used for an assessment of the various environmental accelerations encountered by the TSDS during the mission. It is clear, of course, that the central gravity field of the Earth is the main contributor, followed by the J_2 effect. Additionally, aerodynamic drag starts playing a large role at lower altitudes. Therefore, these effects will be discussed in more detail.

5.1.1. GRAVITY MODEL

As mentioned, the gravity field model used in the simulator consists of the central field term and the J_2 term. In essence, the central field term assumes a spherically symmetrical gravity field, originating in the center of mass of the Earth. When assuming that the mass of a satellite is significantly smaller than that of the Earth, the force on the satellite due to the central field can be found using Newton's second law and law of gravitation [52, Ch. 2.2]. This is shown in Equation (5.1).

$$\mathbf{F}_{cf} = -\frac{\mu}{r^3}\mathbf{R}_s m_s \tag{5.1}$$

In Equation (5.1), the vector $\mathbf{R}_s$ is the position of the satellite with respect to the center of mass of the Earth, r is the magnitude of this vector, and μ is the gravitational parameter of the Earth, which is equal to $398600.441 \cdot 10^9$ m^3/s^2 [62].

While Equation (5.1) offers the greatest contribution to the gravitational force, it also assumes that the gravity field is spherically symmetrical. However, the actual gravity field of the Earth shows irregularities, the largest of which is the J_2 effect [52, Ch. 7.6]. Physically, the J_2 effect describes the fact that the Earth is slightly flattened due to its rotation, resulting in a higher gravitational pull over the equator than over the poles. It is possible to write the perturbing force resulting from the J_2 effect $\mathbf{F}_{J2}$ as shown in Equation (5.2) [64, Ch. 20.1].

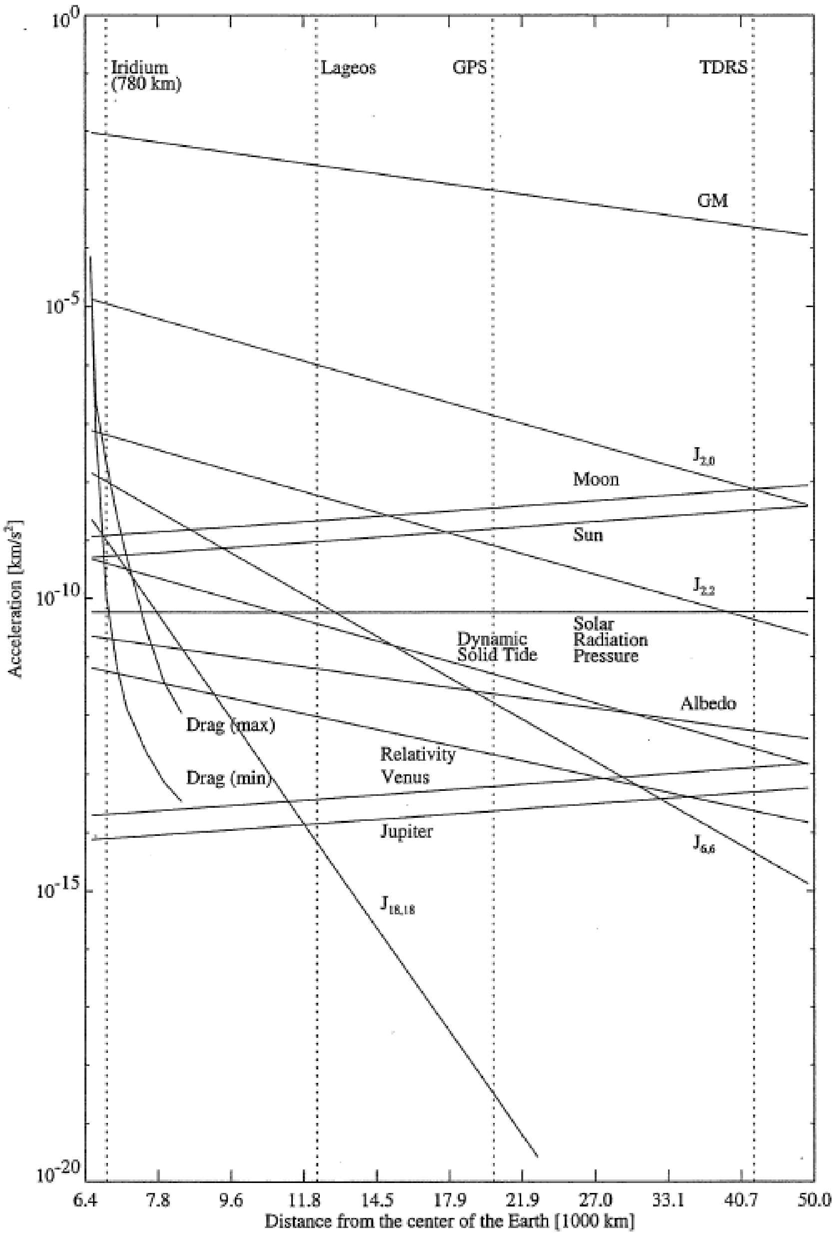

Figure 5.1: Magnitude of various accelerations acting on a satellite in Earth orbit [63, Ch. 3.1].

$$\mathbf{F}_{J2} = -\frac{3}{2}\mu J_2 \frac{R_E^2}{r^5} \begin{bmatrix} x_s\left(1-5\frac{z_s^2}{r^2}\right) \\ y_s\left(1-5\frac{z_s^2}{r^2}\right) \\ z_s\left(3-5\frac{z_s^2}{r^2}\right) \end{bmatrix} m_s \tag{5.2}$$

In Equation (5.2), the dimensionless constant J_2 has a value of $1082.63 \cdot 10^{-6}$ [62]. Also, R_E is used to denote the mean radius of the Earth, with a value of 6378.136 km [62]. Finally, x_s, y_s, and z_s denote the components of $\mathbf{R}_s$ along each of the three axes.

Gravity fields which are not spherically symmetric will in general induce periodic variations in the orbital elements, as well as secular variations in some elements. However, since gravity is a conservative force, the energy of the orbit will not change and thus no secular variations in the semi-major axis or eccentricity will occur [64, Ch. 23.3]. This means that the gravity field will not contribute to the reduction of semi-major axis or change in eccentricity required to deorbit the target.

5.1.2. ATMOSPHERIC MODEL

Aerodynamic drag is one of the most difficult forces to model on satellites in orbit [52, Ch. 7.6]. This is because aerodynamic drag is highly dependent on the atmospheric density, the models of which contain large uncertainties. Additionally, drag is not a conservative force, and will therefore remove energy from the satellite, causing the orbit to decay. The aerodynamic drag force $\mathbf{F}_D$ can be expressed as in Equation (5.3).

$$\mathbf{F}_D = -\frac{1}{2} C_D A \rho |\mathbf{V}_R| \mathbf{V}_R \tag{5.3}$$

Note that this force is denoted as negative, due to the fact that drag always acts in the opposite direction to the velocity vector. Additionally, the drag coefficient C_D is quite difficult to determine, and is often set at ≈ 2 for orbiting satellites [52, Ch. 7.6]. Finally, $\mathbf{V}_R$ is defined as the velocity of the satellite relative to the atmosphere, which in approximation is the velocity of the satellite relative to the ECEF frame. This can be expressed in terms of the inertial velocity $\mathbf{V}_I$ using Equation (4.17), resulting in Equation (5.4).

$$\mathbf{V}_R = \mathbf{V}_I - \boldsymbol{\omega}_E \times \mathbf{R}_I \tag{5.4}$$

As mentioned, the most difficult parameter to determine is the atmospheric density [52, Ch. 7.6]. Ideally, an atmospheric model would have to take latitudinal and longitudinal variations into account, as well as time-varying effects such as diurnal, solar-rotation cycle, Sun-spot cycle, and meteorological variations. This, however, is a tall order, as these parameters show large variations and thus also induce large variations in the properties of the atmosphere.

Multiple theoretical and empirical models of the Earth's atmosphere exist [52, Ch. 7.6]. The NRLMSISE-00 model is the most recent atmosphere model, and is is based on mass spectrometer and radar measurements of the upper atmosphere, along with additional databases from drag measurements [65]. Furthermore, it is the current international standard used for space research [66]. However, it is a relatively complicated model to use, as it depends on both the spatial and temporal state of the satellite under consideration.

Therefore, a set of values was tabulated by altitude for a fixed latitude and longitude, in this case arbitrarily chosen as zero degrees North latitude and zero degrees East longitude. These values were then used for all other latitudes and longitudes. While this is insufficient for detailed mission planning, this strategy should be acceptable for a first-order mission analysis, particularly since the deorbit mission is expected to be short in duration. The resulting atmospheric density ρ as a function of altitude h is shown in Figure 5.2.

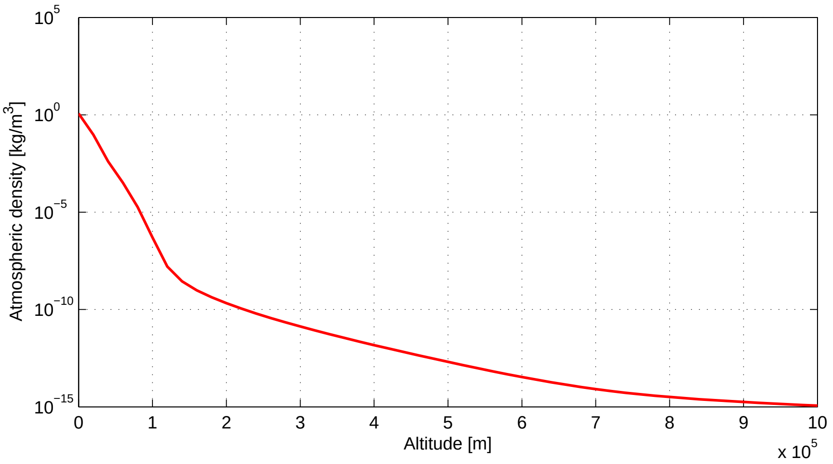

Figure 5.2: Atmospheric density distribution of NRLMSISE-00 for (0N, 0E).

5.2. ORBITAL DYNAMICS MODEL

With the environment defined, it is possible to look at the orbital dynamics of the satellites in the TSDS. A number of different methods of modeling the orbital dynamics will be discussed: First, two-body, or unperturbed, orbital dynamics will be presented, as these provide a good first-order approximation of actual orbits. Second, the concept of orbital maneuvering will be discussed. Third, the relative motion between two satellites in close proximity in unperturbed orbits will be examined. This provides an indication of how the chaser and target will tend to move with respect to each other, Fourth, orbital perturbations will be added to the mix, providing a more realistic model for actual orbital dynamics for simulations.

5.2.1. TWO-BODY DYNAMICS

Two-body dynamics form the classical analysis of orbital motion [52, Ch. 2]. As briefly mentioned in Section 5.1.1, this classical analysis operates under the assumption that the main body has a spherically symmetrical gravity field, and that the mass of the satellite is much smaller than that of the main body. Under these assumptions, Equation (5.1) fully defines the dynamics of the system.

This single dynamical relation allows the derivation of several additional useful equations, offering more insight to the behavior of a two-body system. The first of these relates to the conservative nature of gravity as a force: for a given orbit in a two-body system, it can be shown that the orbital angular momentum of the satellite per unit mass is constant, and can be expressed as in Equation (5.5), which was also shown previously in Equation (4.28) [52, Ch. 2.2].

$$\mathbf{h} = \mathbf{R}_s \times \mathbf{V}_s \tag{5.5}$$

As mentioned, Equation (5.5) defines the specific angular momentum of the orbit of the satellite. It is also possible to find an expression for the specific mechanical energy of the satellite itself. This represents the so-called vis-viva equation, which is presented in Equation (5.6) [52, Ch. 2.2].

$$|\mathbf{V}_s|^2 = \mu\left(\frac{2}{|\mathbf{R}_s|} - \frac{1}{a}\right) \tag{5.6}$$

It can be seen that the vis-viva equation relates the magnitude velocity of the satellite to its distance from the center of the Earth, as well as to the semi-major axis a of the orbit. This makes this equation very useful when performing first-order analyses on the effects of orbital maneuvers.

Besides the two energy relations shown in Equations (5.5) and (5.6), it is possible to derive kinematic relations describing the size and shape of the orbit, as well as the position of the satellite in the orbit [52, Ch. 2.2]. These equations are known collectively as Kepler's laws, and were historically derived by Johannes Kepler before Isaac Newton formulated his laws.

Kepler's first law states that orbits in a two-body system describe conic sections, being circles, ellipses, parabolas, and hyperbolas [52, Ch. 2.2]. Which of these conic sections is described depends on the specific energy of the satellite, and each is governed by slightly different formulations of the same law. However, since only closed orbits (circles and ellipses) will be considered for an ADR mission, only the equations relating to these will be discussed. The corresponding formulation of Kepler's first law can be seen in Equation (5.7), which was also shown in Equation (4.40).

$$|\mathbf{R}_s| = \frac{a(1-e^2)}{1+e\cos(\nu)} \tag{5.7}$$

Kepler's second law states that $\mathbf{R}_s$ sweeps out equal areas in the orbital plane in equal times [52, Ch. 2.1]. For elliptical orbits, this effectively means that satellites spend more time near apoapsis, or the farthest point in the orbit, than at periapsis, which is the nearest point in the orbit. Integrating Kepler's second law over one orbital period t_{orb} brings about Kepler's third law, which defines the total orbital period. This is shown in Equation (5.8) [52, Ch. 2.2].

$$t_{orb} = 2\pi\sqrt{\frac{a^3}{\mu}} \tag{5.8}$$

From Kepler's third law, the mean motion n of the satellite can also be defined [52, Ch. 2.2]. This parameter expresses the average angular velocity of a satellite in its orbit, and is defined as in Equation (5.9).

$$n = \sqrt{\frac{\mu}{a^3}} \tag{5.9}$$

It must be noted that the two-body problem is a strictly planar problem: all motion occurs in a single plane in space known as the orbital plane. Within the constraints of the two-body problem, it is possible to change this orbital plane (as well as other parameters in the orbit) using instantaneous changes to the velocity vector. Such changes are often denoted as impulsive maneuvers or simply ΔVs [52, Ch. 5].

5.2.2. ORBITAL MANEUVERING

The concept of orbital maneuvering is essential for achieving a successful deorbit mission. This field covers the theory of applying a change in momentum, currently achieved by firing rocket engines, to change the orbital state of the satellite [52, Ch. 5.1]. It is particularly convenient to express the effects of orbital maneuvering on the Keplerian elements, and thus two types of maneuvers can be discerned: coplanar maneuvers and out-of-plane maneuvers. Both types allow for the satellite to alter different elements of its orbit.

Specifically in the case of deorbit missions, changes in the semi-major axis of the orbit are desired: to achieve deorbit, it is necessary to place the periapsis deep inside the Earth's atmosphere such that the satellite will burn up. Thus, only coplanar maneuvers will be considered here, as out-of-plane maneuvers do not alter the semi-major axis of the orbit. Furthermore, orbital maneuvers are often approximated as instantaneous changes in the satellite velocity, or ΔVs. For coplanar maneuvers, Equation (5.6) can simply be used to determine the magnitude of a maneuver to transit from one orbit to another [52, Ch. 5]. This is shown in Figure 5.3.

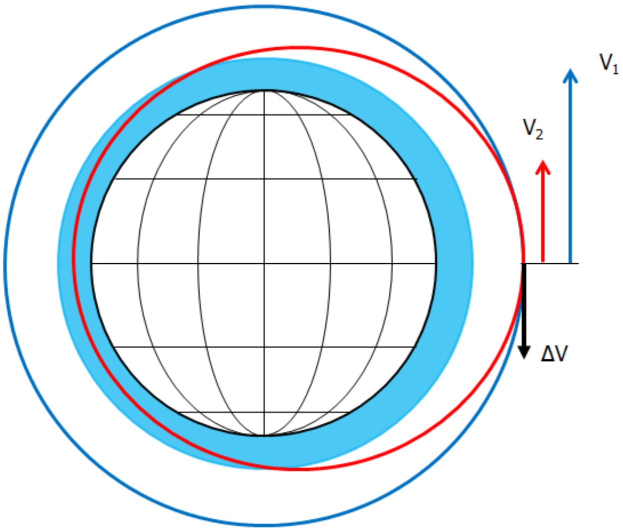

Figure 5.3: Coplanar ΔV to reduce periapsis of an initial circular orbit to within the atmosphere.

Two important notes must still be made regarding maneuvering in a two-body system. First, the most efficient point to change the periapsis of the orbit is at apoapsis [52, Ch. 5.3]. As the ultimate goal of ADR is to lower the periapsis of the target to deep within the atmosphere, it is most efficient to perform a deorbit burn at apoapsis. Second, using ideal rocket theory, it is possible to express the propellant mass required for a certain ΔV [52, Ch. 5.7]. This is commonly known as the rocket equation, or Tsiolkovsky's equation, and is shown in Equation (5.10).

$$\Delta V = I_{sp} g_0 \ln\left(\frac{m_0}{m_f}\right) \tag{5.10}$$

In Equation (5.10), the specific impulse I_{sp} is a measure of the efficiency of the used rocket engine, and g_0 is the surface gravity of the Earth, which is equal to 9.0665 $\mathrm{m/s^2}$ [62]. Moreover, m_0 represents the mass of the satellite at the start of the maneuver, and m_f is the mass of the satellite at the end of the maneuver. This equation can then be rearranged to find an expression for the propellant mass m_{prop} shown in Equation (5.11).

$$m_{prop} = m_0\left(1 - \frac{1}{\exp\left(\frac{\Delta V}{I_{sp} g_0}\right)}\right) \tag{5.11}$$

5.2.3. RELATIVE ORBITAL DYNAMICS

A subset of two-body dynamics considers the motion of two satellites of negligible mass with respect to each other [52, Ch. 5.8]. Specifically, it is often desired to know the motions of a chaser satellite with respect to a target satellite: a Hill frame fixed to the target is used to represent these motions. Also, it is convenient to perform this analysis per unit mass of the chaser. This allows the so-called Clohessy-Wiltshire (CW) equations to be obtained, as seen in Equation (5.12).

$$\begin{aligned} \ddot{x} - 2|\boldsymbol{\omega}|\dot{y} - 3|\boldsymbol{\omega}|^2 x &= \frac{F_x}{m_c} \\ \ddot{y} + 2|\boldsymbol{\omega}|\dot{x} &= \frac{F_y}{m_c} \\ \ddot{z} + |\boldsymbol{\omega}|^2 z &= \frac{F_z}{m_c} \end{aligned} \tag{5.12}$$

In Equation (5.12), $|\boldsymbol{\omega}|$ is the angular velocity of the considered Hill frame with respect to the inertial frame [52, Ch. 5.8]. For satellites orbiting Earth, this is equal to the mean motion n of the target. Furthermore, F_x, F_y, and F_z are all forces acting on the chaser added to forces resulting from orbital perturbations.

The expressions in Equation (5.12) provide the equations of motion along the R-bar, V-bar, and H-bar directions, respectively, the positions along which are denoted by x, y, and z, for simplicity. It must be noted that these equations hold only for near-circular orbits [52, Ch. 5.8]. They can be solved analytically by assuming that all perturbing force components are equal to zero [52, Ch. 5.8]. However, this limits the usefulness for analyzing the internal motion of the TSDS, as significant perturbations will most definitely be involved, particularly resulting from the tether. Thus, these equations can also simply be numerically integrated.

Nonetheless, the general behavior described by Equation (5.12) provides valuable insight to the motion of two satellites in close proximity [52, Ch. 5.8]. Particularly, it is of note that the velocities and accelerations in the x- and y-directions are coupled: a velocity in the positive y-direction causes an acceleration in the positive x-direction, and a velocity in the positive x-direction causes an acceleration in the negative y-direction. This can be explained from two-body dynamics: if two satellites are at the same altitude, but one is traveling faster, it will have a higher apoapsis and thus causes the faster satellite to move in the radial direction with respect to the slower satellite. Subsequently, the orbital period of the "faster" satellite will be longer, and will thus begin to lag behind the "slower" satellite. Such relations are important to consider when, for instance, collision risk is being assessed.

5.2.4. PERTURBED ORBITAL DYNAMICS

While two-body dynamics provide a good starting point for first-order analyses, this theory fails to model the motion of Earth-orbiting satellites to such a degree as to allow for real-world implementations. Therefore, it is essential to include more effects in the dynamical model than simply the central gravity field. Specifically, the environmental model presented in Section 5.1 must be taken into account when simulating the ADR mission. With a two-body system defining the ideal case, any additional forces to this model are collectively referred to as perturbations.

While perturbed orbital dynamics do provide a more realistic model for a satellite, the downside is that the the constant orbital elements from the two-body case are no longer constant. Thus, the orbit continuously changes in time. Several different techniques have been developed to deal with this, which can be grouped into two main categories: numerical methods and analytical solutions.

NUMERICAL METHOD FOR PERTURBED ORBITAL DYNAMICS

To perform accurate simulations including environmental perturbations, Cowell's formulation of the equations of motion can be used [52, Ch. 7.4]. In its most basic form, Cowell's formulation simply adds all perturbing forces, such as gravity-field variations, aerodynamic drag, and thrust, to the central field term and uses a numerical integrator to propagate the resulting equation of motion. This is shown in Equation (5.13), which incorporates the forces derived in Equations (5.1) through (5.3) as well as a thrust force $\mathbf{F}_{thr}$.

$$m_s \ddot{\mathbf{R}}_s = \mathbf{F}_{cf} + \mathbf{F}_{J2} + \mathbf{F}_D + \mathbf{F}_{thr} \tag{5.13}$$

Equation (5.13) provides a very convenient and intuitive formulation of the equations of motion for a satellite in the environment discussed in Section 5.1. All environmental forces in this model can be easily expressed in the ECI frame, and thus integrating the resulting equations of motion in this frame is fairly trivial. Furthermore, this formulation is used in the GGNCSIM libraries, ensuring proper V&V of the implemented routines.

While Equation (5.13) is a valid formulation for each individual body in the TSDS, its formulation as shown only holds for the chaser. Since the target is uncooperative, the thrust forces acting on it will be zero, which also holds for each of the tether nodes. Furthermore, aerodynamic drag will not act on the tether nodes for two reasons: first, the cross-section of the tether is very small [3], and second, the complex geometry of the tether makes determining the effective cross-section and drag coefficient very difficult. It is also not expected that the aerodynamic drag on the tether will be a dominant force in the TSDS.

As a final note on Equation (5.13), it does not yet include the net force resulting from the tether on each body. With the exact method for determining this force detailed in Section 5.4, Equation (5.13) can be simply appended with the net tether force $\mathbf{F}_{teth}$, forming Equation (5.14)

$$m_s\ddot{\mathbf{R}}_s = \mathbf{F}_{cf} + \mathbf{F}_{J2} + \mathbf{F}_D + \mathbf{F}_{thr} + \mathbf{F}_{teth} \tag{5.14}$$

While Equation (5.14) completely governs the orbital motion of each mass element in the TSDS, and forms the basis of the numerical propagation scheme, it does not offer much *a priori* insight into the motion of the TSDS in the described environment [52, Ch. 8.2]. Fortunately, analytical methods for perturbed orbit dynamics also exist, which offer more insight to the behavior of the Keplerian orbital elements in a perturbed environment.

ANALYTICAL SOLUTIONS TO PERTURBED ORBIT DYNAMICS

A common analytical method for dealing with perturbed orbit dynamics is variation of parameters [52, Ch. 8.3]. Specifically, Gauss's formulation of the variation of parameters method allows both conservative forces, such as gravity, and nonconservative forces, such as drag, to be taken into account. The resulting equations are known as the Gauss planetary equations and are shown in Equation (5.15), with the perturbing forces F_x, F_y and F_z being expressed in the Hill frame [64, Ch. 22.3].

$$\begin{aligned}
\frac{da}{dt} &= -2\frac{a^2}{\mu p}\left[F_x e \sin\nu + F_y \frac{p}{|\mathbf{R}_s|}\right] \\
\frac{de}{dt} &= \sqrt{\frac{p}{\mu}}\left[F_x \sin\nu + F_y(\cos E + \cos\nu)\right] \\
\frac{di}{dt} &= F_z \frac{|\mathbf{R}_s|}{\sqrt{\mu p}} \cos u \\
\frac{d\Omega}{dt} &= F_z \frac{|\mathbf{R}_s|}{\sqrt{\mu p}\sin i} \cos u \\
\frac{d\omega}{dt} &= -\sqrt{\frac{p}{\mu}}\left[F_z \frac{|\mathbf{R}_s|}{p}\cot i \sin u + \frac{1}{e}\left(F_x \cos\nu - F_y\left(1 + \frac{|\mathbf{R}_s|}{p}\right)\sin\nu\right)\right] \\
\frac{dM}{dt} &= n - F_x\left[\frac{2|\mathbf{R}_s|}{\sqrt{\mu a}} - \frac{1-e^2}{e}\sqrt{\frac{a}{\mu}}\cos\nu\right] - F_y \frac{1-e^2}{e}\sqrt{\frac{a}{\mu}}\left(1 + \frac{|\mathbf{R}_s|}{p}\right)\sin\nu
\end{aligned} \tag{5.15}$$

In Equation (5.15), u refers to the argument of latitude, which is defined as $\omega + \nu$, and p is also known as the semiparameter, which is defined for circular and elliptical orbits as $a(1-e^2)$ [52, Ch. 2.4]. These parameters, and the used Hill frame, are shown in Figure 5.4.

It is possible to predict the specific behavior resulting from the J_2 effect and aerodynamic drag, as well as thrust along each of the three axis of the H frame, using the Gauss planetary equations. Starting with the J_2 effect, this perturbation has an effect on the semi-major axis a, inclination i, RAAN Ω, and argument of periapsis ω of the orbit under consideration [64, Ch. 21.2, 23.2]. As a function of argument of latitude u, the variances in these elements over one orbit can be expressed as shown in Equation (5.16).

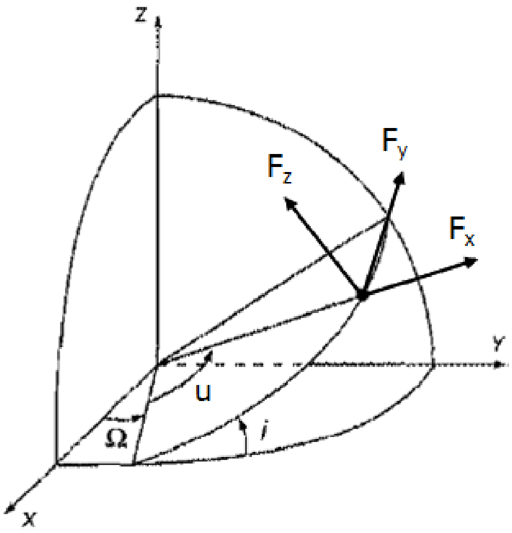

Figure 5.4: Definition of the Hill frame and u used for the Gauss planetary equations [64, Ch. 22.3].

$$\begin{aligned}
\Delta a &= -3 J_2 \frac{R_E^2}{|\mathbf{R}_{s,0}|} \sin^2 i_0 \sin^2 u \\
\Delta i &= -\frac{3}{4} J_2 \frac{R_E^2}{|\mathbf{R}_{s,0}|^2} \sin 2 i_0 \sin^2 u \\
\Delta\Omega &= -\frac{3}{2} J_2 \frac{R_E^2}{p^2} \cos i_0 \left[u - \frac{1}{2} \sin 2u \right. \\
&\quad \left. + \frac{1}{6} e \left(8 \sin\omega - 3 \sin(\omega + u) - 6 \sin(\omega - u) + \sin(\omega - 3u) \right) \right] \\
\Delta\omega &= \frac{3}{2} J_2 \frac{R_E^2}{p^2} \left[(3 - 4 \sin^2 i) u - \frac{1}{2} (1 - 4 \sin^2 i) \sin 2u + \right. \\
&\quad e \left(\sin\omega - \sin(\omega - u) + \frac{1}{12} (2 - 5 \sin^2 i) \left[8 \sin\omega - 3 \sin(\omega + u) - 6 \sin(\omega - u) + \sin(\omega - 3u) \right] \right) + \\
&\quad \left. \frac{1}{e} \left(\sin\omega - \sin(\omega - u) - \frac{1}{4} \sin^2 i \left[8 \sin\omega - 3 \sin(\omega + u) - 6 \sin(\omega - u) + \sin(\omega - 3u) \right] \right) \right]
\end{aligned} \tag{5.16}$$

It can be seen from Equation (5.16) that all four parameters will vary periodically over one orbit. Additionally, it can be seen that the RAAN and the argument of periapsis include a secular term, meaning that these parameters will drift due to the J_2 effect. These secular terms $\dot{\Omega}_{sec}$ and $\dot{\omega}_{sec}$ can be written as a function of time as shown in Equation (5.17) [52, Ch. 8.6].

$$\begin{aligned}
\dot{\Omega}_{sec} &= -\frac{3}{2} n J_2 \frac{R_E^2}{p^2} \cos i \\
\dot{\omega}_{sec} &= \frac{3}{4} n J_2 \frac{R_E^2}{p^2} \left(4 - 5 \sin^2 i \right)
\end{aligned} \tag{5.17}$$

The primary purpose of the Gauss planetary equations in the context of this research was to provide sound analytical results against which the results of the numerical simulations could be checked. However, the Gauss planetary equations could in principle be used in the numerical propagation scheme, although they suffer from the same singularities as the Keplerian elements [52, Ch. 8.3]. This could be remedied by formulating the Gauss equations in terms of an alternate elements set, such as the modified equinoctial elements or the USM. Again, though, the Cartesian elements are used as integration variables, so these alternate formulations will not be discussed here.

5.3. ATTITUDE DYNAMICS MODEL

While the orbital dynamics of the TSDS largely govern its mission trajectory, the rotational motions of the chaser and target are instrumental in actually achieving a successful deorbit. This is due to the fact that the thrusters on the chaser are fixed with respect to the chaser body-fixed (G_C) frame, and thus must be pointed in the correct direction for the momentum to be transferred across the tether to the target. Furthermore, the tether is not fixed to the center of mass of the chaser or target, which could induce large torques on each body. First, the models used for the chaser and target bodies will be presented. Second, the dynamics of these bodies will be summarized.

5.3.1. CHASER AND TARGET BODY MODELS

In essence, the chaser and target will be approximated by two rigid bodies with masses m_C and m_T and inertia tensors $\mathbf{I}_C$ and $\mathbf{I}_T$, respectively, values of which were provided [3]. Since the mass of the chaser may vary with expelled propellant, the initial inertia tensor of the chaser was scaled with the ratio of the instantaneous chaser mass to the initial chaser mass. This scaling assumes an axisymmetrical use of propellant; whether this is realistic or not is left outside the scope of this research. Since the target is completely inert, its inertia tensor will be constant. The two inertia matrices are expressed in Equation (5.18):

$$\mathbf{I}_C = \frac{m_C}{m_{C,0}} \begin{bmatrix} 1450 & 145 & 150 \\ 145 & 2850 & 280 \\ 150 & 280 & 1900 \end{bmatrix} \qquad \mathbf{I}_T = \begin{bmatrix} 129000 & 4500 & 1500 \\ 4500 & 125000 & 1800 \\ 1500 & 1800 & 17000 \end{bmatrix} \tag{5.18}$$

As mentioned, the satellite bodies will be approximated as rigid bodies. While this simplifies the analysis by decoupling the translation and rotation of each satellite, it is not fully representative of the actual situation: the real target, Envisat, has a very large solar panel attached to one side, which would display significant flexible modes. Furthermore, the chaser would most likely also have a solar panel to provide electric power, which would also display flexible modes [3]. However, due to time constraints it was chosen not to take this into account.

5.3.2. RIGID BODY ATTITUDE DYNAMICS

To describe the rotational dynamics of a rigid body, the angular momentum vector $\mathbf{H}$ can be used. If a generic body-fixed G frame with its origin in the center of mass of the body is considered, the angular momentum is a function of the inertia matrix and the body angular velocity vector $\boldsymbol{\omega}_G$ [58, Ch. 4.2]. This situation is visualized in Figure 5.5, with the three components of $\boldsymbol{\omega}_G$ also noted. Thus, it is possible to write the angular momentum vector in this frame as shown in Equation (5.19):

$$\mathbf{H}_G = \mathbf{I}_G \boldsymbol{\omega}_G \tag{5.19}$$

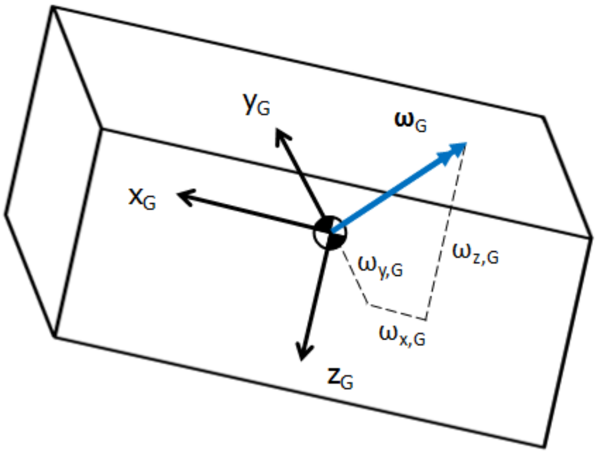

Figure 5.5: Definition of the angular velocity vector in the body-fixed G frame.

The time rate of change of the angular momentum vector in the inertial frame $\mathbf{H}_I$ is equal to the moment acting on the center of mass of the considered body. It is then possible to define this moment vector $\mathbf{M}$ as a function of the time rate of change of $\mathbf{H}_G$ using Equation (5.20), also known as Euler's moment equation [58, Ch. 4.5]:

$$\mathbf{M} = \dot{\mathbf{H}}_I = \dot{\mathbf{H}}_G + \boldsymbol{\omega}_G \times \mathbf{H}_G \tag{5.20}$$

It is possible to rewrite Equation (5.20) to be explicit in the inertia properties of the rotating body using Equation (5.19) [59, Ch. 6.4]. Thus, Equation (5.21) is obtained:

$$\mathbf{M} = \mathbf{I}_G \cdot \dot{\boldsymbol{\omega}}_G + \boldsymbol{\omega}_G \times \mathbf{I}_G \cdot \boldsymbol{\omega}_G \tag{5.21}$$

The external moment vector is the sum of all environmental moments, control moments, and moments caused by the tether. Since these are generally expressed as forces, as in Section 5.1, the corresponding moments can be found through Equation (5.22):

$$\mathbf{M}_{ext} = \sum \mathbf{R}_{off,i} \times \mathbf{F}_{ext,i} \tag{5.22}$$

In Equation (5.22), the offset vector $\mathbf{R}_{off}$ is the position vector from the center of mass of the body to the point at which the considered external force $\mathbf{F}_{ext}$ acts, expressed in the G frame. This can be the center of pressure for aerodynamic drag, or the tether connection point (TCP) for the tether forces.

With Equation (5.21), the rate of change of the angular velocities in the body-fixed frame can be found as a function of the external moment acting on the body. The angular velocities themselves can then be used to find the rate of change of the quaternion parameters defining the instantaneous orientation of the body [59, Ch. 5.5]. This relations is shown in Equation (5.23).

$$\dot{\mathbf{q}} = \frac{1}{2}\begin{bmatrix} 0 & \omega_{z,G} & -\omega_{y,G} & \omega_{x,G} \\ -\omega_{z,G} & 0 & \omega_{x,G} & \omega_{y,G} \\ \omega_{y,G} & -\omega_{x,G} & 0 & \omega_{z,G} \\ -\omega_{x,G} & -\omega_{y,G} & -\omega_{z,G} & 0 \end{bmatrix}\mathbf{q} = \frac{1}{2}\begin{bmatrix} q_4 & -q_3 & q_2 & q_1 \\ q_3 & q_4 & -q_1 & q_2 \\ -q_2 & q_1 & q_4 & q_3 \\ -q_1 & -q_2 & -q_3 & q_4 \end{bmatrix}\begin{bmatrix} \omega_{x,G} \\ \omega_{y,G} \\ \omega_{z,G} \\ 0 \end{bmatrix} \tag{5.23}$$

Using Equations (5.21) and (5.23), it is possible to express the complete angular state of the body as well as the derivative thereof. These equations are also implemented in the GGNCSIM libraries, and thus form the core of the numerical propagation scheme for the spacecraft attitude [67, Ch. 4.3].

5.4. TETHER DYNAMICS MODEL

Perhaps the most important mathematical model required for the tethered ADR mission is the model of the tether itself. This is due to fact that the tether forms the only physical link between the chaser and the target, and thus any thrust produced by the chaser must be transferred to the target through the tether. This makes the system dynamics much more complex than if a rigid connection were considered. First, the chosen mathematical model will be presented, being the so-called "lumped-mass" model [3, 68]. Second, a basic harmonic analysis will be performed on the TSDS. Finally, the implementation and verification of the developed model will be described.

5.4.1. LUMPED-MASS MODEL

As mentioned above, the model chosen to represent the dynamics of the tether itself is the lumped-mass model. In this model, the tether is discretized into N point masses, also called nodes, spaced equally along the natural tether length L_0. These nodes are then connected by $N+1$ linear tether elements: one connecting the target to the first node, one between each subsequent node, and the final element connecting the N^{th} node to the chaser. This is shown schematically in Figure 5.6.

To account for the elastic behavior of the tether model, each tether element is modeled as a Kelvin-Voigt material, meaning that each element is assumed to behave as a parallel spring-damper system [3]. This choice of model allows both tether tension and viscous damping in the tether to be taken into account. Of course, due to the nature of a tether, these forces will only be present if the tether element under consideration is extended past its natural length. Since the cross-sectional area of the tether is expected to be small [3], bending resistance in the tether will be neglected: thus, each node imposes no restrictions on the rotation angle between the elements connected to it. A schematic representation of the Kelvin-Voigt model of two adjacent tether nodes and the connected tether elements is given in Figure 5.7, along with the corresponding

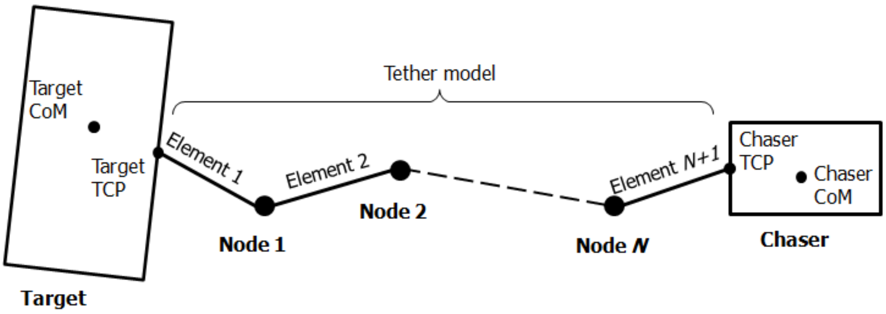

Figure 5.6: Schematic representation of the lumped-mass tether model.

free-body diagram of the tether nodes. In Figure 5.7, k_i and c_i represent the spring constant and damping coefficient of the i^{th} tether element, respectively. These parameters define the magnitudes of the tension force $\mathbf{F}_{ti}$ and damping force $\mathbf{F}_{di}$, respectively

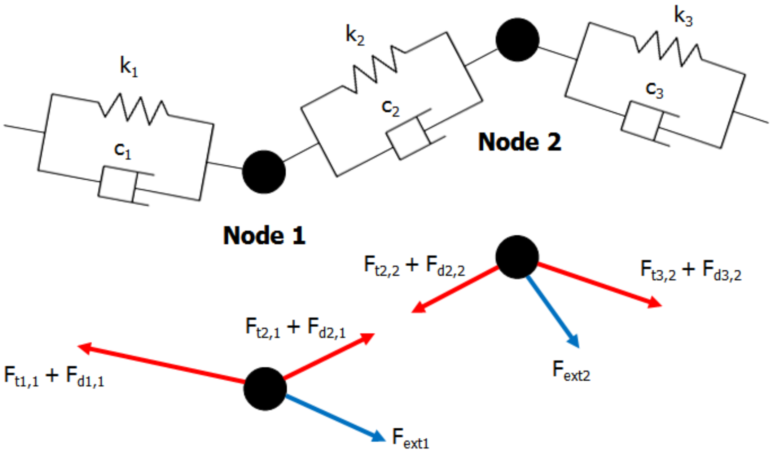

Figure 5.7: Schematic representation of the Kelvin-Voigt model of the tether elements.

The tension and damping forces act solely along the line of each tether element. Thus, the magnitude of each force to be expressed by one-dimensional equations, using the length of the element and the rate of extension thereof as the state variables governing the magnitude of each force. With the tether element length x and the rate of extension $\dot{x}$ defined using the local coordinate system shown in Figure 5.8, Equations (5.24) and (5.25) give the magnitude of the tension force F_t and damping force F_d, respectively [69, Ch. 1][3]:

$$F_t = \begin{cases} -k(x - x_0) & \text{if } x > x_0 \\ 0 & \text{if } x \leq x_0 \end{cases} \tag{5.24}$$

$$F_d = \begin{cases} -c\dot{x} & \text{if } x > x_0 \\ 0 & \text{if } x \leq x_0 \end{cases} \tag{5.25}$$

The formulation of the tension force F_t in Equation (5.24) is essentially Hooke's law of linear elasticity [69, Ch. 1]. This additionally allows k to be expressed in terms of physical tether properties. Specifically, the cross-sectional area A, length L, and the Young's modulus E_{mat} of the tether determine k according to Equation (5.26) [69, Ch. 1.5]:

$$k = \frac{AE_{mat}}{L} \tag{5.26}$$

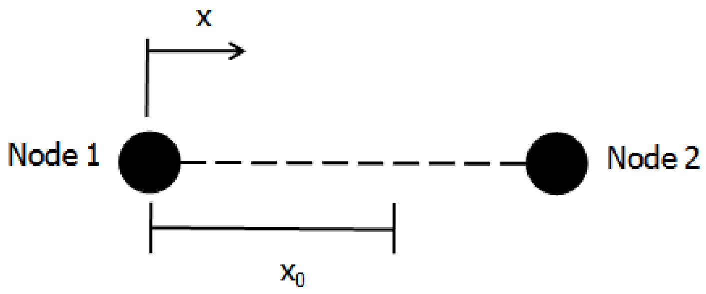

Figure 5.8: Tether element local coordinate system, with x_0 denoting the natural length.

The damping constant c is much more difficult to determine from the basic material and structural properties of the tether [69, Ch. 1]. No in-depth analysis will be done towards the exact determination of suitable values of c: the benchmark values presented by ESA will simply be used [3].

Due to the lumped-mass model discretizing the continuous tether into several point masses and tether elements, the spring and damping constants of each element in the tether will not be the same as that of the entire tether [69, Ch. 1.5]. This can be explained using the example of a tether with $N = 1$ and a spring constant k: for a total tether extension $(x - x_0)$, each element will only be extended by $(x - x_0)/2$ if the node is in equilibrium. Thus, for the same amount of tensile force to be exerted on each end mass, the spring constant of each element must be equal to $k_N = 2k$. The same principle holds for the damping constant of each element c_N, with both relations also expressed in Equation (5.27):

$$\begin{aligned} k_N &= k(N+1) \\ c_N &= c(N+1) \end{aligned} \tag{5.27}$$

The one-dimensional case presented in Equations (5.24) and (5.25) can then easily be transformed to the three-dimensional case using the relative position vector from the first to the second node $\mathbf{x}_{rel}$, the norm of which defines the element length. This is shown for the tension force vector $\mathbf{F}_t$ in Equation (5.28):

$$\mathbf{F}_t = \begin{cases} -k(|\mathbf{x}_{rel}| - x_0)\frac{\mathbf{x}_{rel}}{|\mathbf{x}_{rel}|} & \text{if } |\mathbf{x}_{rel}| > x_0 \\ 0 & \text{if } |\mathbf{x}_{rel}| \leq x_0 \end{cases} \tag{5.28}$$

To define the damping force in the three-dimensional case, it is first necessary to project the relative velocity vector between the first and second node $\dot{\mathbf{x}}_{rel}$ onto $\mathbf{x}_{rel}$, as the damping force can only act along the tether element. This projection is done using Equation (5.29) [70, Ch. 6]:

$$\dot{\mathbf{x}}_{proj} = \left(\dot{\mathbf{x}}_{rel} \cdot \frac{\mathbf{x}_{rel}}{|\mathbf{x}_{rel}|}\right)\frac{\mathbf{x}_{rel}}{|\mathbf{x}_{rel}|} \tag{5.29}$$

Using Equation (5.29), the relative velocity vector of two adjacent nodes is projected on to the tether element between these two. However, to determine the actual rate of extension $\boldsymbol{\epsilon}$ of the element, it is important to consider if $\dot{\mathbf{x}}_{proj}$ is in the same direction as the relative position, or opposite to this. This is determined using Equation

$$\boldsymbol{\epsilon} = \begin{cases} \dot{\mathbf{x}}_{proj} & \text{if } (\mathbf{x}_{rel} \cdot \dot{\mathbf{x}}_{rel}) > 0 \\ 0 & \text{if } (\mathbf{x}_{rel} \cdot \dot{\mathbf{x}}_{rel}) = 0 \\ -\dot{\mathbf{x}}_{proj} & \text{if } (\mathbf{x}_{rel} \cdot \dot{\mathbf{x}}_{rel}) < 0 \end{cases} \tag{5.30}$$

The rate of extension obtained in Equation (5.30) can be used to express the damping force $\mathbf{F}_d$ to be expressed as shown in Equation (5.31):

$$\mathbf{F}_d = \begin{cases} -c\boldsymbol{\epsilon} & \text{if } |\mathbf{x}_{rel}| > x_0 \\ 0 & \text{if } |\mathbf{x}_{rel}| \leq x_0 \end{cases} \tag{5.31}$$

As all nodes in the lumped-mass model are considered as point masses, the motion of each of these can be determined through Newton's second law. Furthermore, using the Cartesian coordinates described in Section 4.2, each node will have a six-element state vector. Thus, the system of equations of the entire tethered system, including the end masses, will be $6(N+2)$ dimensional. However, this system of equations is highly nonlinear, as the tension force depends on the norm of the relative distance, and the damping force depends on the dot product of the relative velocity with the relative position.

Nonetheless, it is possible to set up a nonlinear matrix equation, expressing the derivative of the state as a nonlinear function of the system state. Note that for this notation to hold, the end masses m_T and m_C are also modeled as point masses: how this is implemented in the context of the actual TSDS will be discussed in Section 5.4.3. The resulting system of equations for an N-node tether is shown in Equation (5.32):

$$\begin{bmatrix} \dot{\mathbf{x}}_T \\ \ddot{\mathbf{x}}_T \\ \dot{\mathbf{x}}_1 \\ \ddot{\mathbf{x}}_1 \\ \vdots \\ \dot{\mathbf{x}}_N \\ \ddot{\mathbf{x}}_N \\ \dot{\mathbf{x}}_C \\ \ddot{\mathbf{x}}_C \end{bmatrix} = \begin{bmatrix} \dot{\mathbf{x}}_T \\ \frac{1}{m_T}\left(k_N\left[(|\mathbf{x}_{rel,1T}|-x_0)\frac{\mathbf{x}_{rel,1T}}{|\mathbf{x}_{rel,1T}|}\right]+c_N\boldsymbol{\epsilon}_{1T}+\mathbf{F}_{ext,T}\right) \\ \dot{\mathbf{x}}_1 \\ \frac{1}{m_1}\left(k_N\left[(|\mathbf{x}_{rel,21}|-x_0)\frac{\mathbf{x}_{rel,21}}{|\mathbf{x}_{rel,21}|}-(|\mathbf{x}_{rel,1T}|-x_0)\frac{\mathbf{x}_{rel,1T}}{|\mathbf{x}_{rel,1T}|}\right]+c_N\left[\boldsymbol{\epsilon}_{21}-\boldsymbol{\epsilon}_{1T}\right]+\mathbf{F}_{ext,1}\right) \\ \vdots \\ \dot{\mathbf{x}}_N \\ \frac{1}{m_N}\left(k_N\left[(|\mathbf{x}_{rel,CN}|-x_0)\frac{\mathbf{x}_{rel,CN}}{|\mathbf{x}_{rel,CN}|}-(|\mathbf{x}_{rel,NN-1}|-x_0)\frac{\mathbf{x}_{rel,NN-1}}{|\mathbf{x}_{rel,NN-1}|}\right]+c_N\left[\boldsymbol{\epsilon}_{CN}-\boldsymbol{\epsilon}_{NN-1}\right]+\mathbf{F}_{ext,N}\right) \\ \dot{\mathbf{x}}_C \\ \frac{1}{m_C}\left(k_N\left[(|\mathbf{x}_{rel,CN}|-x_0)\frac{\mathbf{x}_{rel,CN}}{|\mathbf{x}_{rel,CN}|}\right]+c_N\boldsymbol{\epsilon}_{CN}+\mathbf{F}_{ext,C}\right) \end{bmatrix} \tag{5.32}$$

The terms $\mathbf{x}_{rel,ij}$ and $\boldsymbol{\epsilon}_{ij}$ from Equation 5.32 are defined in Equations (5.33) through (5.35):

$$\mathbf{x}_{rel,ij} = \mathbf{x}_i - \mathbf{x}_j \tag{5.33}$$

$$\boldsymbol{\epsilon}_{ij} = \begin{cases} \dot{\mathbf{x}}_{proj,ij} & \text{if } (\mathbf{x}_{rel,ij}\cdot\dot{\mathbf{x}}_{rel,ij}) > 0 \\ 0 & \text{if } (\mathbf{x}_{rel,ij}\cdot\dot{\mathbf{x}}_{rel,ij}) = 0 \\ -\dot{\mathbf{x}}_{proj,ij} & \text{if } (\mathbf{x}_{rel,ij}\cdot\dot{\mathbf{x}}_{rel,ij}) < 0 \end{cases} \tag{5.34}$$

$$\dot{\mathbf{x}}_{proj,ij} = \left(\dot{\mathbf{x}}_{rel,ij}\cdot\frac{\mathbf{x}_{rel,ij}}{|\mathbf{x}_{rel,ij}|}\right)\frac{\mathbf{x}_{rel,ij}}{|\mathbf{x}_{rel,ij}|} \tag{5.35}$$

From Equation (5.32), it can be seen that the possibility exists to add an external force $\mathbf{F}_{ext}$ to each tether node, as also seen in Figure 5.7. This can include gravitational or aerodynamic forces, which gives a more accurate representation of a tether in orbit. Thus, the developed model could even include electrodynamic forces on the nodes, allowing it to be used for the analysis of EDTs in the future.

5.4.2. TSDS HARMONIC ANALYSIS

As the lumped-mass model detailed in the previous section consists of linear springs and dampers, it is possible to make first-order predictions of the harmonic motion of the system using analytical methods for damped harmonic oscillators. The classical theories for this type of system typically involve a mass connected to a fixed wall, illustrated in Figure 5.9, which is again a one-dimensional system. Then, the general differential equation of motion for the mass can be formulated as shown in Equation (5.36) [69, Ch. 1]:

$$m\ddot{x} + c\dot{x} + kx = F \tag{5.36}$$

Note that in Equation (5.36), x is defined from the equilibrium position of the mass, and that the spring will thus also generate a restoring force when under compression.

The homogeneous solution to Equation (5.36) can be used to define the so-called damping ratio ζ and natural frequency ω_n, shown respectively in Equations (5.37) and (5.38) [69, Ch. 1.3]:

$$\zeta = \frac{c}{2\sqrt{km}} \tag{5.37}$$

$$\omega_n = \sqrt{\frac{k}{m}} \tag{5.38}$$

The parameters defined in Equations (5.37) and (5.38) then can be used to express the damped natural frequency ω_d, assuming an underdamped situation, shown in Equation (5.39):

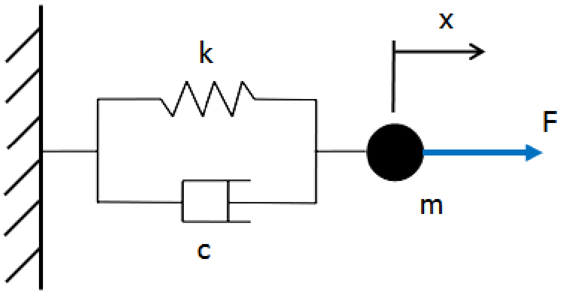

Figure 5.9: Classical definition of a damped harmonic oscillator.

$$\omega_d = \omega_n \sqrt{1-\zeta^2} \tag{5.39}$$

Physically, the damped natural frequency defines the period of a single oscillation when the system is subjected to nonzero initial conditions and zero net external force. Finally, the motion can be described as a function of time as shown in Equation (5.40) [69, Ch. 1.3]. Note that if c is nonzero, the oscillation will be subject to an exponential decay.

$$x = \sqrt{\frac{(\dot{x}_0 + \zeta\omega_n x_0)^2 + (x_0\omega_d)^2}{\omega_d^2}} \exp(-\zeta\omega_n t) \sin\left(\omega_d t + \operatorname{atan}\left(\frac{x_0\omega_d}{\dot{x}_0 + \zeta\omega_n x_0}\right)\right) \tag{5.40}$$

The preceding analysis holds for cases in which ζ is smaller than one, known as an underdamped system [69, Ch. 1.3]. A special case for the system behavior exists if ζ is equal to one, known as a critically-damped system. In this case, the system returns to its equilibrium position without oscillating in the shortest possible time. If ζ is higher than one, the system is overdamped, which means it takes longer than the critical case to return to the equilibrium position, again without oscillating. For the proposed tether models, the system will always be underdamped.

It is desirable to find similar expressions to Equations (5.37) - (5.40) describing the internal motions of the TSDS: not only does this give an indication of the amplitudes and periods of the the oscillations which will occur during deorbit burns, but it will also provided a benchmark against which to verify the behavior of the developed lumped-mass model. When simplifying the TSDS to the two end masses (the chaser and the target) and a single element, two important differences remain with the classical analysis. First, the tether only gives a force when extended past its natural length and does not provide a restorative force when under compression. Second, the system is “free” in inertial space, and thus does not have the unyielding boundary condition presented by the fixed wall in the classical case.

To remedy this deplorable situation, a new differential equation will be derived in the form of Equation (5.36), describing the motion of the chaser with respect to the target. To make this possible, the assumption will be made that the chaser is subject to a constant force F, as it would be during a deorbit burn. This causes the tether to continually be in tension, and thus x_{rel} will always be larger than x_0. First, from the free-body diagram shown in Figure 5.10, the equations of motion for both masses in “inertial” space can be constructed as shown in Equation (5.41).

$$\begin{aligned} m_1\ddot{x}_1 &= F_d + F_t = c\dot{x}_{rel} + kx_{rel} \\ m_2\ddot{x}_2 &= F - F_d - F_t = F - c\dot{x}_{rel} - kx_{rel} \end{aligned} \tag{5.41}$$

To obtain the differential equation for the relative motion, the two relations in Equation (5.41) were subtracted from each other to obtain the acceleration of m_2 with respect to m_1. This is shown in Equation (5.42).

$$\begin{aligned} \ddot{x}_{rel} &= \ddot{x}_2 - \ddot{x}_1 \\ &= -c\dot{x}_{rel}\left(\frac{1}{m_2} + \frac{1}{m_1}\right) - kx_{rel}\left(\frac{1}{m_2} + \frac{1}{m_1}\right) + \frac{F}{m_2} \end{aligned} \tag{5.42}$$

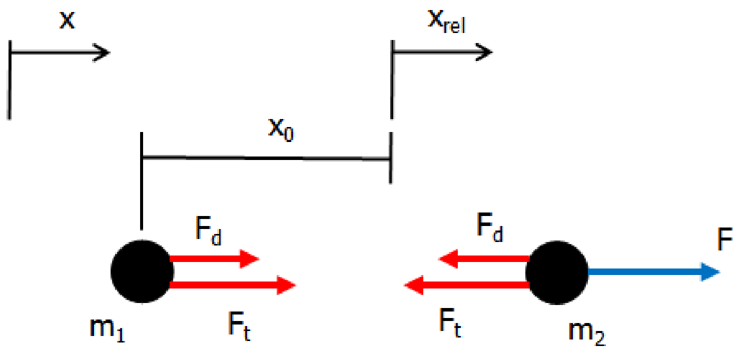

Figure 5.10: Free-body diagram of a “free” damped harmonic oscillator.

In Equation (5.42), m_2 can be brought to the left-hand side, resulting in Equation (5.43). The right-hand side of this equation is then only dependent on the ratio of the two masses.

$$m_2\ddot{x}_{rel} = (-c\dot{x}_{rel} - kx_{rel})\left(1+\frac{m_2}{m_1}\right)+F \tag{5.43}$$

Finally, Equation (5.43) can be rearranged to yield a similar form to Equation (5.36), and thus allowing the analysis to be performed more conveniently. The result is shown in Equation (5.44).

$$\frac{m_2}{1+\frac{m_2}{m_1}}\ddot{x}_{rel} + c\dot{x}_{rel} + kx_{rel} = F \tag{5.44}$$

With Equation (5.44) obtained, new expressions can be found for ζ, ω_n, and ω_d. These are shown in Equationa (5.45) through (5.47), with the primes denoting that these variables are for the “free” case.

$$\zeta' = \frac{c}{2\sqrt{k\frac{m_2}{1+\frac{m_2}{m_1}}}} \tag{5.45}$$

$$\omega'_n = \sqrt{\frac{k}{\frac{m_2}{1+\frac{m_2}{m_1}}}} \tag{5.46}$$

$$\omega'_d = \omega'_n\sqrt{1-\zeta'^2} \tag{5.47}$$

Equations (5.45) through (5.47) can then be used in Equation (5.40) to analyze the harmonic motions of the simplified TSDS.

As a final step, a relation was found for the equilibrium position as a function of the chaser and target masses, the tether length and spring constant, and the thrust level. In the equilibrium position, the relative velocity and acceleration between the two masses must be zero. Thus, Equation (5.43) can be written as shown in Equation (5.48), yielding the equilibrium position x_{eq}. Note that x is zero at a distance x_0 from m_1, as seen in Figure 5.10, so for the actual separation between m_1 and m_2, x_0 must be added to the obtained result.

$$\begin{gathered} m_2\ddot{x}_{rel} = -kx_{eq}\left(1+\frac{m_2}{m_1}\right)+F=0 \\ x_{eq} = \frac{F}{k\left(1+\frac{m_2}{m_1}\right)} \end{gathered} \tag{5.48}$$

5.4.3. TETHER MODEL IMPLEMENTATION

The method presented in the preceding subsections was implemented in Simulink in a C code S-function. Thus, the tether model can easily be used in conjunction with the GGNCSIM libraries, which are also written as C code S-functions [8, Ch. 15.2]. The working of the developed S-function will first be described; then, the model verification will be presented.

S-FUNCTION OVERVIEW

The created S-function takes the position and velocity of all the tether nodes and the TCPs on the chaser and target, along with the external force vector on each tether node, as inputs. Furthermore, a switch is included which allows the tether to be cut. This can prevent large errors from occurring once the TSDS is too low in the atmosphere, as drag on the tether is not taken into account. It then returns the velocity and acceleration of each tether node, as well as the force vector acting on both TCPs. The inputs and outputs of the S-function are further summarized in Table 5.1.

Table 5.1: Inputs and outputs of tether model S-function.

Inputs	
$\mathbf{x}_{TSDS}$	Row vector with the position and velocity components of respectively the target TCP, the tether nodes 1 through N, and the chaser TCP: $[x_{TCP,T} \quad y_{TCP,T} \quad z_{TCP,T} \quad \dot{x}_{TCP,T} \quad \dot{y}_{TCP,T} \quad \dot{z}_{TCP,T}$ $x_1 \quad y_1 \quad z_1 \quad \dot{x}_1 \quad \dot{y}_1 \quad \dot{z}_1$ $\dots$ $x_N \quad y_N \quad z_N \quad \dot{x}_N \quad \dot{y}_N \quad \dot{z}_N$ $x_{TCP,C} \quad y_{TCP,C} \quad z_{TCP,C} \quad \dot{x}_{TCP,C} \quad \dot{y}_{TCP,C} \quad \dot{z}_{TCP,C}]$
$\mathbf{F}_{extNodes}$	Row vector with the force components of the total external force acting on each tether node 1 through N: $[F_{x,1} \quad F_{y,1} \quad F_{z,1}$ $\dots$ $F_{x,N} \quad F_{y,N} \quad F_{z,N}]$
Tether cut switch	Scalar value which will cut the tether if it is larger than zero.
Outputs	
$\mathbf{F}_{TCP,T}$	Row vector with the force components of the force acting on the target TCP: $[F_{x,TCPT} \quad F_{y,TCPT} \quad F_{z,TCPT}]$
$\dot{\mathbf{x}}_{teth}$	Row vector with the velocity and acceleration components of the tether nodes 1 through N: $[\dot{x}_1 \quad \dot{y}_1 \quad \dot{z}_1 \quad \ddot{x}_1 \quad \ddot{y}_1 \quad \ddot{z}_1$ $\dots$ $\dot{x}_N \quad \dot{y}_N \quad \dot{z}_N \quad \ddot{x}_N \quad \ddot{y}_N \quad \ddot{z}_N]$
$\mathbf{F}_{TCP,C}$	Row vector with the force components of the force acting on the chaser TCP: $[F_{x,TCPC} \quad F_{y,TCPC} \quad F_{z,TCPC}]$

For the developed tether model routine, the convention presented in Figure 5.6 was adhered to. This means that node 1 is the tether node closest to the target, and that node N in closest to the chaser. Furthermore, the routine requires the position and velocity of the TCPs of the chaser and target, which need not be identical to the position and velocity of the center of mass of each satellite. These values can be obtained from the state of the considered satellite using Equation (5.49).

$$\begin{aligned} \mathbf{R}_{TCP} &= \mathbf{R}_s + \mathbf{R}_{off,TCP} \\ \mathbf{V}_{TCP} &= \mathbf{V}_s + \boldsymbol{\omega}_s \times \mathbf{R}_{off,TCP} \end{aligned} \tag{5.49}$$

To determine the state derivative of the tether nodes, a variation of Equation (5.32) was used: as the actual TSDS consists of end masses which are not point masses, the resulting tether forces in the TCPs of the chaser and target are determined, rather than the accelerations $\ddot{\mathbf{x}}_T$ and $\ddot{\mathbf{x}}_C$. Then, these TCP forces on the chaser and target can be simply added into the mathematical model for these bodies as an additional disturbance. This improves the modularity of the tether model routine, and thus helps it fit within the GGNCSIM design philosophy [8, Ch. 15].

TETHER MODEL VERIFICATION

With the dynamics of the TSDS being highly uncertain in the context of the proposed ADR mission, it is essential to properly verify and validate the designed tether model. In this context, verification is defined as "confirmation [...] that specified requirements have been fulfilled", while validation entails the "confirmation [...] that the particular requirements for a specific intended use are fulfilled" [8, Ch. 15.3]. Put differently, verification is the process of confirming that the model is performing as is expected from the theory implemented inside it, while validation is the process of confirming whether the model is approximating reality to a sufficient degree. Therefore, this section will focus on verification of the tether model, as the validity of Kelvin-Voigt materials is well-established in the literature.

As discussed in Chapter 3, orbital tethers have seen minimal real-world use, and current research being performed is focused on different modes of use compared to the proposed ADR mission. However, it is still possible to perform a simple test to verify the designed tether model, in the form of a simple harmonic oscillator with damping subject to a constant force. This draws on the methodology presented in Sections 5.4.1 and 5.4.2, allowing the simulation results to be compared to the analytical predictions.

For this test case, two end-masses were chosen, with mass values representative of the chaser and the target of 1500 kg and 7500 kg, respectively. Then, these end-masses were connected by a tether with properties representative of ESAs nominal tether model from Table 2.1: a natural length L_0 = 200 m, a number of nodes $N = 2$, a tether spring constant K = 10 N/m, a tether damping constant C = 1 Ns/m, and a tether mass m_{teth} = 5 kg. This system model was simulated with a constant thrust force of 500 N acting on the chaser mass element. The scenario is shown schematically in Figure 5.11.

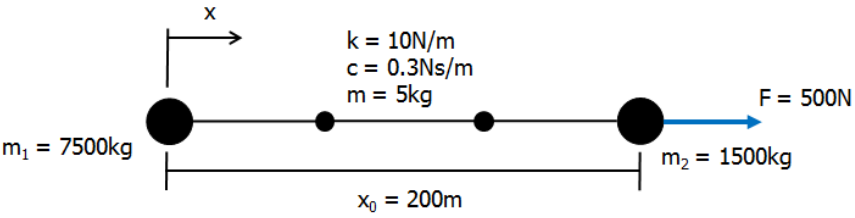

Figure 5.11: Schematic depiction of verification scenario in which the chaser is subject to a constant force.

For this simulation, the chaser is initially located at 200 m along the x-axis, with the thrust acting in the positive x-direction as well. Additionally, the initial relative velocity between the chaser and the target is set to zero. Thus, the tether is initially at its natural length, and therefore should be in tension for the duration of the simulation. This is because viscous damping will dissipate a small amount of energy from the system, causing the amplitude of the oscillation to slowly decrease.

For the described model of the TSDS, it is possible to determine the damping ratio ζ, natural frequency ω_n, and damped natural frequency ω_D using Equations (5.45) through (5.47). Working out the numbers returns $\zeta = 0.0013$, $\omega_n = 0.0894$ and $\omega_D = 0.0894$ rad/s. Due to the low value of ζ, ω_n and ω_d are practically identical. Furthermore, this value of the damped natural frequency translates to an oscillation period of 70.25 s. Since the tether is continuously in tension, it is possible to use Equation (5.40) to approximate the theoretical behavior of the oscillation. Leaving out the periodic term, it is possible to determine the oscillation envelope x_{lim} as shown in Equation (5.50):

$$x_{lim} = \sqrt{\frac{(\dot{x}_0 + \zeta\omega_n x_0)^2 + (x_0\omega_d)^2}{\omega_d^2}}\exp(-\zeta\omega_n t) \tag{5.50}$$

It can be determined from Equation (5.48) that the equilibrium position for the described model of the TSDS is at $x = 241.7$ m. Thus, the initial offset x_0 has a value of -41.7 m. Then, Equation (5.50) can be used to determine the maximum amplitude at any given time. Taking a simulation end time of $t = 1000$ s, the maximum amplitude at this instance is found to be 37.0 m.

Running the simulation for the same period of time, it is possible to compare the simulation results with the predicted value of the oscillation period and envelope. The system behavior, and the analytical prediction of the oscillation envelope, is shown in Figure 5.12.

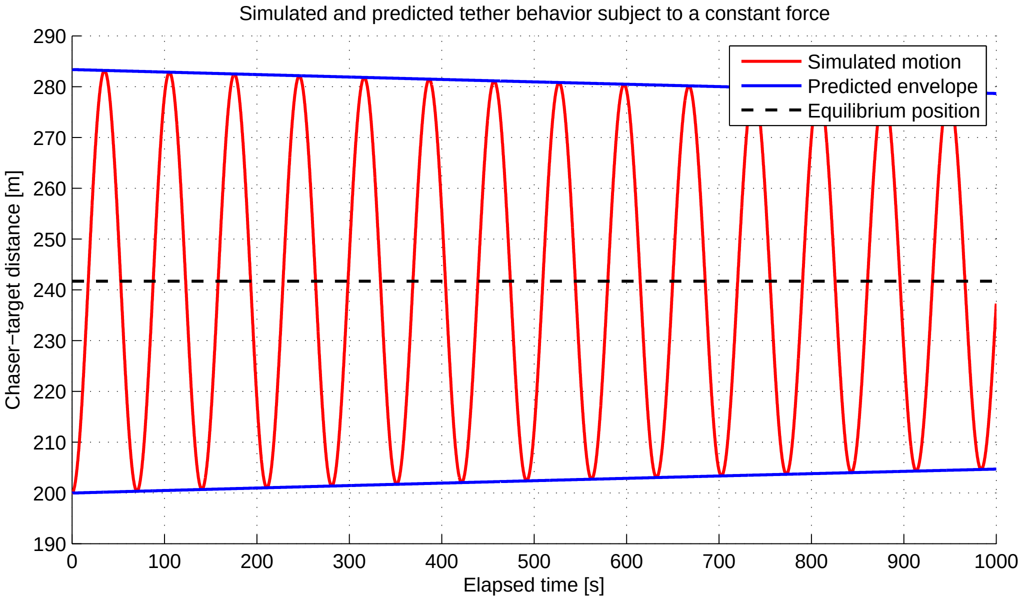

Figure 5.12: Simulated and predicted TSDS behavior subject to a constant force.

From the results, it was found that the oscillation period of the system is 70.30 s, which compares very well to the predicted period of 70.25 s. Furthermore, it can be seen in Figure 5.12 that the analytical envelope is a very good fit for the simulated system behavior.

6

CONTROL THEORY

In the previous chapter, mathematical models were developed to describe the dynamical behavior of the TSDS in orbit. However, to accomplish a successful ADR mission, it is necessary to apply steering forces and moments to the chaser. To achieve this, some form of control algorithm must be implemented.

This chapter will therefore discuss the theoretical background for two types of control algorithms: the LQR and the SMC. The LQR is based on so-called classical control theory, which uses techniques for finding analytical solutions to control problems [71, Pref.]. Conversely, the SMC is an example of modern control theory, relying predominantly on numerical methods to design the controller. Both types of controller will be implemented in the guidance and control system of the chaser, allowing for a good comparison of the "old" and the "new". While many, many different control algorithms exist, these were selected as being most suitable for the tethered ADR scenario, which will be detailed further in this chapter.

First, basic principles of control theory which are applicable to both classical and modern controllers will be discussed in Section 6.1. Second, the LQR will be covered in Section 6.2, followed third by the SMC in Section 6.3. Then, the system mathematical models used in the guidance and control systems will be discussed in Section 6.4. Finally, the system response of these mathematical models will be treated in Section 6.5.

6.1. BASIC PRINCIPLES OF CONTROL THEORY

In this section, the basic principles of control theory will be discussed. Control, in general, serves to generate commands for actuators such that the difference between a desired state and the actual state of the system under consideration is minimized [9, Ch. 6.1]. What this desired state is at any given time is left to the designer, and is not further considered in this section.

For control to be achieved, a mathematical model of the system under consideration is required [71, Ch. 3.1]. This mathematical model must be able to determine the output of the system for any given input, so the controller will know how much input is necessary to achieve a desired output. These models are mathematical approximations of how the system behaves, and can be represented in a number of different ways. Most common among these are differential equations and state equations [71, Ch. 3.2, 4.1], which are both formulated in the time domain.

When dealing with a system with multiple inputs and multiple outputs, which is representative of satellites in orbit, it is common to use the state-space representation of the system [71, Ch. 5.1]. When considering a linear (or linearized) system, the state derivative vector can thus be expressed as a linear combination of the state vector itself and a control vector, as shown in Equation (6.1):

$$\begin{aligned} \dot{\mathbf{x}}(t) &= \mathbf{A}\mathbf{x}(t) + \mathbf{B}\mathbf{u}(t) \\ \mathbf{y}(t) &= \mathbf{C}\mathbf{x}(t) + \mathbf{D}\mathbf{u}(t) \\ \mathbf{x}(t_0) &= \mathbf{x}_0 \end{aligned} \tag{6.1}$$

In this state-space representation, $\mathbf{x}(t)$ is an n-dimensional state vector of the system, $\mathbf{u}(t)$ is an m-dimensional input (or control) vector, and $\mathbf{y}(t)$ is a p-dimensional output vector [71, Ch. 5.1]. The matrices $\mathbf{A}$, $\mathbf{B}$, $\mathbf{C}$, and $\mathbf{D}$ are the system, input, output, and feedforward matrices, respectively [71, Ch. 3.7]. These matrices have the respective dimensions of $n \times n$, $n \times m$, $p \times n$, and $p \times m$ [71, Ch. 5.1]. The first equation is known as the dynamic equation, the second equation is called the output equation, and the last equation simply introduces a shorthand notation for the initial state [71, Ch. 3.7].

The formulation shown in Equation (6.1) is ideally suited for classical control theory, as this generally considers controllers with linear systems [71, Ch. 5.1]. Thus, this representation can be used for an LQR. However, modern control techniques are not limited to linear systems, although they can be applied to these. In the case of a nonlinear system, the state-space equations take the form presented in Equation (6.2), which is nonlinear in both the state and control vectors [71, Ch. 3.7]:

$$\begin{aligned}\dot{\mathbf{x}}(t) &= \mathbf{f}(t, \mathbf{x}, \mathbf{u}) \\ \mathbf{y}(t) &= \mathbf{g}(t, \mathbf{x}, \mathbf{u})\end{aligned} \tag{6.2}$$

In Equation (6.2), **f** and **g** are generic nonlinear vector functions of the state and control vectors, describing the state derivative and output vectors, respectively. The shorthand notation for the initial state $\mathbf{x}_0$ from Equation (6.1) is, of course, still valid.

It must be noted that the preceding discussion on linear and nonlinear systems is for the system model implemented in the controller. The actual plant being driven by the controller may be either linear or nonlinear, independent of what type of mathematical model is implemented in the controller. The validity of the implemented model, however, must be determined by the designer.

For both LQRs and SMCs, state feedback control is generally used as a control law [71, Ch. 11.3] [72, Ch. 1.1]. In the case that the control vector **u** is linear in the system state, this allows it to be generically expressed as shown in Equation (6.3), in which **K** is known as the gain matrix:

$$\mathbf{u}(t) = -\mathbf{K}(t)\mathbf{x}(t) \tag{6.3}$$

Note that if not all of the system states are observable, the output of the system must be used instead. While this case will not be further considered, a generic form for an output feedback law is given in Equation (6.4):

$$\mathbf{u}(t) = -\mathbf{K}(t)\mathbf{y}(t) \tag{6.4}$$

As can be seen in Equation (6.3), the control approaches zero as the state of the system approaches zero. Thus, due to the negative sign, the state feedback control law will tend to to drive the system state towards zero. This makes it convenient to reformulate Equation (6.3) as shown in Equation (6.5).

$$\mathbf{u}(t) = -\mathbf{K}(t)\mathbf{x}_{err}(t) \tag{6.5}$$

Equation (6.3) replaces the absolute state of the system from Equation (6.3) with a state error, such that the error will be driven to zero instead of the state itself. This allows a certain hold point or reference trajectory to be followed [71, Ch. 11.4]. In the subsequent sections, the problem of determining **u** for both an LQR and an SMC will be treated.

It must be noted that there are many different methods of determining appropriate controls for specific systems. The LQR was selected as it provides a well-documented classical control technique, which is additionally based on optimal control theory. Thus, the resulting controls are optimal controls for the given inputs. Many other options exist from the classical theory, such as PID controllers and pole placement [71], but these do not explicitly ensure the results to be optimal in control effort. The selection of the SMC as a modern technique for comparison was based on a quick survey ([60, 73, 74]) of most commonly used control systems for satellites, and is relatively arbitrary: other options include model-reference adaptive control, fuzzy control, and H_∞ control [71]. The precise suitability of these choices is not further considered in this research, and thus these alternatives will not be discussed, either.

6.2. LINEAR-QUADRATIC REGULATION

The LQR is a staple of classical control theory, based on optimal control theory [71, Ch. 11.1]. Specifically, the LQR is designed to find a control vector **u** which minimizes a certain quadratic cost function. Generically, this cost function can be written as shown in Equation (6.6) [9, Ch. 6.5]:

$$\mathbf{J} = \int_0^\infty (\mathbf{x}^T \mathbf{Q}_w \mathbf{x} + \mathbf{u}^T \mathbf{R}_w \mathbf{u})\, dt \tag{6.6}$$

The first term in the integrand in Equation (6.6) is the control deviation, and the second term is the control effort [9, Ch. 6.5]. The matrices **Q** and **R** are real positive semi-definite and real symmetric positive definite, respectively. These matrices can be used to tune the responsiveness and the magnitude of the control signals. Multiple methods exist to solve for these matrices, usually in an iterative fashion [9, Ch. 6.5]. The most basic approach is knwon as Bryson's rule, which defines $\mathbf{Q}_w$ and $\mathbf{R}_w$ as shown in Equation (6.7) [9, Ch. 6.5]:

$$\begin{aligned} \mathbf{Q}_w &= \text{diag}\left\{ \frac{1}{\Delta x^2_{1,max}} \quad \frac{1}{\Delta x^2_{2,max}} \quad \cdots \quad \frac{1}{\Delta x^2_{n,max}} \right\} \\ \mathbf{R}_w &= \text{diag}\left\{ \frac{1}{\Delta u^2_{1,max}} \quad \frac{1}{\Delta u^2_{2,max}} \quad \cdots \quad \frac{1}{\Delta u^2_{m,max}} \right\} \end{aligned} \tag{6.7}$$

In Equation (6.7), $\Delta x_{i,max}$ and $\Delta u_{j,max}$ are the maximum allowable amplitude of the i^{th} state vector element and the maximum allowable value of the j^{th} control vector element [9, Ch. 6.5].

As a state feedback law is used, it is possible to substitute Equation (6.3) into Equation (6.6), with the result shown in Equation (6.8) [9, Ch. 6.5]:

$$\mathbf{J} = \int_0^\infty \mathbf{x}^T(\mathbf{Q}_w + \mathbf{K}^T\mathbf{R}_w\mathbf{K})\mathbf{x}dt \tag{6.8}$$

To solve Equation (6.8), Lyapunov stability analysis can be used [9, Ch. 6.5]. For this analysis, Equation (6.9) has been proven to hold:

$$(\mathbf{A} - \mathbf{BK})^T\mathbf{P} + \mathbf{P}(\mathbf{A} - \mathbf{BK}) = -(\mathbf{Q}_w + \mathbf{K}^T\mathbf{R}_w\mathbf{K}) \tag{6.9}$$

In Equation (6.9), **P** is a positive definite matrix, which, through continuation of the Lyapunov stability analysis, can be expressed in terms of **A**, **B**, $\mathbf{Q}_w$, and $\mathbf{R}_w$, shown in Equation (6.10) [9, Ch. 6.5]:

$$\mathbf{A}^T\mathbf{P} + \mathbf{PA} - \mathbf{PBR}_w^{-1}\mathbf{BP} + \mathbf{Q}_w = 0 \tag{6.10}$$

Equation (6.10) is known as the matrix Riccati equation, for which there are standard solving algorithms in control-system design tools [9, Ch. 6.5]. Finally, it is possible to express the gain matrix **K** in terms of the matrices **R**, **B**, and **P**, shown in Equation (6.11) [9, Ch. 6.5]:

$$\mathbf{K} = \mathbf{R}_w^{-1}\mathbf{B}^T\mathbf{P} \tag{6.11}$$

It is of note that the methodology presented in Equations (6.8) through (6.11) only holds for linear time-invariant systems [71, Ch. 11.3]. This means that a single fixed **K** exists for a system with fixed **A** and **B** matrices. Thus, if this is not the case, it is necessary to either re-solve the matrix Riccati equation every time the system dynamics significantly change, or to interpolate between pre-determined values of **K** for different system configurations.

This section aimed to provide a concise overview of the main principles of the LQR, and has therefore omitted detailed derivations. These can be found throughout the literature on control theory, for instance [71, Ch. 11].

6.3. SLIDING MODE CONTROL

Sliding mode control, also called variable structure control, is a type of control in which the control law changes its structure according to certain switching conditions [75]. In doing so, it is possible to achieve asymptotic stability even if the results of each control law in itself are unstable, as long as the correct switching logic is implemented [75] and the switching function can be done at sufficiently high speeds [11]. As with the LQR, an SMC is generally designed to drive the system state, or state error, to zero.

Conceptually, this can be visualized by considering a system with two states, x_1 and x_2. In the resulting state space, the so-called switching surface σ can be defined as a function of the two states: as it is assumed that the goal of this example is to drive the system state to zero, σ is chosen to pass through the origin. This switching function then divides the state space into two regions: one "above" the switching surface, and one "below" the switching surface. This is visualized in Figure 6.1, with σ defined as a linear function of x_1 and x_2. Note that, in this case, σ is not so much a switching surface, but rather a switching line.

In Figure 6.1, the state trajectory of the system as a function of time is also shown. This state trajectory is influenced by two different values of the control vector $\mathbf{u}(t)$: one is valid when the state is above the switching surface, and the other is valid when the state is below the switching surface. This divides the state trajectory

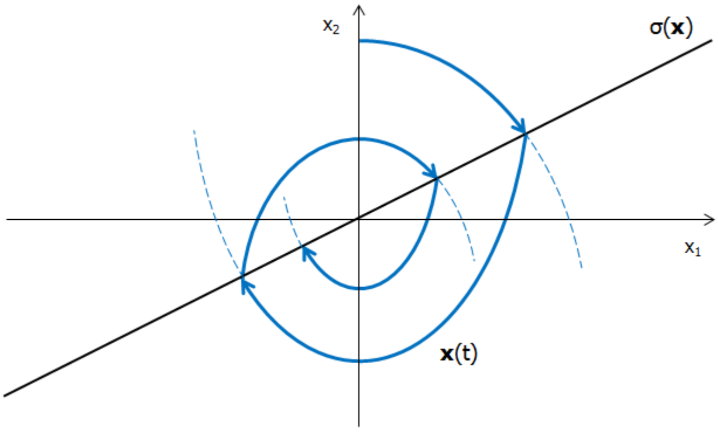

Figure 6.1: Graphical representation of a linear switching surface σ in two-dimensional state space, with the state trajectory as a function of time (adapted from [11]).

into a number of segments, in each of which one of the two controls is acting on the system. It can be seen that each individual segment of the state trajectory does not drive the system state towards zero. However, by switching between the two control laws at the switching surface, the system state is driven towards zero [11].

In general, then, for an ideal SMC, each entry in the control vector $\mathbf{u}(t)$ can take two values: a "positive" value when the system state is above the corresponding switching surface, and a "negative" value when the system state is below the corresponding switching surface [11]. Thus, the entries $u_i(t)$ of $\mathbf{u}(t)$ can be expressed as in Equation (6.12):

$$u_i(t,x) = \begin{cases} u_i^+(t,x) & \text{if } \sigma_i(x) > 0 \\ u_i^-(t,x) & \text{if } \sigma_i(x) < 0 \end{cases} \quad \text{for } i = 1,\dots,m \tag{6.12}$$

In Equation (6.12), $\sigma_i(x) = 0$ is the i^{th} switching surface, and m is the dimension of the control vector [11]. Often, as shown in the example in Figure 6.1, switching surfaces have a linear definition, as this allows analysis techniques to be used similar to those for classical linear systems.

The sliding mode itself is the motion of the system along the intersection of all the different switching surfaces [11]. As all switching surfaces are defined to pass through the desired point in the state space, so will the intersection of these surfaces: thus, the sliding mode will also drive the system to this desired point. This formulation deals with general multidimensional problems: in the case of the two-dimensional example discussed previously, with only a single switching line, this would mean that the system state stays on the switching line as soon as it intersects it. This scenario is shown in Figure 6.2.

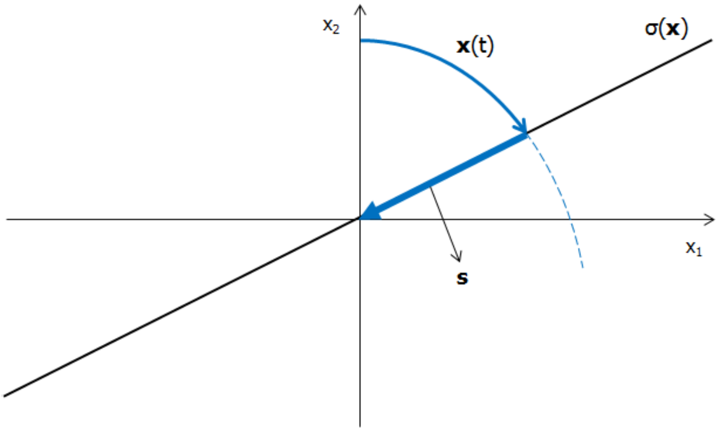

Figure 6.2: Graphical representation of a sliding mode **s** along the linear switching surface σ in two-dimensional state space (adapted from [11]).

For sliding mode control to be effective, it is necessary to construct the switching surfaces such that the system, when restricted to the surface, responds in the desired manner,: this implies that the state tends towards the desired point [11]. In the case of the example, the desired result is to drive the system state to zero. Then, appropriate switched control laws must be found, including appropriate values for the feedback gains. These must not only keep the system on the sliding mode once it has been intersected, but should also drive the system state to the sliding mode when the state has not yet intersected the sliding mode. Once on the sliding mode, the system state will be very quickly driven to the desired point.

The examples shown in Figures 6.1 and 6.2 deal with a two-dimensional case, as this is most convenient for visualizing the working of an SMC. Of course, the concept can be extended to any number of dimensions, at the cost of gradually losing the ability to visualize the system behavior. To provide a slightly more representative example, consider a three-dimensional state space with variables x_1, x_2, and x_3. Then, consider two switching surfaces, σ_1 and σ_2, coinciding with the x_1x_2-plane and x_1x_3-plane, respectively. This scenario is graphically depicted in Figure 6.3.

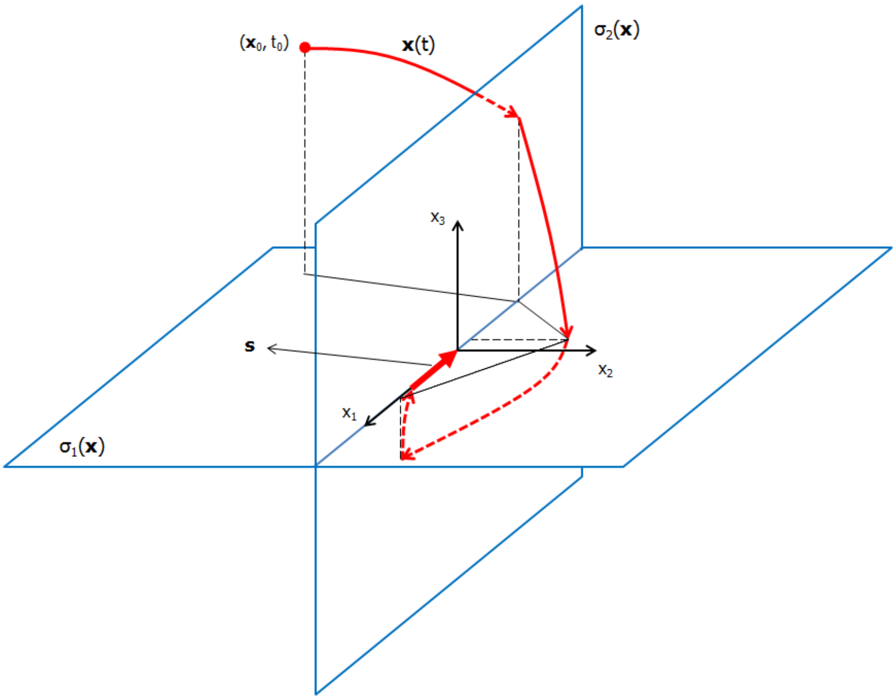

Figure 6.3: State trajectory and resulting sliding mode **s** in three-dimensional space with two switching surfaces (adapted from [11]).

The state trajectory in Figure 6.3 shows the effect of the switched controls: as soon as one of the switching surfaces is intersected, the control law is changed and thus the state trajectory follows a different path. This continues until eventually the intersection between σ_1 and σ_2 is reached, at which point the sliding mode is initiated. The system state is then driven to zero along the sliding mode.

As mentioned, the two major components of designing a sliding mode controller is to first construct switching surfaces such that the desired behavior is displayed, and second to finding the feedback gains which drive the state to the sliding mode and keep it there [11]. These two processes will be discussed subsequently.

6.3.1. Constructing Appropriate Switching Surfaces

Numerous techniques exist to determine appropriate functions for $\boldsymbol{\sigma}$ [72, Ch. 4.1] [11]. As mentioned, the selection of these surfaces is critical, as it is desired that the system behaves in a certain manner when restricted to these surfaces. Furthermore, the surfaces must also be designed such that a sliding mode actually exists. It is possible to ensure the existence of the sliding mode using the so-called method of equivalent control. The switching surfaces must then be designed based on the constraints imposed by this method.

Method of equivalent control

The method of equivalent control is a straightforward technique for constructing switching surfaces, which guarantee the existence of a sliding mode [11]. More specifically, this method will determine the system motion when restricted to a switching surface. If the sliding mode exists, then $\dot{\boldsymbol{\sigma}}(\mathbf{x}) = \boldsymbol{\sigma}(\mathbf{x}) = 0$ for all $t \geq t_0$, in which t_0 is the time when the state of the system intersects the switching surface. Using the chain rule, the result shown in Equation (6.13) is obtained [11]:

$$\left[\frac{\partial \boldsymbol{\sigma}}{\partial \mathbf{x}}\right] \dot{\mathbf{x}} = \left[\frac{\partial \boldsymbol{\sigma}}{\partial \mathbf{x}}\right] (\mathbf{f}(t,\mathbf{x}) + \mathbf{B}(t,\mathbf{x})\mathbf{u}_{eqv}) = 0 \tag{6.13}$$

In Equation (6.13), $\mathbf{u}_{eqv}$ is the equivalent control which must be solved for to make this equation hold [11]. To do so, it is assumed that $\left[\frac{\partial \boldsymbol{\sigma}}{\partial \mathbf{x}}\right] \mathbf{B}(t,\mathbf{x})$ is nonsingular for all x and t, which allows the equation shown in Equation (6.14) to be set up.

$$\mathbf{u}_{eqv} = -\left[\left[\frac{\partial \boldsymbol{\sigma}}{\partial \mathbf{x}}\right] \mathbf{B}(t,x)\right]^{-1} \left[\frac{\partial \boldsymbol{\sigma}}{\partial \mathbf{x}}\right] \mathbf{f}(t,\mathbf{x}) \tag{6.14}$$

It is possible to rewrite Equation (6.14) to find a solution for $\dot{\mathbf{x}}$, shown in Equation (6.15) [11]. This equation represents the dynamics of the system on the switching surface.

$$\dot{\mathbf{x}} = \left[I - \mathbf{B}(t,x)\left[\left[\frac{\partial \boldsymbol{\sigma}}{\partial \mathbf{x}}\right] \mathbf{B}(t,\mathbf{x})\right]^{-1} \left[\frac{\partial \boldsymbol{\sigma}}{\partial \mathbf{x}}\right]\right] \mathbf{f}(t,\mathbf{x}) \tag{6.15}$$

Equations (6.12) through (6.15) hold for any arbitrary switching surface. A special case exists when the switching surface is linear in $\mathbf{x}$: in this case, $\boldsymbol{\sigma}(\mathbf{x})$ can be written as shown in Equation (6.16) [11].

$$\boldsymbol{\sigma}(\mathbf{x}) = \mathbf{S}\mathbf{x} \tag{6.16}$$

In the case of linear switching surfaces defined by Equation (6.16) and a linear system description as shown in Equation (6.1), it is possible to simplify $\mathbf{u}_{eqv}$ as shown in Equation [72, Ch. 3.3]:

$$\mathbf{u}_{eqv}(t) = -\mathbf{S}\mathbf{B}^{-1}\mathbf{S}\mathbf{A}\mathbf{x}(t) \tag{6.17}$$

For this linear case, Equation (6.15) can then be written as in Equation (6.18) [72, Ch. 3.3]:

$$\dot{\mathbf{x}}(t) = \left(I - \mathbf{B}(\mathbf{S}\mathbf{B})^{-1}\mathbf{S}\right)\mathbf{A}\mathbf{x}(t) \tag{6.18}$$

The method of equivalent control provides relations which, when adhered to, ensure the existence of a sliding mode. However, the exact design of the switching surface matrix $\mathbf{S}$ is still a very broad field from this starting point, allowing many different properties for the system behavior to be included in the design. As this is such a broad topic, a method of determining $\mathbf{S}$ based on optimal control theory was selected. This choice was made to be able to compare between the performance of an ordinary LQR and an SMC with switching surfaces based on the same principles.

Selecting switching surfaces based on optimal control theory

To actually determine the switching surface matrix $\mathbf{S}$, it is convenient to construct a canonical form of the system equations known as the regular form [72, Ch. 4.2]. The regular form is brought about by defining a transformation $\mathbf{T}_r$ based on the QR-decomposition of $\mathbf{B}$. Applying this transformation to the $\mathbf{A}$, $\mathbf{B}$, and $\mathbf{S}$ matrices yields the results shown in Equation (6.19).

$$\begin{aligned} \mathbf{T}_r\mathbf{A}\mathbf{T}_r^T &= \mathbf{A}_{reg} = \begin{bmatrix} A_{11} & A_{12} \\ A_{21} & A_{22} \end{bmatrix} \\ \mathbf{T}_r\mathbf{B} &= \mathbf{B}_{reg} = \begin{bmatrix} 0 \\ B_2 \end{bmatrix} \\ \mathbf{S}\mathbf{T}_r^T &= \mathbf{S}_{reg} = \begin{bmatrix} S_1 & S_2 \end{bmatrix} \end{aligned} \tag{6.19}$$

Using Equation (6.19), it is possible to formulate the regular form of the state equation from Equation (6.1) [72, Ch. 4.2]. The regular form of the state vector $\mathbf{x}_{reg}$ can thus be partitioned as shown in Equation (6.20), with the regular form of the switching surface $\boldsymbol{\sigma}_{reg}$ defined in Equation (6.21).

$$\begin{aligned}\dot{\mathbf{x}}_{reg1}(t) &= A_{11}\mathbf{x}_{reg1}(t) + A_{12}\mathbf{x}_{reg2}(t)\\ \dot{\mathbf{x}}_{reg2}(t) &= A_{21}\mathbf{x}_{reg1}(t) + A_{22}\mathbf{x}_{reg2}(t) + B_2\mathbf{u}(t)\end{aligned} \tag{6.20}$$

$$\boldsymbol{\sigma}_{reg} = S_1\mathbf{x}_{reg1}(t) + S_2\mathbf{x}_{reg2}(t) \tag{6.21}$$

The first relation in Equation (6.20) describes the so-called reduced order system, which in turn describes the motion of the system when restricted to the sliding mode [72, Ch. 4.2]. Defining the quadratic cost function, similar to Equation (6.6), using the non-regular state $\mathbf{x}$ as shown in Equation (6.22), the transformation $\mathbf{T}_r$ can then be applied to $\mathbf{Q}_w$, as seen in Equation (6.23).

$$\mathbf{J} = \frac{1}{2}\int_{t_s}^{\infty} \mathbf{x}^T\mathbf{Q}_w\mathbf{x}dt \tag{6.22}$$

$$T_r\mathbf{Q}_w T_r^T = \mathbf{Q}_{reg} = \begin{bmatrix} Q_{11} & Q_{12}\\ Q_{21} & Q_{22}\end{bmatrix} \tag{6.23}$$

Combining Equations (6.22) and (6.23), it is possible to determine the cost function in terms of the regular form, which is shown in Equation (6.24) [72, Ch. 4.2]. Note that t_s is the time at which the sliding mode is intercepted.

$$\mathbf{J} = \frac{1}{2}\int_{t_s}^{\infty} \mathbf{x}_{reg1}^T Q_{11}\mathbf{x}_{reg1} + 2\mathbf{x}_{reg1}^T Q_{12}\mathbf{x}_{reg2} + \mathbf{x}_{reg2}^T Q_{22}\mathbf{x}_{reg2}dt \tag{6.24}$$

It is desirable to formulate Equation (6.24) such that $\mathbf{x}_{reg1}$ has the role of the system state and the control input is a function of $\mathbf{x}_{reg2}$ [72, Ch. 4.2]. Doing this will allow for the methods used for solving standard LQR problems to be applied. This formulation is presented in Equation (6.25).

$$\begin{aligned}J &= \frac{1}{2}\int_{t_s}^{\infty} \mathbf{x}_{reg1}^T\hat{\mathbf{Q}}\mathbf{x}_{reg1} + \hat{\mathbf{u}}^T Q_{22}\hat{\mathbf{u}}dt\\ \hat{\mathbf{Q}} &= Q_{11} - Q_{12}Q_{22}^{-1}Q_{21}\\ \hat{\mathbf{u}} &= \mathbf{x}_{reg2} + Q_{22}^{-1}Q_{21}\mathbf{x}_{reg1}\end{aligned} \tag{6.25}$$

Using Equation (6.25), the reduced-order system equation can be written in terms of $\mathbf{x}_{reg1}$ and $\hat{\mathbf{u}}$, shown in Equation (6.26) [72, Ch. 4.2]:

$$\begin{aligned}\dot{\mathbf{x}}_{reg1} &= \hat{\mathbf{A}}\mathbf{x}_{reg1}(t) + A_{12}\hat{\mathbf{u}}(t)\\ \hat{\mathbf{A}} &= A_{11} - A_{12}Q_{22}^{-1}Q_{21}\end{aligned} \tag{6.26}$$

With Equation (6.26) being in the same form as a generic state-space description as shown in Equation (6.1), a matrix Riccati equation can be formulated to find the optimal control [72, Ch. 4.2]. This relation is shown in Equation (6.27).

$$\hat{\mathbf{A}}^T P_1 + P_1\hat{\mathbf{A}} - P_1A_{12}Q_{22}^{-1}A_{12}^T P_1 + \hat{\mathbf{Q}} = 0 \tag{6.27}$$

Finally, solving this equation returns an optimal $\hat{\mathbf{u}}$, which can be used to obtain the corresponding relation for $\mathbf{x}_{reg2}$ from Equation (6.25), as seen in Equation (6.28) [72, Ch. 4.2].

$$\mathbf{x}_{reg2} = -Q_{22}^{-1}(A_{12}^T P_1 + Q_{21})\mathbf{x}_{reg1} \tag{6.28}$$

To use the resulting optimal control of the reduced-order system to construct the switching surface matrix $\mathbf{S}$, it must be recalled that during sliding motion, the regular form of the switching function $\boldsymbol{\sigma}_{reg}$ from Equation (6.21) is equal to zero [72, Ch. 4.2]. In addition, the assumption can be made that the matrix product $\mathbf{SB}$ from Equation (6.18) is nonsingular, which is necessary if a solution is to exist. This translates to the requirement that S_2 must also be nonsingular, such that Equation (6.21) can be rewritten as shown in Equation (6.29).

$$\mathbf{x}_{reg2}(t) = -S_2^{-1}S_1\mathbf{x}_{reg1}(t) \tag{6.29}$$

When comparing Equations (6.28) and (6.29), an expression relating S_1 and S_2 to the optimal control can be found. If S_2 is chosen as the identity matrix, it is possible to formulate **S** using Equation (6.19) as shown in Equation (6.30) [72, Ch. 4.2].

$$\mathbf{S} = [S_1 S_2]\, T_r = \left[I(Q_{22}^{-1}(A_{12}^T P_1 + Q_{21})) \quad I \right] T_r \tag{6.30}$$

Using Equation (6.30), an optimal switching surface matrix can be found for a given system. However, it is still necessary to find the actual controls which will drive the system to the sliding mode and keep it there. This will be discussed subsequently for state feedback control.

6.3.2. DETERMINING APPROPRIATE CONTROLS

As with the determination of the switching surfaces themselves, there are numerous techniques for determining the control vector to achieve the desired behavior of the system [72, Ch. 3]. It was chosen to use a so-called control diagonalization method due to its straightforward implementation [11].

CONTROL DIAGONALIZATION

The control diagonalization method is a means of reducing a multiple-input multiple-output system into several single-input-single-output systems, a conversion which simplifies the controller design [11]. This method involves the construction of a new control vector $\mathbf{u}^*$ through a nonsingular transformation, shown in Equation (6.31). Note that Q_r is an $m \times m$ diagonal matrix, often chosen as the identity matrix.

$$\mathbf{u}^*(t) = Q_r^{-1}(t,x) \left[\frac{\partial \sigma}{\partial x}(x) \right] \mathbf{B}(t,x)\mathbf{u}(t) \tag{6.31}$$

The dynamics of the system using this transformation can then be written as in Equation (6.32) [11]:

$$\dot{\mathbf{x}}(t) = \mathbf{f}(t,\mathbf{x}) + \mathbf{B}(t,x) \left[\frac{\partial \sigma}{\partial x}(x)\mathbf{B}(t,x) \right]^{-1} Q_r(t,x)\mathbf{u}^*(t) \tag{6.32}$$

Finally, it is possible to find control inputs if the switching logic in terms of $\mathbf{u}^*$ is chosen to satisfy Equation (6.33) [11]. Note that q_i is the i^{th} diagonal element of Q_r, s_{ij} is the ij^{th} component of $\frac{\partial \sigma}{\partial x}$, and $f_j(t,x)$ is the equation of motion for the j^{th} state.

$$\begin{aligned} q_i(t,x)u_i^{*+} &< -\sum_{j=1}^{n} s_{ij} f_j(t,x) \text{ for } \sigma_i(x) > 0 \\ q_i(t,x)u_i^{*-} &> -\sum_{j=1}^{n} s_{ij} f_j(t,x) \text{ for } \sigma_i(x) < 0 \end{aligned} \tag{6.33}$$

Again, since linear switching surfaces are considered, $\frac{\partial \sigma}{\partial x}$ is simply **S**. When also considering a linear system, Equation (6.33) can be simplified as shown in Equation (6.34) [11].

$$\begin{aligned} q_i(t,x)u_i^{*+} &< -\left[s_{i1} \quad \cdots \quad s_{in} \right] \mathbf{A}\mathbf{x}(t) \text{ for } \sigma_i(x) > 0 \\ q_i(t,x)u_i^{*-} &> -\left[s_{i1} \quad \cdots \quad s_{in} \right] \mathbf{A}\mathbf{x}(t) \text{ for } \sigma_i(x) < 0 \end{aligned} \tag{6.34}$$

Once $\mathbf{u}^*$ has been obtained, it is possible to convert this back to the actual control vector **u** using Equation (6.35) [11]. Again, for linear switching surfaces, $\frac{\partial \sigma}{\partial x}$ is simply **S**.

$$\mathbf{u}(t) = \left[\frac{\partial \sigma}{\partial x} \mathbf{B}(t,x) \right]^{-1} Q_r(t,x)\mathbf{u}^*(t) \tag{6.35}$$

Equations (6.33) and (6.34) represent sufficient conditions required to ensure the existence and reachability of a sliding mode [11]. Thus, as long as the control vector does not exceed the boundaries imposed by these relations, any value for the control will drive the system onto the sliding mode: the greater this margin is, the more aggressive the control action will be. Therefore, this margin, dubbed the control margin δ_{CM}, forms an important design parameter, as it determines how quickly a system responds to disturbances.

Note, of course, that a more aggressive control action will require more control actuation, and might thus be less efficient that a milder response. Another characteristic related to aggressive control action specific to SMCs is known as chattering, which will be discussed subsequently.

CHATTERING MITIGATION

Chattering is a phenomenon related specifically to SMCs, and is a direct result of the discontinuous control action on both sides of the switching surfaces [72, Ch. 3.7]. This means that when following the control laws presented in Equations (6.12) and (6.31) through (6.35), this discontinuity will result in any deviation from the switching surface of any magnitude will result in a control action driving the system back towards the surface. However, in most systems this will result in a slight overshoot of the switching surface, initiating a control action in the opposite direction. Thus, the system will tend to oscillate, or "chatter", around the switching surface at a high frequency.

To help alleviate this phenomenon, it is common to "soften" the discontinuous control action, resulting in a so-called pseudo-sliding motion [72, Ch. 3.7]. This results in the system being required to remain close to the switching surface rather than exactly on it, allowing less control action to be taken while still retaining a great deal of the stability inherent to "ideal" SMCs.

The most common method of softening the control law is to introduce two new controller parameters: the control boundary layer δ_{BL} [72, Ch. 3.7] and the control deadband δ_{DB} [73]. These define regions in the state space close to the sliding mode in which the control action is either reduced or nullified altogether, which reduces the aggressiveness of the system response to slight deviations and therefore reduces chattering. The control boundary layer and control deadband around a sliding mode **S** in 2D-space can be visualized in Figure 6.4.

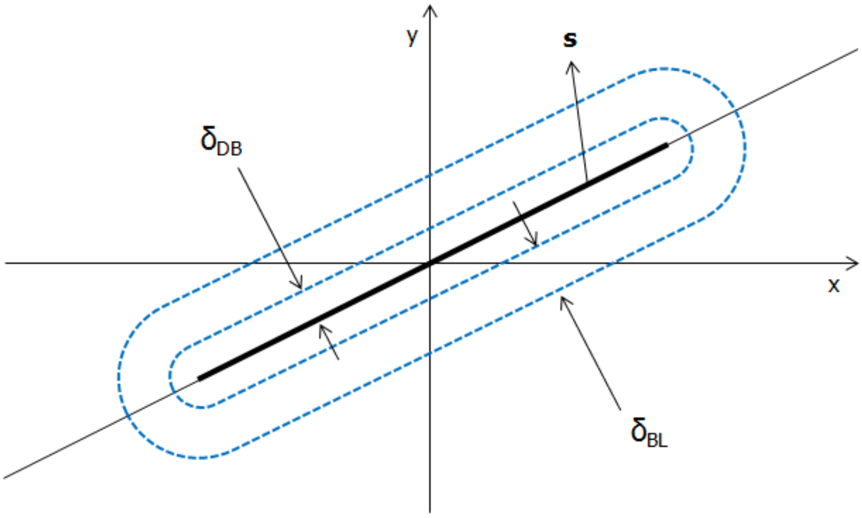

Figure 6.4: Graphical representation of control boundary layer and control deadband around a sliding mode **s** in two-dimensional space (adapted from [72, Ch. 3.7]).

As mentioned, within the boundary layer and deadband, the control action is altered from the nominal case [72, Ch. 3.7]. Specifically, if the system state is within the boundary layer, the nominal control action will be scaled linearly from the nominal control at the edge of the boundary layer to zero at the edge of the deadband. If the system state is then within the deadband, the control is set equal to zero [73].

When considering control diagonalization as discussed previously, it does not matter if the modifications to the control within the boundary layer or deadband are applied to $\mathbf{u}^*$ or $\mathbf{u}$, as the two are related by a linear transformation as shown in Equation (6.35). Thus, it was arbitrarily chosen to apply this to $\mathbf{u}^*$, as shown in Equation (6.36), with $\mathbf{u}^*_{nom}$ representing the nominal value.

$$u_i^* = \begin{cases} u^*_{i,nom} & \text{if } |\sigma_i(x)| > \delta_{DB} + \delta_{BL} \\ u^*_{i,nom}\left(\frac{|\sigma_i| - \delta_{DB}}{\delta_{BL}}\right) & \text{if } \delta_{DB} + \delta_{BL} > |\sigma_i(x)| > \delta_{DB} \\ 0 & \text{otherwise} \end{cases} \quad \text{for } i = 1, ..., m \tag{6.36}$$

Equation (6.36) can also be represented graphically. This is shown in Figure 6.5, in which a value of 1 along the y-axis represents the nominal control $\mathbf{u}^*_{nom}$ when above the switching surface and a value of -1 represents the nominal control when below the switching surface.

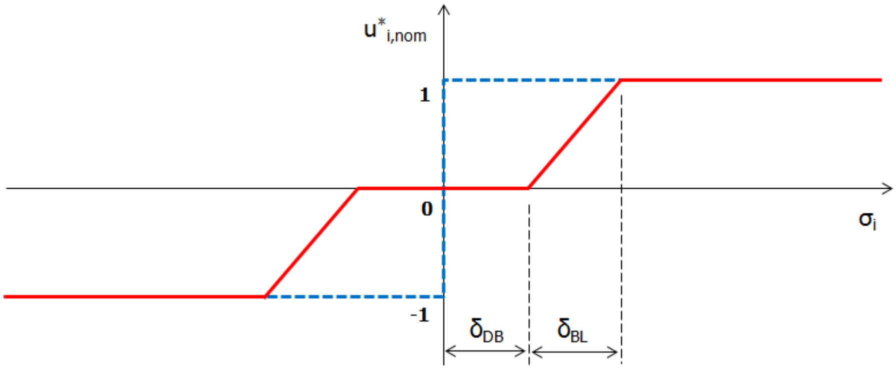

Figure 6.5: Graphical representation of control softening (solid line) near to a switching surface using a boundary layer and deadband (adapted from [72, Ch. 3.7]).

While LQR designs have been subject to enough research to allow the weighting matrices to be estimated through for instance Bryson's rule in Equation (6.7), no such rule exists for the three SMC control parameters discussed in this section. Thus, tuning these parameters represents an important part of the controller design. It is known that δ_{BL} and δ_{DB} should be small values to ensure the system remains near to the sliding mode [72, Ch 3.7]. However, no such knowledge exists for δ_{CM}, although it is known that a larger value will increase the control aggressiveness. Determining appropriate values for δ_{CM}, δ_{BL}, and δ_{DB} will be further treated in Sections 6.5 and 7.6.

6.4. SYSTEM MATHEMATICAL MODELS

It has been made clear in the preceding sections that the selected control algorithms require a mathematical model of the system being controlled to function. This section will present the models selected for this purpose, for both the orbital as well as the angular dynamics of the chaser. Note that the models will only be introduced: actual implementation will be treated in Sections 7.2 and 7.3.

6.4.1. GUIDANCE MATHEMATICAL MODEL

Within the scope of the current research, it would be theoretically possible to have a perfect mathematical model of the system, thus allowing the guidance system to make perfect predictions of the system dynamics. However, in the real world, it is not achievable to have a perfect mathematical model, and thus the guidance system will contain a degree of uncertainty. Therefore, it was chosen to develop a simplified mathematical model of the orbital dynamics of the system to test the capability of the guidance system to deal with unforseen disturbances.

As the chaser and target will permanently be in close proximity due to the influence of the tether, it was decided to develop a guidance system to control the motion of the chaser relative to the target. To this end, the CW equations were chosen as a mathematical model of the system. These equations, first presented in Equation (5.12), are linearized equations, and can thus also be written in the state-space form (Equation (6.1)) shown in Equation (6.37).

$$\begin{bmatrix} \dot{x}_{rel} \\ \dot{y}_{rel} \\ \dot{z}_{rel} \\ \ddot{x}_{rel} \\ \ddot{y}_{rel} \\ \ddot{z}_{rel} \end{bmatrix} = \begin{bmatrix} 0 & 0 & 0 & 1 & 0 & 0 \\ 0 & 0 & 0 & 0 & 1 & 0 \\ 0 & 0 & 0 & 0 & 0 & 1 \\ 3n^2 & 0 & 0 & 0 & 2n & 0 \\ 0 & 0 & 0 & -2n & 0 & 0 \\ 0 & 0 & -n^2 & 0 & 0 & 0 \end{bmatrix} \begin{bmatrix} x_{rel} \\ y_{rel} \\ z_{rel} \\ \dot{x}_{rel} \\ \dot{y}_{rel} \\ \dot{z}_{rel} \end{bmatrix} + \begin{bmatrix} 0 & 0 & 0 \\ 0 & 0 & 0 \\ 0 & 0 & 0 \\ \frac{1}{m_C} & 0 & 0 \\ 0 & \frac{1}{m_C} & 0 \\ 0 & 0 & \frac{1}{m_C} \end{bmatrix} \begin{bmatrix} F_{g,Hx} \\ F_{g,Hy} \\ F_{g,Hz} \end{bmatrix} \tag{6.37}$$

It can be seen in Equation (6.37) that the system matrix is only dependent on the mean motion n of the satellite under consideration. Thus, it forms a very simple formulation of the relative dynamics of the chaser with respect to the target. Furthermore, no perturbations are included in this formulation: thus, the ability of each system to deal with the simulated orbital perturbations can be analyzed.

Again, it is mentioned that the exact implementation of this model in the simulation of the TSDS will be discussed in Section 7.2.

6.4.2. CONTROL MATHEMATICAL MODEL

As with the guidance system, it is necessary to have a mathematical model of of the attitude dynamics of the chaser to design a closed-loop control system. Again, it was chosen to implement a simplified model of the rotational dynamics. This simplified model can simply be represented by Equations (5.21) and (5.23), and thus does not take moments induced by the environment or tether tension into account. This was done, as the tether tension is nearly independent on the angular state of the chaser, and much more dependent on the orbital state of the chaser relative to the target.

In contrast to the CW equations used in the guidance system, Equations (5.21) and (5.23) are nonlinear, meaning the state derivative cannot be expressed as a linear combination of the state vector elements. Written in matrix form, the equations of motion take the form shown in Equation (6.38), with $\boldsymbol{\Omega}$ defined in Equation (6.39):

$$\begin{bmatrix}\dot{q}_1\\ \dot{q}_2\\ \dot{q}_3\\ \dot{q}_4\\ \dot{\omega}_x\\ \dot{\omega}_y\\ \dot{\omega}_z\end{bmatrix} = \begin{bmatrix} 0 & \omega_{z,G}/2 & -\omega_{y,G}/2 & \omega_{x,G}/2 & 0 & 0 & 0\\ -\omega_{z,G}/2 & 0 & \omega_{x,G}/2 & \omega_{y,G}/2 & 0 & 0 & 0\\ \omega_{y,G}/2 & -\omega_{x,G}/2 & 0 & \omega_{z,G}/2 & 0 & 0 & 0\\ -\omega_{x,G}/2 & -\omega_{y,G}/2 & -\omega_{z,G}/2 & 0 & 0 & 0 & 0\\ 0 & 0 & 0 & 0 & & & \\ 0 & 0 & 0 & 0 & & \boldsymbol{\Omega}\mathbf{I}_C & \\ 0 & 0 & 0 & 0 & & & \end{bmatrix} \begin{bmatrix}q_1\\ q_2\\ q_3\\ q_4\\ \omega_x\\ \omega_y\\ \omega_z\end{bmatrix} + \begin{bmatrix}0 & 0 & 0\\ 0 & 0 & 0\\ 0 & 0 & 0\\ 0 & 0 & 0\\ & & \\ & \mathbf{I}_C^{-1} & \\ & & \end{bmatrix} \begin{bmatrix}M_{c,Gx}\\ M_{c,Gy}\\ M_{c,Gz}\end{bmatrix} \tag{6.38}$$

$$\boldsymbol{\Omega} = \begin{bmatrix} 0 & -\omega_z & \omega_y\\ \omega_z & 0 & -\omega_x\\ -\omega_y & \omega_x & 0\end{bmatrix} \tag{6.39}$$

Since the chaser exists in three-dimensional space, the control moment vector $\mathbf{M}_{c,G}$, representing the control moments around the axes of the chaser body-fixed frame, consists of only three elements. Therefore, only three of the four quaternion elements can be physically controlled, requiring an equation to be found which allows the complete attitude to be controlled. To do this, it is possible to use Equation (4.7) to express q_4 in terms of the other three quaternion elements. Then, Equation (5.23) can be expressed as in Equation (6.40) [76]:

$$\begin{bmatrix}\dot{q}_1\\ \dot{q}_2\\ \dot{q}_3\end{bmatrix} = \frac{1}{2}\begin{bmatrix}\sqrt{1-q_1^2-q_2^2-q_3^2} & -q_3 & q_2\\ q_3 & \sqrt{1-q_1^2-q_2^2-q_3^2} & -q_1\\ -q_2 & q_1 & \sqrt{1-q_1^2-q_2^2-q_3^2}\end{bmatrix} \begin{bmatrix}\omega_x\\ \omega_y\\ \omega_z\end{bmatrix} \tag{6.40}$$

Using Equation (6.40), a controllable nonlinear system can be derived from Equation (6.38). This system is shown in Equation (6.41):

$$\begin{bmatrix}\dot{q}_1\\ \dot{q}_2\\ \dot{q}_3\\ \dot{\omega}_x\\ \dot{\omega}_y\\ \dot{\omega}_z\end{bmatrix} = \frac{1}{2}\begin{bmatrix}\sqrt{1-q_1^2-q_2^2-q_3^2} & -q_3 & q_2\\ q_3 & \sqrt{1-q_1^2-q_2^2-q_3^2} & -q_1\\ -q_2 & q_1 & \sqrt{1-q_1^2-q_2^2-q_3^2}\\ & 2\boldsymbol{\Omega}\mathbf{I}_C & \end{bmatrix} \begin{bmatrix}\omega_x\\ \omega_y\\ \omega_z\end{bmatrix} + \begin{bmatrix}0 & 0 & 0\\ 0 & 0 & 0\\ 0 & 0 & 0\\ & \mathbf{I}_C^{-1} & \end{bmatrix} \begin{bmatrix}M_{c,Gx}\\ M_{c,Gy}\\ M_{c,Gz}\end{bmatrix} \tag{6.41}$$

However, it is clear that Equation (6.41) is a nonlinear equation, as the system matrix is a nonlinear combination of both the quaternion element as well as the angular rates. Thus, to apply an LQR or a linear SMC to this system, it must first be linearized, which can be achieved through Taylor series expansion [76]. Doing this permits the linearized system to be expressed as shown in Equation (6.42):

$$\begin{bmatrix} \dot{q}_1 \\ \dot{q}_2 \\ \dot{q}_3 \\ \dot{\omega}_x \\ \dot{\omega}_y \\ \dot{\omega}_z \end{bmatrix} = \begin{bmatrix} 0 & 0 & 0 & 1/2 & 0 & 0 \\ 0 & 0 & 0 & 0 & 1/2 & 0 \\ 0 & 0 & 0 & 0 & 0 & 1/2 \\ 0 & 0 & 0 & 0 & 0 & 0 \\ 0 & 0 & 0 & 0 & 0 & 0 \\ 0 & 0 & 0 & 0 & 0 & 0 \end{bmatrix} \begin{bmatrix} q_1 \\ q_2 \\ q_3 \\ \omega_x \\ \omega_y \\ \omega_z \end{bmatrix} + \begin{bmatrix} 0 & 0 & 0 \\ 0 & 0 & 0 \\ 0 & 0 & 0 \\ & & \\ & \mathbf{I}_C^{-1} & \\ & & \end{bmatrix} \begin{bmatrix} M_{c,Gx} \\ M_{c,Gy} \\ M_{c,Gz} \end{bmatrix} \tag{6.42}$$

Equation (6.42) represents a controllable linear system description for the angular dynamics of the chaser. Like Equation (6.37), it is a very simple formulation, and does not take any disturbances into account, again allowing for analysis of the ability of the control algorithms to cope with uncertainties. Furthermore, the implementation in the simulation of the TSDS will be discussed in Section 7.3.

6.5. SYSTEM RESPONSE

With the linear system mathematical models presented in Section 6.4, it is possible to analyze the system response of each of these to the described LQR and SMC algorithms. To do so, the response of the linear system to a step input in one of its controls was determined, by which the stability and performance of the controller can be analyzed [71, Ch. 4]. First, the step response of the guidance model will be investigated to both the LQR and SMC, and second, the same will be done for the control model. Note that these linear mathematical models will be implemented to control nonlinear systems in the full simulation.

6.5.1. GUIDANCE MODEL STEP RESPONSE

To model the step response of the guidance system, it is necessary to select a value for the mean motion n of the system, such that the system matrix $\mathbf{A}_g$ is fully defined. For a circular orbit at an altitude of 800 km, representative of the initial condition proposed by ESA [3], n is found equal to $1.038 \cdot 10^{-3}$ rad/s using Equation (5.9). Thus, this value was used for the subsequent step response analysis of the guidance system. Then, it is possible to determine this step response using both the LQR and SMC algorithms, which is done subsequently.

A scenario is considered with the chaser initially in the origin of the H frame at zero velocity. Furthermore, this state corresponds to the desired hold point. Then, a unit-step input is added to one of the control elements of the controlled system, and the resulting system behavior can be observed. It is noted that the initial chaser mass, 1500 kg, is used throughout the analysis.

LQR GUIDANCE SYSTEM STEP RESPONSE

From Section 6.2, it was shown that the performance of an LQR depends on the $\mathbf{Q}_w$ and $\mathbf{R}_w$ matrices. For the $\mathbf{R}_{w,g}$ matrix, good values can be found using Bryson's rule (Equation (6.7)), as each element of the control vector $\mathbf{u}$ has the same maximum amplitude of 50 N [3]. Thus, the $\mathbf{R}_{w,g}$ matrix for the guidance system can be expressed as shown in Equation (6.43).

$$\mathbf{R}_{w,g} = \begin{bmatrix} 4 \cdot 10^{-4} & 0 & 0 \\ 0 & 4 \cdot 10^{-4} & 0 \\ 0 & 0 & 4 \cdot 10^{-4} \end{bmatrix} \tag{6.43}$$

While Bryson's rule can also be used to determine the $\mathbf{Q}_w$ matrix, it was decided to include the influence of varying this parameter in the step response analysis. Thus, $\mathbf{Q}_{w,g}$ was chosen as a diagonal matrix with constant values along the diagonal, using the values of Δx_{max}^2 shown in Equation 6.44:

$$\Delta x_{max}^2 = \begin{bmatrix} 1 \cdot 10^{-5} & 1 \cdot 10^{-4} & 1 \cdot 10^{-3} & 1 \cdot 10^{-2} & 1 \cdot 10^{-1} \end{bmatrix} \tag{6.44}$$

For each resulting $\mathbf{Q}_{w,g}$ matrix, the step response of the system position and velocity was determined. Specifically, the case was considered with the unit-step function added to the first entry of the control vector, corresponding to a force in the x_H direction. The system position and velocity along this axis, as a function of Δx_{max}^2, are plotted in Figures 6.6 and 6.7, respectively.

Figure 6.6 shows the position of the chaser along the x_H axis, divided by the nominal value of this position dictated by the step function. This nominal value corresponds to the new equilibrium position of the chaser, and can be approximated by the value of the position at the end of the simulated interval, $t = 50$ s: it can be seen that all oscillations have died out by this time. Thus, the behavior of each scenario can be easily

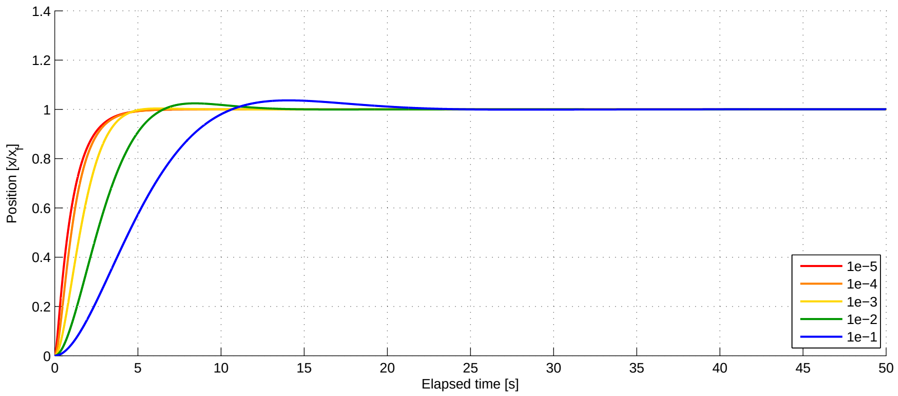

Figure 6.6: Step response of the LQR guidance system on the position of the chaser, for different values of Δx^2_{max}.

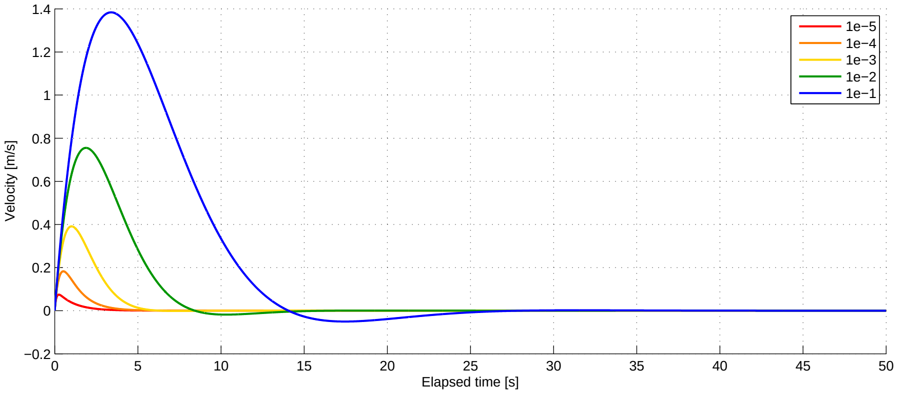

Figure 6.7: Step response of the LQR guidance system on the velocity of the chaser, for different values of Δx^2_{max}.

compared, even though these nominal values themselves might be different. Figure 6.7 simply shows the velocity of the chaser along the x_H axis.

It can be seen in Figures 6.6 and 6.7 that increasing the value of Δx^2_{max} results in a longer rise time and a larger overshoot, both on the position and velocity of the chaser. For $\Delta x^2_{max} = 1 \cdot 10^{-1}$, the rise time for the position is nearly 7 s, and the overshoot is around 4%. In contrast, the rise times for $\Delta x^2_{max} = 1 \cdot 10^{-4}$ and $\Delta x^2_{max} = 1 \cdot 10^{-5}$ are nearly identical at 2 s, and both don't show any significant overshoot. When considering the velocity, it can be seen that if $\Delta x^2_{max} = 1 \cdot 10^{-1}$, the velocity peaks at 1.4 m/s before decreasing, and shows a -0.05 m/s overshoot before settling around $t = 30$ s. Again, this is much less for $\Delta x^2_{max} = 1 \cdot 10^{-4}$ and $\Delta x^2_{max} = 1 \cdot 10^{-5}$, which have peak velocities around 0.2 m/s and 0.1 m/s, respectively, and are both settled back at zero by $t = 5$ s.

This behavior, for both position and velocity, is closely mirrored when considering a step input along the other two H-frame axes. Therefore, it was decided to weight each position element and each velocity element of $\mathbf{Q}_{w,g}$ equally. It was also chosen to apply more weight to the velocity elements: it is not desirable to have the position response be too aggressive, as this might cause unintentional tensioning of the tether. However, it is desirable to limit the relative velocity as much as possible. Thus, a value of Δx^2_{max} of $1 \cdot 10^{-2}$ was chosen for the position elements, and a value of Δx^2_{max} of $1 \cdot 10^{-4}$ was chosen for the velocity elements.

SMC GUIDANCE SYSTEM STEP RESPONSE

To analyze the system response of the SMC, the same scenario was used as for the LQR: a unit step is applied to the first element of the control vector, and the system response in terms of position and velocity is analyzed.

It was determined in Section 6.3 that the switching surfaces of the SMC would be designed based on the same principles as the LQR. For this analysis, it was chosen to use the values determined previously for $\mathbf{Q}_{w,g}$, thus allowing a good comparison to be made between the two algorithms. Furthermore, it was determined that three additional controls parameters would be necessary: the control margin δ_{CM}, the control boundary layer δ_{BL}, and the deadband δDB, with the latter two providing "softening" of the control action. However, for this analysis, it was chosen to consider an ideal SMC, and thus δ_{BL} and δ_{DB} were set to zero: proper determination of these values will be done in Section 7.6.

Similar to the LQR analysis, different simulations were run with different values of the guidance control margin $\delta_{CM,g}$. The range of values analyzed are shown in Equation (6.45):

$$\delta_{CM,g} = \begin{bmatrix} 5\cdot 10^{-4} & 1\cdot 10^{-3} & 1\cdot 10^{-2} & 5\cdot 10^{-2} & 1\cdot 10^{-1} \end{bmatrix} \tag{6.45}$$

Performing the analysis in the same way as for the LQR system, the system position and velocity under the influence of a step input are shown in Figures 6.8 and 6.9, respectively. Again, these show the normalized position and non-normalized velocity of the chaser.

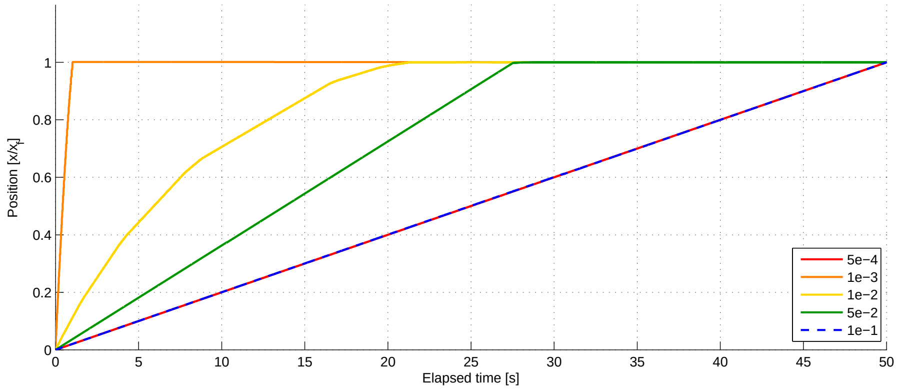

Figure 6.8: Step response of the SMC guidance system on the position of the chaser, for different values of $\delta_{CM,g}$.

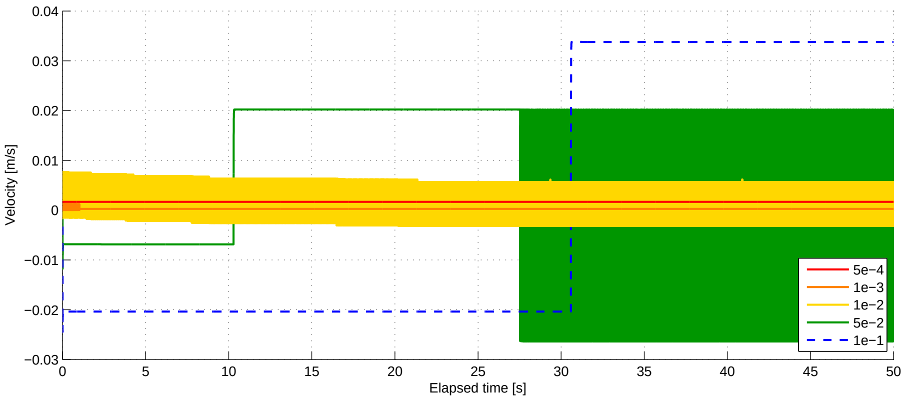

Figure 6.9: Step response of the SMC guidance system on the velocity of the chaser, for different values of $\delta_{CM,g}$.

From Figure 6.8, it can be seen that the system response is highly dependent on the value of $\delta_{CM,g}$: if this is too high or too low (in this case, $1\cdot10^{-1}$ or $5\cdot10^{-4}$, respectively), the system does not respond sufficiently to the disturbance. This is evidenced by the linearly increasing position, which characterizes the systems inability to stabilize the position. In the best case, though, with $\delta_{CM,g} = 1\cdot10^{-3}$, the system response is much quicker than the LQR, with a rise time of 0.8 s. Furthermore, it can be seen in Figure 6.9 that the chaser velocities are kept much lower with the SMC system than the LQR system: maximum chaser velocities are only in the order of cm/s. Finally, it can be seen that the velocity is stabilized for the cases that $\delta_{CM,g} = 5\cdot10^{-4}$ and $\delta_{CM,g} = 1\cdot10^{-1}$, even though the position is not. This indicates that for these values the system is able to nullify its acceleration, while maintaining a constant velocity.

Figure 6.9 also highlights the problem of chattering: the system velocities for $\delta_{CM,g} = 1\cdot10^{-2}$ and $\delta_{CM,g} = 5\cdot10^{-2}$ oscillate at a very high frequency about zero, at such a rate that the waveforms appear simply as blocks. While this does indicate that the sliding mode has been intersected, and is not an issue for the analysis of the ideal guidance model, this can be problematic when considering the implementation in the full nonlinear simulation, due to the high associated accelerations. Thus, a control boundary layer and deadband are proven to be essential when considering SMCs: the selection of these parameters, along with the selection of the control margin, is presented in Section 7.6.

While the comparison of the step response of the LQR and SMC guidance system seems to indicate that the LQR is more stable and much smoother than that of the SMC, it is once again stressed that this step response is performed to illustrate the operating principles of both controllers. As mentioned, no control softening was applied, which would greatly reduce the problem of chattering [11]. Therefore, final judgement of the most suitable controller will be performed based on the performance in the full simulation, described in Chapters 7 and 8.

6.5.2. CONTROL MODEL STEP RESPONSE

To model the step response of the control system, the same general strategy is followed as for the guidance system. In this case, there is no dependency of the system matrix on an external parameter, such as n, allowing straightforward implementation of Equation (6.42). Also, the initial chaser inertia tensor is used, shown in Equation 6.46:

$$\mathbf{I}_C = \begin{bmatrix} 1450 & 145 & 150 \\ 145 & 2850 & 280 \\ 150 & 280 & 1900 \end{bmatrix} \tag{6.46}$$

The scenario is considered with the initial orientation of the chaser body-fixed G frame being identical to that of the external inertial I frame, with zero angular velocity. This situation corresponds to a quaternion vector $\mathbf{q} = [0001]$. Then, as with the guidance system analysis, a unit-step input is added to one of the control elements of the controlled system. This will be done first for the LQR and second for the SMC

LQR CONTROL SYSTEM STEP RESPONSE

As with the LQR guidance system, the performance of the LQR control system depends on the chosen $\mathbf{Q}_w$ and $\mathbf{R}_w$ matrices. Again, it is possible to determine a good value for the $\mathbf{R}_{w,c}$ matrix by using Bryson's rule and the maximum control magnitude, which is 20 Nm for each element of the control vector [3]. The resulting $\mathbf{R}_{w,c}$ is shown in Equation (6.47):

$$\mathbf{R}_{w,c} = \begin{bmatrix} 2.5\cdot10^{-3} & 0 & 0 \\ 0 & 2.5\cdot10^{-3} & 0 \\ 0 & 0 & 2.5\cdot10^{-3} \end{bmatrix} \tag{6.47}$$

To determine the sensitivity of the system behavior to the $\mathbf{Q}_{w,c}$ matrix, the values of the diagonal entries were once again varied, using the values from Equation (6.44). Then, the system response in terms of attitude and rotational rate to the unit step function could be determined, which is shown in Figures 6.10 and 6.11, respectively.

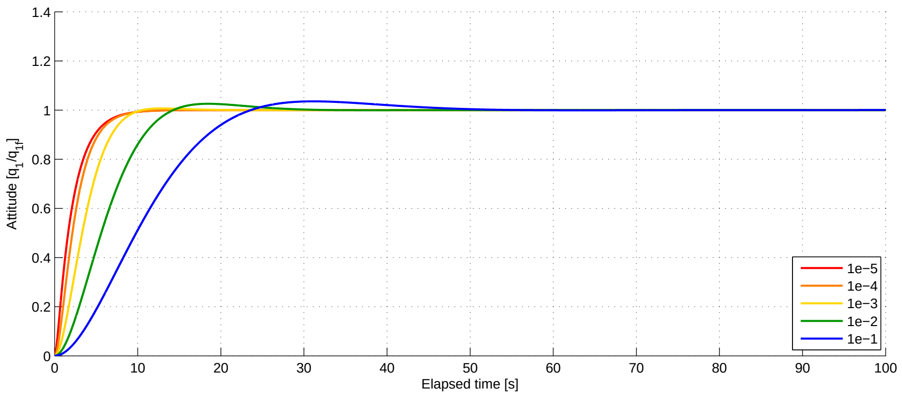

Figure 6.10: Step response of the LQR control system on the attitude of the chaser, for different values of Δx_{max}^2.

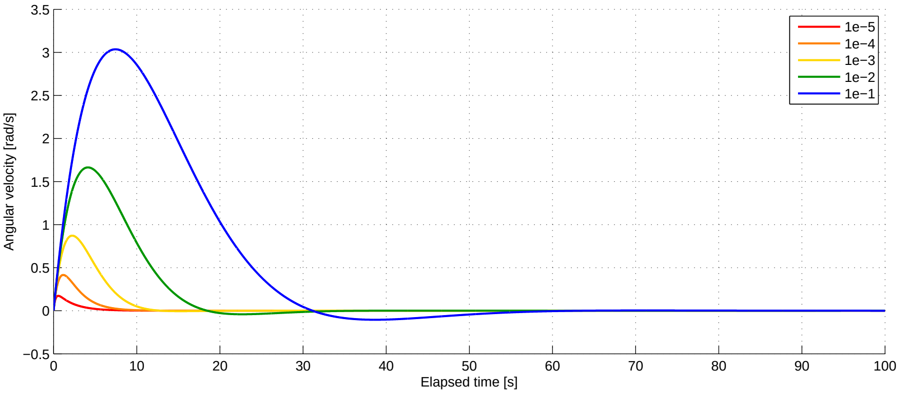

Figure 6.11: Step response of the LQR control system on the rotational rate of the chaser, for different values of Δx^2_{max}.

Figure 6.10 shows the time response of the first quaternion element q_1 to the unit step function. It is noted that, again, this has been normalized by the nominal value dictated by the step response of the system, which corresponds to the position at the end of the simulated interval, $t = 100$ s. Figure 6.11 shows the rotational rate of the chaser about its x_G axis.

Comparing Figures 6.10 and 6.11 to Figures 6.8 and 6.9, it can be seen that the behavior is very similar, with the only major difference being the scaling along the time axis: increasing the value of Δx^2_{max} results in a longer rise time and a larger overshoot, both on the position and velocity of the chaser. For $\Delta x^2_{max} = 1 \cdot 10^{-1}$, the overshoot is again around 4%; the rise time, however, is longer, clocking in at 14 s. Again, the rise times for $\Delta x^2_{max} = 1 \cdot 10^{-4}$ and $\Delta x^2_{max} = 1 \cdot 10^{-5}$ are nearly identical, this time being roughly 4 s. When considering the velocity, it can be seen that if $\Delta x^2_{max} = 1 \cdot 10^{-1}$, the velocity peaks at 3 rad/s before decreasing, and shows a -0.1 rad/s overshoot before settling around $t = 70$ s. Again, this is much less for $\Delta x^2_{max} = 1 \cdot 10^{-4}$ and $\Delta x^2_{max} = 1 \cdot 10^{-5}$, which have peak velocities around 0.9 rad/s and 0.4 rad/s, respectively, and are both settled back at zero by $t = 10$ s.

Continuing the parallel behavior with the guidance system, the described behavior of the control system is closely mirrored when considering step inputs about the other body axes. In contrast to the guidance system, however, it is desirable for the control system to be fairly aggressive in its response, such that the chaser remains stable during burns [3]. Therefore, it was chosen to set the value of Δx^2_{max} to $1 \cdot 10^{-4}$ for both the attitude as well as the rotational rate elements of $\mathbf{Q}_{w,c}$.

SMC CONTROL SYSTEM STEP RESPONSE

As with the SMC guidance system, it was chosen to implement an ideal SMC to investigate the system response of the SMC control system: thus, no control boundary layer or deadband is present to "soften" the control action. The range of values specified by Equation (6.45) were used for the control margin $\delta_{CM,c}$ during the step response analysis of the SMC control system. The results of this analysis on the normalized attitude and non-normalized rotational rate are presented in Figures 6.12 and 6.13, respectively.

It can be seen in Figure 6.12 that if the control margin is too low, $1 \cdot 10^{-1}$ in this case, the system does not respond sufficiently to the disturbance, again evidenced by the linearly increasing value of q_1. As with the SMC guidance system, this indicates that the chaser can nullify its angular acceleration, but not its angular velocity. It can also be seen that the rise time and overshoot is heavily dependent on the control margin: for $\delta_{CM,c} = 1 \cdot 10^{-3}$, the rise time is 7 s and there is no overshoot, while for $\delta_{CM,c} = 1 \cdot 10^{-3}$, the rise time is nearly 43 s, and the overshoot is 23%. From Figure 6.13, it can be seen that the angular velocities are, again, much lower than for the LQR control system, with maximum amplitudes of 0.06 rad/s as opposed to 3 rad/s.

Figure 6.12 also nicely shows the rather jagged system behavior as a result of the discontinuous switching of the controls: rather than the gradual oscillations seen in Figure 6.10, the system response abruptly changes once a switching surface has been intersected. This does drive the system to the sliding mode fairly directly, which in turn drives the system to the desired state: the sharp peaks seen at $t = 5$ s, $t = 32$ s, and $t = 66$ s coincide with the times at which chattering starts, and thus when the system intersects the sliding mode. However, due to this significant chattering, it is concluded that control softening must be done for the SMC control system, as well. Selection of appropriate values for the control boundary layer and deadband will be discussed in Section 7.6.

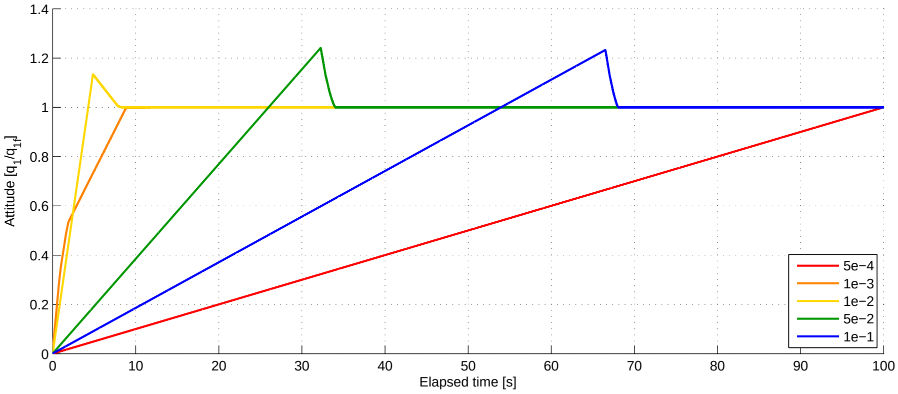

Figure 6.12: Step response of the SMC control system on the attitude of the chaser, for different values of $\delta_{CM,c}$.

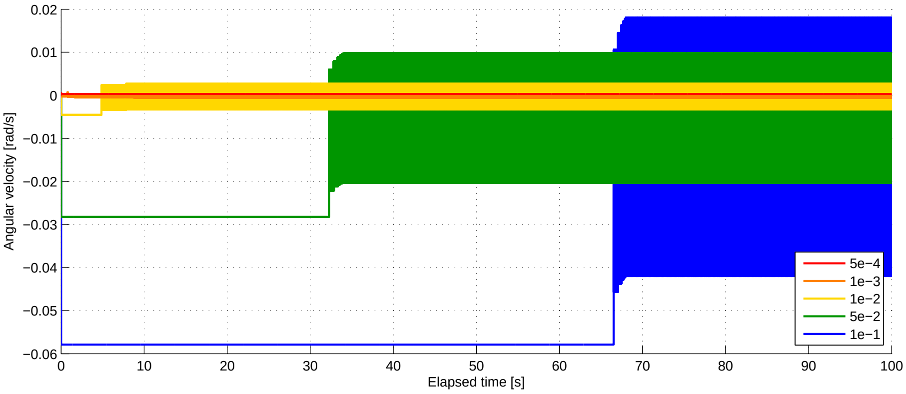

Figure 6.13: Step response of the SMC control system on the rotational rate of the chaser, for different values of $\delta_{CM,c}$.

As this the guidance system, it is again noted that the SMC step response analyses were intended to provide an overview of the basic working principle of SMC controllers. Therefore, the determination of the most suitable control algorithm will be done based on the full simulation.

7

SIMULATOR DEVELOPMENT

Using the mathematical models developed in Chapter 5 and the control algorithms discussed in Chapter 6, it is possible to develop the simulator for the TSDS. This process ecompasses a number of different steps. First, it is necessary to build the environmental model and the resulting dynamics on the elements of the TSDS, as well as selecting an appropriate propagation scheme. This was done using the GGNCSIM libraries, and is detailed in Section 7.1.

Following this, it is possible to design the actual GC system for the chaser. As mentioned, two different GC systems will be developed, with an LQR-based system providing a benchmark for a system based on SMCs. This makes it possible for the most suitable system to be selected in Chapter 8. The guidance logic will be developed in Section 7.2, followed by the logic for the control system in Section 7.3.

With the guidance and control logic developed, it is then possible to analyze the model of the tether itself, during which an appropriate number of nodes will be selected. Finally, the design of the LQR and SMC-based control systems themselves processes will be detailed in Sections 7.5 and 7.6, respectively.

As a visual aid, the architecture of the entire simulator is provided in Figure 7.1. This figure shows the relations between the various dynamics models and controllers present in the simulator, each of which will be discussed in this Chapter.

7.1. DYNAMICS MODEL DEVELOPMENT

As has been mentioned, the dynamics model for the TSDS was implemented in Simulink, using the GGNCSIM libraries developed by Dutch Space (now Airbus Defence & Space Netherlands). This section will give a brief overview of the models used to simulate the orbital and angular motions of the elements in the TSDS in Section 7.1.1. A suitable propagation scheme was also selected during this process, shown in Section 7.1.2. Finally, several unit tests are performed to verify that the model is functioning properly, which is shown in Section 7.1.3.

7.1.1. DYNAMICS MODEL IMPLEMENTATION

The GGNCSIM libraries provide a very versatile basis for the simulation of orbiting spacecraft. Four of these libraries were extensively used in the development of the simulator. First, the "Math" library covers a wide range of elementary and intricate mathematical operations, including vector and quaternion algebra [67, Ch. 4.1]. This library also includes functions for vector transformations, based on both quaternions and DCMs, which is exceedingly useful when performing reference frame transformations.

Second, the "Utilities" library contains operations for time and coordinate transformations [67, Ch. 4.2]. This includes transformations from ECI to ECEF, Cartesian to spherical, and position to altitude, as well as the reverse transformations. Together with the Math library, these two libraries provide the complete mathematical basis for the equations of motion of an orbiting satellite.

To construct the equations of motion of and around the center of mass of the satellite, the environmental loads can be defined using the "Environment" library [67, Ch. 4.2]. This library contains models for the gravity field, magnetic field, atmosphere, and solar radiation environment around the Earth. However, of these, only the gravity models will be implemented, as the atmospheric models consisted of a very coarse

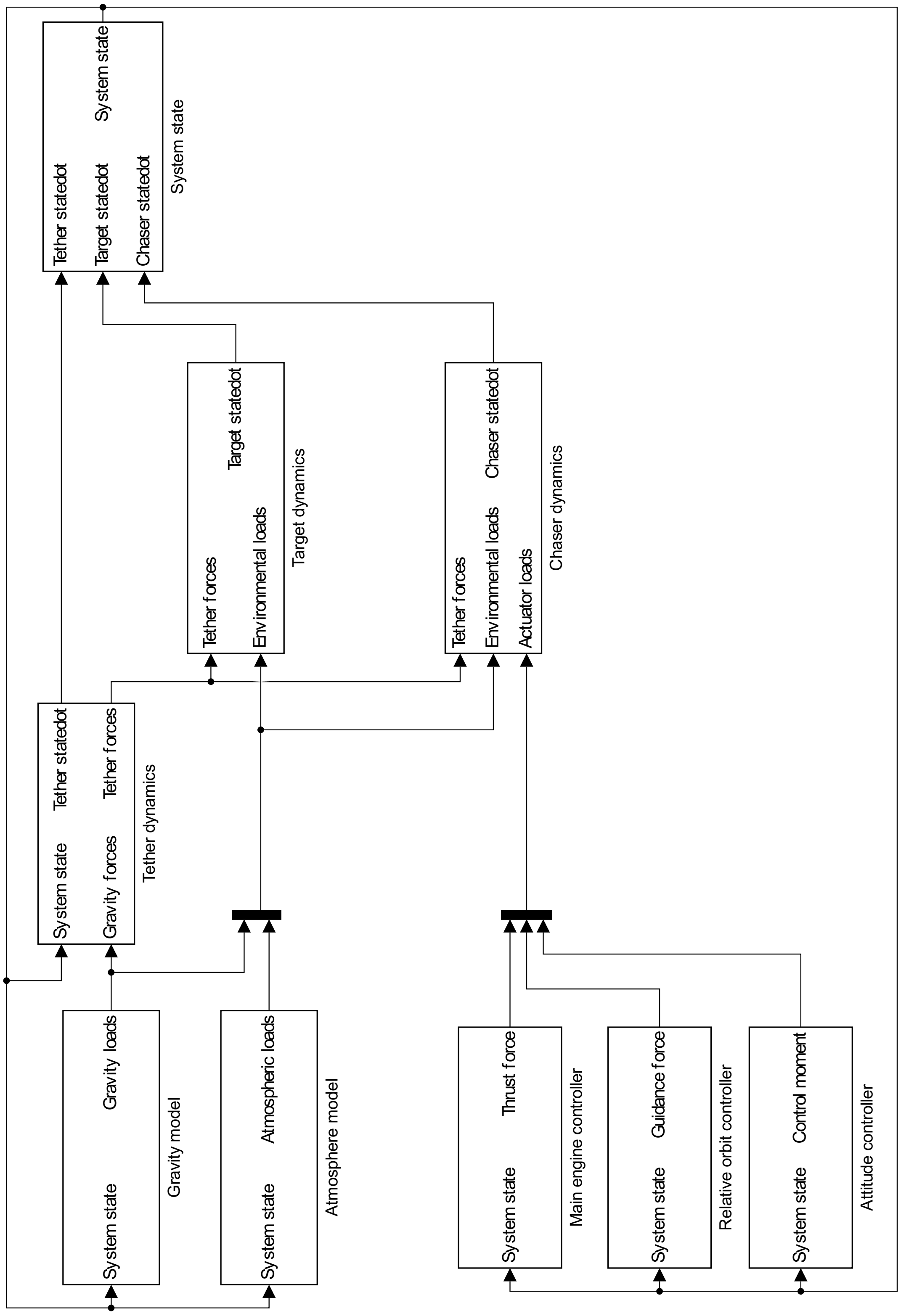

Figure 7.1: Schematic overview of developed simulator architecture.

tabulation of the outdated MSIS86 model, while the NRLMSISE-00 model described in Section 5.1 is much more up-to-date.

Finally, the "Flight Dynamics" library was used to actually determine the state derivative of the satellite. This library contains both rigid-body and flexible-body dynamics models, although only rigid-body models were used, and includes both translational and rotational motion [67, Ch. 4.3]. The force and moment models include effects such as aerodynamic drag and solar radiation pressure on different geometries. Of course, the routine developed to determine the tether forces described in Section 5.4 will also be included in the force and moment model.

ORBITAL MOTION MODEL

In essence, the orbital motion model uses the GGNCSIM libraries to sum all forces acting on each element in the TSDS and to determine the acceleration according to Newton's second law. Because of this, this method is often known as the Newton equations [67, Ch 4.3]. The technique is essentially very similar to Equation (5.14), except that the central field gravity term is also determined as a force acting on the vehicle.

To compute the aerodynamic drag on the chaser and target, the physical models shown in Figures 4.5 and 4.6 were implemented. The GGNCSIM Flight Dynamics library includes models for determining the instantaneous drag on such rectangular prisms based on the attitude of the satellite. For the target, a compound model was created including the effect of the large solar panel attached to the "bottom" of the satellite body. Again, it is noted that due to the difficulty of modeling aerodynamic drag on the tether, this was neglected for the performed simulations.

ANGULAR MOTION MODEL

In a similar fashion to the orbital motion model, the angular motion model uses the GGNCSIM libraries to determine all moments acting on the chaser and target and sums these up, defining a total resulting moment on each body. Then, Equations (5.21) and (5.23) are used to express the state derivative of each satellite. Due to the use of the Euler moment equations, this method is thus known as the Euler equations [67, Ch 4.3]. Again, it is noted that since each tether node is treated as a point mass, these elements are not subject to these equations.

Combined, the orbital and angular motion models implement the so-called Newton-Euler equations for the chaser and the target [67, Ch 4.3]. This method is applicable to rigid bodies, as it decouples the translational and rotational motions. This also allows correct implementation to be conveniently verified, as the rotation of an object should kinematically have no effect on its translation.

7.1.2. NUMERICAL PROPAGATOR SELECTION

An important aspect of the development of the simulator is to select an appropriate numerical propagation scheme. Doing so reduces numerical errors, thus increasing the accuracy of the simulation. Simulink includes several integrators which can be used to propagate the differential equations of motion, the most common of which are described in Table 7.1 [77].

Table 7.1: Summary of several included numerical methods in MATLAB/Simulink

Routine	**Description**
`ode45`	`ode45` uses a Dormand-Prince algorithm to propagate the differential equations [78]. As such, it is a single-step solver, and it is best suited to solve nonstiff equations. MathWorks recommends to try this routine first to the problem to be solved, as it shows good all-round performance.
`ode113`	`ode113` uses an Adams-Bashforth-Moulton variable order solver [78]. As opposed to `ode45`, it is therefore a multi-step solver: however, the self-starting issues with multi-step solvers are taken care of in the routine. It can be more efficient than `ode45` if the tolerances are very stringent or if the function being propagated requires a lot of computational effort. It is also best suited for nonstiff equations.

It should be noted that many other solvers exist in Simulink besides the two shown in Table 7.1, although these all serve more specialized purposes [77]. Furthermore, parameters such as the relative tolerance and minimum and maximum allowed step sizes can be varied, providing the possibility for tuning each solver.
The selection of a suitable propagation scheme was based on two properties: computer run time and numerical accuracy. To analyze this, a test case was constructed consisting of a TSDS in a circular equatorial

orbit at 800 km altitude under the sole influence of the Earth's central field. The chaser and target were given a slight relative velocity, and the system was then allowed to freely drift for a period of 25000 s. This period corresponds to roughly four orbital periods, which is the theoretical maximum duration of the mission assuming continuous operations (Section 7.2) The tether model used had a natural length L_0 of 200 m, a spring constant k of 10 N/m, a damping constant c of 0.3 Ns/m, a mass of 5 kg, and two nodes, corresponding to ESA's nominal model [3]. The initial conditions of the chaser and target in the ECI frame are shown in Equation (7.1).

$$\mathbf{R}_{T,0} = \begin{bmatrix} 7178136 \\ 0 \\ 0 \end{bmatrix} \text{[m]} \quad \mathbf{V}_{T,0} = \begin{bmatrix} 0 \\ 7815.5 \\ 0 \end{bmatrix} \text{[m/s]} \quad \mathbf{R}_{C,0} = \begin{bmatrix} 7178136 \\ -190 \\ 0 \end{bmatrix} \text{[m]} \quad \mathbf{V}_{C,0} = \begin{bmatrix} -1 \\ 7815.5 \\ 0 \end{bmatrix} \text{[m/s]} \tag{7.1}$$

Theoretically, under influence of only the central gravity field, the total orbital energy of the orbiting system should stay constant. Some energy might be dissipated through viscous damping in the tether, however, although this is not expected to be very much. Thus, it is expected that the total orbital energy of the system should be constant or should decrease very slightly. The total orbital energy $\mathscr{E}_{tot}$ of each body in the TSDS can be expressed using Equation (7.2), which is a rewritten form of the vis-viva equation from Equation (5.6).

$$\mathscr{E}_{tot} = \sum_{i=1}^{N+2} \left(\frac{|\mathbf{V}_i|^2}{2} - \frac{\mu}{|\mathbf{R}_i|} \right) m_i \tag{7.2}$$

The preceding analysis was performed using both described built-in Simulink solvers, with values for the relative tolerance of $1 \cdot 10^{-6}$, $1 \cdot 10^{-8}$, and $1 \cdot 10^{-10}$. These and all other simulations were run on an HP® EliteBook 8570w, with an Intel® Core™ i7-3630QM clocked at 2.40 GHz. The total system energy over the mission duration was then compared for each propagator configuration, the results of which are shown in Table 7.2.

Table 7.2: Performance of different propagation schemes for $\mathscr{E}_{tot}$.

Solver	**Relative tolerance**	**CPU time [s]**	$\Delta\mathscr{E}_{tot\,tot}$ [J]	**Relative** $\Delta\mathscr{E}_{tot\,tot}$
`ode45`	$1 \cdot 10^{-6}$	50.83	$1.98 \cdot 10^{6}$	$7.92 \cdot 10^{-6}$
	$1 \cdot 10^{-8}$	62.77	$1.69 \cdot 10^{6}$	$6.76 \cdot 10^{-6}$
	$1 \cdot 10^{-10}$	135.57	$1.07 \cdot 10^{6}$	$4.28 \cdot 10^{-6}$
`ode113`	$1 \cdot 10^{-6}$	77.52	$1.06 \cdot 10^{6}$	$4.24 \cdot 10^{-6}$
	$1 \cdot 10^{-8}$	428.76	$1.84 \cdot 10^{5}$	$7.36 \cdot 10^{-7}$
	$1 \cdot 10^{-10}$	3680.4	$1.97 \cdot 10^{4}$	$7.88 \cdot 10^{-8}$

In Table 7.2, $\Delta\mathscr{E}_{tot}$ indicates the total absolute energy change over the mission duration, and the relative $\Delta\mathscr{E}_{tot}$ gives this value as a fraction of the initial value for $\mathscr{E}_{tot}$, which is equal to $-2.50021 \cdot 10^{11}$ J. The absolute values of $\Delta\mathscr{E}_{tot}$ against time are also plotted in Figure 7.2.

It can be clearly seen that all propagation schemes introduce numerical errors, as the total orbital energy of the TSDS is increasing in all cases, rather than slightly decreasing. Also, `ode45` introduces more numerical errors than `ode113` for the same value for the relative tolerance, with the performance of `ode45` at a relative tolerance of $1 \cdot 10^{-10}$ being practically identical to that of `ode113` at $1 \cdot 10^{-6}$. The CPU time required for `ode113` in this situation is also less than for `ode45`.

However, while stricter requirements on the relative tolerance drastically reduce the numerical errors for `ode113`, doing so also vastly increases the CPU time. Furthermore, when looking at the relative values for the change in total orbital energy, these are in the order of 10^{-6} for all tolerances of `ode45`, and can be even lower for `ode113` when using a stricter tolerance.

In the simulated scenario, an error of 10^{-6} in the orbital energy corresponds to a same order of error in the position and velocity of the satellite. Thus, these errors correspond to an order of meters and centimeters per second, respectively. Therefore, it was decided to simply implement `ode45` with a relative tolerance of 10^{-6}, as this results in shorter CPU times for a similar order of accuracy compared to the other tolerance settings.

7.1.3. DYNAMICS MODEL VERIFICATION

An additional advantage of using the GGNCSIM libraries is that these models have been extensively verified and validated by the developers [8, Ch. 15], effectively reducing the amount of V&V effort required for this area. However, it is good practice to check the designed model to ensure that the verified and validated

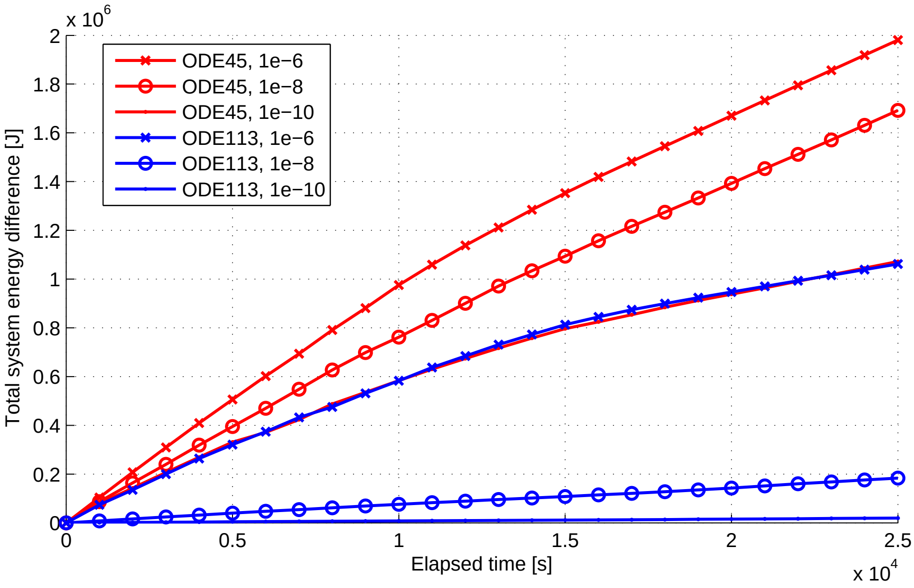

Figure 7.2: Graphical depiction of the numerical errors in ϵ_{tot} for different propagation schemes.

library models have been correctly implemented. Therefore, a number of these checks will be performed on the orbital and angular dynamics models.

ORBITAL MOTION MODEL VERIFICATION

The verification of the orbital model will consist of two tests, both designed to confirm that the simulated orbital environment is accurate: first, an unperturbed Kepler orbit will be modeled using the GGNCSIM libraries. Second, the J_2 effect will be added, and the precession of the orbital elements will be compared to the analytical solutions.

Note that the correct implementation can only be verified, and that the validity of the obtained solutions must be considered separately. However, the validity of the chosen environmental model, which governs the orbital dynamics presented here, has already been discussed in Section 5.1.

The first test considers a satellite around Earth under the sole influence of the central-body term. Ideally, the results of the numerical propagation should therefore be a very good fit for the two-body dynamics described in Section 5.2. This satellite was given the initial conditions in the ECI frame shown in Equation (7.3).

$$\mathbf{R}_0 = \begin{bmatrix} 7178136 \\ 0 \\ 0 \end{bmatrix} \text{ [m]} \qquad \mathbf{V}_0 = \begin{bmatrix} 0 \\ 7815.5 \\ 0 \end{bmatrix} \text{ [m/s]} \tag{7.3}$$

The initial conditions shown in describe an equatorial orbit with a periapsis altitude of 800 km and an eccentricity of 0.1. The equations of motion were propagated for five orbits, corresponding to 35,443 s. Doing this, and comparing the resulting orbit to the theoretical two-body case, gave errors in the order of 10^{-7} m, which verifies the correct functioning of the central field force.

The second test adds the J_2 effect to the central gravity field. In this case, a satellite was placed in an orbit around the Earth with an inclination of 98° to allow precession of the RAAN and argument of periapsis to occur. The chosen inclination corresponds to the actual inclination of Envisat. Furthermore, a periapsis altitude of 800 km and an eccentricity of 0.1 were once again applied, and the inital RAAN and argument of periapsis were both set to $\pi/2$ to avoid numerical problems which occur when these values are near zero. This corresponds to the initial conditions shown in Equation (7.4), again given in the ECI frame.

$$\mathbf{R}_0 = \begin{bmatrix} 999003 \\ 0 \\ 7108279 \end{bmatrix} \text{ [m]} \qquad \mathbf{V}_0 = \begin{bmatrix} 0 \\ -7815.5 \\ 0 \end{bmatrix} \text{ [m/s]} \tag{7.4}$$

With the values for the Keplerian elements mentioned previously, it is possible to analytically express the drift rates of the RAAN and argument of periapsis using Equation (5.17). These theoretical drift rates were then compared to the simulated RAAN and argument of periapsis. The results of this analysis are shown in Figure 7.3, again for a simulation time of 35,443 s (or five orbits).

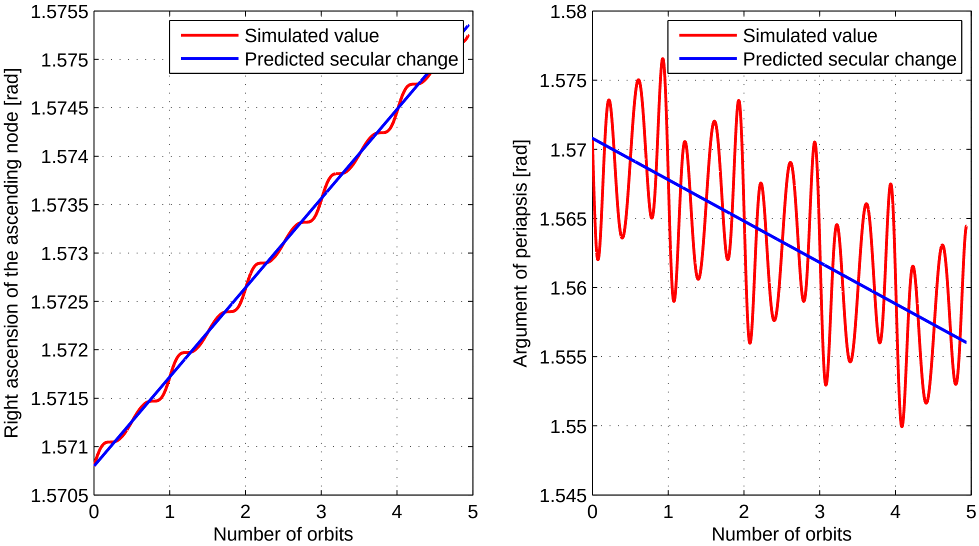

Figure 7.3: Simulated and predicted behavior of the RAAN and argument of periapsis.

It can be seen that the simulated orbital elements show regular oscillations with every orbital period, as predicted by Equation (5.16). Furthermore, the mean values of these oscillations closely follow the secular changes predicted by the Gauss planetary equations. Thus, it is concluded that the complete gravity model has been properly implemented.

ANGULAR MOTION MODEL VERIFICATION

For the angular motion of the chaser and target, it is important to remember that according to the Newton-Euler equations, translation and rotation are uncoupled. Therefore, it was decided to verify the correct implementation of these equations by simulating a body rotating at a constant rotational rate and moving at a constant velocity in inertial space. With no forces acting on the body, it is expected that the distance to the origin will linearly increase with time, and that the rotation angle will also linearly increase.

To this end, a body with the mass properties of the target was placed in inertial space, without any external forces acting on it. Then, it was given an initial velocity in the z-direction of 1 m/s and an initial rotation about the x-axis of 0.1 rad/s. In this situation, the Newton-Euler equations predict that the distance traveled will linearly increase, along with the roll angle. However, due to the nonzero products of inertia of the target seen in Equation (5.18), it was expected that there would be a coupling between the rotations. Therefore, variations about the pitch and yaw axes were expected as well. The results are shown in Figures 7.4 and 7.5.

It is abundantly clear from Figures 7.4 and 7.5 that the model was not functioning as expected: translation and rotation were strongly coupled and also vary in time, without external forces acting on the model. The problem was traced to the specific routines determining the derivative of the satellite state, which do so by solving the equations of motion in the G frame [67, Ch. 4.3]. As this requires additional transformations to be valid, it is possible that the errors were due to unintuitive implementation requirements. While the issue was discussed with the makers of GGNCSIM, the exact source of the problem could not be identified for this particular implementation.

In an attempt to circumvent the problem, an older version of the same routine was used, which solves the equations of motion in the “traditional” I frame. Implementing this model, and performing the same analysis, returns the result shown in Figures 7.6 and 7.7.

It can be seen in Figures 7.6 and 7.7 that the behavior using the old GGNCSIM routine returns the expected behavior: translation and rotation are uncoupled, the roll angle increases nearly linearly, and the pitch and

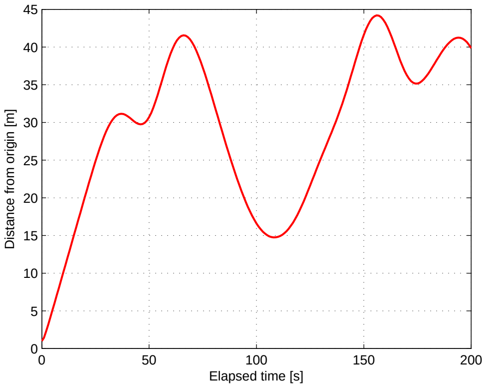

Figure 7.4: Distance from the body to the origin in inertial space as a function of time.

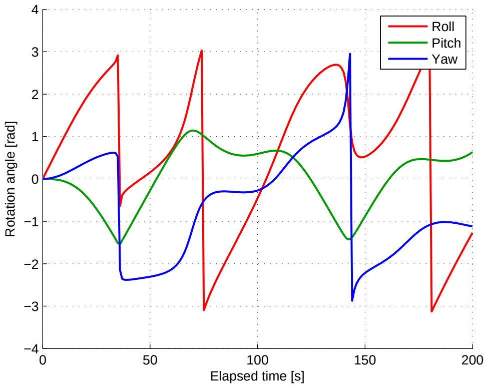

Figure 7.5: Roll, pitch, and yaw angles of the body as a function of time.

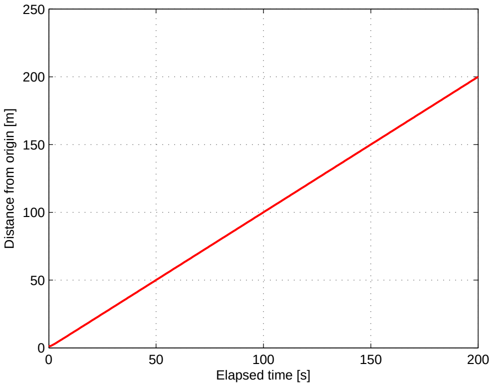

Figure 7.6: Distance from the body to the origin in inertial space as a function of time, using old GGNCSIM routine.

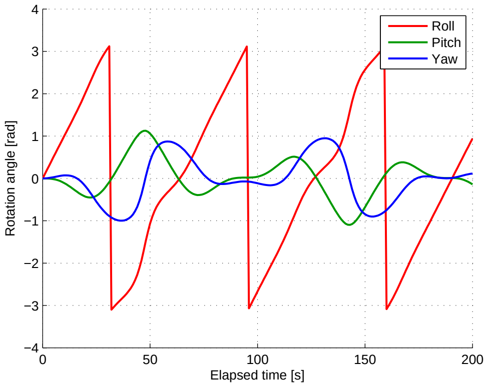

Figure 7.7: Roll, pitch, and yaw angles of the body as a function of time, using old GGNCSIM routine.

yaw angles show coupling with the roll angle. Based on these results, the development of the simulator used for this research was continued with the old GGNCSIM routine for solving the equations of motion.

7.2. GUIDANCE LOGIC DEVELOPMENT

To perform a deorbitation mission, it is required to remove energy from the orbiting satellite. This will reduce the periapsis of the orbit, which will increase the aerodynamic drag on the system and cause it to lose more energy, eventually falling back to the surface or burning up in the process. A straightforward way to achieve this is to use some form of propulsion to slow the satellite down by applying a thrust in the opposite direction to the velocity [52, Ch. 5].

This same principle holds for the TSDS, albeit with an important footnote: since the chaser will hold the propulsion system, it is necessary to transfer the force generated by the propulsion system through the tether to the target. As the tether will only transfer forces when in tension, it is necessary for the chaser to be “behind” the target during the deorbit burns, such that the tether tension force at the target is directed opposite to its velocity.

Thus, the design of the guidance system was split into two different aspects. First, a system was developed to control the main propulsion system such that the main engine burns are efficient at deorbiting the TSDS. Second, a closed-loop guidance logic was designed controlling the relative motion of the chaser with respect to the target, using the mathematical models presented in Section 6.4.1. Furthermore, a preliminary analysis towards system failure modes was performed.

7.2.1. MAIN ENGINE CONTROLLER

The main propulsion system is responsible for delivering the appropriate impulse to deorbit the TSDS. To effectively design a controller for this system, a number of different elements has to be developed. First, a model of the main propulsion system was necessary, as this will determine how long and how efficient the deorbit mission will be. Second, a reference trajectory is required for the deorbit mission. With this done, it is possible to design the logic of the controller itself.

MAIN PROPULSION SYSTEM MODEL

The main propulsion system installed on the chaser consists of a conventional high-thrust chemical propulsion system [3]. The thrust level of this propulsion system was not yet fixed, but was estimated to be between 500 N and 2500 N. Therefore, it is important to analyze several different thrust levels, to determine which configuration will be the most advantageous.

Based on the given thrust level, it is assumed that the main thrusters will be the European Apogee Motor (EAM), manufactured by Airbus Defence & Space [79]. These engines have a nominal thrust level of 500 N, allowing multiples of these to be used for higher thrust levels. The specific impulse of the EAM is rated at 325 s. Using these values, it is possible to determine the mass flow rate $\dot{m}$ of the engine as shown in Equation (7.5) [58, C.2]. Note that the worked-out value holds for a single engine.

$$\dot{m}_{main} = \frac{F_{thr}}{I_{sp} g_0} = 0.157\,\text{kg/s} \tag{7.5}$$

As mentioned, the model for the chaser will allow for a variable mass. Therefore, the mass-flow rate determined in Equation (7.5) can be used to determine the mass of the chaser at any given time using Equation (7.6). Again, this equation assumes a single engine, but the mass flow rate can be simply multiplied by the number of engines used.

$$m_C(t) = \int_{t_0}^{t} m_{C,0} - \dot{m}_{main} dt \tag{7.6}$$

Since the chaser is the only element in the TSDS which varies in mass during the deorbit mission, the TSDS mass can be determined by simply adding the tether and target mass to the variable chaser mass.

Considering the range of thrust values given, it was chosen to perform further analysis on thrust levels corresponding to integer number of EAMs, or 500 N, 1000 N, 1500 N, 2000 N, and 2500 N. These thrust levels will be further evaluated with respect to burn time and number of burns in the next subsection.

REFERENCE DEORBIT TRAJECTORY

To determine the amount of propellant needed to perform the deorbit mission, and the corresponding burn time(s), it is necessary to have a certain reference trajectory. The first step towards constructing such a reference trajectory is to determine a terminal condition for the mission. Specifically, the target periapsis altitude is the main driver for this, as targeting an exact landing site is outside the scope of this research. Based on ESAs ATV reentry profile, which has a similar size and mass to the target, a periapsis altitude of 0 km (sea level) is targeted for an appropriate re-entry profile [80].

To this terminal condition, the first-order maneuver analysis presented in Section 5.2.1 to be used, which allows the total ΔV_{tot} for the maneuver to be determined. With the initial altitude being 800 km, the final altitude being 0 km, and assuming a two-body system, this ΔV can be found using Equation (7.7). Note that a_{tr} is the transfer orbit semi-major axis, defined by Equation (7.8).

$$\begin{aligned}\Delta V_{tot} =& ||\mathbf{V}_0| - |\mathbf{V}_f|| = \frac{\mu}{R_E + h_0} - \mu\left(\frac{2}{R_E + h_0} - \frac{1}{a_{tr}}\right) \\ =& 223.2\,\text{m/s}\end{aligned} \tag{7.7}$$

$$a_{tr} = \frac{(R_E + h_0) + (R_E + h_f)}{2} \tag{7.8}$$

The result obtained from Equation (7.7) defines the total velocity increment which must be delivered to the system to achieve an appropriate deorbit trajectory, if tangential burns are used. This velocity increment can also be represented by the integral of the acceleration of the system, which can be written as shown in Equation (7.9), with t_b representing the total required burn time.

$$\Delta V_{tot} = \int_{t_0}^{t_b} \frac{F_{thr}}{m_{TSDS}(t)} dt \tag{7.9}$$

Naturally, the total required burn time t_b is dependent on the thrust level. Considering the thrust levels mentioned in the previous subsection, it was possible to solve Equation (7.9) for each of these, returning the total required burn times shown in Table (7.3). Using Equation (7.5) and the results from Table 7.3, it is also possible to determine the total propellant mass required to achieve the specified velocity increment. This works out to be 656.3 kg of propellant, a value which is independent of thrust level. As this mass is expelled from the chaser, this implies that the mass of the chaser will vary significantly throughout the mission. This must be taken into account when designing the GC system as a whole.

Table 7.3: Total burn times for varying thrust levels.

Thrust level [N]	**Total burn time [s]**
500	3868
1000	1934
1500	1289
2000	967
2500	774

It is important to note that the main engine(s) are fixed in orientation with respect to the chaser body-fixed frame [3]. Specifically, the thrust is directed along the positive x-axis of this frame. This means that the engines cannot be gimballed to correct for disturbances.

MAIN ENGINE CONTROLLER LOGIC

While guidance systems are traditionally closed-loop to account for disturbances [9, Ch. 6], the main engine controller will be treated differently. In essence, the main engine controller will simply activate the main engine(s) at the correct time and keep them operational for the correct duration, and is thus effectively an open loop system. Thus, it is dependent on the relative guidance system, discussed in Section 7.2.2, and the control system (Section 7.3) to ensure the correct orientation of the thrust vector.

It is stipulated that each individual burn may not last longer than 20 minutes (1200 s) [3]. Therefore, it is necessary for multiple burns to be performed for thrust levels of 500 N, 1000 N, and 1500 N. If multiple burns are required, each burn after the initial burn will then be initiated at apoapsis of the resulting orbit, as this is the most efficient point in the orbit to alter the periapsis [52, Ch. 5.3].

Furthermore, it is required that the thrust vector is oriented along the y-axis of the Hill frame centered on the target [3]. As the engines are fixed in orientation with respect to the chaser body-fixed frame, maintaining this orientation will be a primary objective for the control system, which will be discussed in Section 7.3.

It can be seen from Table 7.3 that thrust levels of 1000 N and 1500 N will require two burns, and that thrust levels of 2000 N and 2500 N only require a single burn. For this reason, it seemed superfluous to continue the analysis with all five defined thrust levels. Therefore, only thrust levels of 500 N, 1000 N, and 2000 N were used in the further analysis, corresponding to missions with four burns, two burns, and one burn, respectively. These profiles are graphically depicted in Figure 7.8. As a final note, each main engine burn will, in fact, be 967 s in duration, independent of the thrust level used. Each different thrust level then simply uses a different number of these burns.

7.2.2. RELATIVE GUIDANCE SYSTEM

With the main engine controller being essentially an open-loop system, it was required to have some form of closed-loop guidance logic to account for errors. To meet this need, a guidance system governing the relative motion of the chaser with respect to the target was developed, using the model presented in Section 6.4.1. First, the mathematical model used in this system will be tailored to the specific mission, after which the guidance logic will be discussed.

GUIDANCE MODEL

As discussed in Section 6.4, Equation (6.37) represents a very convenient form of the CW equations for the guidance system. However, as the periapsis is reduced during the course of the mission, the mean motion n will not be constant. Using Equation (5.9), it is possible to determine the theoretical limits of n which

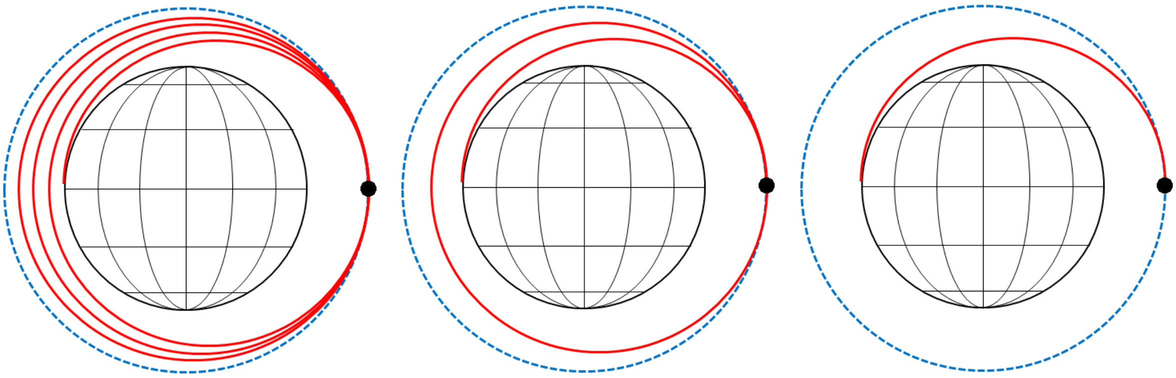

Figure 7.8: Graphical representation of the reference trajectories for 500 N, 1000 N, and 2000 N, respectively. The dashed line is the initial orbit, and the black dots represent the burn locations.

will be encountered during the mission. Thus, for the initial circular orbit at 800 km altitude, n is equal to $1.038 \cdot 10^{-3}$ rad/s; for the final transfer orbit with an apoapsis altitude of 800 km and a periapsis altitude of 0 km, n is equal to $1.131 \cdot 10^{-3}$ rad/s. As the difference between these values is less than 10%, it was decided to use the average n, with a value of $1.085 \cdot 10^{-3}$ rad/s. This allows the system matrix to remain constant throughout the mission, simplifying the controller design in Sections 7.5 and 7.6.

However, while the system matrix $\mathbf{A}_g$ in Equation (6.37) can be approximated as constant, the same cannot be done for the input matrix $\mathbf{B}_g$. This is because $\mathbf{B}_g$ is dependent on the chaser mass, and the chaser mass was found to vary significantly (43.8%) due to the propellant expelled by the main engine. Methods used to take the variable chaser mass into account in the input matrix will also be discussed in Sections 7.5 and 7.6.

The mass of the chaser will be further affected by the relative guidance forces $F_{g,Hx}$, $F_{g,Hy}$, and $F_{g,Hz}$, which are generated by small thrusters mounted on the chaser. Specifically, these thrusters will be able to generate up to 50 N of force along each of the axes of the chaser body-fixed frame, in both the positive and negative directions [3]. Based on these specifications, it was assumd that the performance of these guidance thrusters could be modeled on the 10 N bipropellant thruster manufactured by Airbus Defence & Space [81]. These thrusters deliver a nominal 10 N of thrust at a specific impulse of 291 s. Therefore, a number of these will be used to deliver the required amount of thrust.

As the guidance force vector $\mathbf{F}_{g,H}$ is defined in the Hill frame, it is necessary to transform these forces to the chaser body-fixed frame to determine how much thrust each set of guidance thrusters must deliver. The resulting guidance force vector $\mathbf{F}_{g,G}$ can be used to append Equation (7.6) to include the mass expelled by the relative guidance system, resulting in Equation (7.10).

$$m_C(t) = \int_{t_0}^{t} m_{C,0} - \dot{m}_{main} - \frac{F_{g,Gx} + F_{g,Gy} + F_{g,Gz}}{I_{sp} g_0} dt \tag{7.10}$$

GUIDANCE LOGIC

Two distinctly different modes can be identified for the relative guidance system: guidance during deorbit burns and guidance during the coasting periods between burns. In both cases, it is necessary that the guidance system prevents the chaser from colliding with the target. Additionally, during burns it is necessary for the impulse generated by the main engine to be effectively transferred through the tether to the target.

Furthermore, it is advantageous if the guidance system is able to minimize the rotational energy of the target during and after burns. If the target still has a large amount of rotational energy when a burn is terminated, the danger exists that the tether will be wrapped around the target. While this wrapping effect is not simulated, it is still an important consideration to minimize its risk of occurrence, as such a scenario could be disastrous during an actual mission. During a burn, there is little risk of tether wrapping, as the tether tension will tend to align the TCP of the target with its center of mass along the tension vector.

Besides minimizing the amount of rotational energy in the target, it is also advantageous to minimize the energy in the tether after a burn is terminated. This is due to the fact that if the tether is in tension when the burn is terminated, the tensile force will drive the chaser and target towards each other, placing them on a collision course. The guidance thrusters would then have to nullify the resulting motion, causing either significant propellant expenditure or a collision nonetheless, if the thrusters do not have enough capacity to nullify the relative motion. The primary objectives of the relative guidance system can thus be summarized:

1. Ensure correct positioning of the chaser with respect to the target during deorbit burns
2. Prevent the chaser from colliding with the target at any time
3. Minimize the potential energy in the tether at burn termination
4. Minimize the rotational energy of the target to prevent tether wrapping
5. Minimize the propellant consumption while still achieving the preceding objectives

To accomplish these objectives, both relative guidance modes will be based on the same concept: steering the chaser towards a specific hold point, forming in essence a regulation problem. As mentioned previously, it is necessary for the chaser to be “behind” the target for the tension vector to be in the opposite direction to the absolute velocity vector. Therefore, during burns, a hold point will be established along the y-axis of the Hill frame, with the x- and z-components set equal to zero to ensure the tension vector is in the correct orientation. Specifically, the chaser will establish the hold point at the equilibrium point of the system, as described by Equation (5.48). This ensures that a minimum guidance effort is required during deorbit burns. Furthermore, the three velocity components will also be driven to zero. This is illustrated in Figure 7.9, with y_b being defined in Equation (7.11):

$$y_b = \frac{F_{thr}}{k\left(1 + \frac{m_C(t)}{m_T}\right)} + \frac{L_C + L_T}{2} \tag{7.11}$$

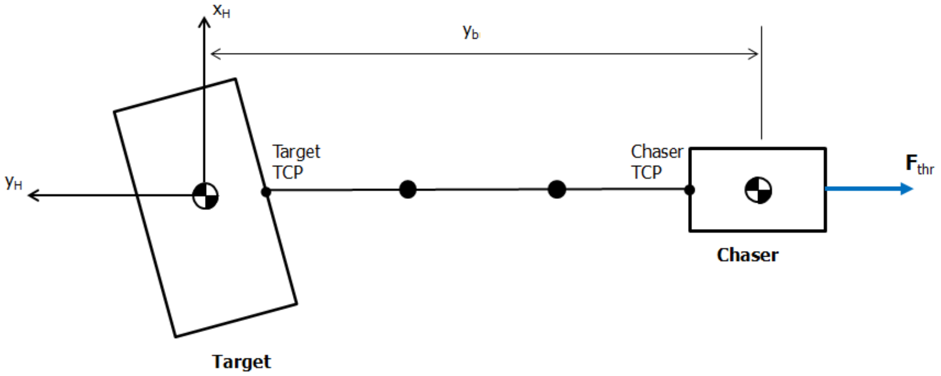

Figure 7.9: Graphical depiction of the hold point established during deorbit burns. Note that the x, z, and velocity components are zero.

The hold point established during burns should be effective at achieving objectives 1, 2, and 5 mentioned earlier. To help achieve objectives 3 and 4, it would, for instance, be possible to throttle the thrust down at the end of a burn, rather than discontinuously cutting the thrust.

In the coasting period between burns, a different hold point is established. This hold point will be focused on reducing the rotation of the target, as well as minimizing propellant consumption during the coasting phase. Returning to the CW equations in Equation (5.12), in the absence of external forces, it can be seen that the chaser will drift with respect to the target if the x or z components of its state are nonzero, even if the initial velocity is zero. Therefore, it is beneficial for this coasting hold point to be established along the y-axis, thus nullifying any tendency of the chaser to drift.

This phenomenon can also be explained from the point of view of classical orbital mechanics: if the chaser is displaced along the Hill frame’s x- or z-axis, it is effectively in a slightly different orbit than the target and will therefore have different long-term orbital elements. If it is on the y-axis, however, the chaser occupies the same orbital track as the target, and will only have a different true anomaly. Of course, this only holds if the chaser is in close enough proximity to the target for the linearized CW equations to be valid.

To reduce target rotation, it was decided to place the coasting hold point at a position along the y-axis such that the tether would just be held in tension. Since the target has a finite dimension, any target rotation would theoretically cause more tension in the tether, which would result in a restoring moment induced by the tether tension force. This is illustrated in Figure 7.10, with the expression for the y-offset given in Equation (7.12), with δ_L being a small positive distance. Relatively arbitrarily, δ_L was set to 1 m.

$$y_{hold} = L_0 + \frac{L_C + L_T}{2} + \delta_L \qquad (7.12)$$

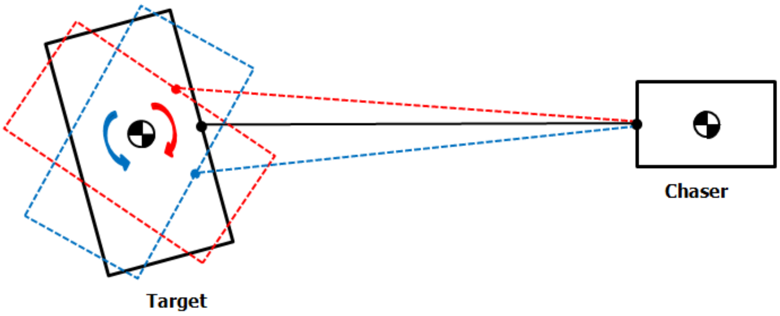

Figure 7.10: Graphical depiction of the hold point established during coasting periods. This shows the tether extension due to target rotation as well as the corresponding restoring moment.

The two different hold points determined should allow the objectives of the relative guidance system to be achieved. For clarity, the state at each hold point is summarized in Table 7.4. Note again that the coordinates are given in the Hill frame centered on the target.

Table 7.4: Summary of hold points for different guidance modes.

Coordinate	**Burn hold point**	**Coasting hold point**
x [m]	0	0
y [m]	$-y_b$	$-y_{hold}$
z [m]	0	0
$\dot{\mathbf{x}}$ [m/s]	$\mathbf{0}$	$\mathbf{0}$

7.2.3. GUIDANCE SYSTEM SAFETY

An important aspect to be considered for ADR is the safety of the removal activities during the mission. Naturally, it is futile to perform ADR if the risk of generating more space debris while doing so is high, as this will only exacerbate the problem. Orbital tethers, specifically, are fairly susceptible to failure due to debris impacts, although methods exist to mitigate this problem [28] [46]. Nonetheless, it is essential to analyze potential failure modes of the TSDS to allow contingency plans to be developed.

Three main failure modes can be identified which prevent the ADR mission from being carried out successfully: failure of the main engines, failure of the guidance thrusters, and failure of the tether. While failure of the main and guidance thrusters are applicable to space missions in general, there are implications of such failures which are unique to the TSDS. Each will be briefly discussed subsequently.

FAILURE OF THE MAIN ENGINES

Failure of the main propulsion system is a mission-critical problem in any space mission. However, the implications of a main engine failure during a deorbit burn of the TSDS are much more immediate. To illustrate this, recall Figure 5.10: in the absence of the external force **F**, the resulting tensile forces in the tether will direct the end masses towards each other. This corresponds to the situation in which the main engines on the chaser fail during a burn, as illustrated in Figure 7.11.

Table 7.5: Equilibrium position of nominal TSDS at different thrust levels.

Thrust level [N]	**Equilibrium position [m]**
500	L_0+41.7
1000	L_0+83.3
2000	L_0+166.7

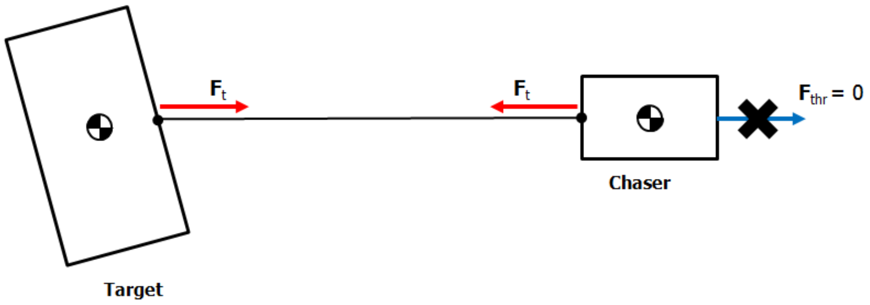

Figure 7.11: Force balance on TSDS after main engine failure.

Assuming that the guidance thrusters have not failed at the same time, it is possible that these will be able to provide the necessary thrust to avoid a collision. Therefore, this situation was simulated for a main engine failure when the chaser is stable at the burn hold point. Assuming a tether with $k = 10\,\text{N/m}$ and $L_0 = 200\,\text{m}$ [3], it is possible to use Equation (5.48) to determine the equilibrium position for each thrust level, shown in Table 7.5.

Using the data from Table 7.5, the guidance thrusters were set to fire at maximum thrust towards the target in an attempt to avoid a collision. The results of this simulation are shown in Figures 7.12 and 7.13.

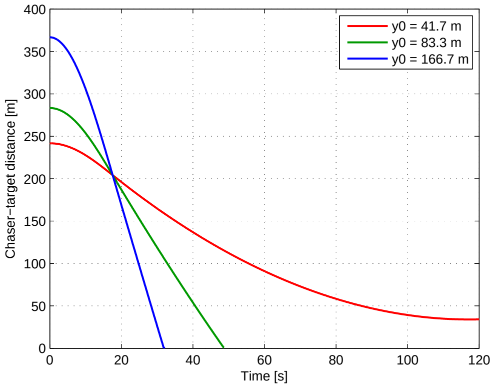

Figure 7.12: Chaser-target distance after main engine failure, applying 50 N along the negative y-axis.

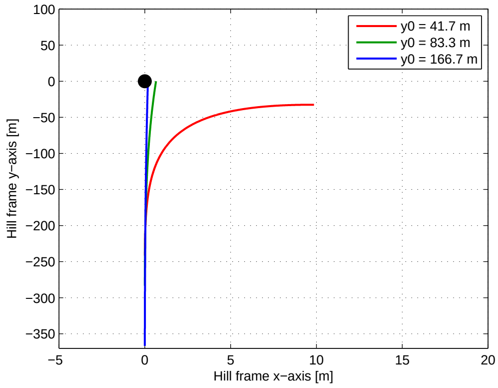

Figure 7.13: Trajectories in Hill frame corresponding to the situations in Figure 7.12, with the target in the origin.

It can be seen in Figure 7.12 that from an equilibrium position corresponding to 500 N, the chaser is able to avoid collision by thrusting towards the target. However, closest approach is 34 m, which can still be considered dangerously close [7]. For the other two initial conditions, collision cannot be avoided. From the other two initial conditions, the scenario is more grim: for the corresponding equilibrium positions of 1000 N thrust and 2000 N thrust, the chaser collides with the target after 49 s and 32 s, respectively. Furthermore, it can be seen from Figure 7.13 that thrusting towards the target causes the chaser to move in along the positive x-axis, as well.

Thus, it is concluded that when thrusting towards the target, it is only possible to recover from a main engine failure if a nominal thrust level of 500 N is used. For the other two cases, the guidance thrusters are unable to nullify the relative velocity, thus necessitating further thrusting normal to the target direction to avoid a collision. From the CW equations, it can be seen that a velocity in the positive x-direction will result in a negative acceleration in the y-direction. Therefore, this normal thrust is best applied in the positive x-direction.

A second simulation was then performed with maximum guidance thrust applied in the negative y-direction and the positive x-direction. Applying this strategy gives the results shown in Figures 7.14 and 7.15.

It can be seen in Figure 7.14 that the new strategy is able to prevent certain collision for all thrust levels: the closest approach for the 500 N equilibrium is more than 100 m, for 1000 N it is 46 m, and for 2000 N it is 17 m. Furthermore, all trajectories move quickly in the positive x-direction: thus, collision can be avoided in for all

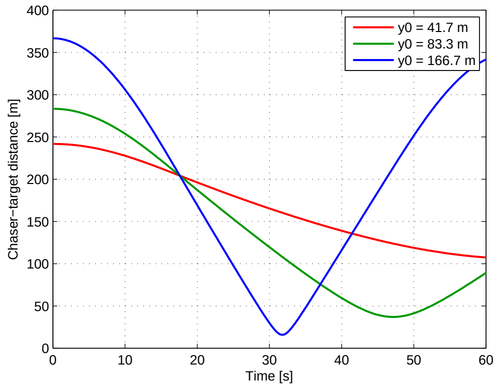

Figure 7.14: Chaser-target distance after main engine failure, applying 50 N along the -y-axis and 50 N along the +x-axis.

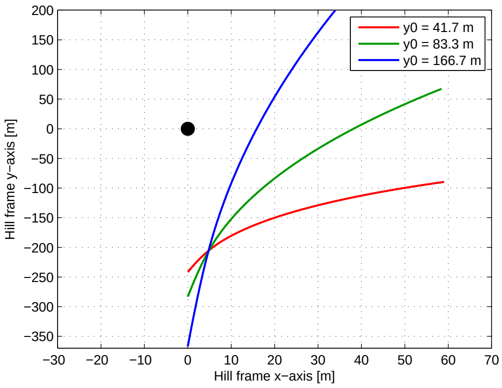

Figure 7.15: Trajectories in Hill frame corresponding to the situations in Figure 7.14, with the target in the origin.

scenario's. However, in the case of 2000 N, the closest approach is only slightly more than the largest target dimension (≈ 14 m) [3]. Also, while not shown in Figure 7.14 for the sake of clarity, in this case the chaser is unable to nullify its relative velocity before the distance is larger than the tether natural length. Thus, the tether is put in tension, resulting in a highly chaotic and unstable system.

The above results do indicate that simply cutting the main thrust at the end of each burn, with any thrust level more than 500 N, will also result in a dangerous situation: much guidance actuation would be required to restore the system to a stable equilibrium for the coasting period until the next burn.

Therefore, to compare all thrust levels effectively, it was assumed that the main engines could be throttled. Doing this gradually reduces the mechanical energy in the tether, and thus also reduces the guidance actuation required to stabilize the system. As a first approximation, it was assumed that the thrust would be throttled down linearly in time at the end of each burn, such that the total expelled propellant is the same as a nominal full-throttle burn. This is visualized in Figure 7.16.

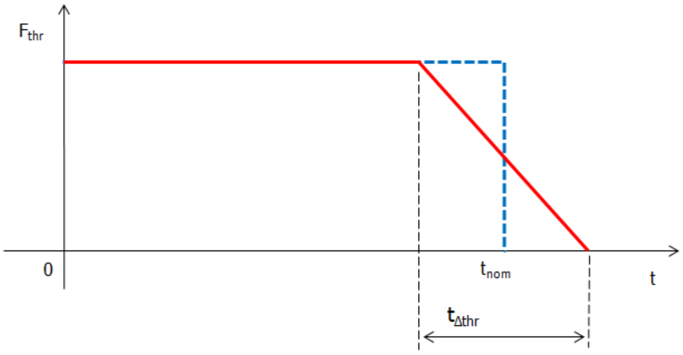

Figure 7.16: Graphical representation of main engine throttling (solid line) compared to the nominal burn (dashed line).

To determine an appropriate value for $t_{\Delta thr}$, it was examined how the TSDS would behave in a critically damped case. This condition implies that Equation (5.45), which is an approximation of the harmonic behavior of the TSDS, is equal to one. It can be seen that this value is dependent both on the spring constant k of the tether, as well as the chaser mass and target masses.

Therefore, an analysis of the system behavior was performed for both the initial chaser mass as well as an assumed final chaser mass of $m_0/2$. Each analysis placed the chaser at equilibrium positions corresponding to the three thrust levels investigated (500 N, 1000 N, and 2000 N) for both the initial and final chaser masses. Then, the behavior of the critically damped system was to be evaluated for each equilibrium position and both mass configurations. The results of this analysis for a natural tether length of 200 m and a spring constant k of 10 N/m, corresponding to the nominal tether model, are shown in Figure 7.17.
The graphs in Figure 7.17 are typical of a critically damped system: the chaser returns to the equilibrium

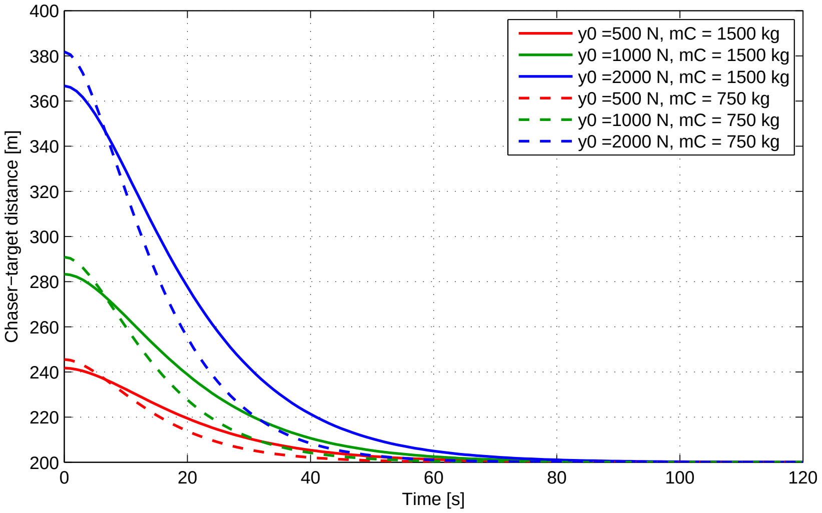

Figure 7.17: Simulated critically-damped behavior of the TSDS with varying initial conditions.

position of the system, in this case the tether natural length, smoothly and without oscillating. Also, it can be seen that when considering as system with a less massive chaser, the equilibrium position is approached more rapidly than in the system with the initial chaser mass. Nonetheless, all curves have approached the natural tether length to within a 0.1% error by t=100 s. Therefore, this value was selected as a constant for $t_{\Delta thr}$ for the nominal tether models treated in this section.

However, since the critical damping ratio is dependent on k, as mentioned, the value for $t_{\Delta thr}$ will be modified to approximate the same behavior when examining tether parameter combinations with different values of k. This is shown in Section 8.1.

FAILURE OF THE GUIDANCE THRUSTERS

In the case of guidance thruster failure at the equilibrium position, the main engines are the only actuators available to avoid collision. In this case, it is possible to either throttle down the main engine as described previously, or to operate the engine in pulsed mode, to gradually reduce the tension in the tether. The exact algorithms governing such an operation are outside the scope of this research. In either case, once the tension has been removed from the tether, the system will be passively safe, as the chaser is located behind the target and will therefore not move towards it according to the CW equations.

Establishing a stable equilibrium would require a large amount of control actuation to orient the main engines. However, it is possible that, if the system can be recovered to a stable state, it would still be possible to complete the deorbit mission. As mentioned, though, the exact planning for this contingency is outside the scope of this research.

Of course, in the case that the guidance thrusters fail at the same time as the main engines during a burn, the chaser will inevitably collide with the target. In this case, it might prove prudent to cut the tether if both systems fail, as this will minimize the severity of the collision by minimizing the relative velocity. However, the tether itself might cause severe damage. The case of unintentional tether failure will be investigated next.

FAILURE OF THE TETHER

Failure of the tether represents instantaneous mission failure, as the tether is the only means by which the chaser can deliver a deorbiting impulse to the target. To minimize the risk of such a scenario occurring, strategies such as multiple tether lines and knots in the tether lines can be applied [28]. Thus, if one of the lines is severed by for instance a small space debris impact, the entire tether is not compromised. However, it is nonetheless important to investigate the effect of a complete failure of the tether, a situation represented in Figure 7.18.

It is apparent from Figure 7.18 that a tether failure during a burn will in no case result in collision between the chaser and the target, as the main thrust force directed away from the target results in a relative acceleration of the chaser away from the target. However, as mentioned previously, the tether segments themselves

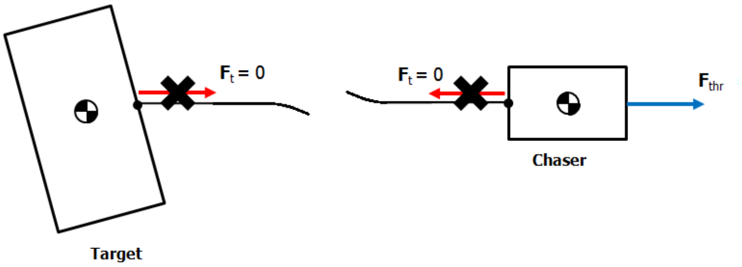

Figure 7.18: Force balance on TSDS after tether failure.

will most likely snap back towards both the target and the chaser, possibly causing significant damage. This, potentially, will result in fragments of the chaser being ejected, creating additional space debris.

If the tether would be severed during a coasting arc, the implications for the space debris environment would be less severe. This is because there is very little mechanical energy in the tether during these phases. Such a situation would still result in mission failure, though.

7.3. CONTROL LOGIC DEVELOPMENT

As mentioned in Section 7.2, the control system of the chaser is essential for aligning the main thrust vector in the correct direction. Failure to do so will result a reduced ability of the chaser to successfully deorbit the target. Therefore, the control system is subject to stringent pointing accuracy requirements [3]. First, the development of the control logic will be detailed, and second, the control model itself is designed.

CONTROL LOGIC

In contrast to the guidance system, the control law is essentially very simple. Specifically, it is required to keep the chaser level with the local horizon represented by the y- and z-axes of the target-fixed Hill frame [3]. This is graphically depicted in Figure 7.19.

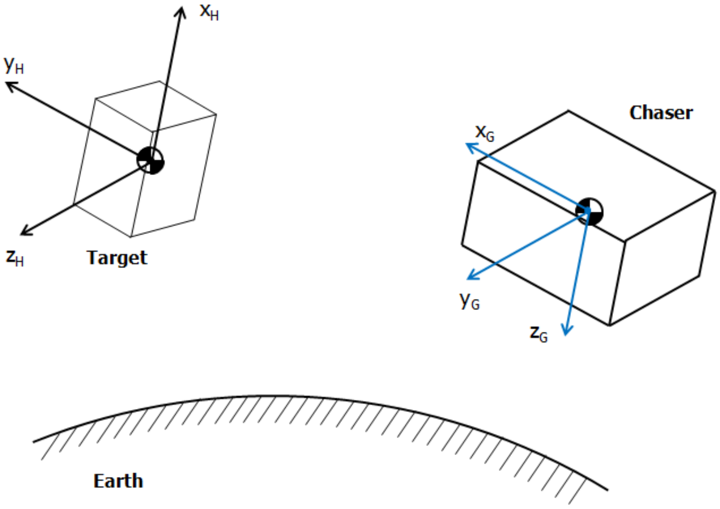

Figure 7.19: Nominal orientation of the chaser body-fixed frame with respect to the Hill frame centered on the target.

It can be seen in Figure 7.19 that the nominal orientation aligns x_G with y_H, y_G with z_H, and z_G with $-x_H$. The main challenge for the control system is that this must occur to within a very high precision, with a maximum allowed deviation from this nominal case during burns of 1° [3]. This, again, effectively constitutes a regulation problem, and the controller will attempt to drive the error between the current satellite angular state and the desired state to zero.

The angular state error consists of two different elements: the quaternion and the angular velocities. While the angular velocities can simply be subtracted to yield the error, determining the quaternion error requires the use of Equation (4.15). The nominal quaternion value describing the rotation from the Hill frame to the satellite body-fixed frame can be derived from the DCM describing this same transformation. This DCM is given by Equation (7.13), describing the G frame in terms of the H-frame axes.

$$C_{H2G} = \begin{bmatrix} 0 & 0 & -1 \\ 1 & 0 & 0 \\ 0 & 1 & 0 \end{bmatrix} \tag{7.13}$$

It is apparent from Equation (7.13) that numerical issues will not arise when using any of the conversion sets presented in Equations (4.11) through (4.14), as the diagonal entries are zero. Thus, arbitrarily selecting Equation (4.11), the nominal quaternion describing the rotation from the H frame to the G frame can be expressed found as shown in Equation (7.14).

$$\begin{aligned} q_4 &= \frac{1}{2} \\ q_1 &= \frac{-1}{4q_4} = -\frac{1}{2} \\ q_2 &= \frac{1}{4q_4} = \frac{1}{2} \\ q_3 &= \frac{-1}{4q_4} = -\frac{1}{2} \end{aligned} \tag{7.14}$$

The nominal quaternion found in Equation (7.14) can be used in conjunction with the actual quaternion of the chaser (with respect to the H frame) to determine the error quaternion using Equation (4.15). This error quaternion can then be driven to zero by the control system.

It is expected that the tether will induce the largest disturbance torques on the chaser. As mentioned, this effect cannot be conveniently taken into account in the mathematical model used in the control system, and thus will be considered an “unforseen” disturbance.

CONTROL MODEL

The mathematical model of the control system is given by Equation (6.42), which, unlike the guidance system, does not require any additional values to be determined in the system matrix. It is then assumed that the control moments on the chaser are generated by pairs of attitude control thrusters, capable of delivering 20 Nm of torque about each axis of the chaser body-fixed frame [3]. As with the guidance thrusters, these control thruster will also expend propellant. To determine the propellant consumption of these thrusters, the applied moment was transformed into a thrust force with an assumed moment arm, as shown in Equation (7.15):

$$M_{c,Gi} = 2 \cdot L_{arm} F_{c,Gi} \tag{7.15}$$

Using a value of 1 m (half the smallest dimension of the chaser) for L_{arm}, it was found that 10N thrusters at full thrust would provide the maximum control moment of 20 Nm. Thus, Airbus’ 10 N bipropellant thruster was used to model the performance of these thrusters, allowing Equation (7.10) to be appended again, as shown in Equation (7.16):

$$m_C(t) = \int_{t_0}^{t} m_{C,0} - \dot{m}_{main} - \frac{F_{g,Gx} + F_{g,Gy} + F_{g,Gz}}{I_{sp} g_0} - 2\frac{F_{c,Gx} + F_{c,Gy} + F_{c,Gz}}{I_{sp} g_0} dt \tag{7.16}$$

It can be seen that Equation (6.42) is not explicitly dependent on the chaser mass m_C. However, the inertia matrix of the chaser is dependent on the ratio of the instantaneous chaser mass to the initial chaser mass, as shown in Equation (5.18). Thus, as with the guidance system, the input matrix $\mathbf{B}_c$ cannot be approximated as constant. Methods used to take this into account in the input matrix will be discussed in Sections 7.5 and 7.6.

7.4. TETHER MODEL ANALYSIS

With the “ordinary” dynamics of the TSDS and the developed guidance and control logic discussed in the previous sections, it is possible to investigate the effect of varying the number of nodes N in the tether. This step is essential for obtaining a tether model that sufficiently reflects the expected actual motion of the tether with low computational effort. Then, the results of this analysis can be applied to investigating actual physical tether properties in Section 8.2. To begin the analysis, three tether models were presented by ESA with constant physical properties but with a different value for N [3]. These tether models are presented in Table 7.6.

Table 7.6: Tether node combinations proposed by ESA [3].

Model number	E_{mat} [Pa]	A [m^2]	L_0 [m]	m [kg]	N	c [Ns/m]	c_N [Ns/m]	k [N/m]	k_N [N/m]
N0	$1 \cdot 10^8$	$2 \cdot 10^{-5}$	200	[-]	0	0.3	0.3	10	10
N2	$1 \cdot 10^8$	$2 \cdot 10^{-5}$	200	5	2	0.3	0.9	10	30
N4	$1 \cdot 10^8$	$2 \cdot 10^{-5}$	200	5	4	0.3	1.5	10	50

The three proposed models consist physically of ESA's nominal-parameter tether model, with zero, two, and four nodes, respectively. Of these configurations, ESA has additionally identified the $N2$ model as the nominal benchmark. However, to get a clear understanding of increasing the number of nodes, two extra models were included in the analysis, with ten and twenty nodes, respectively. These are also shown in Table 7.7.

Table 7.7: Additional tether node combinations for more detailed analysis.

Model number	E_{mat} [Pa]	A [m^2]	L_0 [m]	m [kg]	N	c [Ns/m]	c_N [Ns/m]	k [N/m]	k_N [N/m]
N10	$1 \cdot 10^8$	$2 \cdot 10^{-5}$	200	5	10	0.3	3.3	10	110
N20	$1 \cdot 10^8$	$2 \cdot 10^{-5}$	200	5	20	0.3	6.3	10	210

Using the five tether models described in Tables 7.6 and 7.7, a scenario was constructed to analyze the differences in tether behavior. This scenario corresponds strongly to the initial phase of the first deorbit burn of the nominal mission [3]: first, the target is placed in an 800 km altitude orbit at 98° inclination. Then, the chaser is placed at $x_H = -2$ m, $y_H = -201$ m, and $z_H = -1.5$ m with respect to the target, with zero relative velocity. This initial condition is slightly modified from the nominal one, in that it ensures that the tether is always in tension. The tether nodes are then equally spaced between the chaser and target. At $t = 0$ s, a thrust force is applied in the negative y_H direction, with the LQR described in Section 7.5 providing relative guidance.

The three different thrust levels described in Section 7.2 were examined (500 N, 1000 N, and 2000 N), with each combination of tether model and thrust level being simulated for 300 s. Thus, a total of 15 different scenarios were examined. For each scenario, the maximum transverse oscillation amplitude in the tether was plotted as a function of time. Additionally, the required guidance propellant and CPU time was measured for each simulation. The tether oscillation amplitudes can be seen in Figure 7.20 for the 500 N scenario, in Figure 7.21 for the 1000 N scenario, and in Figure 7.22 for the 2000 N scenario.

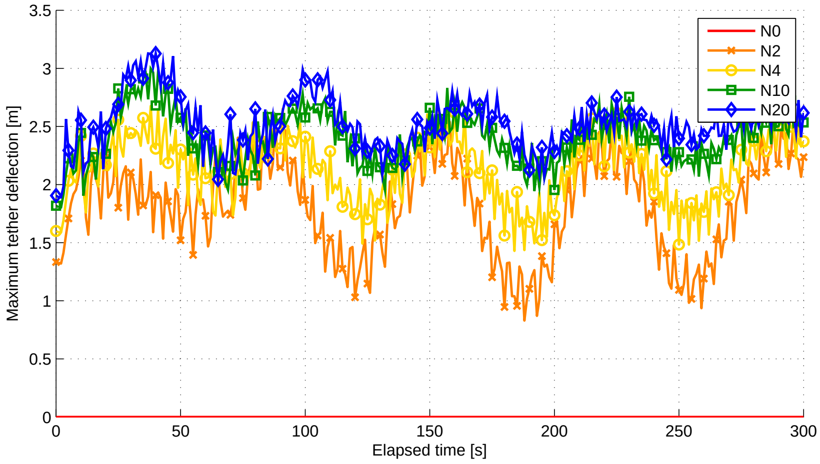

Figure 7.20: Maximum deflections of each tether model during deorbit burn at 500 N of thrust.

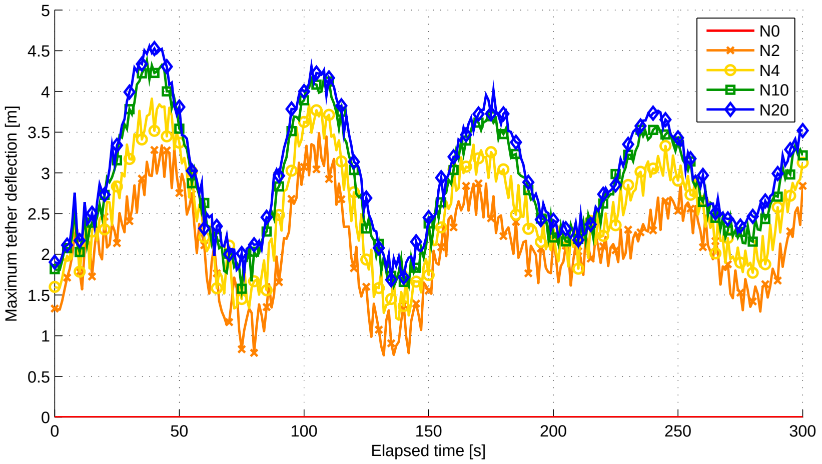

Figure 7.21: Maximum deflections of each tether model during deorbit burn at 1000 N of thrust.

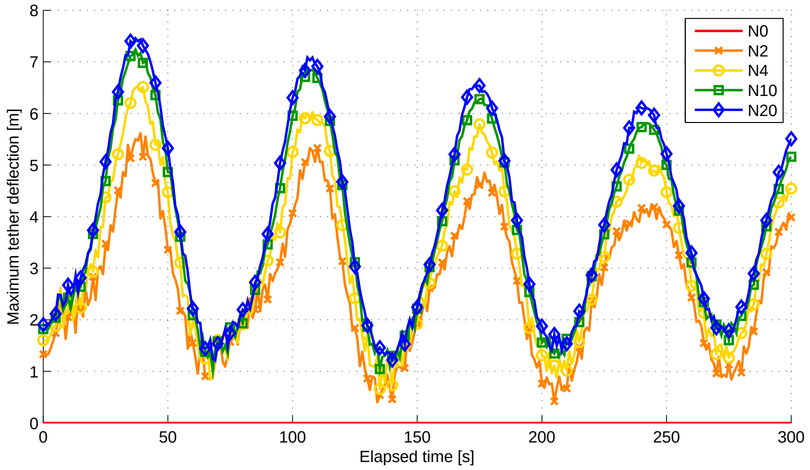

Figure 7.22: Maximum deflections of each tether model during deorbit burn at 2000 N of thrust.

From Figures 7.20 through 7.22, it can be immediately seen that a tether model with zero nodes does not show any transverse oscillations, as can be expected. All other models, independent of the number of nodes implemented, do display transverse oscillations. The amplitudes of these oscillations varies between the number of nodes in the tether model and the thrust level applied: higher thrust levels and more nodes in the tether induce higher amplitudes in the tether. Additionally, it can be seen that the amplitude of the oscillations slowly decrease: this is primarily due to the fact that the guidance system establishes the burn hold point during this period.

Furthermore, the period of these oscillations seems to vary slightly between thrust levels: lower thrust levels have periods in the order of 60 s, while the higher thrust levels have oscillations in the order of 70 s. Theoretically, according to Equation (5.47), the period should only be dependent on the chaser and target masses and the tether spring constant. It is possible that the higher relative velocities present under higher thrust levels influence the relative dynamics of the chaser and target, lengthening the oscillation period.

However, it can also be seen that the general oscillatory behavior of the tether is very similar for all models with nonzero nodes. Also, it can be seen that the differences between the N10 and N20 models are much smaller than between the N4 and N10 models in terms of oscillation amplitude. Thus, it would seem that 10 nodes is a good model for the tether behavior, as increasing the number of nodes does not significantly alter these amplitudes. However, to confirm or dispute this claim, the measured CPU time and amount of propellant required can also be compared. These results are shown in Table 7.8.

Table 7.8: Guidance propellant consumption over 300 s and total CPU time per tether model and thrust level.

Thrust level [N]	Tether model	Required propellant [kg]	CPU time [s]
500	N0	6.24	1.68
	N2	5.63	2.38
	N4	5.62	3.40
	N10	5.64	8.83
	N20	5.64	19.68
1000	N0	7.99	1.72
	N2	7.69	2.64
	N4	7.69	4.05
	N10	7.70	10.08
	N20	7.70	26.22
2000	N0	9.81	1.76
	N2	10.14	3.03
	N4	10.18	4.85
	N10	10.18	10.82
	N20	10.16	32.98

From Table 7.8, several general trends can be seen. First, it is clear that CPU time increases almost linearly with the number of nodes used in the model. This makes sense, as a larger number of nodes means that a larger state vector must be propagated by the simulator. It can also be seen that while the amount of propellant required is dependent on the thrust level, the differences in required propellant between the different models for each individual thrust level are negligible. This result suggests that the larger oscillation amplitudes shown by the models with more nodes do not significantly affect the performance.

For this reason, it was chosen to implement the N2 model in the final simulations. This is due to the fact that the general oscillatory behavior in terms of period seems independent of the number of nodes used in the tether. Also, the larger amplitudes shown by higher-order tether models do not seem to influence the performance of the guidance system. Finally, the N2 model requires the least computation time of the models with nonzero nodes, thus allowing simulations to be performed faster.

7.5. LQR CONTROLLER DESIGN

The guidance and control models developed in Sections 7.2 and 7.3 presented controllable linear state-space equations for the relative orbital dynamics of the chaser with respect to the target and the attitude dynamics of the chaser. This section will present guidance and control systems based on LQRs using these equations and the developed guidance and control laws. First, the guidance system will be treated, followed by the control system.

7.5.1. LQR GUIDANCE SYSTEM

The mathematical model implemented in the guidance system was presented in Section 7.2.2. The linear state-space model was constructed in Equation (6.37), in which the system matrix $\mathbf{A}_g$ was assumed to be constant, using an average value for the mean motion n. However, as detailed finally in Equation (7.16), the mass of the chaser will vary significantly during the mission, with the main engines alone expending 656.3 kg of propellant. Therefore, the guidance input matrix $\mathbf{B}_g$ cannot be approximated as constant, as the initial mass of the chaser is only 1500 kg.

Theoretically, it would be possible to re-solve the matrix Riccati equation every time the chaser mass is updated. However, as the Riccati equation is solved through numerical means, this would decrease the performance of the simulator significantly. Thus, it was chosen to construct two sets of gain matrices: the initial gain matrix $\mathbf{K}_{g,LQR0}$ for the initial chaser mass $m_{C,0}$ and the final gain matrix $\mathbf{K}_{g,LQRf}$ for an assumed chaser final mass $m_{C,f}$. The gain matrix actually used by the LQR guidance system $\mathbf{K}_{g,LQR}$ was then obtained by linearly interpolating between the two gain matrices based on the instantaneous chaser mass, as shown in Equation (7.17).

$$\mathbf{K}_{g,LQR} = \begin{cases} \frac{m_C - m_{C,0}}{m_{C,f} - m_{C,0}} \left(\mathbf{K}_{g,LQRf} - \mathbf{K}_{g,LQR0}\right) + \mathbf{K}_{g,LQR0} & \text{if } m_C > m_{C,f} \\ \mathbf{K}_{g,LQRf} & \text{if } m_C < m_{C,f} \end{cases} \tag{7.17}$$

Note that Equation (7.17) has an added condition which sets a lower limit on the gain matrix, based on an assumed final mass. This prevents numerical instabilities which could result from the chaser expelling more mass than its total initial mass. Additionally, if this were to occur, the GC system would require excessive amounts of propellant, and would need to be modified to improve performance.

To find suitable $\mathbf{Q}_g$ and $\mathbf{R}_g$ matrices, the results obtained in Section 6.5.1 were used: this specifies a value of $1/(1 \cdot 10^{-2})$ for the position elements of $\mathbf{Q}_g$, $1/(1 \cdot 10^{-4})$ for the velocity elements of $\mathbf{Q}_g$, and $1/(50^2)$ for $\mathbf{R}_g$. Doing this gives the $\mathbf{Q}_g$ and $\mathbf{R}_g$ matrices shown in Equation (7.18):

$$\mathbf{Q}_g = \begin{bmatrix} 1 \cdot 10^2 & 0 & 0 & 0 & 0 & 0 \\ 0 & 1 \cdot 10^2 & 0 & 0 & 0 & 0 \\ 0 & 0 & 1 \cdot 10^2 & 0 & 0 & 0 \\ 0 & 0 & 0 & 1 \cdot 10^4 & 0 & 0 \\ 0 & 0 & 0 & 0 & 1 \cdot 10^4 & 0 \\ 0 & 0 & 0 & 0 & 0 & 1 \cdot 10^4 \end{bmatrix} \qquad \mathbf{R}_g = \begin{bmatrix} 4 \cdot 10^{-4} & 0 & 0 \\ 0 & 4 \cdot 10^{-4} & 0 \\ 0 & 0 & 4 \cdot 10^{-4} \end{bmatrix} \tag{7.18}$$

For both the initial mass case and the assumed final mass case, the matrix Riccati equation can then be solved, yielding corresponding gain matrices according to Equation (6.11). Assuming a final mass of $0.5 m_{C,0}$, the gain matrices shown in Equation (7.19) were found:

$$\begin{gathered} \mathbf{K}_{g,LQR0} = \begin{bmatrix} 500 & -0.31608 & 0 & 5147.8 & 4.8768 \cdot 10^{-7} & 0 \\ 0.31608 & 500 & 0 & 4.8768 \cdot 10^{-7} & 5147.8 & 0 \\ 0 & 0 & 500 & 0 & 0 & 5147.8 \end{bmatrix} \\ \mathbf{K}_{g,LQRf} = \begin{bmatrix} 500 & -0.16033 & 0 & 5074.4 & 6.2735 \cdot 10^{-8} & 0 \\ 0.16033 & 500 & 0 & 6.2735 \cdot 10^{-8} & 5074.4 & 0 \\ 0 & 0 & 500 & 0 & 0 & 5074.4 \end{bmatrix} \end{gathered} \tag{7.19}$$

The diagonal elements of the two gain matrices in Equation (7.19) are very similar in columns 4-6, differing by only 1.4%, and identical in columns 1-3. Therefore, it could be concluded that a single, average gain matrix could be used However, the off-diagonal elements differ by roughly a factor two: therefore, it was decided to implement the linear interpolation between the two.

Note that the values for $\mathbf{Q}_g$ and $\mathbf{R}_g$ used to generate the gain matrices in Equation (7.19), while being based on Bryson's rule, have by no means been optimized for, for instance, the amount of propellant required. However, the selected values should provide a good reference design from which to compare the different simulation models.

7.5.2. LQR CONTROL SYSTEM

As was mentioned in Section 7.3, the control input matrix $\mathbf{B}_c$ cannot be approximated as constant, as the chaser inertia matrix is assumed to vary as much as the chaser mass. Thus, the same problem exists as for the guidance system described previously, and the same solution methodology is applied to the control system. As the inertia matrix of the chaser is linear in the chaser mass, Equation (7.17) can also be used for the control system, in the form shown in Equation (7.20)

$$\mathbf{K}_{c,LQR} = \begin{cases} \frac{m_C - m_{C,0}}{m_{C,f} - m_{C,0}} \left(\mathbf{K}_{c,LQRf} - \mathbf{K}_{c,LQR0}\right) + \mathbf{K}_{c,LQR0} & \text{if } m_C > m_{C,f} \\ \mathbf{K}_{c,LQRf} & \text{if } m_C < m_{C,f} \end{cases} \tag{7.20}$$

To obtain the $\mathbf{Q}_c$ and $\mathbf{R}_c$ matrices, the results obtained in Section 6.5.2 were used: this specifies a value of $1/(1 \cdot 10^{-4})$ for both the attitude elements and rotational rate elements of $\mathbf{Q}_g$, and $1/(20^2)$ for $\mathbf{R}_g$. The corresponding matrices can be seen in Equation (7.21):

$$\mathbf{Q}_c = \begin{bmatrix} 1\cdot10^4 & 0 & 0 & 0 & 0 & 0 \\ 0 & 1\cdot10^4 & 0 & 0 & 0 & 0 \\ 0 & 0 & 1\cdot10^4 & 0 & 0 & 0 \\ 0 & 0 & 0 & 1\cdot10^4 & 0 & 0 \\ 0 & 0 & 0 & 0 & 1\cdot10^4 & 0 \\ 0 & 0 & 0 & 0 & 0 & 1\cdot10^4 \end{bmatrix} \qquad \mathbf{R}_c = \begin{bmatrix} 2.5\cdot10^{-3} & 0 & 0 \\ 0 & 2.5\cdot10^{-3} & 0 \\ 0 & 0 & 2.5\cdot10^{-3} \end{bmatrix} \tag{7.21}$$

As with the guidance system, the matrix Riccati equation can then be solved for the initial mass case and the final mass case, yielding corresponding gain matrices according to Equation (6.11). Again assuming a final mass of $0.5m_{C,0}$, the gain matrices shown in Equation (7.22) were found.

$$\begin{aligned} \mathbf{K}_{c,LQR0} &= \begin{bmatrix} 2000 & 0 & 0 & 2626 & -51.5 & -56.3 \\ 0 & 2000 & 0 & -51.5 & 3113 & -95.4 \\ 0 & 0 & 2000 & -56.3 & -95.4 & 2791 \end{bmatrix} \\ \mathbf{K}_{g,LQRf} &= \begin{bmatrix} 2000 & 0 & 0 & 2334 & -29.6 & -31.8 \\ 0 & 2000 & 0 & -29.6 & 2617 & -55.7 \\ 0 & 0 & 2000 & -31.8 & -55.7 & 2428 \end{bmatrix} \end{aligned} \tag{7.22}$$

As with the LQR guidance system, the diagonal entries of the two gain matrices are similar in columns 4-6 and identical in columns 1-3. However, the difference between the diagonal entries of columns 4-6 of the two gain matrices is more significant, being 12.5%. Again, the off-diagonal elements differ by roughly a factor two. Therefore, it was also chosen to implement linear interpolation between the two gain matrices for the LQR control system.

It is again stressed that the values used for the weighting matrices $\mathbf{Q}_c$ and $\mathbf{R}_c$ are by no means propellant optimal, but simply represent a good reference design by which the different simulation models can be compared.

7.6. SMC CONTROLLER DESIGN

Besides using LQRs to design controllers for the guidance and control models developed in Sections 7.2 and 7.3 based on linear SMCs. In contrast to the controller design based on LQRs, the design of ac SMC-based control system does not permit "good" values of the controls to be selected *a priori*. Thus, it is necessary to perform some kind of selection process, rather than simply following a pre-set rule of thumb. As with the previous section, first the guidance system will be treated, followed by the control system.

7.6.1. SMC GUIDANCE SYSTEM

As with the LQR-based guidance system, it is necessary to find an expression for the SMC guidance vector $\mathbf{u}_{g,SMC}$ which takes the mass variation of the chaser into account. The same approach could be taken as in Section 7.5 by interpolating between a gain matrix based on the initial mass and one based on an assumed final mass. However, it was decided to first work out the SMC design for the initial mass, before a method of taking the chaser mass variation into account is determined.

First, the regular form has to be constructed to allow the switching surface matrix $\mathbf{S}_g$ to be determined based on optimal control theory. When determining the transformation $\mathbf{T}_{r,g}$ based on the QR-decomposition of $\mathbf{B}_g$ [72, Ch. 3.4, 4.2], the result shown in Equation (7.23) is obtained.

$$\mathbf{T}_{r,g} = \begin{bmatrix} -1 & 0 & 0 & 0 & 0 & 0 \\ 0 & -1 & 0 & 0 & 0 & 0 \\ 0 & 0 & -1 & 0 & 0 & 0 \\ 0 & 0 & 0 & -1 & 0 & 0 \\ 0 & 0 & 0 & 0 & -1 & 0 \\ 0 & 0 & 0 & 0 & 0 & -1 \end{bmatrix} \tag{7.23}$$

Applying the transformation $\mathbf{T}_{r,g}$ to the system matrix as shown in Equation (6.19), it is possible to find that $\mathbf{A}_{g,reg} = \mathbf{A}_g$ and that $\mathbf{Q}_{g,reg} = \mathbf{Q}_g$. Using the definition of $\mathbf{Q}_g$ shown in Equation (7.18), it is possible to solve the matrix Riccati equation of the reduced order system, resulting in the switching surface matrix $\mathbf{S}_g$ shown in Equation (7.24).

$$S_g = \begin{bmatrix} -0.1 & 0 & 0 & -1 & 0 & 0 \\ 0 & -0.1 & 0 & 0 & -1 & 0 \\ 0 & 0 & -0.1 & 0 & 0 & -1 \end{bmatrix} \tag{7.24}$$

The result shown in Equation (7.24) is independent of $\mathbf{B}_g$, as the reduced system is constructed using only $\mathbf{A}_g$ and $\mathbf{Q}_g$. This result can then be used to determine the control vector $\mathbf{u}_g$ according to Equation (6.35). Since linear switching surfaces are being considered, this relation can be rewritten as shown in Equation (7.25), when assuming $\mathbf{Q}_r$ is the identity matrix.

$$\mathbf{u}_g = \left[\mathbf{S}_g \mathbf{B}_g\right]^{-1} \mathbf{u}_g^* \tag{7.25}$$

The value of $\mathbf{u}_g^*$ is dependent on the instantaneous state of the system as shown in Equation (6.34), must be rewritten to include the control margin $\delta_{CM,g}$. The resulting expressions for the elements of $\mathbf{u}_g^*$ are shown in Equation (7.26).

$$\begin{aligned} u_{g,i}^{*+} &= -\begin{bmatrix} s_{i1} & \cdots & s_{in} \end{bmatrix} \mathbf{A}_g \mathbf{x}_g - \delta_{CM,g} \text{ for } \sigma_i(x) > 0 \\ u_{g,i}^{*-} &= -\begin{bmatrix} s_{i1} & \cdots & s_{in} \end{bmatrix} \mathbf{A}_g \mathbf{x}_g + \delta_{CM,g} \text{ for } \sigma_i(x) < 0 \end{aligned} \tag{7.26}$$

Thus, it can be seen in Equation (7.25) that the only term dependent on the input matrix is $\left[\mathbf{S}_g \mathbf{B}_g\right]^{-1}$. This term is worked out for the initial chaser mass in Equation (7.27).

$$\left[\mathbf{S}_g \mathbf{B}_g\right]^{-1} = \begin{bmatrix} -1500 & 0 & 0 \\ 0 & -1500 & 0 \\ 0 & 0 & -1500 \end{bmatrix} = m_{C,0} \begin{bmatrix} -1 & 0 & 0 \\ 0 & -1 & 0 \\ 0 & 0 & -1 \end{bmatrix} \tag{7.27}$$

It is apparent from Equation (7.27) and (7.25) that the control vector can be expressed in terms of the instantaneous chaser mass. Thus, the interpolation method described for the LQR design is not necessary for the SMC design, even though the construction of the switching surfaces is based on the same principles.

Note, of course, that the parameter $\delta_{CM,g}$ has been introduced, with the sole requirement that the value thereof is larger than zero. Furthermore, control softening proved necessary to mitigate chattering, for which Equation (6.36) was implemented. Doing so introduces the two additional parameters $\delta_{BL,g}$ and $\delta_{DB,g}$, which can also take any value larger than (or, theoretically, equal to) zero.

To find appropriate orders of magnitude for each of these three parameters, a coarse grid search was performed. It was assumed that each of the parameters would be relatively small constants: for $\delta_{BL,g}$ and $\delta_{DB,g}$, this was chosen to still allow the system to remain close to the sliding mode, and for $\delta_{CM,g}$, this was done to reduce the aggressiveness of the controls. The range of values used for each of the parameters is shown in Table 7.9.

Table 7.9: SMC parameter ranges for initial grid search.

Parameter	**Value range**
δ_{BL}	[0, 0.001, 0.01, 0.1]
δ_{DB}	[0, 0.001, 0.01, 0.1]
δ_{CM}	[0.001, 0.01, 0.1]

Note that in Table 7.9 a value of zero were also included for $\delta_{BL,g}$ and $\delta_{DB,g}$, to investigate the case of no boundary layer or no deadband. However, the "ideal" SMC case of no boundary layer and no deadband was not considered, due to the extreme chattering resulting from this.

When excluding the combination of $\delta_{BL,g} = 0$ and $\delta_{DB,g} = 0$, 45 combinations of the values shown in Table 7.9 can be made. Each combination was implemented in a simulation of the full deorbit mission with all thrust levels and the nominal tether model described in Section 7.4: this tether model has a natural length L_0 of 200 m, a mass m of 5 kg, a spring constant k of 10 N/m, a damping constant c of 0.3 Ns/m, and two nodes. As it was identified in Section 6.5.1 that some combinations could result in the system responding insufficiently to disturbances, these simulations were also subject to the constraint that the chaser may not deviate too much from the y-axis of the H_T frame. This limit was arbitrarily set to 10 m, thus ensuring the chaser remains close to the H_T frame y-axis. Any parameter combination exceeding these bounds at any time was discarded.

The selection of the most appropriate parameter combination was based on minimum propellant expelled across the range of thrust levels: the constraint imposed on the maximum deviation from the H_T frame y-axis should ensure that all resulting solutions are stable. Note that during this process, the attitude control of the chaser was performed by the LQR-based attitude controller described previously. The three best parameter combinations for each thrust level, and the corresponding propellant mass, are shown in Table 7.10.

Table 7.10: Guidance SMC parameter selection from initial grid search.

Thrust level [N]	**Parameter**	**Best values**		
500	$\delta_{BL,g}$	0.1	0.1	0.1
	$\delta_{DB,g}$	0.1	0	0.01
	$\delta_{CM,g}$	0.1	0.1	0.1
	$m_{prop,g}$ [kg]	85.96	129.50	130.70
1000	$\delta_{BL,g}$	0.1	0.001	0
	$\delta_{DB,g}$	0.1	0.1	0.1
	$\delta_{CM,g}$	0.1	0.1	0.1
	$m_{prop,g}$ [kg]	54.48	64.76	67.14
2000	$\delta_{BL,g}$	0	0.01	0.1
	$\delta_{DB,g}$	0.1	0.1	0.1
	$\delta_{CM,g}$	0.1	0.1	0.1
	$m_{prop,g}$ [kg]	23.75	25.00	27.98

From Table 7.10, it is clear that a boundary layer $\delta_{BL,g}$ of 0.1, a deadband of $\delta_{DB,g}$ of 0.1, and a control margin $\delta_{CM,g}$ of 0.1 provide good results across the range of thrust levels. Therefore, these values were selected for implementation in the SMC guidance system, ans should provide good performance with which the different simulation models can be compared. However, it is once again stressed that these values represent an order-of-magnitude approximation only, and that the fine-tuning of these is outside the scope of this research.

7.6.2. SMC CONTROL SYSTEM

The design of the SMC control system follows much the same pattern as that of the SMC-based guidance system detailed in the previous section. Thus, the control vector $\mathbf{u}_{c,SMC}$ must be determined, again taking the variation of the chaser inertia matrix into account. To start the process, $\mathbf{T}_{r,c}$ can be determined based on the QR-decomposition of $\mathbf{B}_c$, with the result shown in Equation (7.28). Again, the subsequent analysis is performed for the initial inertia matrix.

$$\mathbf{T}_{r,c} = \begin{bmatrix} -0.994 & 0.071 & 0.078 & 0 & 0 & 0 \\ -0.059 & -0.988 & 0.145 & 0 & 0 & 0 \\ -0.087 & -0.140 & -0.986 & 0 & 0 & 0 \\ 0 & 0 & 0 & -0.994 & -0.059 & -0.087 \\ 0 & 0 & 0 & 0.071 & -0.988 & -0.140 \\ 0 & 0 & 0 & 0.078 & 0.145 & -0.986 \end{bmatrix} \tag{7.28}$$

The transformation in Equation (7.28) can then be applied to the system and weighting matrices $\mathbf{A}_c$ and $\mathbf{Q}_c$, respectively. Doing this, it is found that the identity of $\mathbf{Q}_{c,reg} = \mathbf{Q}_c$ still holds. However, $\mathbf{A}_{c,reg}$ takes the form shown in Equation (7.29).

$$\mathbf{A}_{c,reg} = \begin{bmatrix} 0 & 0 & 0 & 0.489 & -0.076 & -0.072 \\ 0 & 0 & 0 & 0.052 & 0.475 & -0.146 \\ 0 & 0 & 0 & 0.091 & 0.135 & 0.473 \\ 0 & 0 & 0 & 0 & 0 & 0 \\ 0 & 0 & 0 & 0 & 0 & 0 \\ 0 & 0 & 0 & 0 & 0 & 0 \end{bmatrix} \tag{7.29}$$

Taking $\mathbf{Q}_c$ to be the same as shown in Equation (7.21), it is again possible to solve the matrix Riccati equation of the reduced order system. Doing so results in the switching surface matrix shown in Equation (7.30).

$$S_c = \begin{bmatrix} -0.994 & -0.059 & -0.087 & -0.994 & -0.059 & -0.087 \\ 0.071 & -0.988 & -0.140 & 0.071 & -0.988 & -0.140 \\ 0.078 & 0.145 & -0.986 & 0.078 & 0.145 & -0.986 \end{bmatrix} \tag{7.30}$$

Again, this result is independent of $\mathbf{B}_c$. Then, with the switching surface matrix obtained, it is possible to determine the appropriate control vector $\mathbf{u}_c$. As with the guidance system, it is possible to define this control vector as shown in Equation (6.34), which reduces to Equation (7.31) for a linear switching surface. The diagonalized control vector can be expressed as shown in Equation (7.32).

$$\mathbf{u}_c = [\mathbf{S}_c\mathbf{B}_c]^{-1}\mathbf{u}_c^* \tag{7.31}$$

$$\begin{aligned} u_{c,i}^{*+} &= -\begin{bmatrix} s_{i1} & \cdots & s_{in} \end{bmatrix}\mathbf{A}_c\mathbf{x}_c - \delta_{CM,c} \text{ for } \sigma_i(x) > 0 \\ u_{c,i}^{*-} &= -\begin{bmatrix} s_{i1} & \cdots & s_{in} \end{bmatrix}\mathbf{A}_c\mathbf{x}_c + \delta_{CM,c} \text{ for } \sigma_i(x) < 0 \end{aligned} \tag{7.32}$$

To fully determine the control, the $[\mathbf{S}_c\mathbf{B}_c]^{-1}$ term has to be evaluated. $\mathbf{B}_c$ is dependent on the inverse of the inertia matrix, which in turn is linearly dependent on the chaser mass according to Equation (5.18). Thus, the $[\mathbf{S}_c\mathbf{B}_c]^{-1}$ term is linearly dependent on the chaser mass, an can be written as shown in Equation (7.33).

$$[\mathbf{S}_c\mathbf{B}_c]^{-1} = \frac{m_c}{m_{C,0}}\begin{bmatrix} -1420 & 267.2 & 239.8 \\ 0 & -2786 & 679.1 \\ 0 & 0 & -1926 \end{bmatrix} \tag{7.33}$$

Again, the parameters $\delta_{BL,c}$, $\delta_{DB,c}$, and $\delta_{CM,c}$, which were evaluated in the same fashion as presented in the previous section. However, for this analysis, the additional constraint is imposed that the maximum deviation may not be larger than 1°.

The values investigated for each parameter are identical to the results presented in Table 7.9, with the results being presented in Table 7.11. Note that in for this analysis the guidance system was set to use the control parameter values determined in the previous section, which were shown to be stable with the LQR control system. To enforce the constraint that the maximum angular deviation between the G_C frame and the H_T frame was less than 1°, all SMC parameter combinations in the control system exceeding this constraint at any time were discarded. The results in Table 7.11 are part of the filtered set of results, containing only valid controller set-ups.

Table 7.11: Control SMC parameter selection from initial grid search.

Thrust level [N]	**Parameter**	**Best values**		
500	$\delta_{BL,c}$	0.01	0.001	-
	$\delta_{DB,c}$	0.001	0.001	-
	$\delta_{CM,c}$	0.1	0.01	-
	$\mathrm{m}_{prop,c}$ [kg]	27.02	27.39	-
1000	$\delta_{BL,c}$	0.001	0.001	0.01
	$\delta_{DB,c}$	0.001	0	0.001
	$\delta_{CM,c}$	0.01	0.01	0.1
	$\mathrm{m}_{prop,c}$ [kg]	18.89	20.13	21.26
2000	$\delta_{BL,c}$	0.01	0.01	0.001
	$\delta_{DB,c}$	0.001	0	0.001
	$\delta_{CM,c}$	0.1	0.1	0.1
	$\mathrm{m}_{prop,c}$ [kg]	13.56	14.29	14.38

From Table 7.10, it can be seen that a boundary layer $\delta_{BL,c}$ of 0.01, a deadband of $\delta_{DB,c}$ of 0.001, and a control margin $\delta_{CM,c}$ of 0.1 provide the best results across the range of thrust levels. Therefore, these values were selected for implementation in the SMC-based control system. Again, these values represent suitable orders-of-magnitude of the controller parameters, the fine-tuning of which is outside the scope of this research.

8

SIMULATION RESULTS

At last, this chapter will present the simulations that were performed and the results thereof. To gain a complete understanding of the TSDS during the course of the mission, several types of simulation were performed: first, tether models were tested with varying natural lengths, spring constants, and damping constants, allowing the effect of these parameters to be evaluated on the system performance. With the resulting understanding of the effect of various tether parameters on the system dynamics, a nominal model was chosen and a Monte Carlo analysis was performed on the initial conditions of the simulation. Doing so, it is possible to evaluate the sensitivity of the terminal conditions to these variations. This then leads to the most promising combination of tether parameters and controller options being selected.

The simulation parameters and simulation plan will be presented first in Section 8.1. The tether parameter analysis will be shown in Section 8.2. Section 8.3 will then detail the Monte Carlo analysis performed on a selected nominal tether mode. Finally, the selection of suitable tether models and controller options will be performed in Section 8.4

8.1. SIMULATION PLAN

This section will present the general strategy followed for the simulations which were performed, along with the specific parameters which were investigated. First, the general scenario used for all simulations will be summarized in Section 8.1.1. Second, the simulation plan for the tether parameter analysis will be presented in Section 8.1.2. Finally, the strategy for the Monte Carlo analysis will be shown in Section 8.1.3.

8.1.1. GENERAL SIMULATION PARAMETERS

The described ADR scenario begins with the TSDS in a circular SSO at 800 km altitude [3]. This corresponds to a semi-major axis a of 7178.136 km, an eccentricity e of zero, and an inclination i of 98.6° [52, Ch. 10.4]. The initial RAAN, however, is unspecified, as is the initial position of the TSDS in its orbit. Because the general area targeted for satellite disposal is the South Pacific Ocean, it was decided that the initial condition of the TSDS would lie in the equatorial plane: if the first deorbit burn is initiated at the equatorial plane, this ensures that the periapsis will generally lie below the equator on the other side of the Earth. Furthermore, since the exact timing of the mission is not considered, it was decided to set the inital RAAN to zero.

Zooming in on the TSDS itself, the target is located in the origin of the Hill frame, providing a frame of reference for the relative motions of the chaser [3]. The chaser is located behind, below, and slightly out-of-plane with the target, at such a distance that the tether is held slack. This corresponds to -2 m along the x_H axis, $-(L_0 - 10)$ m along the y_H axis, and -1.5 m along the z_H axis. Furthermore, the relative velocity and angular rates of both satellites are equal to zero, and both are level with the local horizon. The tether nodes are then spaced evenly between the chaser and target states, both in position and velocity. This initial condition is schematically shown in Figure 8.1.

At $t = 0$ in the simulation, the first deorbit burn is initiated. The guidance system will then proceed to perform a burn at each subsequent apoapsis passage, until a terminal condition has been reached. The terminal condition used in this simulation corresponds to either the chaser or the target reaching an altitude of 100 km. This value corresponds to a commonly-used definition of the re-entry interface around the Earth [9, Ch. 4.1], after which point the equations used to model the satellites' motions are no longer sufficient.

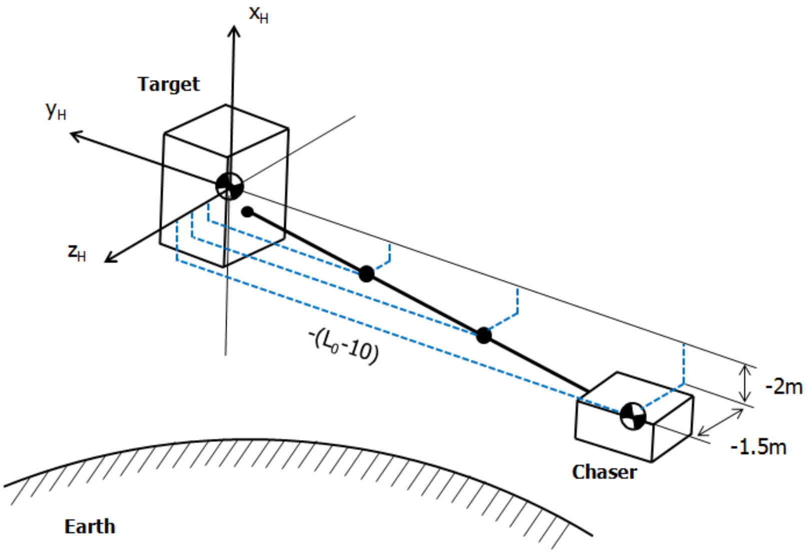

Figure 8.1: Graphical depiction of the nominal initial state of the TSDS.

8.1.2. TETHER PARAMETER ANALYSIS

The tether parameter analysis was performed to gain insight towards the influence of the physical tether model on the system dynamics and resulting mission performance. First, the investigated models will be summarized, followed by an overview of the results that were to be determined.

OVERVIEW OF TETHER SIMULATION MODELS

A number of tether parameter combinations were proposed by ESA for the analysis of the behavior of the TSDS [3]. These different combinations assume a tether with a constant cross-sectional area A and density, and varying lengths L_0, Young's moduli E_{mat}, and damping constants c. The different proposed combinations are shown in Table 8.1.

Table 8.1: Tether parameter combinations proposed by ESA [3].

Model number	E_{mat} [Pa]	A [m^2]	L_0 [m]	m [kg]	N	c [Ns/m]	c_N [Ns/m]	k [N/m]	k_N [N/m]
ESA1	$1 \cdot 10^8$	$2 \cdot 10^{-5}$	200	5	2	0.3	0.9	10	30
ESA2	$1 \cdot 10^8$	$2 \cdot 10^{-5}$	800	20	2	0.3	0.9	2.5	7.5
ESA3	$4 \cdot 10^8$	$2 \cdot 10^{-5}$	80	2	2	0.3	0.9	100	300
ESA4	$1 \cdot 10^8$	$2 \cdot 10^{-5}$	200	5	2	0.001	0.003	10	30

It must be noted that two additional tether parameter combinations were proposed with an alternate number of nodes [3]. However, the effect of varying the number of nodes was investigated in Section 7.4, and these models are therefore omitted here: the number of nodes used is two for all models.

Upon inspection of the models shown in Table 8.1, it was apparent that the four proposed models do not allow the effect of each parameter individually to be analyzed: model ESA1 represents the nominal tether model; model ESA2 is a longer tether than the nominal case, with an identical cross-section and Young's modulus; model ESA3 is a shorter tether than the nominal case, and additionally has a higher Young's modulus; and model ESA4 has a lower damping coefficient than the nominal case.

Therefore, it was decided to investigate the various combinations of the tether parameters varied in the ESA proposed models. For the three proposed tether lengths, models were created, which alternately represented the nominal material properties, the case with a higher Young's modulus, and the case with the low damping coefficient. These combinations, which include the four ESA models, are shown in Table 8.2.

As mentioned in Section 7.2, it is very beneficial for the stability of the system if the main engines are gradually throttled down. The time during which the main engines are throttled down was chosen to approximate the behavior of a critically damped system, which was shown for the case of $k = 10$ N/m in Figure 7.17. However, from Table 8.2, it can be seen that the value of k varies significantly.

Table 8.2: Final tether parameter combinations for ADR analysis.

Model number	E_{mat} [Pa]	A [m^2]	L_0 [m]	m [kg]	N	c [Ns/m]	c_N [Ns/m]	k [N/m]	k_N [N/m]
N_{nom}	$1 \cdot 10^8$	$2 \cdot 10^{-5}$	200	5	2	0.3	0.9	10	30
N_{LD}	$1 \cdot 10^8$	$2 \cdot 10^{-5}$	200	5	2	0.001	0.003	10	30
N_{HT}	$4 \cdot 10^8$	$2 \cdot 10^{-5}$	200	5	2	0.3	0.9	40	120
S_{nom}	$1 \cdot 10^8$	$2 \cdot 10^{-5}$	80	2	2	0.3	0.9	25	75
S_{LD}	$1 \cdot 10^8$	$2 \cdot 10^{-5}$	80	2	2	0.001	0.003	25	75
S_{HT}	$4 \cdot 10^8$	$2 \cdot 10^{-5}$	80	2	2	0.3	0.9	100	300
L_{nom}	$1 \cdot 10^8$	$2 \cdot 10^{-5}$	800	20	2	0.3	0.9	2.5	7.5
L_{LD}	$1 \cdot 10^8$	$2 \cdot 10^{-5}$	800	20	2	0.001	0.003	2.5	7.5
L_{HT}	$4 \cdot 10^8$	$2 \cdot 10^{-5}$	800	20	2	0.3	0.9	10	30

Therefore, additional analyses of the critically damped system were performed, corresponding to each additional unique value of k, being 2.5 N/, 25 N/m, 40 N/m, and 100 N/m. As the critically damped behavior is independent of the initial conditions, it was arbitrarily chosen to use a natural length L_0 of 200 m for all analyses. The behavior of each system is shown in Figures 8.4 through 8.2.

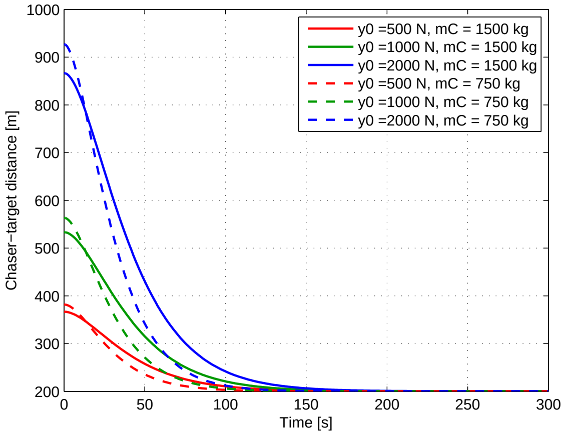

Figure 8.2: Simulated critically-damped behavior of the TSDS with k=2.5 N/m.

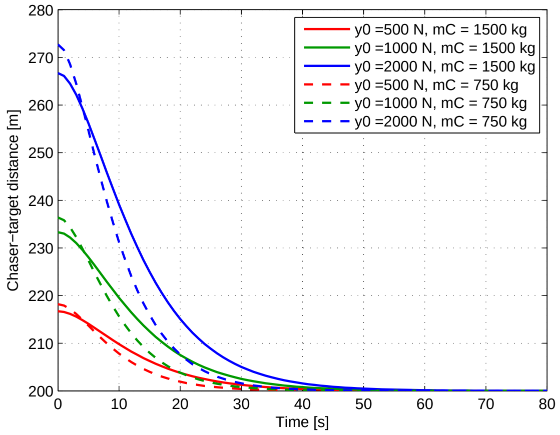

Figure 8.3: Simulated critically-damped behavior of the TSDS with k=25 N/m.

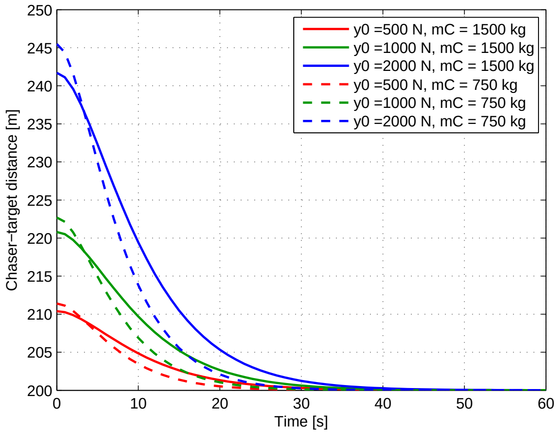

Figure 8.4: Simulated critically-damped behavior of the TSDS with k=40 N/m.

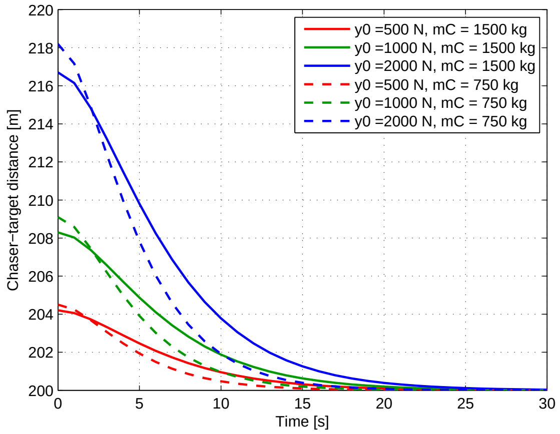

Figure 8.5: Simulated critically-damped behavior of the TSDS with k=100 N/m.

Based on the behavior seen in Figures 8.2 through 8.5, it was possible to determine values for $t_{\Delta thr}$, for each value of k, which approximate critical damping behavior. These results are shown in Table 8.3, along with the result obtained in Section 7.2. Note that an error of 0.1% of the natural length was again used as the tolerance.

Table 8.3: Chosen values for $t_{\Delta thr}$ for each k.

k [N/m]	$\mathbf{t}_{\Delta thr}$ [s]
2.5	231
10	100
25	55
40	41
100	22

With the values shown in Table 8.3, it is possible to have each system approximate the same behavior, despite the differences in physical tether parameters. Thus, the behavior of each tether parameter model can be more effectively compared.

DESIRED OUTPUTS OF TETHER MODEL ANALYSIS

The results of the tether parameter analysis were compared on three different fronts. First, it was assumed that since the overall configuration of the chaser is the same for all models, the total propellant required is a measure of the cost-effectiveness of each solution. Therefore, the propellant fractions were calculated for each simulation scenario and compared to each other to find the most propellant-optimal solutions.

Second, the oscillatory behavior of the tether was examined: large and/or violent oscillations pose a general threat to the safety and reliability of the mission, as material failure of the tether is not considered. If the tether were to fail due to excessive loading, the mission would be a failure. Thus, slow oscillations with low amplitudes are preferred over violent oscillations with large amplitudes.

Third, and finally, the rotation of the target was investigated, which also poses a threat to the safety and reliability of the mission. If the target rotates too much, the tether could end up wrapped around the target, potentially severing itself or appendages on the target. Obviously, this would result in an increase in space debris, rather than removal thereof. Thus, the total rotation of the target was calculated and compared between different simulation scenarios.

8.1.3. MONTE CARLO ANALYSIS

An important aspect of any analysis is to perform a sensitivity analysis of the simulation to the initial conditions. Such an analysis offers insight towards the precision of the final solution if the initial conditions are slightly offset with respect to the nominal mission, without the control parameters having been changed. First, the parameters which were varied will be summarized. Second, the desired outputs from these simulations will be discussed.

OVERVIEW OF MONTE CARLO SIMULATIONS

It was decided to investigate the sensitivity of the terminal conditions of the TSDS to variations in the relative initial state of the chaser with respect to the target. This was chosen due to the close proximity of the chaser and the target, which is in the order of hundreds of meters: even small errors on the scale of the individual orbits of the chaser and target will results in a significant variation of the relative geometry. Therefore, such errors were deemed most likely to affect the performance of the GC system. Note again that in this case, the terminal conditions were defined as either the chaser or the target reaching an altitude of 100 km.

To determine the sensitivity of the simulation of the ADR mission to the initial conditions, a Monte Carlo analysis was performed. The essence of this analysis is to apply random small variations to the initial conditions and to compare how the system behaves. As the initial condition being varied is the state of the chaser with respect to the target, four different sets of elements can be varied: the relative position, the relative velocity, the relative orientation, and the relative angular rates.

To perform a meaningful Monte Carlo analysis, suitable ranges must be found within which to randomly vary the initial relative state of the chaser. To do so, it was decided to do this based on the navigation models, originally presented as part of the research proposed by ESA [3]. In the worst case, the sensors would make 4.5% errors in the range from the chaser to the target, and have a 3.5° error in the line of sight to the target. Furthermore, the error in the orientation of the chaser could be as much as 15°.

For the variations in the initial position, the range and line-of-sight errors could be used. Specifically, the variation along the y_H axis can be expressed by simply adding and subtracting the range error from the nominal position. Then, the radial offset about the y_H axis can be expressed using the tangent of the line-of-sight error multiplied by the nominal position along the y_H axis. Note that this radial offset is then the variation range along both the x_H and the z_H axes. This is visualized in Figure 8.6.

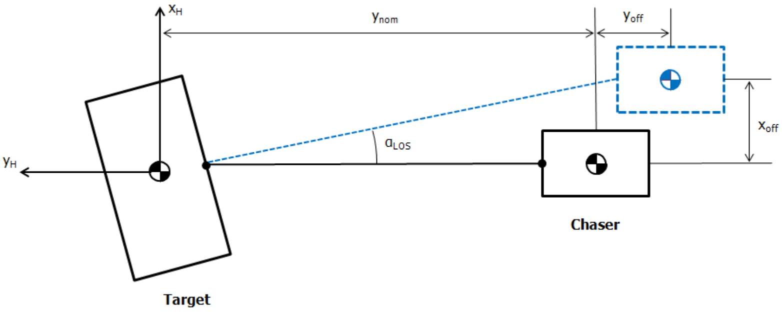

Figure 8.6: Graphical depiction of the variation of the chaser initial position based on the range and line-of-sight α_{LOS} errors.

To determine the initial angular offset of the chaser with respect to the nominal case, which is level with the local horizon, a random rotation axis $\mathbf{e}_{err}$ is first defined in the Hill frame. Then, a random rotation α_{err}, with a maximum magnitude of the aforementioned $15° = 0.262$ rad, is applied around this rotation axis, effectively defining an error quaternion. This allows Equation (4.23) to be used to determine a new initial quaternion.

To complete the variation ranges for the initial chaser state, arbitrary limits of 1 m/s and 0.1 rad/s were set on the velocity and angular rate variations, respectively. The resulting range of values investigated during the Monte Carlo analysis is then summarized in Table 8.4.

Table 8.4: Monte Carlo simulation variation limits on the initial chaser relative state.

Parameter	Unit	Lower limit	Nominal value	Upper limit
$x_{H,0}$	[m]	$-2-(L_0-10)\tan(\alpha_{LOS})$	-2	$-2+(L_0-10)\tan(\alpha_{LOS})$
$y_{H,0}$	[m]	$-1.045(L_0-10)$	$-(L_0-10)$	$-0.955(L_0-10)$
$z_{H,0}$	[m]	$-1.5-(L_0-10)\tan(\alpha_{LOS})$	-1.5	$-1.5+(L_0-10)\tan(\alpha_{LOS})$
$\dot{x}_{H,0}$	[m/s]	-1	0	1
$\dot{y}_{H,0}$	[m/s]	-1	0	1
$\dot{z}_{H,0}$	[m/s]	-1	0	1
$e_{err,x}$	[-]	-1	0	1
$e_{err,y}$	[-]	-1	0	1
$e_{err,z}$	[-]	-1	0	1
α_{err}	[rad]	-0.262	0	0.262
$\omega_{xG,0}$	[rad/s]	-0.1	0	0.1
$\omega_{yG,0}$	[rad/s]	-0.1	0	0.1
$\omega_{zG,0}$	[rad/s]	-0.1	0	0.1

DESIRED OUTPUTS OF MONTE CARLO ANALYSIS

The primary focus of the performed Monte Carlo analysis was to determine the spread of terminal points when subjecting the initial values to slight variations. Two different methods are used to investigate the system precision. First, the physical spread of the terminal points on the sphere of the Earth will be determined. This shows the ability of the simulated system to deorbit the target within a desired range. In this case, the ideal target location is determined by the SPOUA (see also Section 4.1).

Second, the offset of the terminal points with respect to the nominal terminal point will be plotted in histograms. This shows the numerical grouping of simulation results, along with any type of distribution these results may have. Using these techniques, the sensitivity of the terminal points to the slightly varied initial conditions can be effectively assessed.

8.2. TETHER PARAMETER ANALYSIS

The first step towards determining suitable options for the ADR mission is to investigate the effect of varying the physical parameters mentioned in Section 8.1.2. To gain insight to the influence of these parameters, simulations were performed on the scenario described in Section 8.1.1 in which each combination of tether model (nine in total), thrust level (three in total), and controller type (two in total) were evaluated for a total of 54 combinations.

To determine the suitability of each combination for the ADR mission, three key elements were evaluated for each simulation. First, the consumed propellant mass for each combination was considered, for which it is of course desirable to select options that consume less propellant while still accomplishing the mission. Second, the oscillatory behavior of the tether itself in each simulation combination is examined, permitting the severity of the induced oscillations to be quantified: it is desirable to select options that do not cause violent motions in the tether itself. Third, the aspect of target rotation is investigated: as the target is completely non-cooperative, it will be wholly at the mercy of the torques induced by the tether. If this is too severe, the tether may begin to wrap around the target.

8.2.1. PROPELLANT CONSUMPTION

As mentioned, the first aspect by which the suitability of each tether parameter model is judged is the propellant mass consumed by the GC. As in any space mission, mass is an important driver for the mission costs: thus, reducing the required amount of propellant is an effective method of keeping costs down.

To this end, the propellant mass components and total required propellant mass for each simulation were determined using the methods detailed in Sections 7.2 and 7.3. Again, it is stressed that the deorbit reference trajectory was selected such that a constant amount of propellant is used for the main engines, irrespective of thrust level or controller type: thus, any deviation from the nominal value of 656.3 kg will indicate that the chaser has not been able to perform a nominal deorbit burn. It is reiterated that an I_{sp} of 325 s has been assumed for the main engines and an I_{sp} of 291 s has been assumed for the guidance and control thrusters, with the control thrusters operating on a 1 m moment arm.

Furthermore, the LQR and SMC control parameters were kept constant, such that the ability of each GC system to adapt to varying conditions could be examined. In general, a higher guidance propellant consumption for a given thrust level and controller type will indicate that the GC system has more difficulty establishing each hold point. The results of this analysis are shown in Table 8.5 for the LQR-based GC system and in Table 8.6 for the SMC-based GC system.

To allow the analysis of these numbers to be more effective, first some general trends will be observed from the results of both control system types. Then, the results from the LQR system and the SMC system will be examined individually. Finally, a comparison of the performance of both systems will be made.

GENERAL TRENDS IN SYSTEM PROPELLANT CONSUMPTION

When examining the data presented in Tables 8.5 and 8.6, a number of phenomena common to both control system types can be observed. First, and foremost, it can clearly be seen that it is possible to achieve a successful deorbit mission with each combination of tether-parameter model and thrust level: each simulation uses 656.3 kg of propellant for the main engines before encountering the terminal condition.

However, how efficiently each option is at actually achieving this varies significantly between each tether-parameter model and thrust level. The most striking trend is the large dependency of the guidance and control propellant consumption on the thrust level: there seems to be a nearly inversely proportional relationship between the thrust level and the guidance actuation required. This trend is also observable in the control actuation, but to a lesser degree.

To explain this trend, it is possible to refer back to Section 7.2. While the propellant consumption of the main engine is constant for each thrust level, the number of burns required to achieve the necessary change in momentum is not: 500 N of thrust requires four burns, 1000 N of thrust requires two, and 2000 N thrust requires one. Therefore, the guidance propellant consumption is not strictly inversely proportional to the thrust level, but rather directly proportional to the number of burns that are performed. This, in turn, leads to believe that establishing the hold point during the burn is the most demanding phase for the guidance system.

To investigate this claim, it was decided to examine the position error of the chaser along the y_H axis during the a complete deorbit burn and subsequent establishment of the coasting hold point. The results of this analysis for the N_{nom} tether model at each thrust level are shown in Figure 8.7 for the LQR system and in

Table 8.5: Propellant masses for total ADR mission using LQR-based GC system.

Thrust level [N]	Model number	Main engine propellant [kg]	Guidance propellant [kg]	Control propellant [kg]	Total propellant [kg]
500	N_{nom}	656.3	189.4	23.9	867.2
	N_{LD}	656.3	206.9	27.3	890.5
	N_{HT}	656.3	236.0	25.3	917.6
500	S_{nom}	656.3	206.6	28.5	891.5
	S_{LD}	656.3	217.4	29.6	903.4
	S_{HT}	656.3	357.3	29.1	1042.8
500	L_{nom}	656.3	301.4	20.4	927.1
	L_{LD}	656.3	244.1	29.0	897.7
	L_{HT}	656.3	301.2	34.6	979.6
1000	N_{nom}	656.3	98.5	15.1	769.0
	N_{LD}	656.3	100.2	14.0	770.3
	N_{HT}	656.3	132.8	22.9	811.9
1000	S_{nom}	656.3	108.2	19.0	783.5
	S_{LD}	656.3	111.4	20.6	788.2
	S_{HT}	656.3	162.6	20.3	839.2
1000	L_{nom}	656.3	173.4	23.8	851.2
	L_{LD}	656.3	229.9	36.2	911.7
	L_{HT}	656.3	124.2	14.5	791.9
2000	N_{nom}	656.3	47.2	7.7	711.1
	N_{LD}	656.3	50.9	7.6	714.8
	N_{HT}	656.3	51.3	9.0	716.5
2000	S_{nom}	656.3	43.3	8.4	708.1
	S_{LD}	656.3	47.0	10.2	713.5
	S_{HT}	656.3	62.2	12.8	731.2
2000	L_{nom}	656.3	79.8	11.5	745.8
	L_{LD}	656.3	128.5	33.7	818.3
	L_{HT}	656.3	63.6	7.7	728.3

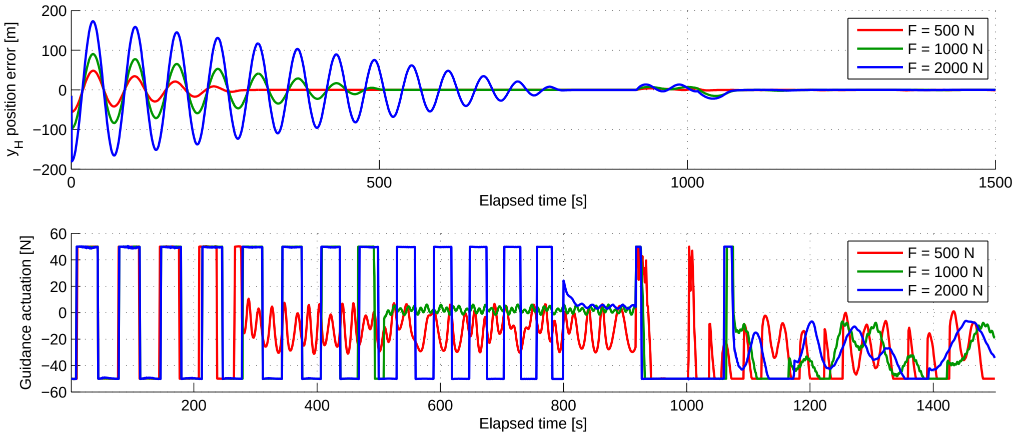

Figure 8.7: Guidance force and position error of the chaser along the y_H axis for the N_{nom} tether model and the LQR system.

Table 8.6: Propellant masses for total ADR mission using SMC-based GC system.

Thrust level [N]	**Model number**	**Main engine propellant [kg]**	**Guidance propellant [kg]**	**Control propellant [kg]**	**Total propellant [kg]**
500	N_{nom}	656.3	95.3	27.0	779.4
	N_{LD}	656.3	93.8	25.7	776.6
	N_{HT}	656.3	43.5	23.2	723.1
500	S_{nom}	656.3	51.6	27.2	735.3
	S_{LD}	656.3	129.4	29.4	815.3
	S_{HT}	656.3	32.0	29.3	717.7
500	L_{nom}	656.3	64.9	29.3	754.5
	L_{LD}	656.3	92.5	38.1	790.6
	L_{HT}	656.3	94.6	32.9	784.5
1000	N_{nom}	656.3	48.8	21.3	726.4
	N_{LD}	656.3	59.4	21.3	737.1
	N_{HT}	656.3	44.7	22.1	723.1
1000	S_{nom}	656.3	43.0	22.4	721.7
	S_{LD}	656.3	62.3	24.0	742.7
	S_{HT}	656.3	29.5	23.8	709.6
1000	L_{nom}	656.3	49.8	27.8	734.9
	L_{LD}	656.3	56.9	28.2	741.9
	L_{HT}	656.3	44.4	19.8	720.5
2000	N_{nom}	656.3	25.5	13.6	695.4
	N_{LD}	656.3	29.1	13.7	699.1
	N_{HT}	656.3	30.3	13.7	700.4
2000	S_{nom}	656.3	26.6	14.8	697.7
	S_{LD}	656.3	31.0	15.9	703.2
	S_{HT}	656.3	31.8	17.2	705.4
2000	L_{nom}	656.3	38.7	13.4	708.4
	L_{LD}	656.3	42.7	14.8	713.9
	L_{HT}	656.3	28.5	14.0	698.9

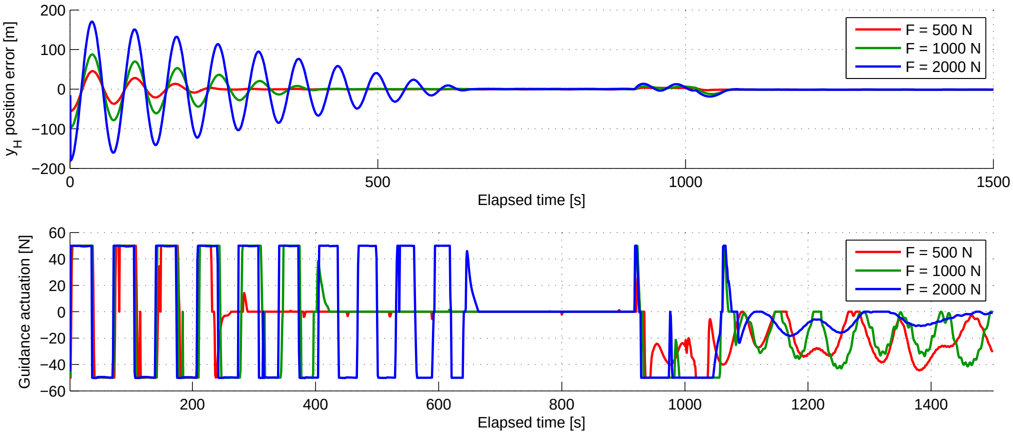

Figure 8.8: Guidance force and position error of the chaser along the y_H axis for the N_{nom} tether model and the SMC system.

Figure 8.8 for the SMC system. Also shown are the corresponding absolute guidance forces, as this shows the response of the guidance system.

Figures 8.7 and 8.8 show the position error and guidance actuation along the y_H axis for the first 1500 s of each respective deorbit mission. This period allows for the observation of the entire deorbit burn and subsequent establishment of the coasting hold point. Thus, conclusions can be drawn regarding the influence of both the burn and coasting phases on the guidance propellant consumption.

Both Figures 8.7 and 8.8 show the same general system behavior. First, at $t = 0$ s, the main engines are activated, and thus the guidance system is set to the burn hold point, resulting in a large position error. Second, it can be seen that directly following this, the system shows a decaying oscillation around the burn hold point as the guidance system establishes the burn hold point: maximum guidance thrust is applied throughout most of this damping phase, as seen by the near-square-wave behavior of the guidance actuation. It is of note that the oscillations are more quickly damped by the SMC system than by the LQR system: in the worst case, the LQR-system oscillations are damped by $t = 800$ s, while the SMC system has achieved this by $t = 650$ s.

Once the burn hold point is established, very little guidance effort is required. Then, as the coasting hold point is established around $t = 1000$ s, maximum guidance thrust is once again applied. This seems to indicate that the guidance system is attempting to nullify the velocity of the chaser as the main engines are throttled down. Then, after the coasting hold point is established, the LQR system once again requires more guidance actuation than the SMC system to maintain this hold point.

From Figures 8.7 and 8.8, it is clear seen that higher thrust levels require more guidance actuation to establish the burn hold point. However, during the coasting phase it can be seen that significant guidance actuation is also required. Thus, the claim that the guidance actuation is directly proportional to the number of burns is not strictly correct: the total propellant required for the guidance system is simply dependent on the total duration of the deorbit mission. As higher thrust levels reduce the periapsis to the targeted periapsis in fewer orbits (as seen in Figure 7.8), the mission duration is shorter and thus less propellant is required for the guidance system.

The same analysis can be performed on the control system: the angular errors between the axes of the chaser body-fixed frame G_C and the target Hill frame H were plotted for the same duration, along with the maximum absolute control moments, for each thrust level. The angular errors were derived from the q_4 parameter according to Equation (4.6), and express the total rotation of the G_C frame with respect to the H frame. The results of this are shown in Figure 8.9 for the LQR system and in Figure 8.10 for the SMC system. Figures 8.9 and 8.10 also show the same general system behavior. As the main engine burn is initiated at $t = 0$ s, the tension in tether induces torques on chaser, causing the chaser to oscillate around its center of mass. It can be seen, however, that the SMC system causes smaller oscillations in the chaser position than the LQR system, at the cost of more control actuation during burns: the LQR system never encounters the 20 Nm saturation limit for any of the thrust levels, while the SMC system does for both 1000 N and 2000 N. Once the burn has been terminated around $t = 1000$ s, the SMC system requires less control actuation than the LQR system, and the attitude errors of both the SMC system and the LQR system are in the order of 0.2°.

From Figures 8.9 and 8.10, it is possible to draw the conclusion that the number of burns more strongly

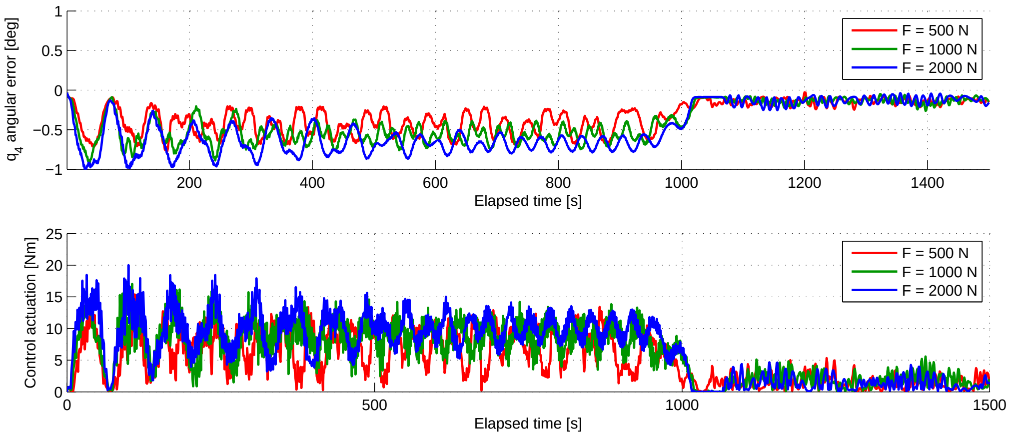

Figure 8.9: Maximum control moment and angular error of the chaser for the N_{nom} tether model and the LQR system.

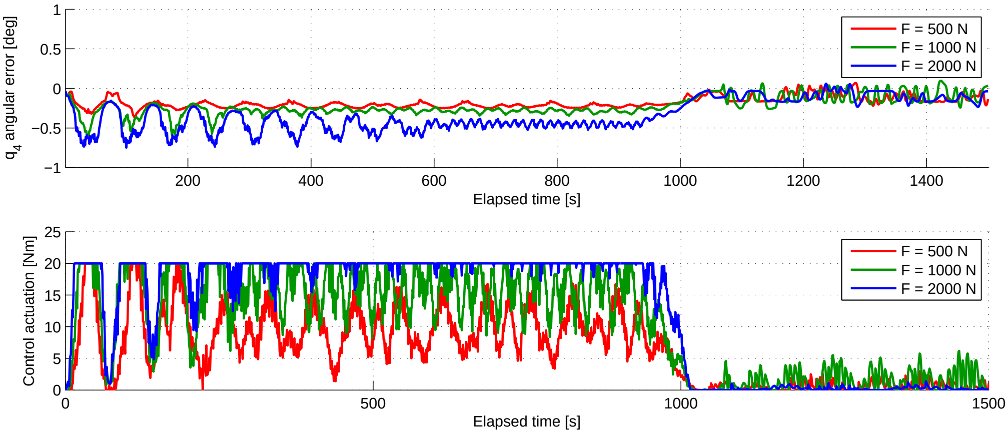

Figure 8.10: Maximum control moment and angular error of the chaser for the N_{nom} tether model and the SMC system.

influences the control system than it does the guidance system: the commanded control moments are significantly higher during main engine burns. However, this does not mean that the total mission duration is not significant, as attitude control is still required after engine burns. Furthermore, coasting phases last significantly longer than burn phases, resulting in a roughly equal contribution of the burn and coasting phases to the control system propellant consumption.

Still, the end result is the same as for the guidance system: higher thrust levels and thus shorter mission times tend to require less total control actuation. It must be noted, however, that the total control propellant is generally much less than the total guidance propellant for a given system configuration. Thus, while the relative improvements in control propellant consumption might be high with increasing thrust levels, the absolute differences are not as large. Therefore, the guidance system performance is considered to be the driver for minimizing propellant mass.

LQR SYSTEM PROPELLANT CONSUMPTION

While the trends described in the preceding analysis generally hold for the results of the LQR system, a number of deviations from this norm can be identified. First, is clear that model S_{HT}, corresponding to a short tether with high tension, requires significantly more guidance propellant at all thrust levels than the other two short tether models. Second, all three long tether models show anomalous behavior: at 500 N, the L_{nom} and L_{HT} models consume significantly more propellant that the L_{LD} model, while for 1000 N and 2000 N the L_{nom} and particularly the L_{LD} models consume significantly more propellant than the L_{HT} model.

First investigating the case of the S_{HT} model, this phenomenon could be fairly easily explained: referring back to Section 7.2.2, the constant δ_L, which determines nominally how far the tether is extended during the coasting phase, was set to a value of 1 m. While with most tether models this entails that the tension in the tether will be less than 40 N, in the case of mode S_{HT} the tension will be 100 N under this extension. Not only is this a factor 2.5 larger than the next largest value of the nominal tether tension during the coasting phase, it is also significantly higher than the saturation limit of the guidance thrusters of 50 N [3]. Thus, the guidance system will continuously attempt to drive the error to zero, but will also constantly be prevented from doing so stably by the tether tension. This can be seen in Figure 8.11, and this behavior is also generally mirrored by the N_{HT} models.

It can be seen in Figure 8.11 that after the coasting hold point is established around $t = 1000$ s, the guidance system often encounters the 50 N saturation limit in the negative y_H-direction, indicating it is constantly pulling at the tether. Furthermore, during this period, the error in the y_H direction is always smaller than -1 m, indicating that the chaser is always closer to the target than it should be. This confirms the hypothesis presented previously.

Second, the case of the long tether models was investigated. The behavior of the long tether models was shown to be very dependent on the thrust level: at a thrust level of 500 N, the L_{nom} and L_{HT} models require more guidance actuation than the L_{LD} model, while at the higher thrust levels, the L_{nom} model requires more propellant than L_{HT}, and the L_{LD} model requires even more than the L_{nom} model. Clearly, this behavior requires some investigation: to this end, the position errors and guidance actuation for each thrust level are

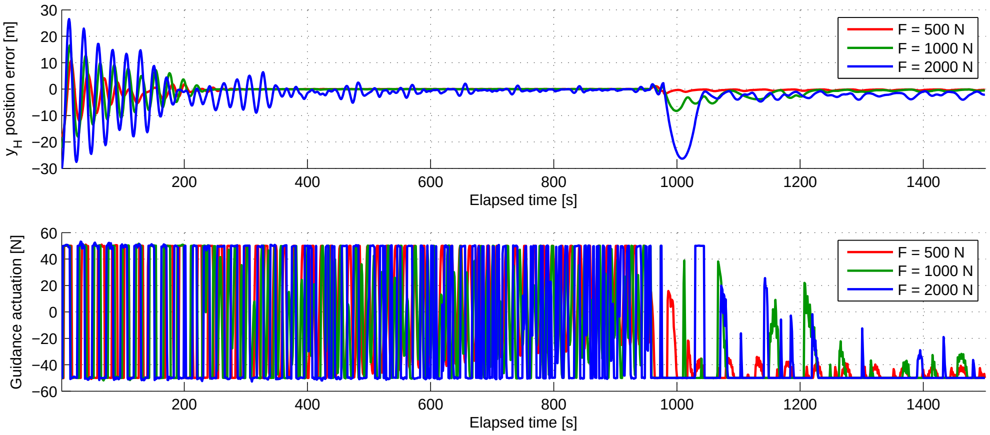

Figure 8.11: Guidance force and position error of the chaser along the y_H axis for the S_{HT} tether model with the LQR system.

shown in Figures 8.12 through 8.14.

A number of different types of behavior can be seen in Figures 8.12 through 8.14. First, it is readily apparent that with the L_{HT} model, the chaser is able to stabilize its motion at the burn hold point much more quickly, which can be seen from the fast damping of the oscillations up to $t = 500$ s. For the L_{nom} and L_{LD} models, much more actuation is required from the guidance system to stabilize the chaser at the burn hold point: in the case of the higher thrust levels, it is not even possible for the guidance system to stabilize itself at the burn hold point before the main engines are throttled down. This is indicated by the significant oscillations around the nominal point at $t = 1000$ s.

Furthermore, after the main engines are cut after roughly $t = 1100$, large errors are still seen, indicating that the guidance system has difficulty establishing the coasting hold point. This is particularly apparent when considering thrust levels of 2000 N: the position errors after the main engines are shut down reach magnitudes of 1400 m for the L_{LD} model before the system is able to recover itself. This places the chaser far in front of the target.

These large errors are due to the fact that the long tethers with a nominal value for E_{mat} end up with a very low value for k: thus, a significant relative velocity will build up before the tether tension reaches a comparable magnitude to the thrust, especially for a thrust of 2000 N. Another effect of these significant relative velocities during operations of the L_{nom} and L_{LD} models can be seen when examining the out-of-line position errors of the chaser. This is shown in Figure 8.15, which the behavior of the L_{LD} closely mirrors. It can be seen that for the highest thrust level, the “radial” position errors become significant. Returning to the CW equations (Equation (5.12)), it can be seen that the acceleration in the x_H direction is coupled to the velocity in y_H direction. Thus, if the relative velocities are allowed to build up too much, which is clearly the case for the L_{nom} and L_{LD} models, the acceleration along the x_H axis is too high for the guidance system to restore, and significant errors will build up.

A further effect of these large radial position errors is that the tether is not closely aligned with the y_H axis. Therefore, the tether tension force will have a significant component in the x_H direction, inducing a large torque about the chaser y_G axis. The effect of this on the chaser attitude error is shown in Figure 8.16.
It can be seen in Figure 8.16 that between $t = 100$ s and $t = 500$ s, the chaser is unable to maintain its pointing requirement when subject to 2000 N of thrust: the maximum angular error is 7° in magnitude, far more than the permitted 1°. This is due to the large torques induced by the tether, which are too large for the control system to correct. It can be seen that the control moment has reached its saturation limit during this period. Furthermore, it can be seen that the large attitude errors occur in the same time frame in which the large errors along the x_H axis also occur.

The fact that the L_{LD} model requires even more guidance actuation than the $Lnom$ model for these higher thrust levels can be explained that since the L_{LD} model has a much lower damping coefficient, the tether motions will be more violent and will exert larger forces on the chaser. However, this explanation does not explain the behavior observed for 500 N of thrust, as at this thrust level the L_{LD} model actually requires the least amount of guidance actuation. Additionally, it can be seen that the largest difference in guidance actuation between L_{nom} and L_{LD} occurs after the burn has been terminated. These anomalous results will be

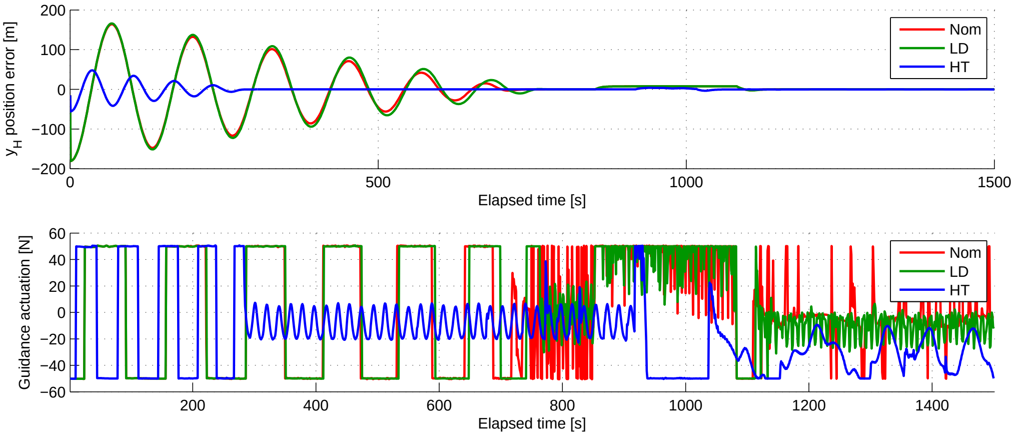

Figure 8.12: Guidance force and position error of the chaser along the y_H axis for the long tether models at 500 N thrust with the LQR system.

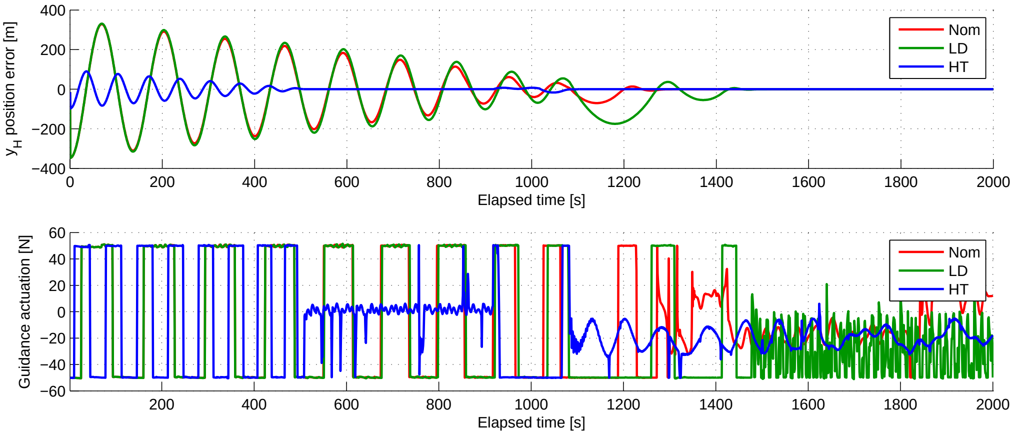

Figure 8.13: Guidance force and position error of the chaser along the y_H axis for the long tether models at 1000 N thrust with the LQR system.

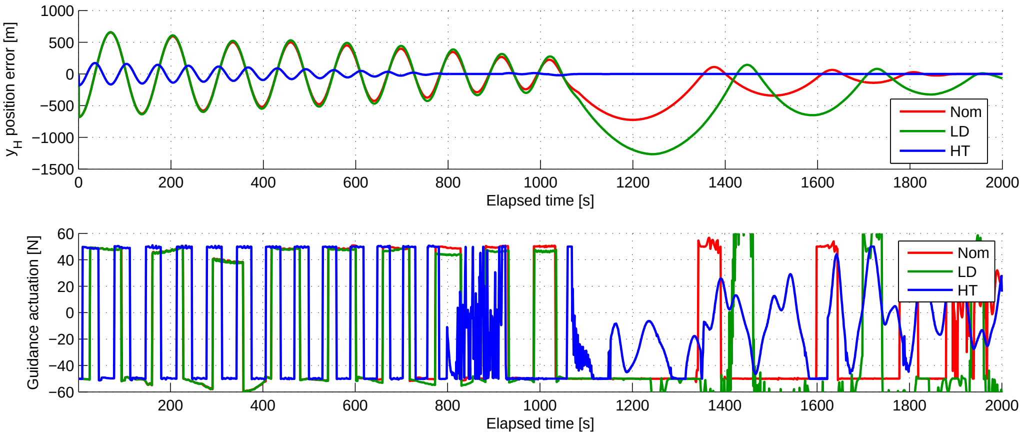

Figure 8.14: Guidance force and position error of the chaser along the y_H axis for the long tether models at 2000 N thrust with the LQR system.

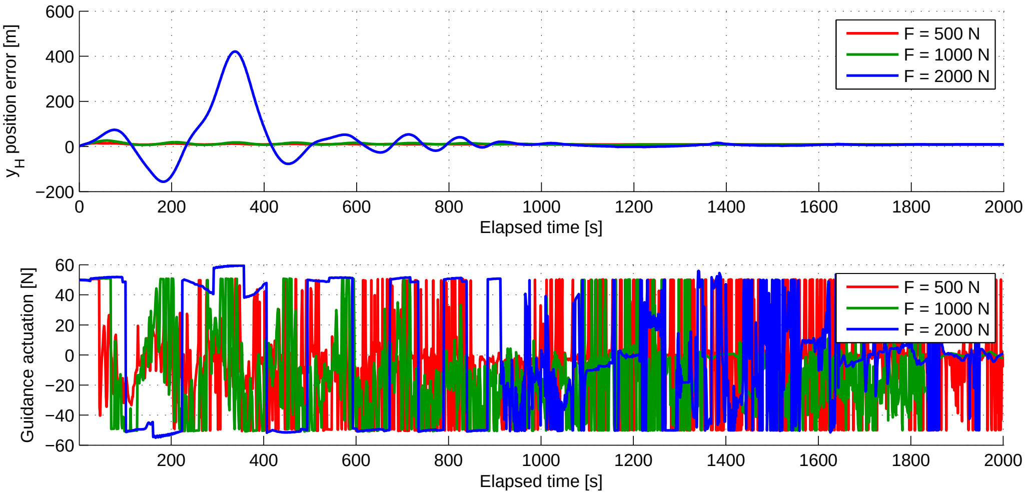

Figure 8.15: Guidance force and position error of the chaser along the x_H axis for the L_{nom} model with the LQR system.

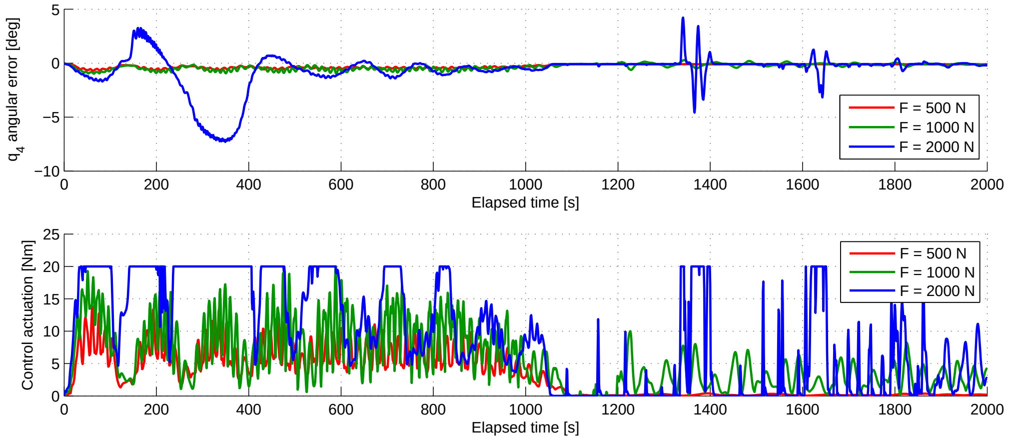

Figure 8.16: Maximum control moment and angular error of the chaser for the L_{nom} tether model and the LQR system.

further investigated in Sections 8.2.2 and 8.2.3.

SMC SYSTEM PROPELLANT CONSUMPTION

When considering the results for the SMC system in Table 8.6, a number of exceptional results can also be noted: first, the S_{LD} and S_{HT} models, corresponding to a short tether with low damping or high tension, respectively, deviate significantly from this trend for thrust levels of 500 N and 1000 N. Specifically, the S_{LD} model requires vastly more guidance propellant than expected, and the S_{HT} model requires significantly less guidance propellant than expected. Second, to a lesser degree, the N_{HT} model and the L_{nom}, both at 500 N, also require significantly less propellant than expected from the trend.

First, the case of the very different results in the short tether models is investigated. The position errors along the y_H axis are shown for all three short tether models at a thrust level of 500 N in Figure 8.17.
In Figure 8.17, it can be seen that all models require a similar amount of time and guidance actuation to establish as stable equilibrium at the guidance hold point. However, in the coasting phase, the propellant consumption for the S_{nom} and S_{LD} models is significantly larger than for the S_{HT} model. However, the expected result is that the S_{HT} model would require more actuation, due to the higher stiffness of the tether. This result will be further investigated in Section 8.2.2.

Then, the significantly lower guidance propellant consumption of the N_{HT} model at 500 N compared to the other two nominal-length models, is examined. The position errors along the y_H axis for all three models are shown in Figure 8.18.

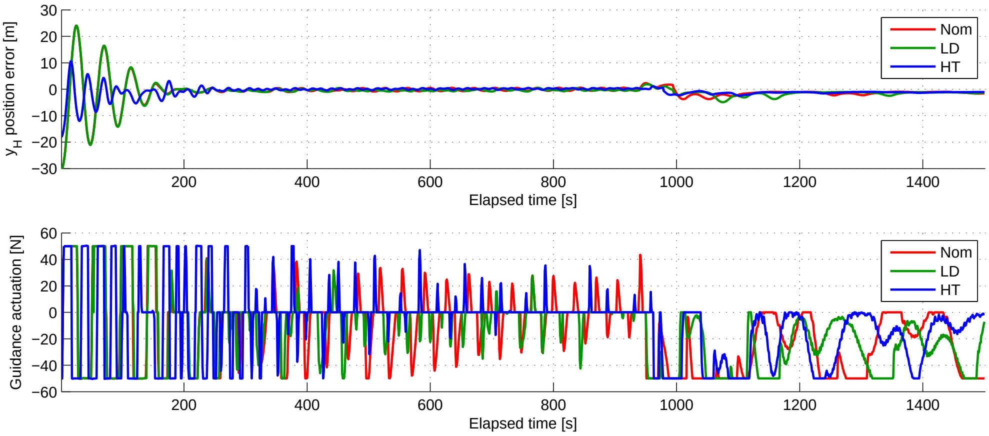

Figure 8.17: Guidance force and position error of the chaser along the y_H axis for the short tether models at 500 N thrust with the SMC system.

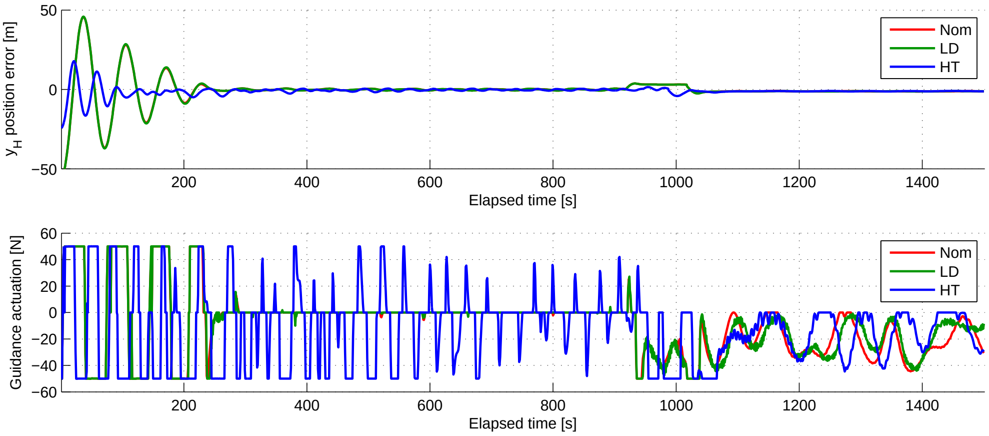

Figure 8.18: Guidance force and position error of the chaser along the y_H axis for the nominal-length tether models at 500 N thrust with the SMC system.

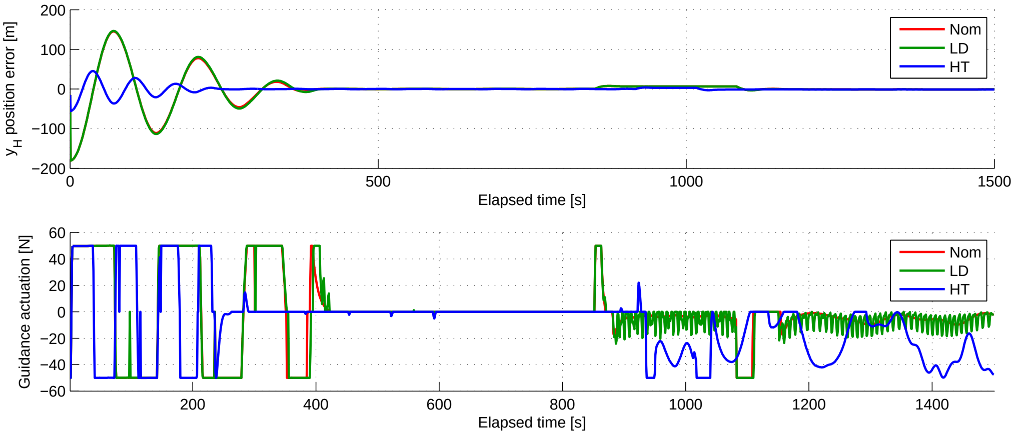

Figure 8.19: Guidance force and position error of the chaser along the y_H axis for the long tether models at 500 N thrust with the SMC system.

In contrast to the results for the short tethers at this thrust level, it is clear that with the N_{HT} model the guidance system is able to stabilize the chaser at the burn hold point in a shorter time than with the other two nominal-length models. Additionally, less guidance actuation is required after the coasting hold point has been established with the N_{HT} model. As with the short tether models, the cause of this will be further investigated in Section 8.2.2.

Finally, it is possible to examine the long tether models at 500 N thrust. Again, the position errors and control accelerations along the y_H axis can be plotted to gain insight towards the tether behavior. This is done in Figure 8.19.

It can be seen that as with the nominal-length tether models, a stable equilibrium at the burn hold point can be established with less actuation from the guidance system for the L_{HT} model than for the other two long models. However, it is apparent that the L_{HT} model requires more guidance actuation after the coasting hold point has been established than the other two models. Furthermore, it can be seen that the L_{LD} model also requires more guidance actuation after the coasting hold point has been established. This is in agreement with the expectation that a low damping in the tether will result in larger amplitudes of the tether model, and thus larger forces on the chaser. These phenomena will also be further treated in Section 8.2.2.

COMPARISON OF GC SYSTEMS

From the preceding analyses, a number of important differences can be seen between the performance of the LQR-based and SMC-based guidance systems. First of all, it is readily apparent that the SMC system requires significantly less guidance actuation than the LQR system to accomplish the mission. This can be quantified quantified by dividing the required propellant mass required for each combination of the SMC system by the corresponding value of the LQR system, the results of which are shown in Table 8.7. Note that the main engine propellant was excluded, as all simulations consume the same amount.

As mentioned, the SMC guidance system consistently requires less propellant to achieve mission success. In the case of the lower thrust levels, the SMC guidance system is much better at dealing with the high-tension tether models in particular, in some cases consuming less than 10% of the propellant required by the LQR system. While these extreme improvements are quite exceptional, the average propellant consumption for the SMC guidance system is 41.4% of that of the LQR guidance system: thus, this still represents a major reduction in required propellant.

However, this trend is not visible in the comparison of the control systems. While the SMC control system is capable of improving the propellant consumption over the LQR control system, with a best value of 77.9%, the average consumption across all thrust levels is 124.2% for the SMC system.

This result does not necessarily indicate that the SMC control system performs worse than the LQR control system: to explain this, Figures 8.9 and 8.10 can be examined again. It is clear that the SMC system keeps the angular error smaller than the LQR system at all times. Referring back to Section 7.6, the control parameters for the SMC were chosen based on an order-of-magnitude analysis, during which all results violating the 1° constraint were discarded. Thus, it is probable that the SMC control parameters could be “loosened”, as the error is well within the constraint, which would reduce the required propellant. However, as mentioned previously, the control parameters for the SMC system were obtained through an order-of-magnitude analysis, and therefore the finer tuning of these was left out of the scope of this research.

As mentioned, though, the guidance system was identified as a far greater driver for the amount of propellant required, and this is reflected in the last column of Table 8.7. Despite the SMC control system generally requiring more propellant than the LQR control system, this is more than compensated by the guidance system. On average, the total required propellant for the SMC system is 89.7% of that required by the LQR system. This value includes the main engine propellant, as the main engines and GC thrusters use the same type of propellant. Thus, this represents the total improvement to the propellant requirement of the chaser as a whole. In terms of the propellant required for the GC system alone, the SMC system uses only 51.8% of the propellant required by the LQR.

Therefore, it appears that the application of a (relatively simple) SMC algorithm can greatly improve the performance of the developed GC system with respect to an LQR. However, the results presented in this section show some anomalous results, the cause of which warranted some additional investigation. Specifically, at 500 N and the LQR system, the L_{LD} model shows unexpected behavior. Furthermore, for the SMC system, the N_{HT} and S_{LD} models will be investigated, both at 500 N thrust as well. Thus, two additional important topics in the dynamics of the TSDS will be discussed in the subsequent sections: oscillations in the tether and rotation of the target.

Table 8.7: Relative propellant consumption of the SMC system compared to the LQR system.

Thrust level [N]	**Model number**	**Guidance propellant fraction**	**Control propellant fraction**	**Total propellant fraction**
500	N_{nom}	0.503	1.130	0.899
	N_{LD}	0.454	0.941	0.872
	N_{HT}	0.184	0.917	0.788
500	S_{nom}	0.250	0.954	0.825
	S_{LD}	0.595	0.994	0.903
	S_{HT}	0.090	1.007	0.688
500	L_{nom}	0.215	1.436	0.814
	L_{LD}	0.379	1.316	0.881
	L_{HT}	0.314	0.949	0.801
1000	N_{nom}	0.496	1.408	0.945
	N_{LD}	0.593	1.516	0.957
	N_{HT}	0.337	0.963	0.891
1000	S_{nom}	0.397	1.181	0.921
	S_{LD}	0.559	1.170	0.942
	S_{HT}	0.181	1.172	0.846
1000	L_{nom}	0.287	1.170	0.863
	L_{LD}	0.247	0.779	0.814
	L_{HT}	0.357	1.360	0.910
2000	N_{nom}	0.539	1.768	0.978
	N_{LD}	0.571	1.805	0.978
	N_{HT}	0.591	1.518	0.978
2000	S_{nom}	0.613	1.754	0.985
	S_{LD}	0.659	1.557	0.986
	S_{HT}	0.512	1.343	0.965
2000	L_{nom}	0.484	1.162	0.950
	L_{LD}	0.333	0.440	0.872
	L_{HT}	0.448	1.830	0.960

8.2.2. TETHER OSCILLATION

It is possible to gain more insight towards the intricacies of the dynamics of the TSDS by observing the oscillations in the tether itself. This will allow the physical causes of the anomalies noted in the previous section to be examined, and will also highlight strengths and weaknesses of certain tether parameter models.

GENERAL TETHER BEHAVIOR

First, the behavior of the nominal model of each tether length will be examined: thus, general trends in the oscillatory behavior of the tether parameter models can be identified. Note that these deflections were investigated for a period of 2000 s after the start of the mission, to allow both the behavior during burns and during coasting phases to be investigated. Furthermore, both GC system types will be included, to identify possible differences between the two. The results for the N_{nom} model are shown in Figures 8.20 and 8.21, the results for the S_{nom} model are shown in Figures 8.22 and 8.23, and the results for the L_{nom} model are shown in Figures 8.24 and 8.25.

From Figures 8.20 through 8.25, a number of general trends can be seen. First, it is apparent that during burns the amplitude of the oscillations in the tether increases with increasing thrust. This is particularly apparent with the N_{nom} and L_{nom} models, although the L_{nom} model also displays the large amplitudes at 2000 N thrust corresponding to the position errors along the x_H axis as a result of the large relative velocities. For the S_{nom} model, the thrust seems to have less influence on the amplitudes.

During coasting phases, however, there is no clear relation between the thrust level used during the burn and the chaser amplitudes. The unpredictability hereof most likely stems from the fact that while critically damped behavior is approximated when throttling down (see Section 7.2), it is approximated with a linear function. Thus, each model is not behaving in exactly the same harmonic way, and thus discrepancies will

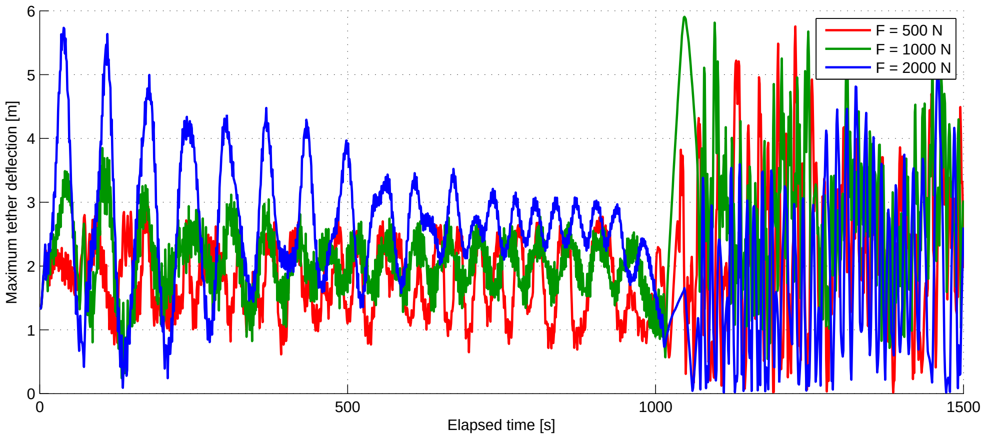

Figure 8.20: Maximum tether deflection of the N_{nom} tether model with the LQR system.

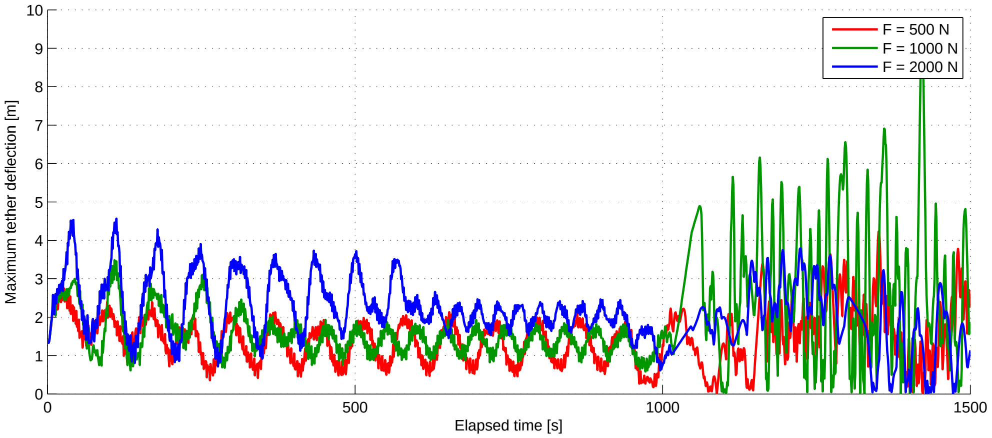

Figure 8.21: Maximum tether deflection of the N_{nom} tether model with the SMC system.

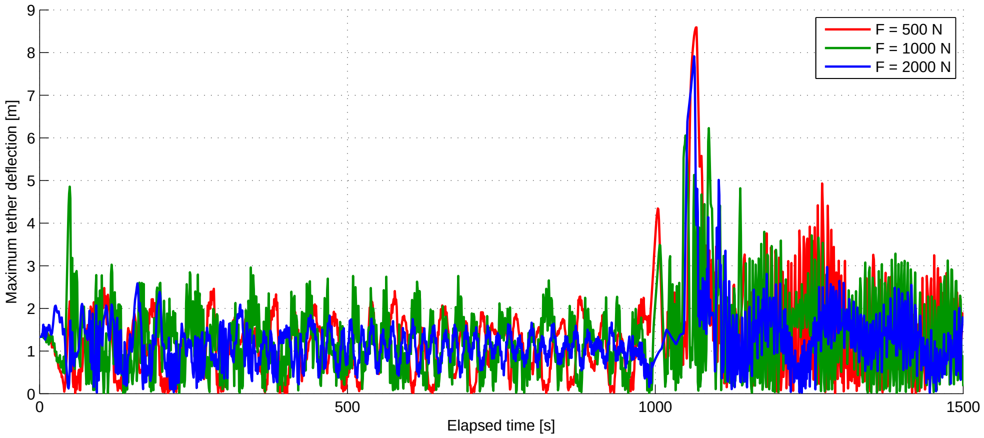

Figure 8.22: Maximum tether deflection of the S_{nom} tether model with the LQR system.

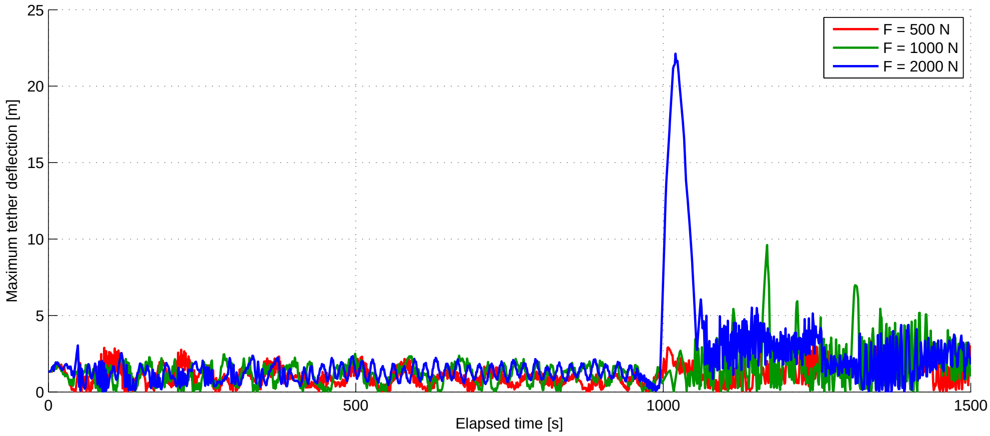

Figure 8.23: Maximum tether deflection of the S_{nom} tether model with the SMC system.

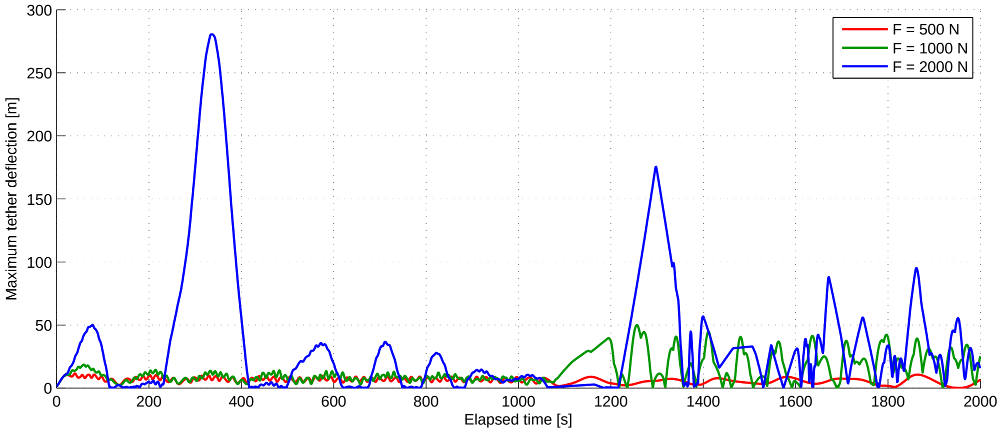

Figure 8.24: Maximum tether deflection of the L_{nom} tether model with the LQR system.

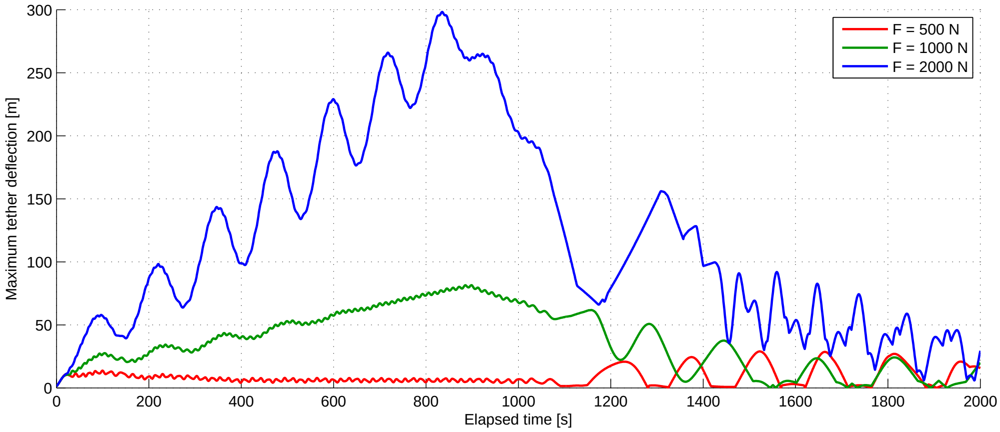

Figure 8.25: Maximum tether deflection of the L_{nom} tether model with the SMC system.

occur when establishing the coasting hold point. However, it can be seen that the amplitude of the oscillations is highly dependent on the tether length: shorter tethers seem to have smaller oscillation amplitudes than longer tethers.

Furthermore, it can be seen that as a general rule, there is not much difference between the LQR and SMC systems when it comes to tether oscillations. The exception to this are the long tether models with 1000 N and 2000 N, in which it is apparent that the SMC system is not as suited as the LQR to restoring the large out-of-line errors caused by the aforementioned large relative velocities.

In any case, it is clear that the oscillatory behavior of the tether after establishing the coasting hold point is very sensitive to the technique used to restore the chaser from the burn hold point to the coasting hold point. Thus, tether motion during coasting will tend to be difficult to predict. Therefore, the oscillations of the anomalous results presented in Section 8.2.1 will be examined next.

SPECIFIC CASE ANALYSES

The first case which was examined concerned the long tether models. Reviewing from Section 8.2.1, it was found that with a LQR system the L_{LD} model required significantly less propellant than the other two models at 500 N and significantly more propellant at higher thrust levels. The oscillatory behavior of the L_{LD} model with the LQR and at all thrust levels is shown in Figure 8.26.

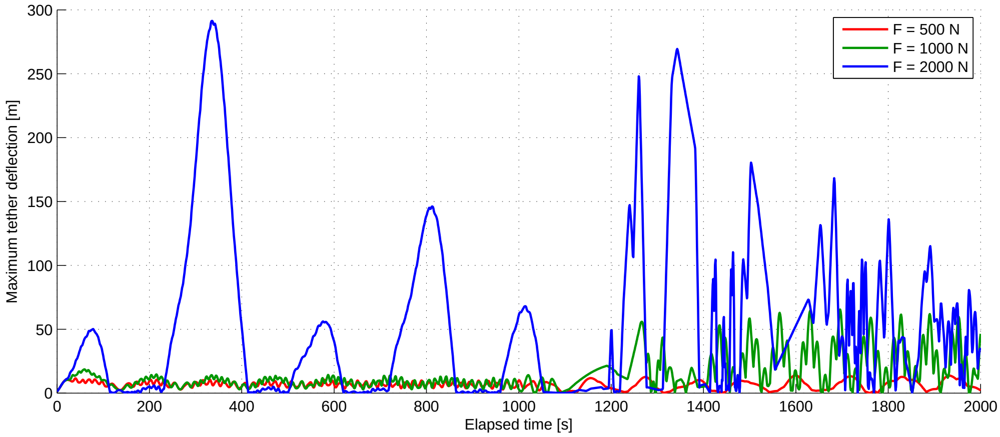

Figure 8.26: Maximum tether deflection of the L_{LD} tether model with the LQR system.

Comparing Figure 8.24 with Figure 8.26, it is clear that the oscillation amplitudes of the L_{LD} are higher than the L_{nom} model, which is in agreement with the expected behavior: with lower damping in the tether, there will be less energy dissipated in the tether and thus the nodes will have more energy. Thus, more actuation by the chaser will be required to stabilize the system, as there is more energy present in the system.

However, this still does not explain the lower propellant consumption of the L_{LD} model with respect to L_{nom} at 500 N, as this result is opposite to the expected result. Therefore, this discrepancy must be caused by some other factor, a prime suspect for which is the rotation of the target. This will be further investigated in Section 8.2.3.

The second case examined was the large variation in propellant consumption for the short tether models at 500 N of thrust using the SMC system: the S_{HT} model consumed significantly less than expected, while the S_{LD} model consumed significantly more than expected. This behavior was also observed in these models at 1000 N thrust. The corresponding oscillation amplitudes at 500 N thrust are shown in Figure 8.27.

Based on the data in Figure 8.27, it can be concluded that the out-of-line deflections are not the cause of the increased propellant consumption of the S_{LD} model: the out-of-line deflections are, in fact, highest for the S_{nom} model and lowest for the S_{HT} model. The low deflections observed for the S_{HT} model, however, are most likely the cause for the reduced propellant requirement for this model.

While the out-of-line deflections are concluded not to be the cause of the large propellant consumption by the S_{LD} model, it is also possible to investigate the in-line oscillations. These oscillations can be visualized using the in-line velocities of the tether nodes themselves, which nominally correspond the velocities of the nodes along the y_H axis. Therefore, the maximum node velocities of the short tether models at 500 N thrust are shown in Figure 8.28.

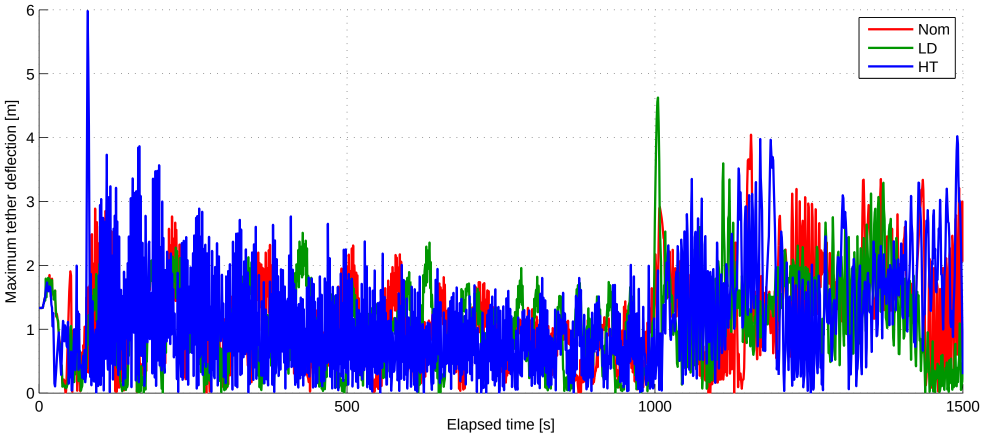

Figure 8.27: Maximum tether deflection of the short tether models at 500 N thrust with the SMC system.

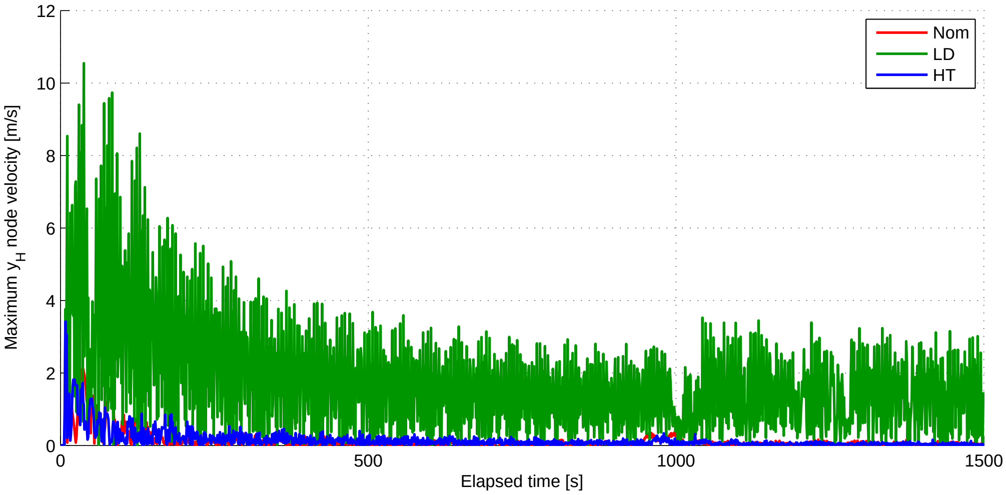

Figure 8.28: Maximum y_H node velocity of the short tether models at 500 N thrust with the SMC system.

It can be clearly seen in Figure 8.28 that the in-line oscillations for the S_{LD} model are far more severe than for the other two models. Thus, the chaser will not only be correcting for out-of-line disturbances, but will have to cope with large in-line disturbances due to the high tether node velocities. This explains the significant increase in guidance propellant requirement for the S_{LD} model.

Third, and finally, the nominal-length models will be compared at 500 N of thrust: in this case, the N_{HT} model requires a factor two less guidance propellant than the other two models. It has been established that the propellant consumption is less both during the burns and during the coasting phases. The out-of-line tether deflections for these models are shown in Figure 8.29.

It can be seen in Figure 8.29 that while the oscillation amplitudes are generally lower for the N_{HT} model, the results are not significantly different. Thus, it is likely that another factor is influencing the good performance of this model: again, target rotation is a suspected cause, and will be investigated in Section 8.2.3.

8.2.3. TARGET ROTATION

A final important aspect of the dynamics of the TSDS is rotation of the target. The target is completely inert, and thus any moment imparted on it will cause it to spin. This spinning motion can cause higher propellant consumption in the best case, and catastrophic failure of the mission in the worst, primarily due to the danger of the tether wrapping around the target and severing itself or appendages of the target. While this effect is not modeled in the simulation, it is clear that little rotation in the target is a desirable feature.

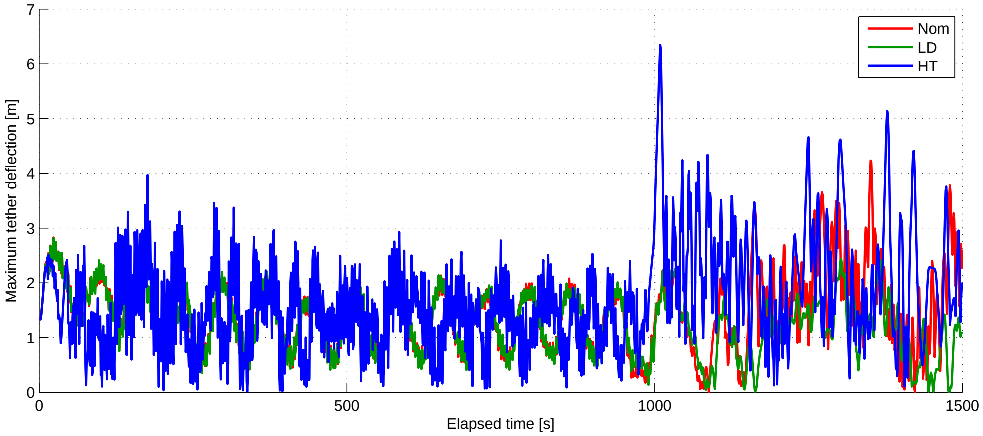

Figure 8.29: Maximum tether deflection of the nominal-length tether models at 500 N thrust with the SMC system.

To approximate the total rotation of the target over the course of the mission lifetime, it is possible to integrate the rotational rates of the target about its body axes. This allows the potential hazards relating to tether wrapping to be identified based on thrust level and tether model. As the mass moment of inertia of the target is smallest around the target body-fixed z-axis, it is expected that the largest rotations will occur around this axis, and thus this value is used as an indication for the target rotation.

GENERAL TARGET ROTATION

This analysis is first performed over the entire mission duration for each thrust level, using the nominal tether models for each length. This gives an indication on the influence of thrust level, which translates to mission duration, on total rotation of the target. Again, this is done for each GC system. The results for the LQR system at 500 N, 1000 N, and 2000 N thrust are shown in Figures 8.30 through 8.32, with those for the SMC shown in Figures 8.33 through 8.35.

It can be seen from Figures 8.30 through 8.35 that target rotation is a significant problem, irrespective of thrust level, tether length, or controller type. In most cases, target rotation exceeds several complete revolutions over the course of the mission, as the total rotation angles are often much larger than 2π. This poses a major threat to the integrity of the tether and thus the safety of the ADR mission.

To assess the ability of each control system to control target rotation, the total rotation of the target about each axis was determined for every simulation scenario. Again, this was done by integrating the rotational rates of the target, only this time about each body axis. The maximum value of these total rotation angles for each simulation scenario is shown in Table 8.8. Note that the values presented are in radians: thus, a value of larger than $2\pi \approx 6.28$ indicates that the target has made one full revolution.

Table 8.8: Maximum target rotation of the LQR and SMC systems.

Tether model	**LQR System**			**SMC System**		
	500 N	1000 N	2000 N	500 N	1000 N	2000 N
N_{nom}	191.2 rad	77.1 rad	4.3 rad	98.5 rad	49.8 rad	2.1 rad
N_{LD}	807.9 rad	26.0 rad	24.6 rad	105.0 rad	48.1 rad	2.7 rad
N_{HT}	112.6 rad	47.3 rad	38.6 rad	98.8 rad	72.5 rad	19.3 rad
S_{nom}	144.6 rad	90.7 rad	1.8 rad	170.9 rad	88.8 rad	13.2 rad
S_{LD}	65.5 rad	324.7 rad	3.5 rad	161.1 rad	174.2 rad	13.8 rad
S_{HT}	32.6 rad	9.7 rad	78.9 rad	40.8 rad	69.6 rad	53.0 rad
L_{nom}	111.7 rad	34.5 rad	10.2 rad	48.1 rad	5.3 rad	11.4 rad
L_{LD}	57.3 rad	179.3 rad	228.7 rad	292.8 rad	9.2 rad	3.9 rad
L_{HT}	10.0 rad	21.7 rad	13.0 rad	150.7 rad	32.0 rad	2.3 rad

It can be clearly seen in Table 8.8, as well as in all figures presented in this section, that the target rotational behavior is highly chaotic. Nonetheless, it is possible to identify that, generally, higher thrust levels induce

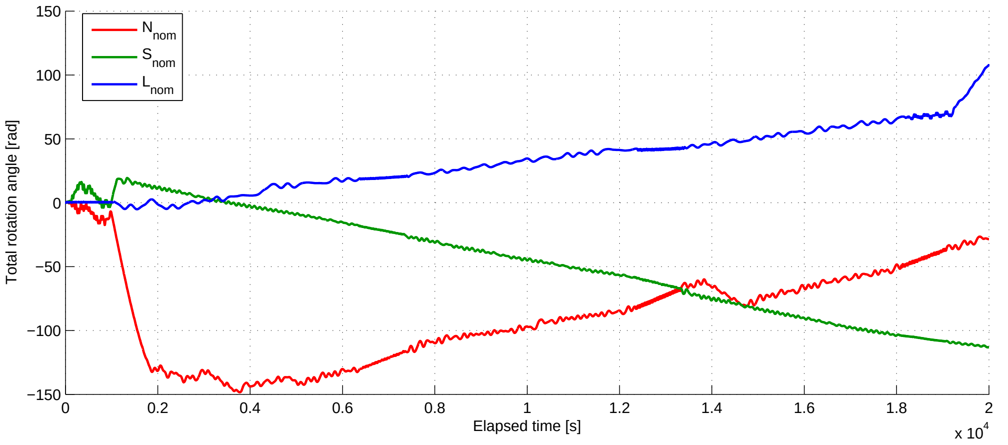

Figure 8.30: Target rotation of the three nominal tether models at 500 N thrust with LQR system.

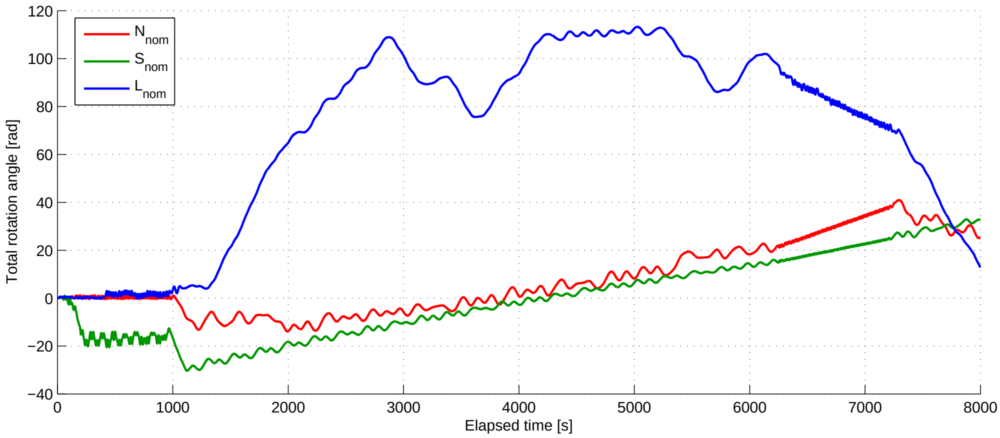

Figure 8.31: Target rotation of the three nominal tether models at 1000 N thrust with LQR system.

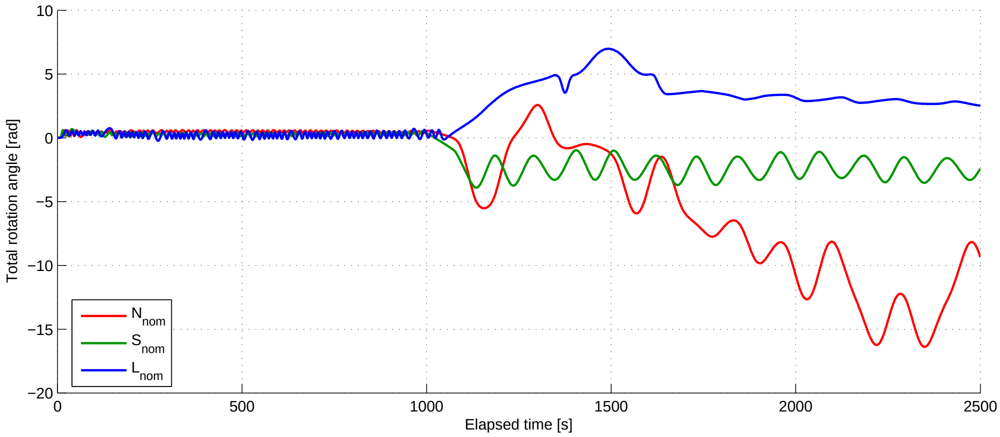

Figure 8.32: Target rotation of the three nominal tether models at 2000 N thrust with LQR system.

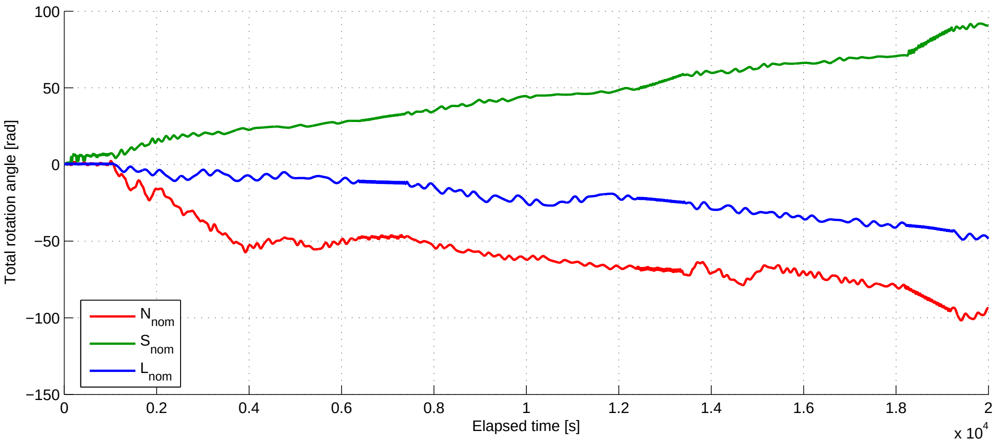

Figure 8.33: Target rotation of the three nominal tether models at 500 N thrust with SMC system.

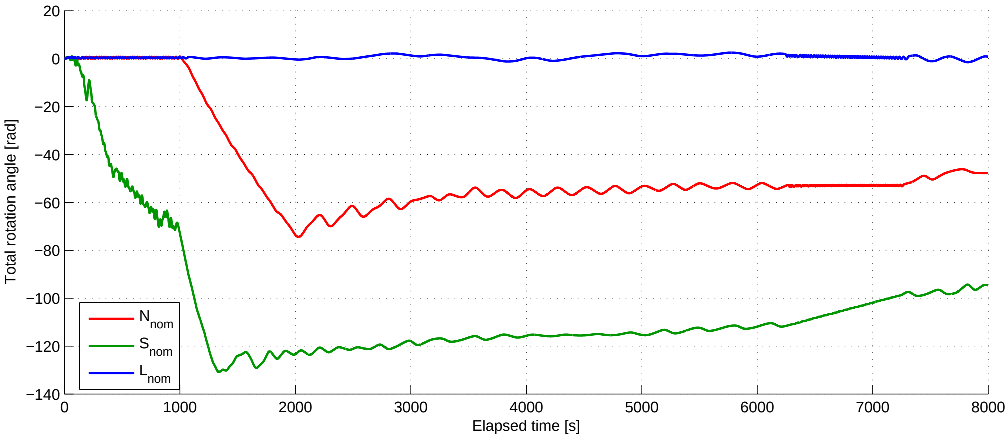

Figure 8.34: Target rotation of the three nominal tether models at 1000 N thrust with SMC system.

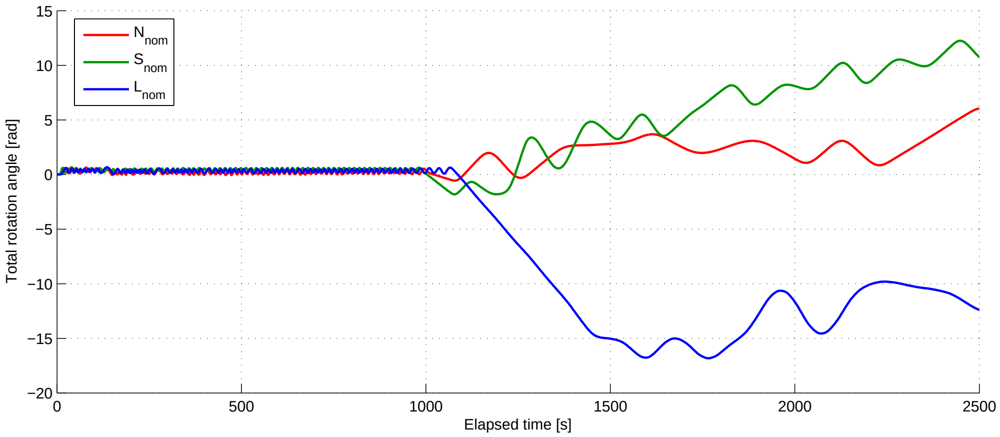

Figure 8.35: Target rotation of the three nominal tether models at 2000 N thrust with SMC system.

less total rotation of the target. Specifically, the results showing a total rotation of less that 2π are promising, as this indicates the target never completed a full revolution and thus no danger of tether wrapping occurred. Referring back to Tables 8.5 and 8.6, it can be seen that these higher thrust levels also generally require the minimum amount of propellant.

SPECIFIC CASE ANALYSIS

For several cases from the previous sections, it was suggested that target rotation could be a driver for the unexpectedly high or low propellant requirements. Specifically, the long tether models using the LQR system at 500 N thrust showed anomalies: the L_{LD} model showed unexpectedly low propellant consumption in this case. Also, the N_{HT} model using the SMC system at 500 N thrust showed low propellant usage compared to the other two nominal-length models. First, the long tether models using the LQR system at 500 N were examined. The target rotation, again around the target z_G axis, is shown in Figure 8.36.

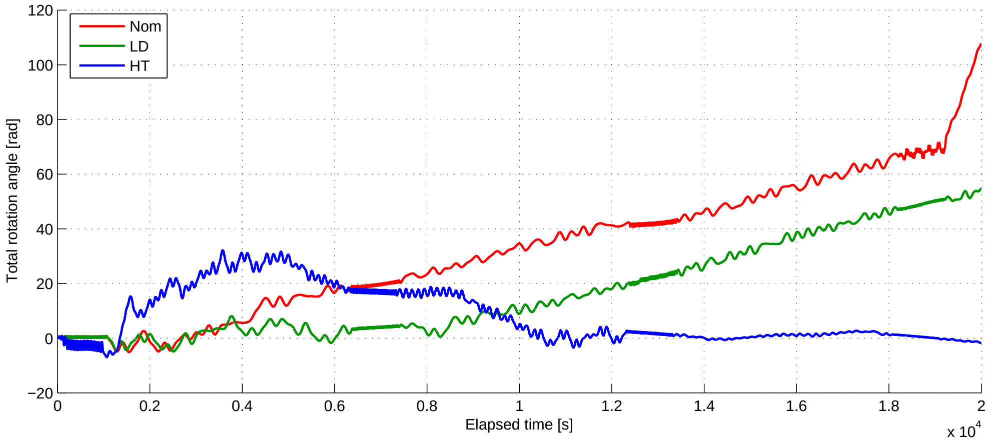

Figure 8.36: Target rotation of the three long tether models at 500 N thrust with LQR system.

It can be seen from Figure 8.36 that the L_{LD} model in this configuration induces less rotation in the target than the L_{nom} model: total rotation for the L_{LD} model is 57.5 rad, compared to the 111.7 rad for the L_{nom} model. This is also reflected in Table 8.8, indicating that the target has indeed rotated most around the z_G-axis. Thus, this could be a possible explanation for the lower propellant usage of the L_{LD} model: if the target rotates less, the tether is subjected to less tensile forces, as the TCP of the target will generally be closer to the chaser. Thus, the GC system has less disturbances to compensate for.

Second, the case of the nominal-length models at 500 N thrust using the SMC system is investigated. In this situation, the N_{HT} model required significantly less propellant than the other two models. As with the previous analyses, the total target rotation about the target z_G axis was determined, the results of which can be seen in Figure 8.37.

From Figure 8.37, it can be seen that the N_{HT} model induces less total rotation in the target than the N_{nom} or N_{LD} models: the total rotation of the N_{HT} model is -60 rad, compared to the -90 rad of the other two models. However, the maximum rotation of the target is not significantly smaller as seen in Table 8.8, indicating that, for the N_{HT} model, maximum rotation does not occur around the z_G-axis. Nonetheless, target rotation can still be identified as a possible reason for the lower propellant requirement.

8.2.4. CONCLUDING REMARKS

From the analyses presented in Sections 8.2.1 through 8.2.3, a number of general conclusions can be drawn regarding the suitability of each tether model, thrust level, and controller type. First considering propellant usage, a general trend that was observed for both controller types and all tether models is that higher thrust levels require less propellant due to the corresponding shorter mission duration. Furthermore, it is also clear that the SMC can offer significant propellant savings, especially when applied to the guidance system.

It was also seen that the long tether models with nominal tension combined with the highest thrust level cause significant relative velocities to build up. This results in large errors along the x_H axis, which can be explained by the coupling of the y_H velocity and x_H position in the CW equations. In the case of long tethers

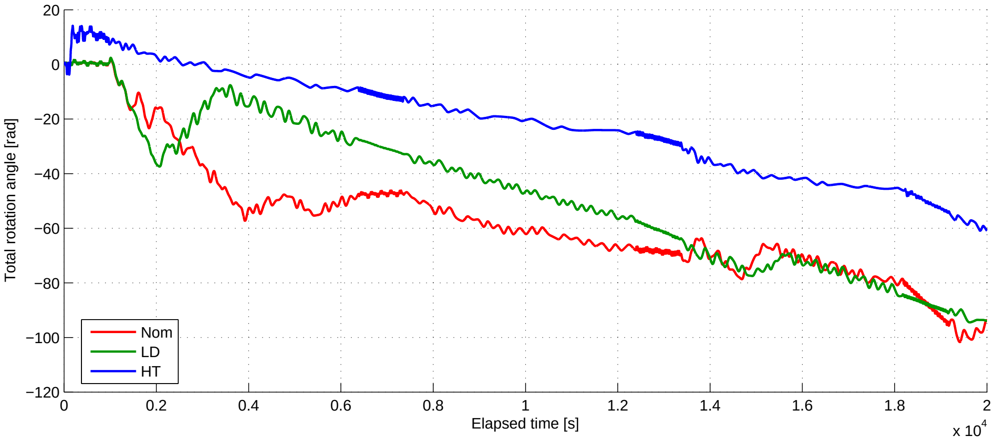

Figure 8.37: Target rotation of the three nominal-length tether models at 500 N thrust with SMC system.

and nominal tension at 2000 N, the resulting accelerations are too large for the guidance thrusters to correct initially. Also, these large x_H offsets subsequently prevent the nominal attitude from being maintained. Therefore, it is suggested that lower thrust levels are generally more suited for the proposed ADR mission, as this reduces both the possibility of large out-of-line error as well as increases the ability of the chaser to restore stable equilibrium at each hold point.

Regarding oscillations in the tether, several general trends could be observed. First of all, higher thrust levels seem to induce larger transverse oscillations in the tether during the burns themselves. Also, tethers with low damping generally exhibit larger oscillations, both in the transverse and particularly in the longitudinal direction. Since more violent oscillations are generally undesirable, it is therefore suggested that tethers with an extremely low damping coefficient be avoided, and that lower thrust levels are more beneficial.

Finally, the problem of rotation of the target was identified. It is abundantly clear that for most simulation scenarios, the target has a general tendency to build up large rotations. This is perhaps the most concerning result of the performed analysis, as large target rotations can cause the tether to wrap around the target as well as produce additional debris. Therefore, this aspect is identified as an important field for future research. Nonetheless, some models were identified showing little target rotation, particularly at higher thrust levels.

The all-round best performer in terms of propellant use and target rotation was found to be the N_{nom} model at 2000 N of thrust and using SMC system: this scenario returns the absolute minimum of all scenarios tested in terms of propellant required, 695.4 kg total, while keeping maximum total target rotation at a near-minimum 2.1 radians. Furthermore, as shown in Figures 8.38 and 8.39, the performance of this scenario with respect to the guidance and control errors is very good: first, the burn hold point is established in a stable manner by $t = 700$ s, well before the main thrust is throttled down at $t = 900$ s. Second, the coasting hold point is established with minimal oscillation, with a maximum error amplitude of less than 20 m. Third, the attitude error remains within the 1° at all times.

8.3. MONTE CARLO ANALYSIS

As mentioned in Section 8.1.3, a Monte Carlo analysis was performed to determine the sensitivity of the terminal point of the simulation to the initial conditions of the chaser. To achieve this, MATLAB's random number generation was used to determine each set of initial conditions. This random number generator was seeded with the number 42, commonly known to be the answer to the ultimate question of life, the universe, and everything [82].

First, a Monte Carlo simulation was performed for all thrust levels and both controller types, using only the N_{nom} tether model. This was done to identify potential differences in precision between the LQR and SMC systems, as well as offering a first insight towards possible trends. Then, this analysis was extended to the S_{nom} and L_{nom} tether models. It was additionally decided to only perform the Monte Carlo analysis for the nominal tether parameters, to reduce the volume of information.

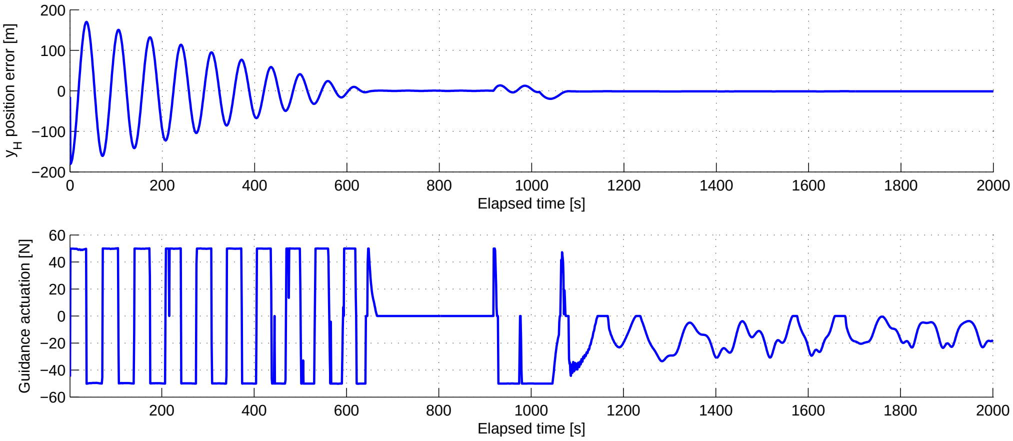

Figure 8.38: Guidance force and position error of the chaser along the y_H axis for the L_{HT} tether model at 2000 N thrust and the SMC system.

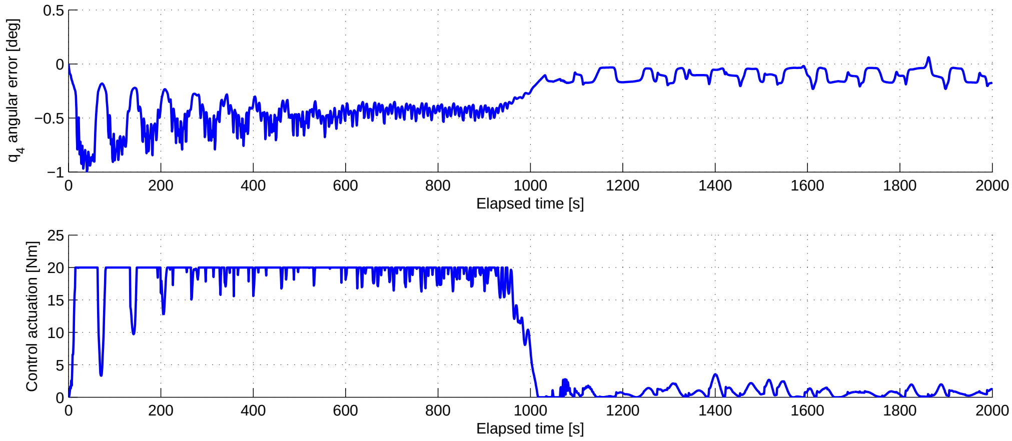

Figure 8.39: Maximum control moment and angular error of the chaser for the L_{HT} tether model at 2000 N thrust and the SMC system.

8.3.1. NOMINAL TETHER MODEL RESULTS

From Section 8.1.3, it can be seen that four distinct subsets of the initial relative state of the chaser were varied, each according to its own set of boundaries: the relative position, the relative velocity, the relative orientation, and the relative angular rates. First, it was decided to randomly vary all parameters simultaneously, as this would allow general trends to be identified.

Therefore, for all three thrust levels and both controller types, 130 simulations are performed while randomly varying all initial conditions. This number was chosen based on the fact that 13 parameters are being varied, which is then increased by an order of magnitude. The results of these simulations are graphically depicted on the sphere of the Earth in Figure 8.40. Note that each line of latitude corresponds to 5° intervals and each line of longitude corresponds to 10° intervals, and that the view is centered on the 180° meridian, as the TSDS is at its descending node at periapsis.

It can be seen in Figure 8.40 that increasing the thrust level causes the precision of the terminal point to increase. This is, again, due to the fact that higher thrust levels result in a shorter mission duration, and thus less disturbances affecting the terminal point can result from, for instance, aerodynamic drag. Furthermore, it can also be seen that the SMC system results in a more precise grouping of the terminal points than the LQR system.

Additionally, it can be seen that the terminal points are spread out primarily in the along-track direction of the orbit. This was expected due to the velocities in LEO being significantly larger than the applied initial disturbances: thus, the impact of the initial disturbances on the direction of travel would be negligible. How-

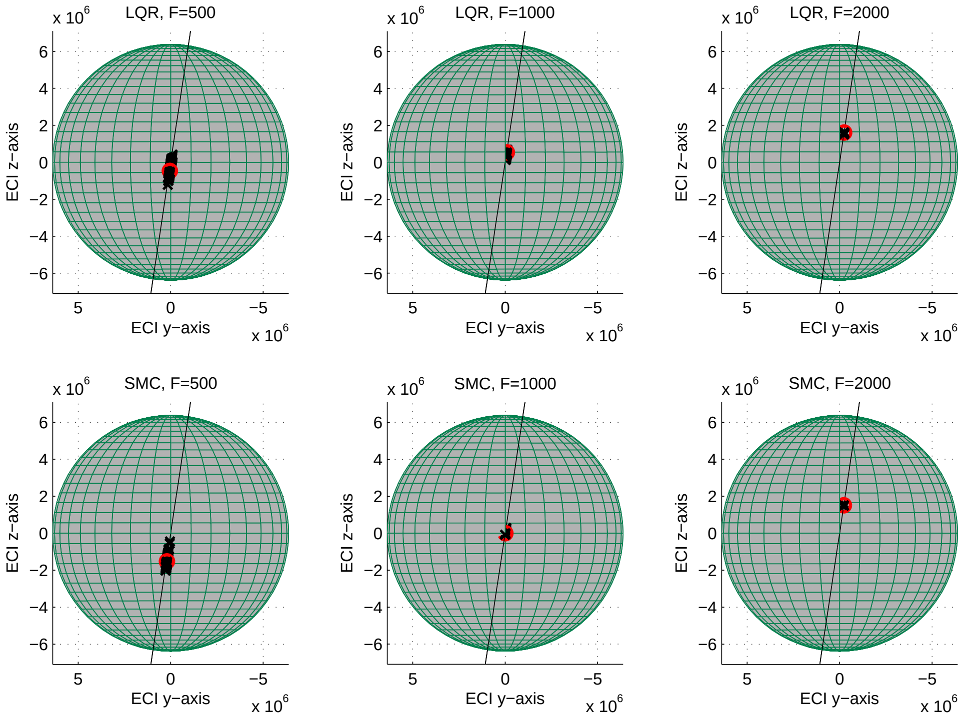

Figure 8.40: Locations of the terminal point on the sphere of the Earth, varying the initial conditions of the chaser. The red dot represents the nominal point, and the black line is the initial orbital plane.

ever, these disturbances do affect the effective magnitude of the deorbit burns, and will thus slightly affect the periapsis location and time. Thus, it is possible to determine the distance between each terminal point and the nominal point, and plot these in a histogram. This is done in Figure 8.41, with the sign of the offset being determined by the along-track position of the terminal point: a negative value indicates the terminal condition was reached “earlier”, and a positive value means the nominal point was overshot.

Figure 8.41 shows several additional trends than could be identified from Figure 8.40. First, it can be seen that, while not perfect, the distribution of the terminal conditions generally resembles a normal distribution: most results are close to the nominal point, with a decreasing number of outliers. Second, it is made clear again that the SMC system results in a tighter grouping of the terminal points than the LQR system. Finally, it is interesting to note that the LQR seems more biased towards overshooting the nominal point, while the SMC system tends to undershooting the nominal point.

Then, the sensitivity of the terminal point to each subset of the initial conditions of the chaser was investigated individually. Thus, the initial position, velocity, orientation, and angular rate were varied in separate simulations. However, as the SMC is more precise than the LQR, these simulations were only performed with the SMC system. For these simulations, again 130 runs were performed while randomly varying the initial conditions. The offsets between each terminal point and the initial point is visualized using histograms in Figures 8.42 through 8.45.

It can be seen from Figures 8.42 through 8.45 that no single subset of the initial conditions of the chaser is significantly more influential than others. Nonetheless, trends can still be identified: first, it can be seen that the grouping of the terminal points is most precise for errors in the initial attitude, being roughly a factor 2 higher than for scenarios introducing position or velocity errors. This can be explained by considering the fact that the tether is attached to the front of the chaser. Once the tether is in tension, the tensile force will pull the chaser into alignment with the tether line, thus aiding the control system in establishing the correct orientation.

This behavior can also be seen at the lower thrust levels for the initial angular rate errors. However, for $F = 2000\,\mathrm{N}$, the spread is much larger than when varying the initial attitude. Furthermore, the position and velocity errors result in very similar behavior and precision of the final points. Finally, the orders of magnitude

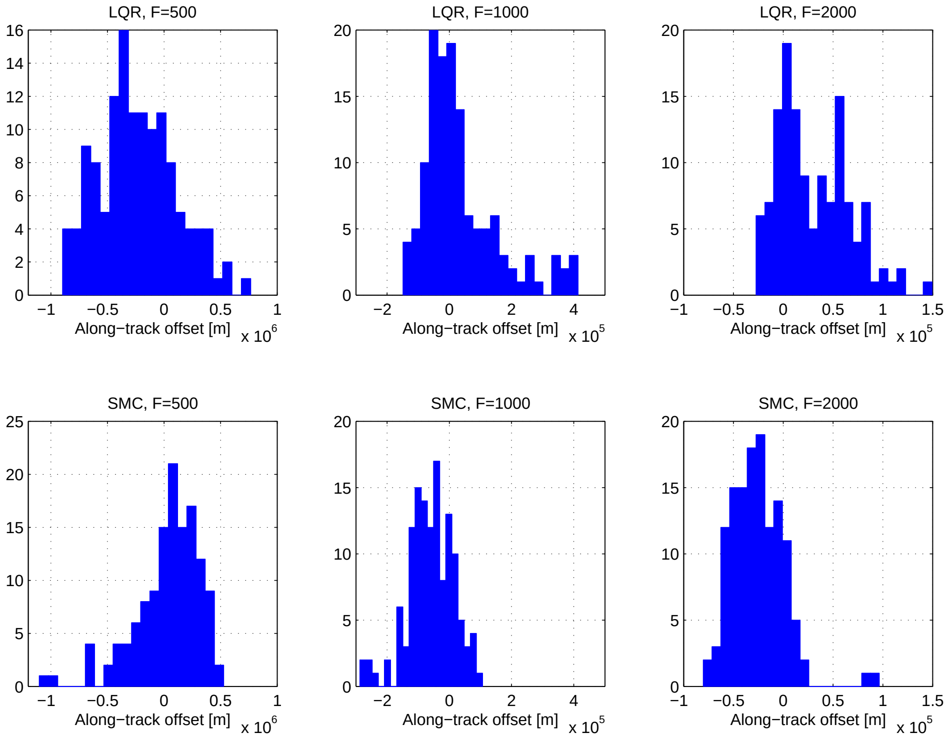

Figure 8.41: Histogram of the offset from the terminal points to the nominal point. A positive value indicates overshoot.

of the errors resulting from all types of perturbation are the same for each scenario: $1 \cdot 10^6$ m for $F = 500$ N, $3 \cdot 10^5$ m for $F = 1000$ N, and $4 \cdot 10^4$ m for $F = 2000$ N. Thus, it can be concluded that the simulation is equally sensitive to any type of perturbation.

8.3.2. SHORT AND LONG TETHER MODEL RESULTS

With the results obtained from the nominal tether model, it was decided to perform a full Monte Carlo analysis, varying all initial parameters, on the S_{nom} and L_{nom} models. Again, only the SMC system was used. The results for 130 runs of each combination of tether model and thrust level are shown in the histograms in Figure 8.46.

It can be seen that the S_{nom} and L_{nom} models generally behave in much the same way as the N_{nom} model: higher thrust levels generally indicate tighter grouping of the terminal points. However, several other effects can be observed. First, it can be seen that at $F = 2000$ N, the S_{nom} scenario has three significant outliers from the main grouping, at overshoot values of 50 km, 75 km, and 105 km. Such large overshoot values cannot be found in either the N_{nom} or L_{nom} scenarios at 2000 N of thrust.

Second, it can be seen that at low thrust values the S_{nom} scenarios are more precise than the L_{nom} scenarios: the maximum offsets are a factor 2 larger larger for the L_{nom} model compared to the S_{nom} model at 500 N and 1000 N of thrust. Furthermore, at 1000 N of thrust, the L_{nom} is strongly biased towards undershooting the nominal point, with a peak value at $-1.5 \cdot 10^5$ m, and does not show any results which overshoot the nominal point. This tendency of the L_{nom} model to undershoot is reflected by the $F = 500$ N scenario, which shows a peak at $-2 \cdot 10^5$ m. The S_{nom} model, on the other hand, is slightly biased towards overshoot at $F = 1000$ N, with a peak at $1.5 \cdot 10^5$ m, and is centered on the nominal value for $F = 500$ N.

Nonetheless, for each thrust level, the results for both the S_{nom} and L_{nom} models are generally in the same order of magnitude, excluding the significant outliers for the S_{nom} model at $F = 2000$ N. Furthermore, referring back to Figure 8.41, the orders of magnitude of the precision are comparable to those of the N_{nom} model. Therefore, it is concluded that the largest influence on the precision of the system comes from the choice of controller type and thrust level, rather than the tether model.

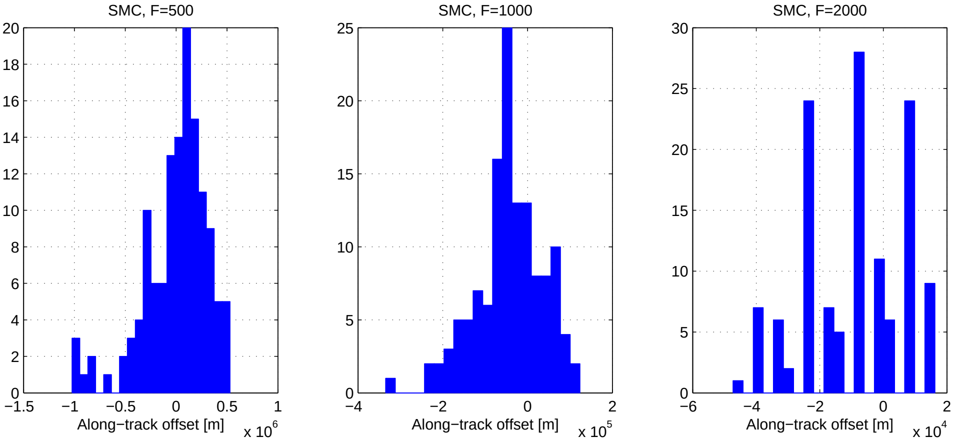

Figure 8.42: Histogram of the offset from the terminal points to the nominal point, when only varying initial position for the N_{nom} model. A positive value indicates overshoot.

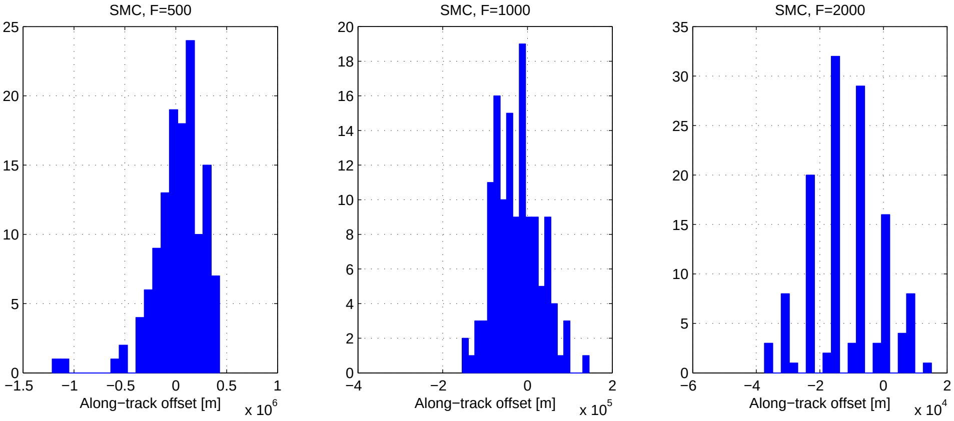

Figure 8.43: Histogram of the offset from the terminal points to the nominal point, when only varying initial velocity for the N_{nom} model. A positive value indicates overshoot.

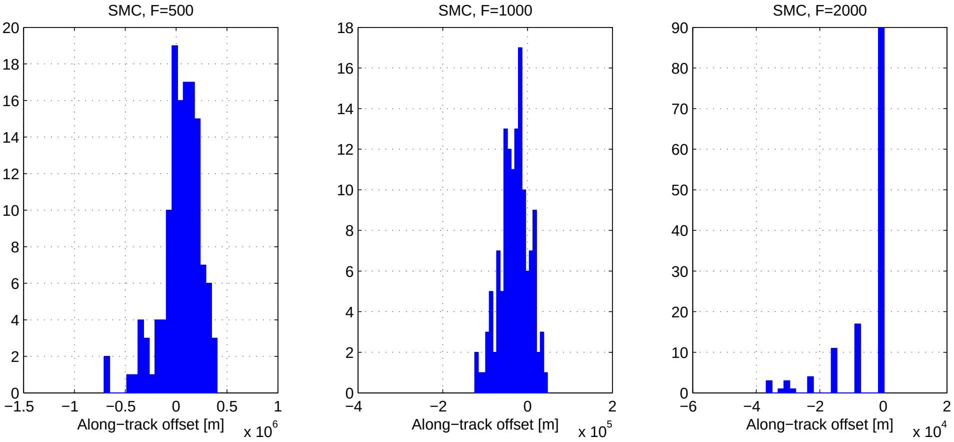

Figure 8.44: Histogram of the offset from the terminal points to the nominal point, when only varying initial orientation for the N_{nom} model. A positive value indicates overshoot.

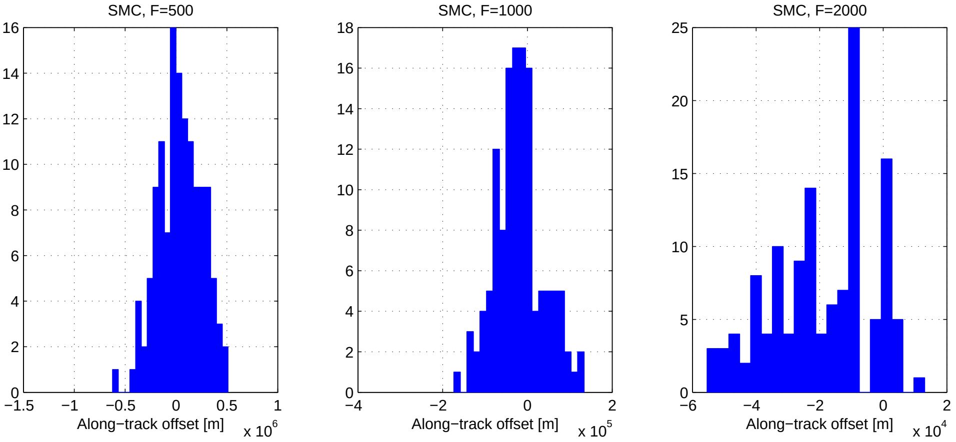

Figure 8.45: Histogram of the offset from the terminal points to the nominal point, when only varying initial angular rates for the N_{nom} model. A positive value indicates overshoot.

8.3.3. CONCLUDING REMARKS

From the performed Monte Carlo analyses, a number of conclusions can be drawn. First, it can be seen that the precision of the terminal points is highly dependent on the chosen thrust level: higher thrust levels, and thus shorter mission durations, increase the precision of the final solutions subject to disturbances. Also, the SMC system tends to be more precise than the LQR system. Furthermore, it was shown that this result is largely independent of which type of disturbance in the initial conditions is encountered, or which tether model is used.

Therefore, if high precision is desired, it is recommended to use higher thrust levels. This simply means that there is less time for perturbations to build up, as higher thrust levels indicate shorter mission times. It was also found that this result is independent of the tether length, and it is thus predicted that it will not be

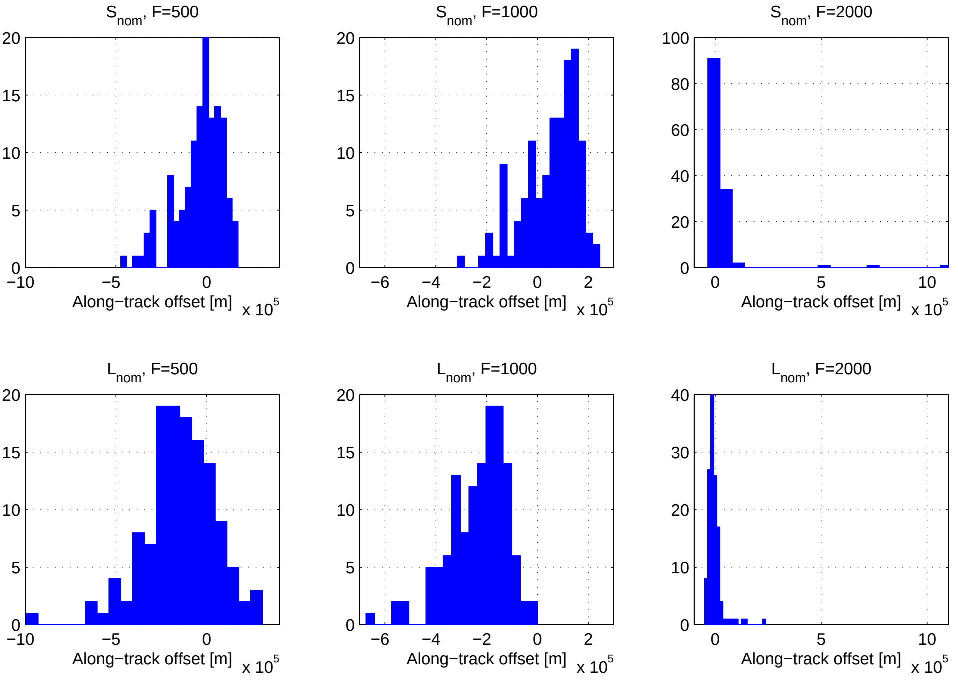

Figure 8.46: Histogram of the offset from the terminal points to the nominal point for the S_{nom} and L_{nom} models. A positive value indicates overshoot.

highly dependent on the physical tether parameters, either.

However, referring back to Figure 4.3, it can be seen that the general target zone on the surface of the Earth, the SPOUA, spans roughly from 30°S to 55°S, thus covering a latitude range of roughly 25°. It can be seen from Figure 8.40 that even with 500 N of thrust, the terminal points cover a region of roughly 15° latitude. Thus, all configurations with the N_{nom} model should be capable of deorbiting the target in the SPOUA, although the exact targeting is not considered here.

8.4. SELECTION OF SUITABLE MODELS

From the results presented in Sections 8.2 and 8.3, it is possible to select the most suitable combinations of tether models and controller options. As has been mentioned, the primary criteria by which the different options are judged are cost-effectiveness, safety, and reliability. In practice, this thus judges the different scenarios based on propellant consumption, tether wrapping, tether oscillations, and collision avoidance in case of main engine failure.

First of all, it can be concluded that as a whole, the SMC-based GC system offers significant reduction in propellant required with respect to the LQR-based system, while adhering to the same constraints. For this reason, it was decided to only consider the SMC system when selecting the most suitable models, due to these large performance gains.

Then, it was determined from Section 8.2.3 that target rotation was a primary driver for the safety, which in turn is a mission-critical requirement. Looking at total rotation angle, the five best simulation scenarios in terms of avoiding tether wrapping are listed in Table 8.9.

Table 8.9: Best SMC system results for target rotation.

Tether Model	**Thrust level [N]**	**Total rotation [rad]**
N_{nom}	2000	2.1
L_{HT}	2000	2.3
N_{LD}	2000	2.7
L_{LD}	2000	3.9
L_{nom}	1000	5.3

Table 8.10: Best SMC system results for propellant consumption.

Tether Model	**Thrust level [N]**	**Total propellant [kg]**
N_{nom}	2000	695.4
S_{nom}	2000	697.7
L_{HT}	2000	698.9
N_{LD}	2000	699.1
S_{LD}	2000	703.2
L_{nom}	1000	734.9

It can be seen that the best results all utilize high thrust levels. It is expected that the short mission times contribute to the low rotation angles: there is simply less time and opportunity for the target to build up significant rotation angles. However, it was seen in Section 8.2.2 that long tether models with nominal stiffness build up significant errors due to large relative velocities at 2000 N of thrust. For this reason, it was decided to discard the L_{LD} tether model at 2000 N as an option from Table 8.9. Due to the higher stiffness of the L_{HT} model, it does not suffer from the same large relative velocities and subsequent errors seen in the other long tether models at 2000 N thrust. Therefore, it was retained for analysis.

With respect to propellant consumption, it was determined in Section 8.2.1 that high thrust levels are the most beneficial when considering total required mission propellant. The five best results for total required mission propellant are shown in Table 8.10. Note that the L_{nom} model at 1000 N of thrust, while not part of this top five, was included as well, as it is a promising performer in terms of target rotation.

Furthermore, it was concluded in Section 8.3 that the high thrust levels which dominate Tables 8.9 and 8.10 are also the best in performance in terms of terminal precision. This result is independent of the tether model considered, and thus it can be concluded that all results shown in Tables 8.9 and 8.10 are good candidates with respect to being the least sensitive to varying initial conditions.

From these results, it seems as though the N_{nom} model at 2000 N thrust is the best option, as it requires the least amount of propellant while also inducing the lowest total rotation of the target. A close second is the L_{HT} model, also at 2000 N thrust, which is second best in terms of target rotation and third best in terms of total propellant consumption.

However, the final criteria on which the candidates would be judged was collision avoidance capability in the case of main engine failure. While strictly speaking this is not part of the nominal mission which was simulated, it is still an important consideration. It was concluded in Section 7.2 that for the N_{nom} model at 2000 N thrust, it would be practically impossible for the guidance system to avoid collision in the event of main thrust failure. This analysis can also be performed on the L_{HT} model at 2000 N thrust, to determine if this performs any better. Again, two cases were considered: first, the guidance thrusters were only fired in the negative y_H direction, and second, the guidance thrusters were fired in both the negative y_H ans the positive x_H direction. The results are shown in Figures 8.47 and 8.48.

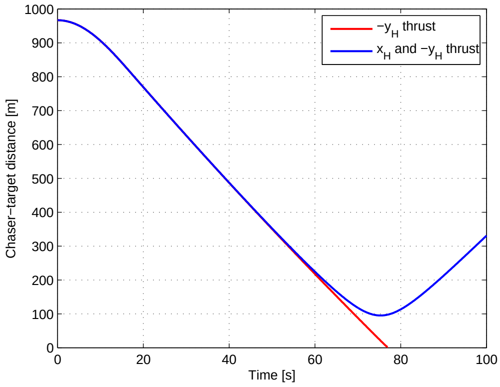

Figure 8.47: Chaser-target distance after main engine failure for L_{HT} at 2000 N thrust, with both guidance thrust cases.

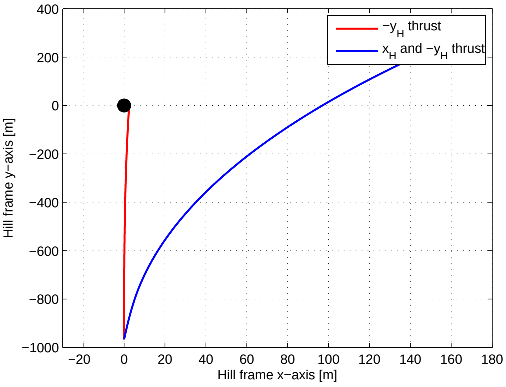

Figure 8.48: Trajectories in Hill frame corresponding to the situations in Figure 8.47, with the target in the origin.

It is clear from Figures 8.47 and 8.48 that solely firing the guidance thrusters towards the target is still not sufficient to avoid collision with the L_{HT} model at 2000 N thrust. However, it is definitely possible for the guidance system to avoid collision when applying an additional normal thrust, thus allowing the system to be recovered and collision to be avoided.

Therefore, the most suitable model for the proposed ADR is determined to be the L_{HT} model at 2000 N of thrust, using the developed SMC-based GC system. This system scores very well in terms of propellant requirement, target rotation, precision, and in collision avoidance capability, and proves that the concept is indeed feasible.

9

CONCLUSIONS AND RECOMMENDATIONS

Based on the results presented in Chapter 8, it is possible to draw a number of conclusions from the performed research. To do so, it is important to recall that the research question was as follows: “How can a tethered system of an active satellite and a large piece of space debris in Low-Earth Orbit be safely, reliably, and cost-effectively removed from orbit?’ Thus, the three primary drivers for the selection of the most appropriate model are reliability, safety, and cost-effectiveness.

From the research objectives, it was additionally made clear that there were two distinct areas of focus: first on the dynamics of the tethered system, and second on the preliminary design of a guidance and control system. Therefore, conclusions will first be drawn relating to both of these fields in Section 9.1. Then, since no research is entirely conclusive, recommendations for future research towards the topic of tethered ADR will be given in Section 9.2.

9.1. CONCLUSIONS

Referring back to Chapter 1, two main goals were defined for the performed research. First, it was necessary to achieve a good understanding of the dynamics of the tethered system, and in particular of the tether itself. This includes the effects of both different modeling parameters as well as different physical parameters of the tether. Second, different methods for providing guidance and control to this tethered system while successfully deorbiting the target were investigated. Therefore, these two aspects will be treated here.

9.1.1. TETHER MODELING

In essence, a single type of mathematical model for the tether dynamics was considered: the lumped-mass model. This model can, in principle, be implemented with any integer number of tether nodes. It was determined that, based on simulations of models with zero, two, four, ten, and twenty nodes, the general oscillatory behavior of the tether was only sufficiently modeled when using a nonzero number of nodes. Therefore, the zero-node model was discarded as a feasible option

Furthermore, it could be seen that while the observed oscillations were very similar for the models with nonzero nodes, the amplitude of these oscillations does slightly increase with increasing number of nodes. However, this came at the cost of CPU time, which increases significantly with the number of nodes in the model. Therefore, it was decided that a two-node tether model would be sufficient for this first-order design problem.

The physical parameters of the tether, being the natural length, Young’s modulus, and damping constant, were observed to have a large impact on the dynamical behavior of the tether. Tether lengths of 80 m, 200 m, and 800 m were considered, and for each length three different parameter combinations were examined: one with nominal stiffness E_{mat} of $1 \cdot 10^8$ Pa and a nominal damping constant c of 0.3 Ns/m, one with a high stiffness of $4 \cdot 10^8$ Pa and nominal damping, and one with nominal stiffness and a low damping of 0.001 Nm/s.

As a general rule, it was found that longer tethers oscillate at lower frequencies and larger amplitudes than shorter tethers, in agreement with classical harmonic oscillation theory. Furthermore, it was also found that lower damping coefficients generally result in larger amplitudes than tethers with nominal damping, both in the transverse and particularly in the longitudinal directions. These longitudinal oscillations can be clearly seen in the velocity of the tether nodes. Specific implications of the tether properties for the mission performance will be discussed next.

9.1.2. GUIDANCE AND CONTROL DESIGN

For the design of the guidance system, a technique guidance law was developed based on nominal-duration deorbit burns and stabilization of the relative state between the chaser and the target at all times during the mission. Likewise, the control system was developed around a single nominal attitude of the chaser at all times, being level with the local horizon. Then, two different control algorithms were used to determine the proper controls: a classical LQR and an SMC with linear switching surfaces also based on quadratic minimization. These GC systems were testes with varying thrust levels of 500 N, 1000 N, and 2000 N, respectively.

COST-EFFECTIVENESS

The propellant consumption of the chaser can be considered a measure of the cost-effectiveness of the system, as the chaser is physically the same for all performed simulations. It was found that the guidance system, rather than the control system or main engine controller, is the main driver for the required mission propellant. Generally speaking, the propellant required is also directly proportional to the mission duration. This implies that high thrust levels are necessary to only require a single burn, and thus deorbit the target within half an orbit. Furthermore, it was found that the SMC system requires significantly less propellant than the LQR system while maintaining a similar error margin.

The dependency of the performance on the tether parameters is more difficult to identify, as the tether itself is intrinsically a system which is very difficult to predict. Nonetheless, several conclusions can still be drawn. As mentioned, tethers with low damping coefficients will build up fast longitudinal oscillations, which adversely affect the amount of required propellant. It was also found that, on average, the length of the tether in itself did not significantly affect the amount of propellant: however, differences in specific system behavior, particularly during the establishment of the hold points, do cause significant differences to occur. Most of the system-specific behavior observed, coincidentally, highlight threats to either the safety or the reliability of the system, and thus will be discussed next.

Nonetheless, it was determined that high thrust levels of 2000 N offer the best performance in terms of overall required propellant. Particularly promising models were the short (80 m) and nominal-length (200 m) tether models with nominal stiffness, and the long tether model (800 m) with high stiffness.

9.1.3. SAFETY AND RELIABILITY

It was found for all investigated simulation scenarios, the designed GC system was able to successfully deorbit the target. While this suggests that the GC is inherently reliable, several phenomena were also identified which pose threats to the safety and reliability. Specifically, these aspects are related to the possibility of the tether wrapping around the target and the risk of collision between the chaser and target.

TARGET ROTATION

Further threats to the safety and reliability of the mission were identified in rotation of the target: due to its passive state, the target will tend to accumulate large rotations when subjected to moments from the tether. These rotations were found to be significant in all but a select few of the simulation scenarios, and are highly dependent on the tranquilization method following each burn.

Even so, a number of scenarios was able to successfully prevent the target from rotating. As with the best options for propellant consumption, these generally used high thrust levels with an SMC-based GC system. The most promising models included the nominal-length models with nominal stiffness and the long tether models with high tension and low damping respectively.

COLLISION AVOIDANCE

When considering a system of two satellites connected by an elastic tether, possible collision is always a very real threat to the safety of the mission. Thus, at the end of each burn, a tranquilization method was used which approximates critically damped behavior by linearly throttling the main engines down at the end of each burn.

Finally, the safety of the system was investigated in the case of failure. Two major failure modes stand out: failure of the main engine and failure of the tether. It was found that failure of the tether would not result in an unsafe situation, as the chaser would be able to maneuver away from the target with relative ease. This is particularly evident during a main engine burn, as the chaser would proceed to accelerate away from the target if the tether is severed.

Failure of the main engines, though, was identified as a crucial failure mode. If the main engines fail during a deorbit burn with a 200 m tether, the guidance system of the chaser is not able to fully nullify the relative velocity of the chaser before colliding with the target, when starting from thrust levels of 1000 N or 2000 N. Therefore, it would be necessary to apply thrust in the outward radial direction as well to avoid collision, in which case it would still be impossible to avoid the target for a thrust level of 2000 N. Additionally, this problem is exacerbated when using short tethers.

While this result seemed to discount the possibility of using high thrust levels from a safety perspective, it was proven that a long tether with high tension is well-capable of avoiding collision in the case of main engine failure, even at 2000 N thrust. This is simply due to the larger distance between the chaser and target, allowing the chaser more time to recover.

Therefore, it was concluded that the best scenario was to use a long tether with high tension at a thrust level of 2000 N with an SMC-based GC system. This system scores exceptionally well in terms of propellant requirement, requiring a total of 698.9 kg of bipropellant, and prevents the target from rotating more than 2.3 rad. Furthermore, it was proven that the system is able to avoid collision in the case of main engine failure.

9.2. RECOMMENDATIONS

The results of the performed research also provide ample opportunities for recommendations for future research. As with the conclusions in the previous section, these recommendations will be given for both the modeling of the tether as well as the design of the GC system. These will also highlight shortcomings of the model used for the performed research, and expected severity of these shortcomings.

9.2.1. TETHER MODELING

When considering the used dynamical model of the tether, it is important to consider the fact that only two nodes were used for rapid first-order analysis. As has been mentioned, the general behavior of a two-node tether was comparable to the behavior of a twenty-node tether in frequency, but displayed differences when considering the amplitude of the oscillations. It is unknown which of the two, however, provide the most valid model of actual tether motions in orbit, which is definitely worth additional research.

Of course, it is possible that better techniques exist to model the tether than the lumped-mass model. Developing such methods could increase the fidelity of the solution, as well as lower the required CPU time. However, to really improve the tether model, it would also be essential to have validation data on the actual motion of orbital tethers under similar circumstances: This would not only allow examination of the precision of the tether models, but of the accuracy as well.

Also, the tether wrapping itself around the target was identified as a potential hazard. This effect is currently not simulated, and while it should, of course, be avoided in some manner, having the ability to model this phenomenon would nonetheless be a valuable addition to the simulation. This would also allow contingency plans to be developed and simulated in the case that tether wrapping would occur.

Finally, in retrospect, only a very finite number of data points was examined: three distinct lengths with three different combinations of two different parameters. While this theoretically should provide a decent first-order look at the influence of each of the parameters, too many anomalous values were present in the simulation results to quantify these relations properly. Furthermore, no attention was paid to the material and physical validity of these values, as these were simply provided [3]. Therefore, more research towards the influence of the tether length, stiffness, and damping on the behavior of the TSDS as a whole is an area where much can be gained.

In terms of more generic modeling of the system dynamics, the addition of flexible appendages to the chaser and target would make a far more realistic model. This is because the chaser and target will have solar panels, which are sufficiently large to display flexible modes. This was identified by ESA as an area to be included in the research towards tethered ADR, as well [3]. Furthermore, there are slight differences in size between the proposed target model and the actual parameters of Envisat [7], particularly in the size of the solar panel.

9.2.2. GUIDANCE AND CONTROL DESIGN

The guidance and control system, while effective in the current simulation at deorbiting the target successfully, also provide plenty of room for improvement. First of all, the designed GC system is by no means an optimal one. The control parameters for both the LQR and SMC were based on order of magnitude analysis, and could therefore potentially reduce the amount of propellant required for the mission. Also, the SMC was built around one particular method of constructing the switching surfaces, as well as one particular method of determining the controls. A plethora of options exist for SMC design [11], and it is therefore unknown if the most suitable option has been selected.

Furthermore, the guidance trajectory is simply based on multiple burns with a fixed nominal duration, and also by no means represents an optimal deorbit trajectory. Besides a possible further reduction in propellant mass, an optimal deorbit trajectory should also include exact timing and targeting, which has not been investigated in this research. However, it has been shown that the current model would be able to deorbit the target within the SPOUA when subject to perturbed initial conditions.

It has also been assumed that the main engines are throttleable, to allow for a more efficient tranquilization phase at the end of each deorbit burn. It is not known if the current generation of spacecraft engines have this capability, which would be essential for the realization of the currently used guidance strategy. If it is not possible, the development of a completely new type of engine could lead to significant additional mission costs, also providing a threat to the mission as a whole.

Further attention must additionally be paid to contingency plans in the event of main engine failure. While it has been demonstrated that with longer tethers and lower thrust levels it is possible to avoid collision in this case, it is important to define plans which will not only avoid collision but also still allow the mission to continue in the case of main engine failure. This might therefore influence the amount of propellant required, or could allow different simulation scenarios to be discarded as infeasible *a priori*.

Additionally, the design of a navigation system has been left out of the performed research, while the design of such a system is distinctly nontrivial. Actually obtaining sufficiently accurate information of a completely passive target is a difficult task to achieve, and the design of this system would be a major step towards the actual implementation of an ADR system.

The most important addition to the GC system, however, would be the inclusion of a system to control the rotation of the target through the tether: while scenarios with the current GC system were found which successfully minimized target rotation, it is uncertain if these results are stable. Thus, a dedicated controller monitoring target rotation would be a valuable addition to the global stability of the found solution. This could for instance be a more advanced guidance system, using the guidance thrusters to apply the correct amount of tension to tranquilize the target, but could also be a system which would be able to control the tension in the tether through for instance a winch. As target rotation embodies one of the greatest threats to the reliability, and indirectly to the safety, of the system, the addition of such a system would be essential to reliably complete the actual mission.

BIBLIOGRAPHY

[1] NASA, *Orbital Debris Quarterly News - Satellite Collision Leaves Significant Debris Clouds,* Available at: http://orbitaldebris.jsc.nasa.gov/newsletter/pdfs/ODQNv13i2.pdf (2009), [Online; accessed 01-November-2013].

[2] Kessler, D. J., Johnson, N. L., Liou, J.-C., and Matney, M., *"The Kessler Syndrome: Implications to Future Space operations", 33rd Annual AAS Guidance and Control Conference,* 6-10 February 2010 (2010).

[3] European Space Agency, *"Statement of Work: Advanced GNC for Active Debris Removal (AGADR)", ESA Document* Appendix 1 to ESA ITT AO/1-7477/13/NL/MH (ESA Estec, 2013).

[4] ESA Earthnet Online, *Envisat - Earthnet Online,* Available at: https://earth.esa.int/web/guest/missions/esa-operational-eo-missions/envisat (2013), [Online; accessed 30-August-2013].

[5] Biesbroek, R.; Hüsing, J.; Wolahan, A., *System and Concurrent Engineering for the e.Deorbit Mission Assessment Studies,* Available at: http://congrexprojects.com/docs/default-source/14c08_docs/system-and-concurrent-engineering-for-the-e-deorbit-mission-assessment-studies.pdf?sfvrsn=0 (2014).

[6] Biesbroek, R., *The e.Deorbit CDF Study - A design study for the safe removal of a large space debris,* Available at: http://iaassconference2013.space-safety.org/wp-content/uploads/sites/19/2013/06/1200_Biesbroek_Innocenti.pdf (2013).

[7] J. A. F. Deloo, *Analysis of the Rendezvous Phase of e.deorbit,* Master's thesis, Delft University of Technology (2015).

[8] Mooij, E.; Ellenbroek, M. H. M., *Rapid Prototyping Technology - Principles and Functional Requirements, Chapter 15* (InTech, 2011).

[9] Mooij, E., *AE4870B - Re-entry Systems* (TU Delft, 2011) [Lecture notes].

[10] Flemming, J.; Benoit, A.; Mignot, J.; Laurens, P., *"ECSS-E60 Control Engineering Standardisation",* in *Proceedings of 6th International ESA Conference on Guidance, Navigation and Control Systems. Loutraki: ESA* (2005).

[11] DeCarlo, R. A., Zak, S. H., and Matthews, G. P., *"Variable structure control of Nonlinear Multivariable Systems: A Tutorial", Proceedings of the IEEE* **76**, 312 (1988).

[12] Wertz, J. R., *Space Mission Engineering: The New SMAD* (Microcosm Press, 2011).

[13] Stansbery, E., and Brown, M., *Orbital Debris Graphics,* Available at: http://orbitaldebris.jsc.nasa.gov/photogallery/beehives.html (2012), [Online; accessed 02-June-2014].

[14] Inter-Agency Space Debris Coordination Committee, *IADC Space Debris Mitigation Guidelines - Revision 1,* (2007).

[15] Goodman, J. C., *"History of Space Shuttle Rendezvous and Proximity Operations", Journal of Spacecraft and Rockets* **43**, 944 (2006).

[16] Bauduin, P., *STS-51A,* Available at: http://weebau.com/flights/sts51a.htm (2006), [Online; accessed 02-June-2014].

[17] Liou, J. C., *"An active debris removal parametric study for LEO environment remediation", Advances in Space Research* **47**, 1865 (2011).

[18] Schall, W. O., *"Orbital debris removal by laser radiation", Acta Astronautica* **24**, 343 (1991).

[19] Monroe, D. K., *"Space debris removal using high-power ground-based laser"*, SPIE Proceedings **2121**, 276 (1994).

[20] Phipps, C. R. et al., *"Removing orbital debris with lasers"*, *Advances in Space Research* **49**, 1283 (2012).

[21] Bonnal, C., Ruault, J.-M., and Desjean, M.-Ch., *"Active debris removal: Recent progress and current trends"*, Acta Astronautica **85**, 51 (2013).

[22] Martin, Th., Pérot, E., Desjean, M.-Ch., and Bitetti, L., *"Active Debris Removal Mission Design in Low Earth Orbit"*, Progress in Propulsion Physics **4**, 763 (2013).

[23] Pergola, P., Ruggiero, A., and Andrenucci, M., *"Low-thrust Missions for Expanding Foam Space Debris Removal"*, *32nd International Electric Propulsion Conference*, 11-15 September 2011 (2011).

[24] Bombardelli, C., and Pelaez, J., *"Ion Beam Shepherd for Contactless Space Debris Removal"*, *Journal of Guidance, Control, and Dynamics* **34**, 916 (2011).

[25] Forward, R. L., Hoyt, R. P., and Uphoff, C. W., *"Terminator Tether™: A Spacecraft Deorbit Device"*, *Journal of Spacecraft and Rockets* **37** (2000).

[26] Uphoff, C. W., Forward, R. L., and Hoyt, R. P., *The 'terminator tether': An efficient mechanism for end-of-life deorbit of constellation spacecraft,* in *Mission Design & Implementation of Satellite Constellations*, Space Technology Proceedings, Vol. 1 (Springer Netherlands, 1998) pp. 347–365.

[27] Heide, E. J. van der, and Kruijff, M., *"Tethers and debris mitigation"*, *Acta Astronautica* **48**, 503 (2001).

[28] Pardini, C., Hanada, T., Krisko, P. H., Anselmo, L., and Hirayama, H., *"Are de-orbiting missions possible using electrodynamic tethers? Task review from the space debris perspective"*, *Acta Astronautica* **60**, 916 (2007).

[29] Pardini, C., Hanada, T., and Krisko, P. H., *"Benefits and risks of using electrodynamic tethers to de-orbit spacecraft"*, *Acta Astronautica* **64**, 571 (2009).

[30] Bombardelli, C., Herrera Montojo, J., Peláez, J., and Iturri-Torrea, A., *"Space Debris Removal with Bare Electrodynamic Tethers"*, *Proceedings of 20th AAS/AIAA Space Flight Mechanics Meeting*, 14-17 February 2010 (2010).

[31] Nishida, S.-I. et al., *"Space debris removal system using a small satellite"*, *Acta Astronautica* **65**, 95 (2009).

[32] Levin, E., Pearson, J., and Caroll, J., *"Wholesale debris removal from LEO"*, Acta Astronautica **73**, 100 (2012).

[33] Pearson, J., Caroll, J., Levin, E., and Oldson, J., *"Active debris removal: EDDE, the electrodynamic debris eliminator"*, in *Proceedings of 61st International Astronautical Congress. Prague: IAC* (2010).

[34] Woffinden, D. C., and Geller, D. K., *"Navigating the Road to Autonomous Orbital Rendezvous"*, *Journal of Spacecraft and Rockets* **44**, 898 (2007).

[35] Polites, M. E., *"Technology of Automated Rendezvous and Capture in Space"*, *Journal of Spacecraft and Rockets* **36**, 280 (1999).

[36] White, M., *JSC Digital Image Collection,* Available at: `http://images.jsc.nasa.gov/luceneweb/caption.jsp?searchpage=true&selections=GT8&browsepage=Go&hitsperpage=5&pageno=10&photoId=S66-25784` (2006), [Online; accessed 02-June-2014].

[37] Kauderer, A., and Dunbar, B., *NASA - Space Station Assembly Elements,* Available at: `http://www.nasa.gov/mission_pages/station/structure/assembly_elements.html` (2013), [Online; accessed 07-May-2013].

[38] Petty, J. I., and Dunbar, B., *NASA - Automated Transfer Vehicle,* Available at: `http://www.nasa.gov/mission_pages/station/structure/atv.html` (2012), [Online; accessed 07-May-2013].

[39] Kauderer, A., and Dunbar, B., *NASA - Dragon,* Available at: `http://www.nasa.gov/mission_pages/station/structure/elements/dragon.html` (2013), [Online; accessed 07-May-2013].

[40] Wright, J., and Dunbar, B., *NASA - Cygnus,* Available at: `http://www.nasa.gov/mission_pages/station/structure/elements/cygnus.html` (2013), [Online; accessed 23-October-2013].

[41] Chen, Y., Huang, R., Ren, X., He, L., and He, Y., *"History of the Tether Concept and Tether Missions: A Review", ISRN Astronomy and Astrophysics,* Vol. 2013, Article ID 502973 (2013).

[42] Ryba, J., and Dunbar, B., *NASA - STS-75,* Available at: `http://www.nasa.gov/mission_pages/shuttle/shuttlemissions/archives/sts-75.html` (2007), [Online; accessed 12-May-2013].

[43] Kramer, H. J., *Space Tethers - eoPortal Directory - Satellite Missions,* Available at: `https://directory.eoportal.org/web/eoportal/satellite-missions/s/space-tethers` (2002), [Online; accessed 02-June-2014].

[44] White, M., *JSC Digital Image Collection,* Available at: `http://images.jsc.nasa.gov/luceneweb/caption.jsp?searchpage=true&photoid=sts075-701-087&hitsperpage=5&photoidsearch=Go&pageno=1&photoId=sts075-701-087` (2006), [Online; accessed 02-June-2014].

[45] Kruijff, M., Heide, E. J. van der, Ockels, W. J., and Gill, E., *"First Mission Results of the YES2 Tethered SpaceMail Experiment", AIAA/AAS Astrodynamics Specialist Conference and Exhibit,* 18-21 August 2008 (2008).

[46] Cartmell, M. P., and McKenzie, D. J., *"A review of space tether research", Progress in Aerospace Sciences,* Vol. 44, No. 1, January 2008, pp. 1-21 (2008).

[47] Kumar, K., and Kumar, K. D., *"Variable attitude maneuver through tether for a 'drifting' twin satellite system in elliptic orbits", Acta Astronautica* **55**, 135 (1999).

[48] Nordley, G., *"Tether-Tossed Mars Mission Examples", 37th AIAA/ASME/SAE/ASEE Joint Propulsion Conference and Exhibit,* 8-11 July 2001 (2001).

[49] Kumar, K. D., and Yasaka, T., *"Satellite Attitude Stabilization Through Kite-Like Tether Configuration", Journal of Spacecraft and Rockets* **39** (2002).

[50] Cho, S., and McClamroch, N. H., *"Attitude Control of a Tethered Spacecraft", American Control Conference, 2003 IEEE,* pp. 1104-1109 (2003).

[51] Wakker, K. F., *Course AE4874, Part 1 - Astrodynamics-I* (TU Delft, 2010) [Lecture notes].

[52] Vallado, D. A., and McClain, W. D., *Fundamentals of Astrodynamics and Applications* (The McGraw-Hill Companies, Inc., 1997).

[53] ESA, *Making sure ATV reentry is safe,* Available at: `http://blogs.esa.int/atv/2013/10/30/making-sure-atv-reentry-is-safe/` (2013), [Online; accessed 20-January-2015].

[54] Mooij, E., *"Orbit-State Model Selection for Solar-Sailing Mission Optimization", AIAA/AAS Astrodynamics Specialist Conference,* 13-16 August 2012 (2012).

[55] Vallado, D. A., *Fundamentals of Astrodynamics and Applications - Second Edition* (Springer, 2001).

[56] Hintz, G. R., *"Survey of Orbit Element Sets", Journal of Guidance, Control, and Dynamics* **31** (2008).

[57] Vittaldev, V., Mooij, E., and Naeije, M., *"Unified State Model theory and application in Astrodynamics", Celestial Mechanics & Dynamical Astronomy* **112**, 253 (2012).

[58] Sidi, M. J., *Spacecraft Dynamics and Control: A Practical Engineering Approach* (Cambridge University Press, 1997).

[59] Wie, B., *Space Vehicle Dynamics and Control - Second Edition* (AIAA, 2008).

[60] Crassidis, J. L., and Markley, F. L., *"Sliding mode control using modified Rodrigues parameters", Journal of Guidance, Control, and Dynamics* **19**, 1381 (1996).

[61] Diebel, J., *Representing Attitude: Euler Angles, Unit Quaternions, and Rotation Vectors,* Available at: http://www.swarthmore.edu/NatSci/mzucker1/e27/diebel2006attitude.pdf (2006), [Online; accessed 10-July-2013].

[62] Wertz, J. R., *Orbit & Constellation Design & Management* (Microcosm Press, 2009).

[63] Montenbruck, O., and Gill, E., *Satellite Orbits - Models, Methods, and Applications* (Springer, 2000).

[64] Wakker, K. F., *Course AE4874, Part 2 - Astrodynamics-II* (TU Delft, 2010) [Lecture notes].

[65] Picone, J. M., Hedin, A. E., Drob, D. P., and Aikin, A. C., *"NRLMSISE-00 empirical model of the atmosphere: Statistical comparisons and scientific issues", Journal of Geophysical Research* **107** (2002).

[66] NRL, *NRLMSISE-00: A New Empirical Model of the Atmosphere - U.S. Naval Research Laboratory,* Available at: http://www.nrl.navy.mil/research/nrl-review/2003/atmospheric-science/picone/ (2003), [Online; accessed 01-November-2013].

[67] Ellenbroek, M. H. M., Mooij, E., and Oort, M. J. A., *Detailed Design of the GGNCS - Issue 1, Revision 0* (Dutch Space, 2007).

[68] Yamaigiwa, Y., Hiragi, E., and Kishimoto, T., *"Dynamic behavior of electrodynamic tether deorbit system on elliptical orbit and its control by Lorentz force", Aerospace Science and Technology* **9**, 366 (2005).

[69] Inman, D. J., *Engineering Vibrations - Third Edition* (Pearson Education, Inc., 2009).

[70] Lay,, D. C., *Linear Algebra and Its Applications - Third Edition* (Pearson Education, Inc., 2006).

[71] Paraskevopoulos, P. N., *Modern Control Engineering* (Marcel Dekker, Inc., 2002).

[72] Edwards, C.; Spurgeon, S. K., *Sliding Mode Control - Theory and Applications* (Taylor & Francis, 1998).

[73] Vadali, S. R., *"Variable-Structure Control of Spacecraft Large-Angle Maneuvers", Journal of Guidance* **9**, 235 (1986).

[74] Dwyer III, T. A.; Sira-Ramirez, H., *"Variable-Structure Control of Spacecraft Attitude Maneuvers", Journal of Guidance, Control, and Dynamics* **11**, 262 (1988).

[75] Utkin, V. I., *"Variable Structure Systems with Sliding Modes", IEEE Transactions on Automatic Control* **AC-22**, 212 (1977).

[76] Yang, Y., *"Analytic LQR Design for Spacecraft Control System Based on Quaternion Model", Journal of Aerospace Engineering* **25**, 448 (2012).

[77] MathWorks Benelux, *Simulink Documentation,* Available at: http://www.mathworks.nl/help/simulink/ (2013), [Online; accessed 17-October-2013].

[78] MathWorks Benelux, *MATLAB® ode45,* Available at: http://www.mathworks.nl/help/matlab/ref/ode45.html (2013), [Online; accessed 01-November-2013].

[79] Airbus Defence & Space, *500N Bipropellant European Apogee Motor,* Available at: http://cs.astrium.eads.net/sp/spacecraft-propulsion/apogee-motors/500n-apogee-motor.html (2015), [Online; accessed 9-March-2015].

[80] Blau, P., *ATV-4 Mission Updates - Spaceflight101,* Available at: http://www.spaceflight101.com/atv-4-mission-updates.html (2013), [Online; accessed 9-March-2015].

[81] Airbus Defence & Space, *10N Bipropellant Thruster,* Available at: http://cs.astrium.eads.net/sp/spacecraft-propulsion/bipropellant-thrusters/10n-thruster.html (2015), [Online; accessed 9-March-2015].

[82] Adams, D., *The Hitchhiker's Guide to the Galaxy* (Pan Books, 1979).